Conductive Metal-Organic Framework Percolation Networks for Chemiresistive Gas Sensing

A thesis submitted for the degree of Doctor of Philosophy

Runze Chen

St. Anne's College

Department of Materials, University of Oxford

Trinity Term 2025

Preface

The studies described in the thesis were all carried out by the author, under the supervision of Prof. Martin R. Castell, at the Department of Materials at the University of Oxford, from October 2021 to September 2025. All the work is original and has not been previously submitted for any degree or qualification at this university or any other institute of education. Where the work of other researchers is drawn upon, it has been referenced and acknowledged. Parts of the work described in Chapters 4 and 5 have been presented at international conferences and/or submitted to peer-reviewed journals as follows:

Conferences

Runze Chen, Abigail M. Lister, Weishuo Li, and Martin R. Castell. "Nanostructured Metal-Organic Framework Percolation Networks for Chemiresistive Gas Sensing via Polystyrene Particles", 6th European Conference on Metal Organic Frameworks and Porous Polymers, Crete, Greece, 2025. (Poster)

Runze Chen, Weishuo Li, Abigail M. Lister, and Martin R. Castell. "Metal-Organic Framework-based Percolation Networks for Gas Sensors with High Sensitivity", 7th Annual UK Porous Materials Conference, Liverpool, UK, 2024. (Poster)

Runze Chen, Weishuo Li, Abigail M. Lister, and Martin R. Castell. "Metal-Organic Framework-based Percolation Network Gas Sensors via Electrochemical Synthesis", 1st Mediterranean Conference on Porous Materials, Crete, Greece, 2023. (Poster)

Approximate word count of this thesis: 37,000 words.

Acknowledgements

For us, there is only the trying. The rest is not our business.

— T. S. Eliot

This thought has accompanied me through the long and demanding journey. I owe this sense of completion to those who stood beside me—above all to my supervisor, Professor Martin Castell. We gave each other the occasional headache—his, I'm afraid, mostly from my all-too-simple mistakes. He now has surely developed an impressive toolkit for treating them; and I, thanks to his patience, have grown into a trained researcher. I could not have reached this point without his guidance and support.

I also owe special thanks to Weishuo and Abi, whose guidance supported and enabled me to start and go through my DPhil projects. I am also grateful for my friends and colleagues in the Surface Nanoscience group—Liren, Yu Wang, Axel, Sparsh, and Zirui—for their kind help. I am lucky to have Jiahao, Jin-chong, Yu Shu, and Mengyun as my collaborators; their collaboration and steady support sustained this work. Thanks to Clara, Jarrod, and Mengqi for their help in XRD experiments. Thanks to Neil and Phani for their help in electron microscopy.

I am beyond grateful to my loving parents; without their nurture, I could not have come this far. My mother was born in a very small village—so small that it had only one street, visible from end to end at a glance. She once told me that the first time she rode a long-distance bus to the city for university, the little brook along the road slowly widened into a great river; as the water grew broader, her tears would not stop. With my parents' support, I have seen the Yangtze River and, at last, come to the United Kingdom. Standing by the Thames, I find my thoughts overflowing.

I also owe my deepest thanks to my wife for her long company and support. I met my wife while studying at Oxford; our story began with London's first snowfall and the sound of an erhu. From then on, a single certainty entered a life full of uncertainties. During my DPhil journey, people I knew left one by one, but she stayed—for me—and since then I have had a small home of my own in this world. We have supported and understood each other throughout. Without her love, I would have struggled to endure the long and cold winter nights in the UK, year after year.

I am grateful to the University of Oxford for providing a remarkable platform—not only for research but also for pursuing new interests. Here I discovered new passions and had the chance to try many sports. I joined the Fencing Club and learned to fence; I went skiing with friends from my college; and I have become intrigued by tennis, which I hope to continue. When my research faltered, these activities helped me manage pressure and stay balanced.

Thanks to everyone and everything I encountered on this journey. Thanks for having the air in my lungs and a few blank pages to fill. May we all make each day count.

Abstract

Chemiresistive gas sensors are used in industrial safety, healthcare, and domestic settings. Most commercially available chemiresistors use metal oxide semiconductors as the active material, which typically require high operating temperatures above 300°C. In contrast, conductive metal-organic frameworks (c-MOFs) have emerged as promising alternatives for developing room-temperature chemiresistors. To date, efforts to enhance the sensitivity of c-MOF-based sensors have primarily focused on the fabrication of thin films.

Percolation networks have been designed to improve the sensitivity of gas sensors based on polymers and metal oxides. Unlike conventional continuous films, the percolation approach involves controlling the material growth to produce networks with limited electrical bridges. These percolation networks are highly responsive to target analytes, as small changes in the limited conduction pathways lead to pronounced changes in electrical resistance. In this thesis, this percolation-based design principle is systematically applied to develop c-MOF percolation networks, and these are shown to have significantly improved sensitivities compared with their thin film counterparts.

The first study investigates the development of percolation networks using an electrochemical deposition strategy. By running the reaction for different durations, sensors representing different MOF growth stages were developed, enabling the identification of those operating in the percolation region.

To further improve the sensitivity, a template-assisted nanostructuring technique was introduced. Polystyrene (PS) nanoparticles were deposited on substrates as a sacrificial template. C-MOFs were then electrochemically deposited onto the templates with controlled

growth. By removing the PS templates using a solvent, c-MOF percolation networks with porous architectures were developed.

Additionally, electrohydrodynamic (EHD) jet printing was also explored to develop MOF percolation networks. By adjusting the ligand-to-metal ratio in the printed inks, the degree of electrical connectivity within the MOF structures was modulated. Inks with lower ligand content produced less interconnected c-MOFs, enabling the formation of percolation networks.

Finally, a simpler strategy based on drop-casting conductive-insulating composites was investigated. In this method, PS was selected as the insulating matrix and a solution-processable c-MOF was developed as the conductive filler. By tuning the PS-to-MOF ratio, sensors operating within the percolation region were successfully fabricated, providing a scalable and accessible alternative for constructing c-MOF percolation networks.

Overall, this thesis demonstrates that percolation theory offers an effective design principle for significantly enhancing the sensitivity of c-MOF-based chemiresistive gas sensors. Through the systematic implementation of diverse strategies, a versatile platform was established for developing high-performance, room-temperature c-MOF percolation gas sensors. These findings not only enrich current sensor design methodologies but also broaden the practical potential of c-MOFs in next-generation gas sensing technologies.

Contents

Chapter 1

Introduction

In recent years, the demand for sensitive gas detection technologies has grown significantly across various fields, including environmental monitoring, industrial safety, healthcare, and domestic applications. Chemiresistive gas sensors are one of the most widely researched and applied technologies for gas detection owing to their simplicity, scalability, and low cost. These sensors operate by detecting changes in electrical resistance that occur when gas molecules interact with the sensing material. When a target gas is introduced to the sensing environment, it either donates or extracts electrons from the surface of the sensing material, resulting in a measurable change in electrical conductivity. This change is then correlated with the gas concentration, allowing for quantitative sensing.

Metal oxide semiconductors (MOS) are the most widely commercialised materials used in chemiresistive gas sensors, known for their stability and cost-effectiveness. However, MOS sensors require elevated operating temperatures (typically above 300°C) to achieve optimal sensitivity, which can limit their suitability in low-power or portable applications.

Conductive metal-organic frameworks (c-MOFs) hold significant potential for use as the active material for chemiresistive gas sensors operating at room temperature. By combining the conductive pathways with structural advantages of MOFs, including high porosity, high specific surface area, and tunable structure, these materials enable improved electron transport, enhanced sensitivity, and lower operating temperatures compared with conventional sensors based on conventional MOFs or MOS.

However, challenges remain in fabricating effective c-MOF-based sensing layers. C-MOF powders are typically synthesised via solvothermal methods, and these powders are then applied to form sensing layers on chemiresistive sensors using ex-situ coating techniques. This approach often leads to a random distribution of c-MOF particles on the substrate, which can cause aggregation in localised areas, reducing the effective surface area available for gas interactions. Furthermore, the large grain size of the MOF particles often results in poor contact between grains and at the grain-to-electrode interface, creating high contact resistance. The resulting high contact resistance undermines the sensitivity as it is relatively unresponsive to gas analytes. Even though c-MOF nano-thin films have been explored to enhance performance, their excessive electrical pathways and inefficient gas diffusion have resulted in only modest improvements compared with the powder-based counterparts.

Percolation theory offers an effective strategy to enhance chemiresistive sensing performance, as established in polymer or MOS materials. In the context of chemiresistive gas sensors, long-range connectivity of sensing materials emerges once the system crosses the percolation threshold, the critical fraction of conducting elements at which a continuous electrical bridge forms across an otherwise insulating matrix or substrate. By designing materials to achieve or surpass this threshold, chemiresistive percolation sensors with limited electrical bridges between electrodes are obtained. These sensors outperform their thin-film counterparts since, near the percolation threshold, even a small number of disruptions to the few conducting paths, due to gas adsorption, causes large changes in the network's overall resistance. The work in this thesis explores the development and application of chemiresistive gas sensors based on c-MOFs, with an emphasis on percolation network design to enhance sensitivity.

The thesis starts with a literature review in Chapter 2, which details the development and principles of c-MOFs, chemiresistive gas sensors, and percolation theory, providing a foundation and background for the work in this thesis.

Chapter 3 introduces the methodologies employed in this thesis. It begins with an introduction to the selected chemicals and substrates. Then, the necessary sensor fabrication methods and characterisation techniques are detailed.

Chapter 4, the first experimental chapter, describes the initial work of developing c-MOF percolation networks via electrochemical deposition on interdigitated electrodes (IDEs). $Cu_3(HHTP)_2$ was selected as the active MOF material, as it is known to respond to a variety of gases such as ammonia. Successful growth of $Cu_3(HHTP)_2$ was confirmed via characterisation techniques including SEM, FTIR, XPS, Raman, and XRD. By running the deposition at specific time intervals, different sensors with different growth stages and different resistance values were developed. The electrical percolation behaviour was investigated via electrical measurements, SEM, and AFM. The sensing responses of all obtained sensors to ammonia were tested. The sensors operating in the percolation region showed effectively enhanced responses compared to a sensor operating in the continuous film region and a sensor prepared with c-MOF powder.

Chapter 5 focuses on further improving the sensitivity of electrochemically grown $Cu_3(HHTP)_2$ percolation sensors. To improve the sensing performance, polystyrene (PS) nanoparticles were deposited onto the surface of IDEs as a sacrificial template. Percolation networks were developed by depositing $Cu_3(HHTP)_2$ onto PS at specific time intervals. The subsequent removal of PS templates resulted in percolation networks with porous structures. The successful deposition of $Cu_3(HHTP)_2$ and electrical percolation behaviour were confirmed by the

aforementioned techniques. The responses to ammonia of templated c-MOF percolation sensors were significantly improved compared with their counterparts prepared in Chapter 4.

Chapter 6 shifts the focus from electrochemical deposition routes to electrohydrodynamic (EHD) jet printing, an alternative technique capable of producing sub-micron patterns on diverse materials and substrates. Precursor strips were first obtained by printing the optimised precursor inks. C-MOF strips were then successfully developed by baking the precursor strips, as confirmed by XRD and FTIR. The percolation networks were developed by controlling the ligand concentration in the ink, where a lower ligand content led to less deposition of c-MOFs onto the substrate. These EHD c-MOF percolation networks showed significantly improved sensitivity to ammonia compared to a c-MOF sensor created by drop-casting.

Percolation networks can be prepared via two main approaches: deposition-control and conductive-insulating composite strategies. The deposition-control strategy, explored in previous chapters, typically presents issues such as complex experimental setups, limited scalability, and poor compatibility with a broad range of substrates. Chapter 7 introduces the conductive-insulating strategy, where a solution-processable $Cu_3(HHTP)_2$ as the conductive filler was mixed with PS as the insulating matrix to formulate composite solutions. By drop-casting these solutions onto substrates with varying filler-to-matrix ratios, sensors with different growth of c-MOFs were obtained, enabling the identification of the percolation threshold through systematic electrical characterisation. The PS-$Cu_3(HHTP)_2$ composite percolation sensors demonstrated much improved responses to ammonia compared with percolation sensors prepared by pure c-MOFs.

Chapter 8 summarises the results presented in this thesis. The limitations of the current research and potential directions for improvement in future work are also discussed.

Chapter 2

Literature review

This thesis aims to apply the principles of percolation theory to the development of chemiresistive gas sensors based on conductive metal-organic frameworks (c-MOFs). In this chapter, a comprehensive review of existing research related to this topic is presented. It begins with an introduction to c-MOFs in Section 2.1, followed by a highlight of a unique category—the triphenylene (HXTP)-based c-MOFs—in Section 2.2. Section 2.3 narrows the focus to the development of HXTP-based c-MOFs in chemiresistive gas sensing. Section 2.4 explores the integration of percolation theory into gas sensor design, detailing its development strategies. Finally, Section 2.5 introduces an advanced fabrication method of electrohydrodynamic (EHD) jet printing, describing its mechanism and development in gas sensors.

2.1 Conductive metal-organic frameworks (c-MOFs)

Conductive metal-organic frameworks (c-MOFs) represent a subset of MOFs that exhibit intrinsic electrical conductivity. These materials integrate their efficient charge transport with the hallmark features of conventional MOFs, such as high specific surface area, porosity, and crystallinity.[1] This unique combination of properties positions c-MOFs as promising materials for applications such as energy storage, electrocatalysis, and chemiresistive sensing.[2-5] This section first introduces the conducting transport mechanisms of c-MOFs, where each mechanism represents a distinct strategy for achieving efficient charge transport, with key examples classified by their distinct pathways included. Recent advances in c-MOF applications are then explored.

2.1.1 Conducting transport mechanisms and design strategies

Since 2009,[6] c-MOFs have been extensively investigated and have obtained increasing attention over the years. As shown in Figure 2.1, strategies for developing c-MOFs are guided by five distinct charge transport mechanisms, including through-plane, through-bond, through-space, hopping, and through-guest, each enabled by a specific type of interaction.[7] Understanding these mechanisms allows for the rational selection of ligands for efficient charge transport.

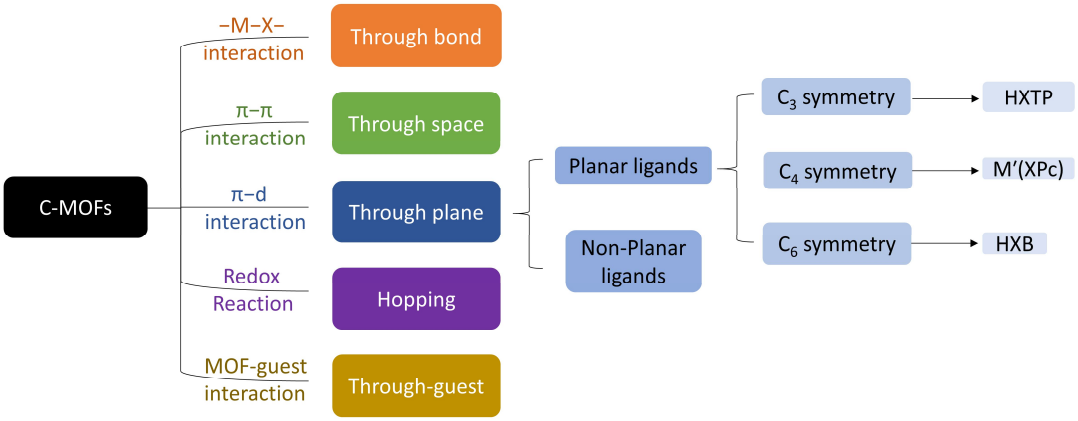

Figure 2.1. (Left) Schematic illustration of various charge transport mechanisms and their associated interactions. (Right) Classification of ligands under through-plane transport mechanism.

2.1.1.1 Through-plane

C-MOFs with the through-plane (also referred to as extended conjugation) mechanism have emerged as the primary focus in this field in recent years.[3, 5, 8] In this mechanism, transitional metal d-orbitals interact with π-electrons in conjugated organic ligands to form an extended π-d conjugation network within the MOF layer. This interaction promotes effective charge carrier mobility, making the material conductive. This mechanism has revolutionised the field of c-MOFs by addressing the critical challenge of designing ordered, highly tunable materials with intrinsic conductivity.

Ligands significantly impact key properties of these c-MOFs, such as electronic conductivity, pore size, topology, and functional versatility. Recently, the variety and number of applied

ligands have grown substantially (Figure 2.2), which are generally categorised as planar or non-planar ligands.[8] Planar ligands coordinate with metal nodes to form planar structures, whereas non-planar ligands typically lead to three-dimensional (3D) networks. Planar ligands can be further categorised based on their symmetry, including C_6, C_3, and C_4 symmetry. These symmetry distinctions result in varied structures and pore sizes in c-MOFs. This section highlights some of the most commonly used ligands, including hexa-substituted benzene (HXB), hexa-substituted triphenylene (HXTP), and M′ (octa-substituted phthalocyanine) (M′(XPc)). Additional ligands are also discussed.

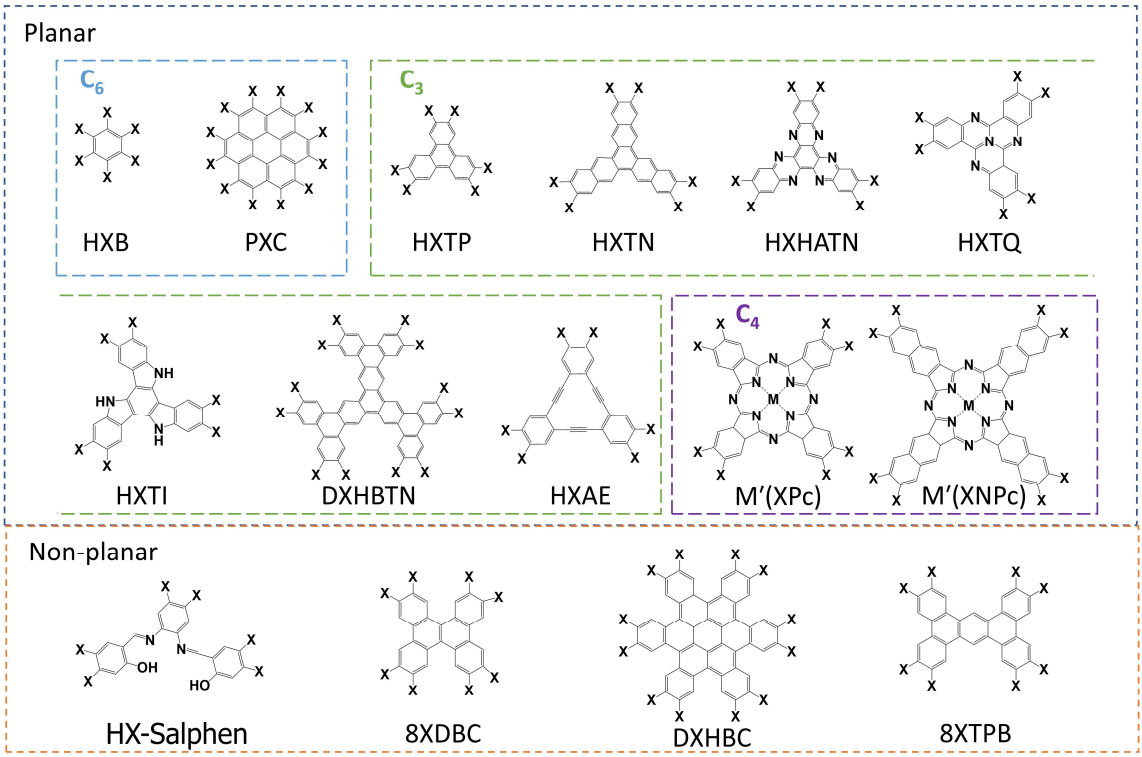

Figure 2.2. Planar and non-planar ligands used for c-MOFs with through-plane mechanism, including hexa-substituted benzene (HXB), per-substituted coronene (PXC), hexa-substituted triphenylene (HXTP), hexa-substituted trinaphthylene (HXTN), hexa-substituted hexazazatrinaphthylene (HXHATN), hexa-substituted tricycloquinazoline (HXTQ), hexa-substituted triindole (HXTI), dodec-substituted hexabenzotrinaphthylene (DXHBTN), hexa-substituted arylene-ethynyl (HXAE), M′ (octa-substituted phthalocyanine) (M′(XPc)), M′ (octa-substituted naphthalocyanine) (M′(XNPc)), hexa-substituted Salphen (HX-Salphen), octa-substituted dibenzo[g,p] chrysene (8XDBC), dodec-substituted hexabenzocoronene (DXHBC), and octa-substituted tetraphenylbenzene (8XTPB).

Hexa-substituted triphenylenes

Hexa-substituted triphenylenes (HXTP) based MOFs have been pivotal in the development of c-MOFs since their emergence. These ligands are derived from triphenylene—a planar, symmetric polycyclic aromatic hydrocarbon composed of four benzene rings, where three peripheral benzene rings are fused along each of their edges with a central benzene ring. Due to this symmetry, each HXTP ligand coordinates with three metal nodes, forming hexagonal pores around 2 nm in size. The ability to substitute all six peripheral positions is a critical feature of HXTP, making them highly versatile for designing tailored materials in c-MOFs.

In 2012, the Yaghi group introduced a notable example by employing an HXTP ligand, hexahydroxytriphenylene (H_6HHTP), with metal nodes (Co^{2+}, Ni^{2+}, and Cu^{2+}) to construct c-MOFs.[9] The results showed each H_6HHTP ligand coordinates with three Cu^{II} centres, leading to a hexagonal structure with a pore size of 1.8 nm and a formula of $Cu_3(HHTP)_2$. $Cu_3(HHTP)_2$ achieved a conductivity of 0.1 S/cm, representing a significant milestone in c-MOF research. HXTP-based MOFs will be discussed in more detail in Section 2.2.

Hexa-substituted benzenes

Hexa-substituted benzenes (HXB) are a versatile class of ligands featuring a benzene ring with six substituents. Compared with other ligands used in c-MOFs, HXB owns the smallest and simplest structure, resulting in much smaller pores, typically less than 1.2 nm. Even though the conjugation system of HXB is relatively simple compared to other ligands, c-MOFs derived from HXB can still exhibit high conductivity.

For example, $Cu_3(HTB)$ (hexathiobenzene), also referred to as $Cu_3(BHT)$ (BHT = benzenehexathiol), showed a non-porous structure with a metal-level conductivity at 2500 S/cm.[10] This exceptional conductivity is attributed to the ligand in $Cu_3(HTB)$, which

coordinates with six Cu^{2+} centres, effectively enhancing the framework's density and the π-d orbital overlap in Cu–S bonds. Interestingly, Cu_3(HTB) also demonstrated superconducting properties, becoming the first c-MOF reported to exhibit superconductivity at 0.25 K.[11] Conversely, $Ni_3(HTB)_2$ showed a porous structure with much lower conductivity at 2.8 S/cm in that the HTB ligand here only bonds to three Ni^{II} metal centres, leading to a hexagonal structure similar to Cu-HHTP.[12] It was reported that its conductivity was tunable under the control of the oxidation state. In the experiment, the $Ni_3(HTB)_2$ was oxidised by tris(4-bromophenyl)aminium hexachloroantimonate or reduced by sodium 2,4,7-trinitrofluorenone. The oxidised $Ni_3(HTB)_2$ showed a higher conductivity of 160 S/cm, while the reduced counterpart exhibited a lower conductivity of 6.7×10^{-3} S/cm.[13]

In addition to HTB-based frameworks, several materials have been synthesised using hexaiminobenzene (HIB) and hexahydroxybenzene (HOB) ligands, such as $Cu_3(HIB)_2$, $Ni_3(HIB)_2$, and $Cu_3(HOB)_2$.[14, 15] The reported room-temperature conductivity of $Cu_3(HIB)_2$ was 6 S/cm and that of $Ni_3(HIB)_2$ was 12.5 S/cm. Meanwhile, their electrical conductivity increased linearly as the temperature increased from 200 to 420 K. $Cu_3(HOB)_2$ showed the lowest conductivity at 7.3×10^{-8} S/cm at room temperature. Its conductivity follows an Arrhenius-type temperature dependence, significantly increasing to approximately 2.0×10^{-6} S/cm at 105°C.

Phthalocyanine-based ligands

Phthalocyanine-based (Pc) ligands are planar, macrocyclic molecules with a conjugated 18 π-electron aromatic system, similar in structure to porphyrins. They consist of four isoindole units connected by four nitrogen atoms with eight substituent positions located on the periphery of each isoindole unit, forming an extended π-conjugated network. Additionally, at the heart of the phthalocyanine molecule lies a central metal ion coordinated by four nitrogen atoms of the

macrocycle. The Pc ligands coordinate with metal nodes to form c-MOFs with a formula of $M_2[M'(XPc)]$, where M′ is the central metal in ligands and M is the coordinated metal node.

For example, in 2018 $Cu_2[Cu(OPc)]$ (Cu(OPc) = copper(II) 2,3,9,10,16,17,23,24- octahydroxy-29H,31H-phthalocyanine) was prepared from a Cu(OPc) ligand and Cu^{II} metal nodes.[16] The ligand coordinates with four metal nodes, leading to a square grid-like framework that featured a 1.3 nm pore size and a low electrical conductivity of 1.6×10^{-6} S/cm at 80°C. Elemental analysis confirmed the presence of ammonium ions within the MOF, implying that $Cu_2[Cu(OPc)]$ was anionic, with ammonium ions serving as counter cations. This negative charge likely accounts for its low electrical conductivity.

One year later, $Cu_2[Ni(OPc)]$ and $Ni_2[Ni(OPc)]$ were synthesised, both exhibiting a square grid-like structure with pore sizes at around 1.8 nm.[17] $Cu_2[Ni(OPc)]$ and $Ni_2[Ni(OPc)]$ showed conductivity of 1.43×10^{-2} S/cm and 7.22×10^{-4} S/cm, respectively, significantly higher than $Cu_2[Cu(OPc)]$. X-ray photoelectron spectroscopy revealed both c-MOFs maintain a charge-neutral skeleton, which explains their higher conductivity.

$Ni_2[Ni(IPc)]$ (IPc = 2,3,9,10,16,17,23,24-octaamino-phthalocyanine) and $Ni_2[Cu(IPc)]$ have also been synthesised, exhibiting square grid-like structures analogous to those of $M_2[M'(OPc)]$ frameworks.[18, 19] $Ni_2[Ni(IPc)]$ demonstrated a higher electrical conductivity of 0.2 S/cm at 300 K, compared to that of 0.01 S/cm for $Ni_2[Cu(IPc)]$.

Other ligands

Except for HXTP, HXB, and M′(XPc), a wide variety of ligands have been utilised to synthesise c-MOFs. For example, Fe-PTC was prepared from 1,2,3,4,5,6,7,8,9,10,11,12-perthiolated coronene (PTC) and iron acetate ($Fe(OAc)_2$).[20] PTC is a planar ligand with C_6 symmetry similar to HXB, which coordinates with six Fe metal nodes to form a triangle lattice with a small pore size of ~0.2 nm. The Fe-PTC showed a high electrical conductivity of ~10 S/cm at room

temperature. Planar ligands with C_4 symmetry have also been explored. Ni′(octahydroxynaphthalocyanine) (Ni′(ONPc)), a derivative of Ni′(OPc) with additional benzene rings fused to its periphery, has been used to coordinate with Cu or Ni to form c-MOFs.[17] The prepared Cu[Ni′(ONPc)] and Ni[Ni′(ONPc)] both exhibited square-grid structures with larger pore sizes of around 2.3 nm, compared with Cu[Ni′(OPc)] or Ni[Ni′(OPc)]. Their electrical conductivities were 3.13×10^{-2} S/cm and 1.78×10^{-2} S/cm, respectively.

Those ligands with C_3 symmetry have also gained attention.[21-23] For instance, 2,3,8,9,14,15-hexahydroxytrinaphthylene (HHTN) was used to synthesise $Cu_3(HHTN)_2$. Due to its slightly larger size compared to HHTP, $Cu_3(HHTN)_2$ adopts a hexagonal lattice with a pore size of ~2.5 nm. However, its intrinsic electrical conductivity (9.01×10^{-8} S/cm at 385 K) was significantly lower than that of $Cu_3(HHTP)_2$ (0.1 S/cm at room temperature). Similarly, $Cu_3(HHHATN)_2$ derived from hexahydroxyl-hexaazatrinaphthylene (HHHATN) exhibited ~2.5 nm pores but a weak conductivity of 1.4×10^{-8} S/cm.[22]

Non-planar conjugated ligands have been developed to construct 3D c-MOFs. For example, 2,3,6,7,10,11,14,15-octahydroxydibenzo[g,p] chrysene (8OH-DBC) was used to prepare Cu-DBC.[24] In $Cu_3(HHTP)_2$, the ligand coordinates with Cu nodes to form a square-planar CuO_4 node, while for Cu-DBC a pair of Cu ions from adjacent layers is further connected by an OH^- bridge, developing a square-pyramidal CuO_5 node. This MOF showed a higher conductivity of 1 S/cm at room temperature, compared to Cu-HHTP.

2.1.1.2 Through-bond

MOFs with coordination/covalent bonds can create continuous through-bond pathways for charge delocalisation, making them conductive. These pathways are typically achieved through MOFs containing $(-M-X-)_n$ lattices (where X is the donor atom of the functional group of the ligand).[25] The well-matched energy levels and good orbital overlap between the metal ion (M)

and donor atoms of the ligand (X) are the key factors for creating charge transport under this mechanism.

A representative example of through-bond conductive pathways is observed in MOF-74-type frameworks (also known as CPO-27). These are constructed from divalent metal ions and the ligand 2,5-dihydroxybenzene-1,4-dicarboxylate (H_4DOBDC), resulting in M_2(DOBDC) structures. These MOFs create one-dimensional (1D) continuous conductive channels consisting of $(-M-O-)_n$ chains. M_2(DOBDC) was extensively studied with different metal nodes, including Mg, Mn, Fe, Co, Ni, Cu, and Zn.[26] Among these frameworks, Fe_2(DOBDC) demonstrated a comparatively higher conductivity at ~3.2×10^{-7} S/cm, while other M_2(DOBDC) MOFs exhibited much lower conductivity from 1.4×10^{-14} to 3.0×10^{-13} S/cm. The analogue of H_4DOBDC, H_4DSBDC (2,5-disulfhydrylbenzene-1,4-dicarboxylate), was also investigated. Compared with M_2(DOBDC), M_2(DSBDC) exhibited much higher conductivity. For example, the conductivity of Mn_2(DSBDC) (2.5×10^{-12} S/cm) is an order of magnitude higher than that of Mn_2(DOBDC) (3.9×10^{-13} S/cm).[27] This indicates the $(-M-S-)_n$ channels promote the charge delocalisation more efficiently than the $(-M-O-)_n$ counterparts.

Another example includes Fe-azolate frameworks.[28] In these frameworks, azolate-based ligands, such as pyrazolate, triazolate, and tetrazolate, coordinate with Fe metal centre to create continuous $(-Fe-N-N-)_n$ channels. These frameworks leverage the mixed valence states of Fe(II) and Fe(III), significantly affecting their conductivity. For instance, Park et al. reported tunable conductivity in MOFs $Fe(tri)_2$, (tri = 1,2,3-triazolate).[29] Initially, a valence-pure $Fe(tri)_2$ containing only Fe(II) was synthesised, showing a low conductivity of 1×10^{-10} S/cm. Subsequently, thianthrenium tetrafluoroborate was introduced to oxidise $Fe(tri)_2$, resulting in the formation of $Fe(tri)_2(BF_4)_x$. This modification significantly enhanced the conductivity, with $Fe(tri)_2(BF_4)_{0.33}$ achieving the highest measured value of 0.3 S/cm.

2.1.1.3 Through-space

Different from through-plane and through-bond mechanisms, which have shown strategies for creating c-MOFs with in-plane charge transport pathways, the through-space mechanism enables the out-of-plane charge transport through π–π stacked organic linkers.[30] The charge carrier efficiency is dependent on the stacking distance and geometry of MOF moieties.

MOF family based on tetrathiafulvalene (TTF) typically operates under the through-space mechanism. TTF is an organosulfur ligand that facilitates strong π–π interaction and close intermolecular contacts within MOFs, promoting charge transport.[31] Examples include Cd_2(TTFTB) (2.9×10^{-4} S/cm), Mn_2(TTFTB) (8.6×10^{-5} S/cm), Co_2(TTFTB) (1.5×10^{-5} S/cm), and Zn_2(TTFTB) (4.0×10^{-6} S/cm).[32] Lanthanide-based frameworks, such as $Tb_3(TTFTB)_2(OAc)(OH)$, also exhibited exceptional conductivity (1.5×10^{-5} S/cm) due to continuous π–π stacking with stacking distances < 4 Å.[33]

Other ligands, such as anthracene, naphthalene, and phenanthroline, also enable through-space charge transport.[34-36] For instance, a semiconducting MOF [Cu(ndc)(1,10-phen)] (ndc = 2,6-naphthalenedicarboxylate and 1,10-phen = 1,10-phenanthroline) was reported.[37] In this structure, each ndc ligand coordinates with two Cu centres to form a two-dimensional network, while the 1,10-phen moieties coordinate with the Cu centres and extend into the interlamellar spaces. The π–π stacking interactions among the 1,10-phen groups provide good electrical conductivity and structural flexibility, resulting in a two-fold interpenetrated three-dimensional supramolecular architecture (Figure 2.3).

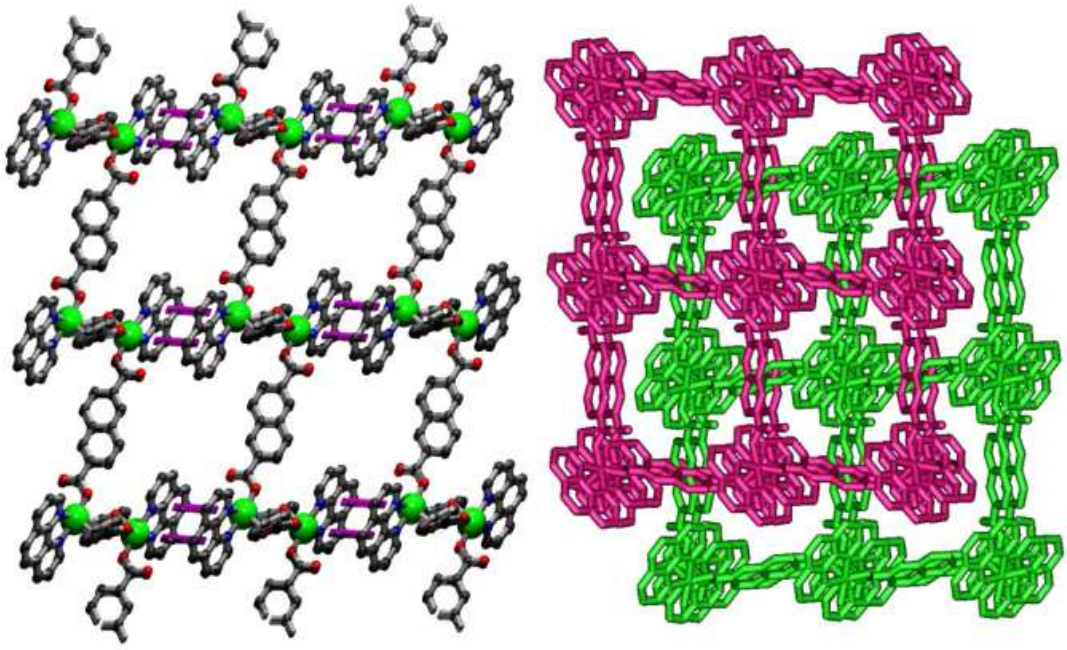

(a) (b)

Figure 2.3. π−π stacking (referred as the purple lines) in conjugated 3D supramolecular structure (a) and illustration of 2-fold interpenetration (b). Reproduced from reference 37.

2.1.1.4 Hopping

Hopping mechanism provides a distinct mode of charge transport in c-MOFs, especially when strong intramolecular or intermolecular interactions are limited to form continuous pathways.[38, 39] In this process, charge transport occurs via localised electron transfer, or "hopping", between spatially discrete redox-active sites. These redox-active sites can be either metal nodes or ligands within the MOF structure, leading to classification into metal-based hopping and ligand-based hopping.

Metal-based hopping involves the transfer of electrons between metal centres. Redox-active metal nodes, such as Fe(II)/Fe(III) or Cu(I)/Cu(II), play a critical role in facilitating this mechanism. One example is $Cu[Cu(pdt)_2]$ (pdt = 2,3-pyrazinedithiolate) reported in 2009.[6] The MOF exhibited mixed valence of Cu composed of a Cu^{I} cation and a $[Cu^{III}(pdt)]^{-}$ anion, leading to its high conductivity of 6×10^{-4} S/cm at 300 K. Another representative example is $Fe_2(BDT)_3$ (H_2BDT = 5,5′-(1,4-phenylene)bis(1H-tetrazole)).[40] The freshly prepared sample only showed

a low conductivity at 6×10^{-5} S/cm at room temperature, while its conductivity significantly increased after exposure to air at ambient environment (0.3 S/cm after 7 d and to 1.2 S/cm after 30 d). This enhancement was attributed to partial oxidation of Fe(II) nodes to Fe(III) by oxygen in the air, which improves charge transport pathways.

In ligand-based hopping, charge transport is facilitated by redox-active ligands. These ligands act as electron reservoirs, transferring localised charges between adjacent sites. Tetraoxolene-based ligands, including H_2dhbq and its derivatives with Cl_2dhbq or Br_2dhbq, are prominent in this category due to their multiple redox states (2−, 3−, 4−) when coordinated with metal nodes (Figure 2.4).[41, 42] J. R. Long et al. reported a 3D MOF $(NBu)_2[Fe_2(H_2dhbq)_3]$ along with its reduced counterpart $Na_{0.9}(NBu_4)_{1.8}Fe_2(dhbq)_3$.[43] By comparing the difference of room-temperature conductivity, with 0.16 S/cm for $(NBu)_2[Fe_2(H_2dhbq)_3]$ and 6.2×10^{-3} S/cm for the reduced counterpart, the authors attribute the exceptional conductivity of $(NBu)_2[Fe_2(H_2dhbq)_3]$ to the electron hopping within $dhbq^{2-/3-}$ redox moieties. Similarly, Dinca et al. investigated a MOF $(Me_2NH_2)_2[Fe_2(Cl_2dhbq)_3]\cdot 2H_2O\cdot 6DMF$ and its reduced form $(Cp_2Co)_{1.43}(Me_2NH_2)_{1.57}[Fe_2(Cl_2dhbq)_3]\cdot 4.9DMF$.[41] They confirmed that the oxidised MOF contains mixed-valence $dhbq^{-2/-3}$ ligands in a 1:2 ratio, whereas the reduced form exclusively comprises $dhbq^{-3}$, leading to the different room-temperature conductivity of 1.4×10^{-2} S/cm and 5.1×10^{-4} S/cm for the oxidised and reduced forms of the MOF, respectively.

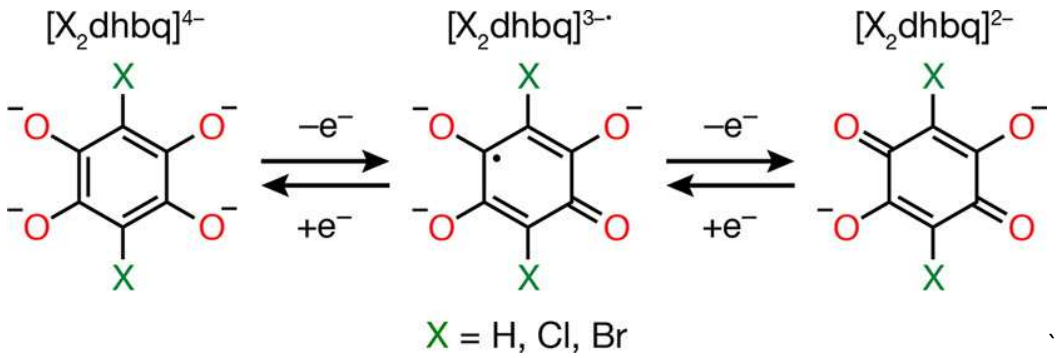

Figure 2.4. Redox states of 4–, 3–, and 2– for dihydroxybenzoquinone (dhbq). Reproduced from reference 7.

2.1.1.5 Through-guest

Initial strategies for obtaining c-MOFs primarily involved introducing external electroactive molecules into MOFs to create charge pathways in the materials through guest-guest or guest-framework interactions.[7]

The introduced guest molecules have a broad range of species, with 7,7,8,8-tetracyanoquinodimethane (TCNQ) being one of the most widely applied guests. In 2014, $Cu_3(BTC)_2$ (also known as HKUST-1; BTC = benzene-1,3,5-tricarboxylate) with tunable electrical conductivity was prepared.[44] The researcher first developed a 100-nm-thick $Cu_3(BTC)_2$ film on a silica wafer and then immersed the MOF film into a TCNQ/CH_2Cl_2 solution for 72 h. The treatment significantly enhanced the room-temperature electrical conductivity of $Cu_3(BTC)_2$ from 1×10^{-8} S/cm to 7×10^{-2} S/cm.

Polymers, including PEDOT (3,4-ethylenedioxythiophene), PANI (polyaniline), and PPy (polypyrrole), were also introduced as guests to promote charge transport in MOFs.[45-47] For example, T. Uemura et al. reported a PEDOT-encapsulated MIL-101(Cr) with a high electrical conductivity at 1.1×10^{-3} S/cm, representing a 10^8-fold increase compared to the pristine MOF.[48] Instead of directly mixing PEDOT and MIL-101(Cr), the monomer (3,4-ethylenedioxythiophene (EDOT)) was introduced into the host MOF, allowing the homogenous dispersion and the precise control of loading rate. Then, the polymerisation of monomer and doping were occurred by using iodine vapour. This method allows the MOF to show high electrical conductivity while maintaining a high specific surface area at 803 m^2/g.

2.1.2 Applications of c-MOFs

c-MOFs are promising candidates for several applications, including electrochemical energy storage,[49] electrocatalysis,[50] and chemiresistive gas sensing,[4] owing to their efficient charge transport combined with the functions of conventional MOFs.

2.1.2.1 Electrochemical energy storage

Electrochemical energy storage is crucial for modern energy systems as it provides a reliable way to store and deliver energy efficiently, making it a key research focus area. C-MOFs have been extensively explored for their potential in supercapacitors and batteries.

Supercapacitor

The rapid electron transfer of c-MOFs enables high capacitance values and excellent rate performance. In 2016, Dinca et al. developed a double-layer capacitance (EDLC) electrode using Ni-HHTP with a gravimetric capacitance of 111 F/g and ~90% retention after 10,000 cycles.[51] Later, Bao et al. reported that HIB-derived MOF-based electrodes (Cu-HIB and Ni-HIB) achieved volumetric capacitances of ~760 F/cm³ and gravimetric capacitances over 400 F/g, with Ni-HIB retaining 90% capacitance after 12,000 cycles.[52]

In addition to neat MOF, composites have been developed to further enhance performance. For instance, $Cu_3(HHTP)_2$ nanowires were developed on reduced graphene oxide to obtain electrodes.[53] The composite exhibited a capacitance of 44.6 mF/cm^2 with good recyclability and mechanical flexibility. Similarly, HHTP-based MOFs were also reported to be deposited onto cellulose nanofibres or polypyrrole (PPy) membranes to prepare flexible supercapacitors,[54, 55] achieving gravimetric capacitances of 116 F/g and 125 F/g, respectively. Jayaramulu et al. reported a device with a high gravimetric capacitance of 651 F/g by covalently attaching UiO-66-NH_2 on the surface of carboxylate-functionalised graphene.[56]

Batteries

In addition to supercapacitors, batteries represent another crucial category in electrochemical energy storage, with Li-ion batteries (LIBs) being the most widely studied due to their high energy density.

Nishihara et al. applied Ni-HIB as a cathode material for LIBs.[57] The material demonstrated a unique dual-ion (Li^+/PF_6^-) insertion/extraction mechanism, enabling the high specific capacities (up to 155 mAh/g) and energy densities (434 Wh/Kg). In parallel, Cu-HHTP nanowires were developed as an anode material for LIBs,[58] exhibiting high specific capacity up to 631 mAh/g and an energy density of 275 Wh/g. The performance maintains 81% capacity retention over 500 cycles. Cu-HHTQ was also explored as the anode electrode.[59] Different from Cu-HHTP, Cu-HHTQ contains the unit of tricycloquinazoline (TQ), a nitrogen-rich aromatic molecule which enables a nine-electron redox process with lithium ions. With more Li^+ loaded, Cu-HHTQ exhibited exceptional specific capacity with 657.6 mAh/g and a capacity retention of 82% after 200 cycles. In addition, Long et al. reported the application of two iron-semiquinoid frameworks, $(H_2NME_2)_2Fe_2(Cldhbq)_3$ and $(H_2NMe_2)_4Fe_3(Cl_2dhbq)_3(SO_4)_2$, for LIBs.[60] These MOFs featured dual metal-centred and linker-centred redox sites, which facilitated efficient electron transfer and a high specific capacity of up to 195 mAh/g.

2.1.2.2 Electrocatalysis

Electrocatalysis plays a pivotal role in energy conversion and sustainable chemical production. C-MOFs have been explored for various electrocatalytic applications including hydrogen evolution reaction (HER), oxygen evolution reaction (OER), oxygen reduction reaction (ORR), and CO_2 reduction reaction (CO_2RR). The HER and OER are key to hydrogen production via water splitting, ORR is critical for energy generation in fuel cells, and CO_2RR offers promising pathways to convert greenhouse gas into valuable chemicals.

Hydrogen and oxygen evolution reactions

HER occurs at the cathode via a two-electron reduction process that generates hydrogen gas, while OER is a four-electron oxidation reaction occurring at the anode. The overpotential in HER or OER is a critical parameter that indicates the additional voltage required beyond the thermodynamic equilibrium potential to drive a reaction at a desired rate, with a lower overpotential implying a more efficient electrocatalyst.

Metal-thiolate MOFs are particularly effective for promoting electrocatalytic activities for HER. For example, Ni-HTTP and Co-HTTP (HTTP = 1,2,5,6,9,10-hexathioltriphenylene) exhibited overpotentials of 333 and 530 mV in HER, respectively.[61, 62] In 2017, a Cu-BHT nanoparticle was reported to show good activity with an overpotential of 450 mV.[63] One year later, the applications of Co-BHT, Ni-BHT, and Fe-BHT for HER were reported.[64] Co-BHT showed an overpotential of 185 mV, much lower than Ni-BHT (331 mV) and Fe-BHT (405 mV), attributed to the lowest transfer resistance of Co-BHT.

In OER, multi-metallic MOFs generally outperform their mono-metallic counterparts. In 2017, Zhao et al. systematically investigated the application of a NiFe-MOF composed of MO_6 metal cluster (M = Ni or Fe) and organic ligand of 2,6-naphthalenedicarboxylate for OER.[65] The NiFe-MOF thin film was developed on nickel foam (NiFe-MOF/NF) as the electrode. The material exhibited the lowest overpotential of 240 mV, compared with Ni-MOF/NF (296 mV), Fe-MOF/NF (354 mV), NF (370 mV), NiFe-MOF powder on NF (318 mV), and calcined NiFe-MOF (336 mV). Additionally, NiFe-MOF/NF demonstrated no detectable activity decay after reacting for 20000 s.

Oxygen reduction reaction

ORR is essentially the reverse cathodic reaction of OER, which transfers two or four electrons. C-MOFs containing M-N_x or M-O_x units are particularly effective ORR catalysts. For example, Dinca et al. deposited Ni-HITP on a glassy carbon electrode, demonstrating that Ni-HITP with

its Ni–N_4 units can catalyse ORR efficiently.[66] In a 0.1 M KOH solution, Ni-HITP exhibited an onset potential of 0.82 V vs the reversible hydrogen electrode (RHE) at a current density of 0.05 mA/cm², along with high selectivity for hydrogen peroxide formation via a two-electron pathway. Yoon et al. synthesised a bimetallic MOF $Co_{0.27}Ni_{0.73}$-HHTP to achieve an ORR via a 4-electron pathway.[67] Pure Ni-HHTP exhibited an onset potential of 0.47 V vs. RHE and a hydrogen peroxide yield of 34.42%, while Co-HHTP had a relatively lower onset potential of 0.42 V with a significantly lower hydrogen peroxide yield of 4.38%. The bimetallic $Co_{0.27}Ni_{0.73}$-HHTP achieved the best balance, with an onset potential of 0.46 V and high selectivity for the 4-electron pathway with a hydrogen peroxide yield of 2.41%.

CO_2 reduction reaction

Reducing CO_2 to valuable chemicals (e.g. CO, HCOOH, CH_4, and CH_3OH) is a strategy to tackle the greenhouse issue. The application of c-MOF in CO_2RR primarily relies on phthalocyanine-based (Pc) MOF. For instance, Cao et al. reported Ni[Ni(OPc)] achieved nearly 100% selectivity (98.4%) for CO production with a high partial CO current density of 34.5 mA/cm^2 at −1.2 V vs. RHE.[68] The selectivity was maintained at 86% after 10 h of operation. Mirica et al. developed four different c-MOFs, including Cu[Co(OPc)], Cu[Co(IPc)], Cu[Ni(OPc)], and Cu[Ni(IPc)], for CO_2RR.[69] The results indicated Cu[Co(OPc)] demonstrated the optimal performance with an 85% efficiency for CO production at -0.74 V vs. RHE and a high current density of −17.3 mA/cm^2. Feng et al. systematically investigated the role of metal centres and their synergistic interactions for CO_2RR by comparing two mono-metallic MOFs (Cu[Cu(IPc)] and Zn[Zn(IPc)]) and two bimetallic MOFs (Cu[Zn(IPc)] and Zn[Cu(IPc)]).[70] Compared with mono-metallic MOFs, bimetallic MOFs demonstrated better performance for CO_2RR. In bimetallic MOFs, Zn[Cu(IPc)] outperformed Cu[Zn(IPc)] attributed to the better synergic effect between CuN_4 and ZnO_4.

2.1.2.3 Gas sensing

With growing demand for real-time gas monitoring in environmental, industrial, and healthcare,[71] c-MOFs with their unique properties have emerged as attractive chemical sensing materials. Among currently developed c-MOF-based gas sensors, two main types, chemiresistive gas sensors and field-effect-transistor (FET)-based sensors, are identified based on their transduction mechanisms.[72]

Chemiresistive gas sensors

The working principles of chemiresistive gas sensors rely on the variation in electrical conductance of active materials upon gas adsorption. Dinca's group reported the first example of chemiresistive gas sensor using a c-MOF Cu-HITP as the sensing material.[73] The Cu-HITP was synthesised via the hydrothermal solution method and deposited on electrodes by simply drop-casting. The sensor showed weak responses to 5 parts per million (ppm) ammonia. The performance of the sensor based on c-MOFs was slightly improved until the breakthrough report in 2017, when Xu et al. fabricated sensors based on Cu-HHTP nanofilm by a spray layer-by-layer method, demonstrating highly selective and sensitive sensors to ammonia in the range of 1-100 ppm[74]. This application will be discussed in more detail in Section 2.3.

Field-effect-transistor-based sensors

FETs are devices made of a source electrode, a drain electrode, a gate electrode, a semiconductor material channel, and an insulating gate oxide layer. In FET-based c-MOF sensors, c-MOFs serve as the semiconductor channel between the source and drain electrodes. When gas analytes are adsorbed onto the c-MOFs, the changes in charge carrier density and the work function modulate the conductivity of the material channel, thereby altering key electrical parameters such as the drain current and threshold voltage. The first example of c-MOFs in

FETs was reported by Xu et al.,[75] where $Ni_3(HITP)_2$ membrane was employed as the active channel material. The resulting porous FETs showed typical p-type behaviour, with a threshold voltage of ~1.1 V and a field-effect hole mobility of 48.6 $cm^2V^{-1}s^{-1}$. Subsequently, Shirsat et al. synthesised nanorods of $Ni_3(HHTP)_2$ as the channel material and evaluated their sensing performance.[76] The devices showed a decrease in drain current with increasing SO_2 concentration, achieving a detection limit of 625 parts per billion (ppb) and a rapid response time of 13 seconds.

2.2 Triphenylene (HXTP)-based c-MOFs

The combination of high conductivity, stability, tunable chemistry, and proven success in diverse applications makes triphenylene-based (HXTP) MOFs the most popular point of research among c-MOFs. This section reviews the composition, properties, and synthesis methods of HXTP-based MOFs.

2.2.1 Design principles of HXTP-based c-MOFs

HXTP linkers are planar ligands with a C_3 symmetry, indicating each HXTP linker typically coordinates with three metal nodes to form a layer of hexagonal structure, resulting in a porous structure with a pore size of ~2 nm (Figure 2.5a). Although each HXTP-based c-MOF layer has a similar structure, changes in factors such as organic linkers, metal nodes, and layer stacking modes significantly influence their electrical and chemical properties. The overall influencing factors and their interrelationships are illustrated in Figure 2.5b.

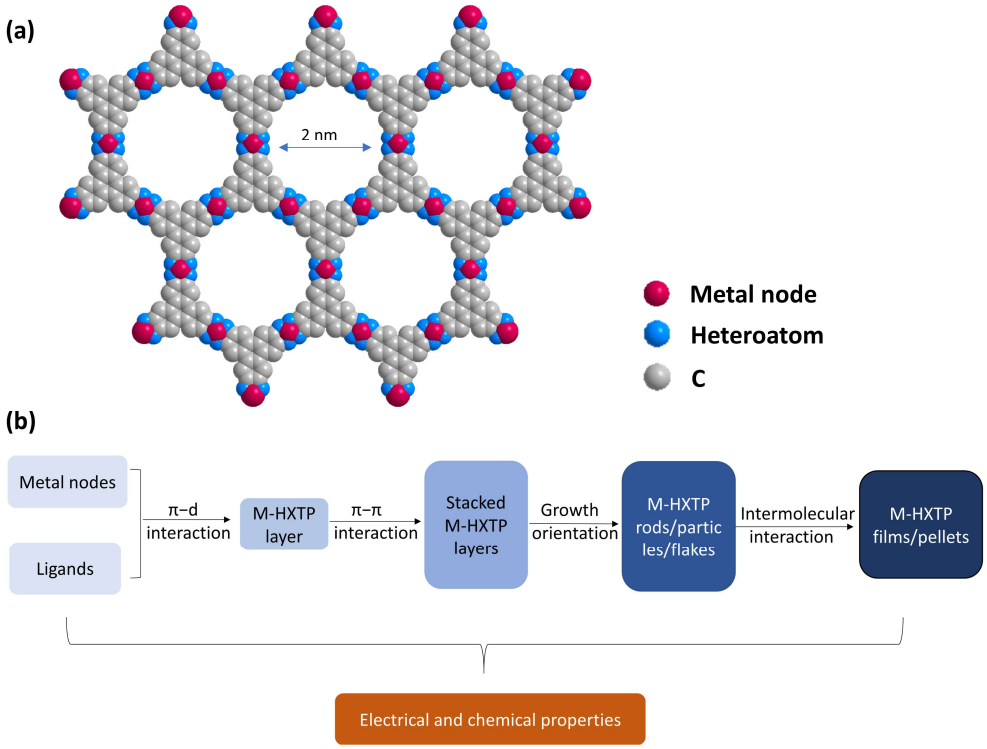

Figure 2.5. (a) Representative structure of an HXTP-based c-MOF layer, featuring HXTP organic linkers interconnected by metal nodes (in red). (b) Schematic diagram of the key factors that influence the material's electrical and chemical properties.

2.2.1.1 Influence of the organic linkers

The ligands used for HXTP-based MOFs are families of hexa-substituted triphenylene, mainly including hexa-hydroxy triphenylene (H_6HHTP) and hexa-amino triphenylene (H_6HATP). The lower electronegativity of nitrogen compared to oxygen results in an elevation of the metal centre's d-orbital energies when coordinated with H_6HATP. This elevation enhances the alignment between the metal d-orbitals and the ligand's π* orbitals, potentially improving electronic interactions within the complex. As a result, MN_4 coordination linkages generally result in frameworks with higher electrical conductivity than the MO_4 counterparts.[77]

For example, in 2012, Yaghi et al. prepared single-crystal Cu-HHTP and measured its conductivity of ~0.2 S/cm at room temperature by a four-point probe method.[9] It is noteworthy that the conductivity of Cu-HHTP significantly varies with its form: pressed Cu-HHTP pellets

typically showed values between 0.002 and 0.045 S/cm, while its thin films exhibited conductivity ranging from 0.002 S/cm to 0.2 S/cm.[78] In 2015, Dinca et al. developed Cu-HITP (obtained from H_6HATP) and measured the conductivity value of 0.2 S/cm on its pressed pellet.[79] A similar value of 0.75 S/cm for Cu-HITP pressed pellet was reported by Dinca et al. in another study.[80] Cu-HITP pressed pellet showed much higher conductivity compared to its Cu-HHTP counterparts, which is consistent with the rule that MN_4 linkages promote better charge delocalisation than MO_4 linkages. This rule is also observed for other M-HXTP MOFs such as Ni-HXTP or Co-HXTP.[77]

2.2.1.2 Influence of the metal nodes

The selection of metal nodes greatly influences the interlayer arrangements and the overlap between metal-d and linker-π orbitals, leading to different electronic conductivities and the type of charge carriers. Therefore, MOFs behave to show either insulating, semiconducting, or metallic behaviour.[80, 81] In 2020, Dinca et al. compared and investigated the different electronic conducting behaviours of Co-HITP, Ni-HITP, Cu-HITP, and their alloys. They first noticed the samples of M-HITP (Co, Ni, Cu) exhibited interlayer distances of 3.29, 3.30, and 3.16 Å, respectively, and interlayer displacements of 1.39, 1.56, and 0.86 Å, respectively. Due to these differences, M-HITP (Co, Ni, Cu) also showed different band gaps of 0.719, 0.291, and 0.429 eV, respectively. By synthesising binary alloys with different ratios of metal nodes, they successfully achieved the continuous tuning of both electrical conductivity and band gaps.

2.2.1.3 Influence of the morphologies

As discussed in Section 2.2.1.1, MOFs' macroscopic presentation in terms of film, pressed pellet, or single crystals greatly influences the electronic conductivity. This section focuses on how particle morphology affects conductivity.

In 2019, Dinca et al. prepared single-crystal Cu-HHTP rods and exfoliated flakes.[82] These distinct morphologies and orientations resulted in markedly different electrical conductivities, with 1.5 S/cm for the rods and 0.5 S/cm for the flakes, respectively. Notably, the rods grew with their long axis perpendicular to the 2D layers, indicating that electrical measurements along the rod's length primarily reflected out-of-plane charge transport, where electrons moved between stacked 2D sheets. This finding is surprising because it was traditionally believed that the conduction mechanism in Cu-HHTP was dominated by the in-plane π–d interactions. Instead, the results reveal that out-of-plane charge transport also plays an important role in the overall conductivity. A comparable outcome was observed in a separate study.[83] These findings clearly indicate that the shape and orientation of HXTP-based c-MOFs can significantly influence their electronic conductivity by determining the dominant charge transport pathways.

2.2.1.4 Influence of the stacking modes

The stacking modes of HXTP-based c-MOFs have a pronounced impact on both electrical and chemical behaviour. These frameworks typically exhibit two primary stacking modes, eclipsed (AA) and slipped (AB) arrangements, shown in Figure 2.6. As discussed in Section 2.2.1.3, both in-plane and out-of-plane transport contribute to the overall conductivity of HXTP-based c-MOFs. It was generally believed that stacking modes mainly affect out-of-plane transport because a perfect AA arrangement aligns the layers directly, thereby maximising π–π orbital overlap. In contrast, the AB stacking mode introduces a lateral displacement that weakens these interactions.

However, a recent study showed that stacking modes also significantly influence in-plane transport. For example, density functional theory (DFT) calculations on Ni-HITP revealed that the in-plane average band dispersion is 190 meV for AA stacking, decreasing to 108 meV and 110 meV for AB stacking with displacements of (2.0 Å, 2.0 Å) and (3.4 Å, 3.4 Å),

respectively.[21] These results indicated that the shift from AA to AB stacking greatly decreased in-plane charge transport, which is likely because the displacement disrupts the π–d interaction that governs electron delocalisation within each layer. Conversely, the out-of-plane average band dispersion was 132 meV for AA stacking, dropped to 41 meV for AB (2.0 Å, 2.0 Å), and then increased markedly to 262 meV for AB (3.4 Å, 3.4 Å). This suggests that the effect of stacking on π–π interactions is more complex than originally thought. When the lateral displacement reaches a certain extent, it may facilitate an even more favourable vertical overlap of π orbitals between adjacent layers, thereby improving vertical conduction. Moreover, when hydrogen sulfide (H_2S) was employed as a guest molecule to evaluate host–guest interactions with various 2D MOFs, the H_2S binding energy was found to be enhanced in the AB stacking mode compared to AA. These observations imply that the altered stacking influences both electrical transport properties and chemical reactivity.

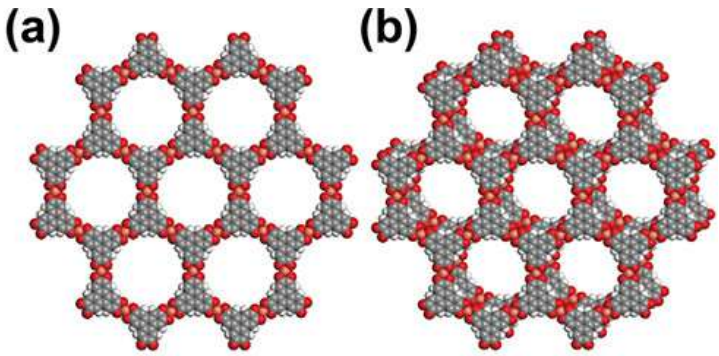

Figure 2.6. Representative stacking modes in M-HXTP. (a) Eclipsed stacking (AA stacking): layers are completely overlapped. (b) Slipped parallel (AB stacking): adjacent layers are slightly displaced alternatively. Reproduced from reference 21.

2.2.2 Synthesis methods for HXTP-based c-MOFs

Different synthesis strategies greatly influence the morphology and structure of MOFs, leading to remarkably diverse properties. This section reviews the current synthesis approaches for HXTP-based MOFs.

2.2.2.1 Hydrothermal solution synthesis

Hydrothermal solution synthesis of HXTP-based MOFs is one of the most classic and straightforward approaches. In a typical protocol, metal salt and ligands were dispersed in the solvent within a sealed vessel at temperatures typically above the solvent's boiling point. The HXTP-based MOF powder with rod-like morphology formed in the solution after a few days.[9, 73] The morphology can be tailored by introducing other substances as the modulator. For example, A. C. Forse et al. prepared Cu-HHTP rods by using DMF as the solvent.[84] By introducing NH_3 and pyridine as the modulators, Cu-HHTP flakes and spherical particles were also synthesised, respectively.

2.2.2.2 Liquid/gas and liquid/liquid interfacial synthesis

Interfacial synthesis enables the formation of uniform ultra-thin films by confining the growth of MOFs at the interfaces. The liquid/gas interfacial synthesis of MOFs is typically achieved by water/air interface. In this case, metal salt was dispersed in a container with water, while a small number of organic linkers were spread onto the surface of the aqueous solution by a syringe, leading to the reaction between organic linkers and metal nodes at water-air interface. Makiura et al. employed this method to obtain Ni-HITP with controlled thickness.[85] Wu et al. achieved the Ni-HITP film at water/air interface in a different way.[86] They dissolved both metal salt and ligands in one beaker with water. Then, a small bottle with triethylamine (TEA) was placed near the beaker. By heating the system, the evaporated TEA spread onto the surface of the precursor solution, which promoted the reaction at water-air interface.

The liquid-liquid interfacial reaction occurs at the interface between two immiscible phases, typically an aqueous phase dissolving metal nodes and an organic phase dissolving ligands. Martí-Gastaldo et al. used this method to prepare Cu-HHTP film at liquid-liquid interface.[87] However, the resulting Cu-HHTP film exhibited partial cracking, indicating a lack of

uniformity. The authors suggested that the liquid–gas interfacial reaction yields a more uniform Cu-HHTP film compared to the liquid–liquid interfacial approach.

2.2.2.3 Layer-by-layer assembling technique

Even though ultra-thin and uniform HXTP-based MOF films were developed by interfacial synthesis, transferring these films from the interface remains a significant challenge. Xu et al. employed a layer-by-layer liquid-phase epitaxial (LPE) method to prepare MOF nanofilms in situ with controlled thickness.[74] Specifically, they first functionalised the substrate with hydroxyl groups to facilitate the oriented growth of the MOF layer. Then, the Cu-HHTP thin films were grown using the LPE method, where the treated substrate was alternately exposed to solutions of metal salt and ligands. Between each step, the substrate was rinsed to remove unreacted components, ensuring precise growth. Each cycle adds ~2 nm of material, creating a thin film with controllable thickness.

2.2.2.4 Electrochemical synthesis

Electrochemical synthesis also enables the in-situ deposition of MOF films on substrates under mild conditions including room temperature and low pressure. Electrochemical synthesis is classified as anodic or cathodic synthesis.

In anodic synthesis, the pre-deposition of metal is required on the working electrode. With an appropriate positive potential applied to the working electrode, the pre-deposited metal was oxidised into corresponding metal ion which provides the source of metal nodes for the reaction. As illustrated in Figure 2.7a, Liu et al. achieved the electrochemically grown large-area Cu-HHTP MOF films on copper anodes.[88] In this process, copper foil served as the anode, while an H_6HHTP solution was deprotonated with ammonia to provide the ligand. Upon applying a controlled voltage, the copper anode was oxidised, releasing Cu^{2+} ions that coordinated with H_6HHTP anions at its surface to form a uniform MOF layer. Later, Lu et al. reported another

novel anodic electrochemical method.[89] Rather than generating the metal source from the working electrode, copper nitrate salt was directly dissolved in the solution. Nitric acid was introduced to limit the deprotonation of H_6HHTP ligand in the solution. Consequently, the reaction only occurs on the anode attributed to the oxidation of redox-active catechol ligands.

For cathodic synthesis, a pro-base was introduced into the solution rather than pre-depositing metal on the electrodes (Figure 2.7b). With a negative potential applied, the pro-base was reduced into a basic substance that promoted the deprotonation of ligands. In 2021, Lu et al. introduced O_2 as the pro-base to prepare Cu-HHTP thin films.[90] In the process, O_2 was reduced to O_2^-, facilitating the reaction between Cu^{2+} and deprotonated H_6HHTP. By varying the applied potentials, reactant concentrations, and time, Cu-HHTP films with thicknesses ranging from 70 nm to 1700 nm were prepared.

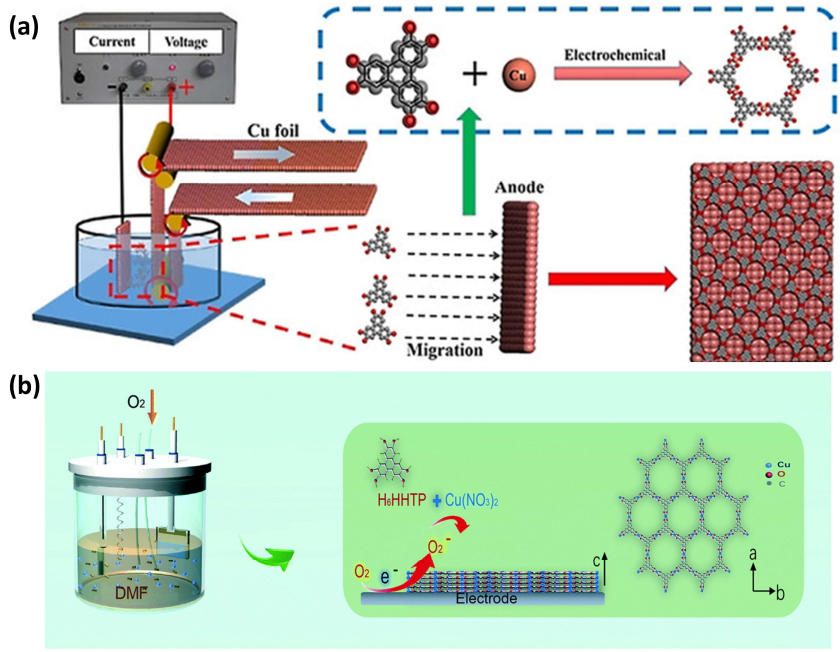

Figure 2.7. Schematic illustration of (a) anodic electrochemical synthesis of Cu-HHTP on Cu foil and (b) oxygen-assisted cathodic electrochemical synthesis of Cu-HHTP. Reproduced from references 88 and 90, respectively.

2.3 HXTP-based c-MOFs in chemiresistive gas sensors

The continuous expansion of human activities has driven a significant increase in the demand for selective, highly sensitive, and reliable gas sensing devices. Over the decades, chemiresistive gas sensors have been developed for monitoring gases in fields of environment, food industry, and healthcare, due to their low production cost and easy processability.[91] In this context, HXTP-based c-MOFs have emerged as a promising class of active materials. This section first introduces the role of HXTP-based c-MOFs in chemiresistive gas sensors. It then outlines essential sensing parameters for evaluating sensing performance and their development in chemiresistive gas sensors. Finally, their gas sensing mechanisms are discussed.

2.3.1 The role of HXTP-based c-MOFs in chemiresistive gas sensors

Metal oxide semiconductors (MOS) were among the earliest and most extensively studied materials for chemiresistive gas sensors, making MOS devices some of the most commercially successful products in this field.[92, 93] However, despite their widespread use, MOS sensors come with notable limitations. The majority of MOS sensors require an operating temperature above 300°C, resulting in relatively high power consumption.[94] Additionally, MOS sensors also show a relatively low response and weak selectivity, making the sensors fail to effectively monitor and tell the target gases apart when dealing with gas mixtures in the real world.

To circumvent the problems with MOS sensors, researchers have explored a range of materials—including polymers,[95] graphene,[96] carbon nanotubes,[97] transition metal dichalcogenides (TMDs),[98] and MOFs—as active sensing elements.[99] MOFs, with their high specific surface areas, large pores, and tunable structures, stand out as particularly promising candidates for gas sensing. Before the synthesis and use of c-MOFs, most MOFs were nearly insulating, limiting their utility in chemiresistive applications. Nevertheless, significant efforts have been made to harness their potential. For example, Zhang et al. investigated the gas sensing potential of a zeolitic imidazolate framework (ZIF) ZIF-67.[100] The prepared ZIF-67 with a high

specific surface area of 1832.2 m^2/g was drop-cast on interdigitated electrodes (IDEs). The obtained sensor demonstrated high sensing responses to formaldehyde, while the operating temperature is required to be 150°C. To enable sensors based on conventional MOFs to operate at room temperature, researchers are left with little choice but to integrate conventional MOFs with other conductive sensing materials for room-temperature applications.[101-103]

The advent of c-MOFs has further advanced MOF-based chemiresistive sensors by addressing the poor conductivity of traditional MOFs. Among these, triphenylene (HXTP)-based c-MOFs have proven pivotal. Their extended π-conjugation and planar geometry facilitate charge delocalisation through stacked 2D sheets, enabling notable electrical conductivity while retaining high porosity. This unique combination makes them ideal for gas sensing, establishing them as the pioneering material in c-MOFs for chemiresistive gas sensors.[73] To date, HXTP-based MOFs remain the most widely studied c-MOFs in chemiresistive gas sensors, with their proven success in detecting a variety of toxic gases with high sensitivity.[104]

2.3.2 Sensing parameters

The principle of chemiresistive gas sensors relies on the change of resistance induced by the interaction between analytes and active materials. The performance of sensors can be effectively assessed by evaluating several key parameters.[105]

2.3.2.1 Response

The response of chemiresistive gas sensors is a crucial factor that quantifies the relative change in resistance upon exposure to an analyte and is defined by Equation 2.1:

$$Response = (R_t - R_0) \,/\, R_0 \tag{2.1}$$

where R_t refers to the resistance after exposure, and R_0 is the original resistance before exposure.

2.3.2.2 Calibration curve

A calibration curve is a plot showing the relationship between response and known analyte concentration. Under low-field, ohmic conduction conditions where charge-carrier mobility is assumed to remain approximately constant, the current density of a bulk semiconductor is proportional to its carrier concentrations.[106] Therefore, gas-induced modulation of carrier density in the low-concentration, non-saturated adsorption regime is expected to result in a linear calibration curve, consistent with Equation 2.2:

$$\Delta R / R_0 = ax \tag{2.2}$$

where a is the slope of the curve, x is the analyte concentration, and $\Delta R / R_0$ is the response.

However, in practice, non-linear behaviour of the calibration curve is often observed and the calibration curve aligns with Equation 2.3:

$$\Delta R / R_0 = ax^{\beta} \tag{2.3}$$

where a is the pre-exponential factor, x is the analyte concentration, and β is the power-law exponent. This model is widely used to describe non-linear behaviour in chemiresistive gas sensors based on various materials including c-MOFs.[4, 74]

2.3.2.3 Sensitivity

Sensitivity S is defined as the slope of the calibration curve at a given gas concentration C_0:[107, 108]

$$S = \left(\frac{dR}{dC}\right)_{C_0} \tag{2.4}$$

If the calibration curve is linear, S is a constant value independent of concentration.

2.3.2.4 Limit of detection (LOD)

LOD indicates the lowest concentration of an analyte that can be reliably detected, which is usually estimated statistically since direct experimental determination can be challenging due to instrument limitations and gas concentration constraints. The LOD is generally calculated based on Equation 2.5:[109]

$$LOD = \left(\frac{3\sigma}{S}\right) \tag{2.5}$$

Where σ is the standard deviation of baseline noise and S is the sensitivity.

In addition to the conventional LOD, an alternative detection limit based on the standard error (SE) of the baseline signal is defined to facilitate interpretation of the statistical detection limit under temporal averaging and finite measurement bandwidth. This metric, denoted as LOD_{SE}, represents the uncertainty of the averaged baseline signal and therefore provides a theoretical lower bound for detection under ideal noise conditions. The SE is calculated as the standard deviation of the baseline signal divided by the square root of the number of data points within the averaging window. The LOD_{SE} is calculated based on Equation 2.6.

$$LOD_{SE} = \left(\frac{3SE}{S}\right) \tag{2.6}$$

2.3.2.5 Response and recovery times

The response and recovery speed are characterised by response time (t_{res}) and recovery time (t_{rec}), respectively. T_{res} refers to the time required for the sensor's response to reach 90% of its saturation value during exposure, while t_{rec} indicates the time needed for the response to return to 10% of its saturation value after removal of the analyte.

2.3.2.6 Selectivity

Selectivity is a measure of the sensor's ability to distinguish the target analyte from interfering species. It is defined as the ratio of the sensor's response to the target analyte to its response to interfering gases:

$$Selectivity = Response_{\text{Analyte}} / Response_{\text{Interfering gas}} \quad (2.7)$$

2.3.2.7 Stability and repeatability

Stability is the ability of a sensor to maintain consistent performance—such as similar responses, recovery time, and LODs—over a longer period under the same operating conditions. Repeatability, on the other hand, refers to the sensor's ability to produce the same response under identical conditions in multiple successive measurements within a single experiment.

It is important to note that these performance metrics can be significantly influenced by external experimental conditions (e.g. gas flow rate, temperature, and humidity) as well as differences in electrode substrates, chamber geometry, and exposure protocols (e.g. analyte concentration and exposure time). Such factors can affect reproducibility and comparability of results across studies. Therefore, it is essential to document all critical testing parameters—including flow rate, temperature, chamber geometry, substrate type, and exposure protocol—in order to enable meaningful comparisons of sensor performance across different laboratories.

2.3.3 Development of HXTP-based c-MOFs in chemiresistive gas sensors

In 2015, Dinca et al. reported $Cu_3(HITP)_2$ as the first successful c-MOF-based chemiresistive gas sensor.[73] Their simple drop-cast devices reversibly detected sub-ppm ammonia, with a response of ~1.1% to 5 ppm ammonia at room temperature. In their follow-up work,[79] an array composed of Cu-HHTP, Ni-HITP, and Cu-HITP was established via drop casting or mechanical abrasion. The sensor array effectively distinguished 200 ppm concentrations of volatile organic compounds (VOCs) with different functional groups including alcohol-, ketone-, aromatic-,

amine-, and aliphatic-containing moieties. The work from Dinca's group demonstrated the potential of applying HXTP-based MOFs in chemiresistive gas sensors.

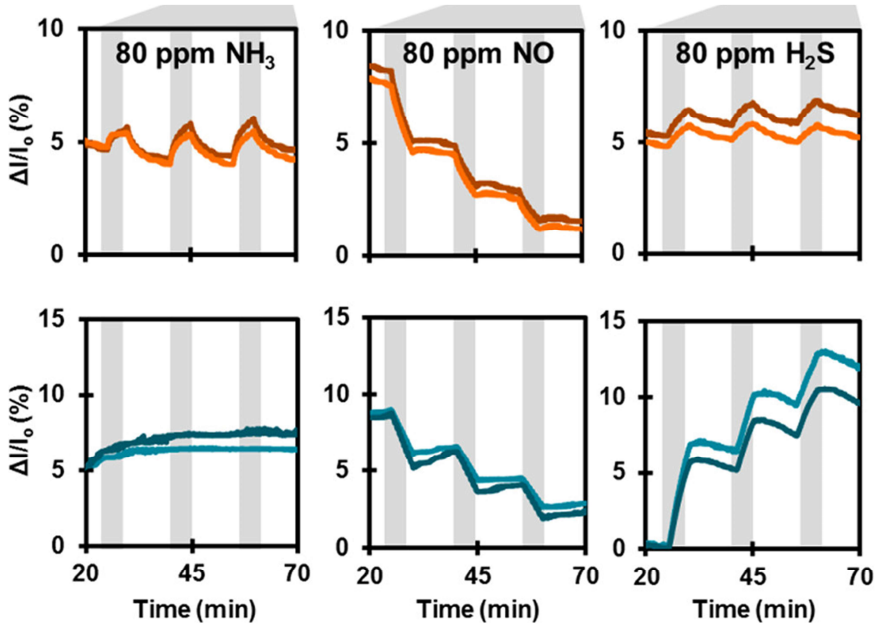

Figure 2.8. Sensing response (left to right, 80 ppm of NH_3, NO, and H_2S) for Cu-HHTP (orange) and Ni-HHTP (blue). Reproduced from reference 110. The grey region refers to the exposure to the analyte, while the white region refers to the exposure to the background gas.

Building on the pioneering work of Dinca's group, in 2016, Mirica et al. developed Cu-HHTP and Ni-HHTP sensors via depositing MOFs on home-made IDEs by drawing graphite on polymer films.[110] The IDEs were first immersed in the precursor solution containing metal salts and organic linkers, followed by heating to grow MOFs in situ onto the IDEs. As shown in Figure 2.8, the resulting sensors exhibited distinct responses to NO, H_2S, and NH_3, with each MOF–analyte combination showing distinct response magnitudes and degrees of reversibility. For example, the Cu-HHTP sensor showed an increase in resistance upon exposure to NH_3 and H_2S, whereas it decreased in response to NO. Additionally, the changes induced by H_2S and NH_3 were reversible while that by NO was irreversible. Meanwhile, the sensor showed low responses to all gases, with only a ~0.7% response to 80 ppm ammonia. To improve the sensing performance,[111] Mirica et al. introduced graphite into M-HHTP (M = Fe, Co, Cu, Ni) to form

MOFs/graphite composite-based sensors. This modification enhanced the sensitivity compared to their earlier report, with the Cu-HHTP composite sensor achieving an improved response of approximately 4.6% to 80 ppm ammonia.

Starting from this period when the studies from Mirica's group extended the detectable range to include H_2S and NO, research on HXTP-based c-MOFs branched into several directions, each targeting different gases, mainly including NH_3, H_2S, and NO_x.

NH_3 sensing

Progress in ammonia sensing was further accelerated by Xu's group. In 2017, they refined the in-situ growth process using a layer-by-layer liquid-phase epitaxial (LPE) method (discussed in Section 2.2.2.3) to deposit an ultrathin (~20 nm) Cu-HHTP film.[74] The MOF nanofilm-based sensor demonstrated exceptional responses of ~33% to 5 ppm ammonia, a rapid response time of 1.36 min, and a theoretical LOD of 500 ppb. The sensor's selectivity, evaluated by comparing the ammonia response to that of interfering gases such as H_2, benzene, CO, and acetone, ranged from 4.55 to 8.25, indicating a level of precision suitable for accurate ammonia detection. This work not only achieved a significant breakthrough in enhancing the ammonia sensing performance of c-MOFs, but also provided a systematic investigation of key parameters, including LOD, selectivity, and response time, offering comprehensive insights into sensor performance.

Between 2017 and 2022, Xu's group further made great contributions to improving the sensitivity and selectivity of HXTP-based c-MOF sensors.[112-116] For example, a metal-free porphyrin-based MOF (Cu-TCPP) was transferred onto $Cu_3(HHTP)_2$ to form a MOF-on-MOF device, which greatly enhanced the sensor's selectivity of benzene over NH_3 from ~0.6 for pure $Cu_3(HHTP)_2$ to ~2.5 for the MOF-on-MOF device. This enhanced selectivity indicates that the MOF-on-MOF architecture preferentially suppresses the response to ammonia while

maintaining a strong interaction with benzene.[112] In another example, dual ligand-based c-MOFs Cu_3(HHTP)(THQ) (THQ = tetrahydroxy-1,4-quinone) were synthesised for ammonia detection.[113]

A landmark paper published in 2021 from Xu's group achieved a sensor with significantly improved NH_3 sensitivity, an ultra-low LOD, and a fast response time.[115] As shown in Figure 2.9, the group first developed a TiO_2 nanowire array onto substrates, which was inert to NH_3. Then, Cu-HHTP was deposited on the surface of TiO_2 by LPE to form Cu-HHTP nanolayers. The obtained sensors with TiO_2-templated 3D Cu-HHTP nanofilm demonstrated a record-high response of ~53% to 5 ppm, a rapid response time of 35 s, and an extremely low LOD of 87 parts per trillion (ppt).

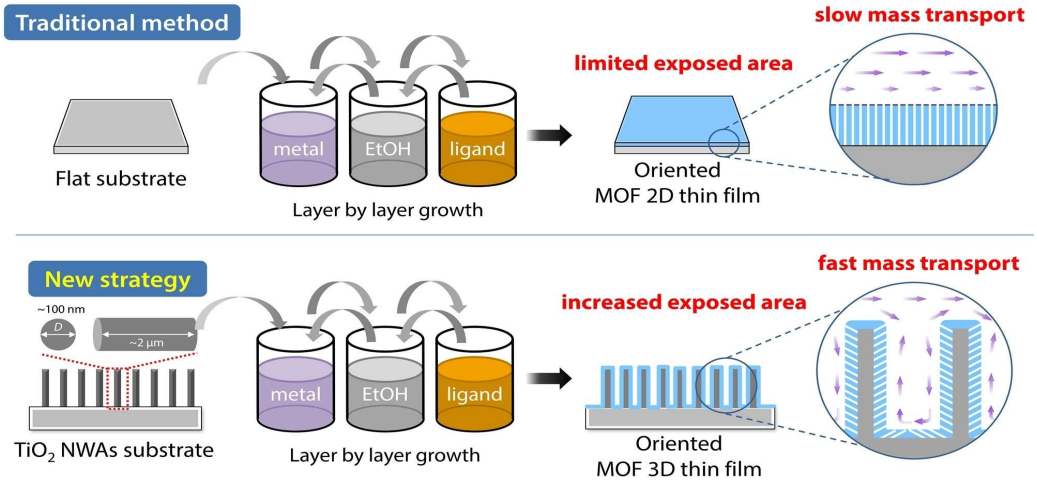

Figure 2.9. Schematic illustration of the MOF nano-thin film prepared by layer-by-layer method (above) and the MOF 3D-nano film prepared by TiO_2 templated strategy (bottom). Reproduced from reference 115.

Recently, some novel strategies have also been explored.[117-119] In one study, a sacrificial-template strategy was developed to transform the insulating ZIF-8 into conductive Zn-HHTP, yielding a unique hierarchical structure.[118] This Zn-HHTP sensor demonstrated a 43.8% response to 50 ppm ammonia and reached saturation in only 9.1 s. In another study, a series of bimetallic HXTP-based MOFs (Co/Cu-HHTP, Ni/Cu-HHTP, and Co/Ni-HHTP) were

synthesised for ammonia detection.[119] Co/Cu-HHTP-based sensors exhibited higher responses and stability to ammonia, compared with either other bimetallic MOFs or their monometallic MOF counterparts.

NO_x sensing

Since 2017, Mirica's group has advanced the use of HXTP-based MOF sensors for NO_x detection, achieving significant sensitivity enhancements.[120-122] However, their approach did not address the irreversible behaviour observed during sensing, which limited practical applications. To overcome this, extensive efforts have been devoted toward mitigating irreversibility in NO_x sensing, with particularly notable contributions from Kim's group.[123-128]

In 2019, Kim's group encapsulated catalytic Pd or Pt nanoparticles into the Cu-HHTP and prepared a monometallic-functionalised (Pd/Pt) Cu-HHTP sensor.[123] The Pd/Pt was introduced as ultra-small nanoparticles (~2 nm) embedded in MOF pores. When used as the active layer in sensors, both Pd-Cu-HHTP and Pt-Cu-HHTP demonstrated reversible detection to 5 ppm NO_2 with improved responses of −62.11% and −57.38%, respectively, compared with the pristine MOF counterpart (−29.95%).

Building on this, Kim's group published two additional studies in 2021. In one work, they developed bimetallic-functionalised sensors by introducing both Pt and Ru into Cu-HHTP's pores.[125] Here, Ru sites provided stronger NO_2 adsorption while Pt assisted in transferring the adsorbed species, thereby reducing the energy barrier for NO_x desorption. The sensors demonstrated an improved response of −53.0% to 2 ppm NO_2 with excellent selectivity of NO_2 against interferents including NH_3, H_2S, CO, NO, and so on (each more than 9). In another study, they introduced a scalable microfluidic channel-embedded solution shearing (MiCS) method.[126] This approach continuously delivered separate solutions of metal salts, ligands, and a Pt precursor through microfluidic channels integrated into a shearing blade onto a heated

substrate. This one-step process enabled the simultaneous formation of Pt and Cu-HHTP thin films, resulting in an outstanding sensor response of –89.9% to 3 ppm NO_2.

The three studies above collectively introduced metal nanoparticles into MOF pores to enhance sensitivity and reversibility. However, embedding these particles blocked the pores, reducing the specific surface area and hindering rapid gas diffusion. In contrast, the latest work from Kim's group in 2024 developed a single-atom catalyst (SAC)-functionalised conductive Cu-HITP via electrochemical synthesis.[128] In this approach, the introduced Pd atoms were stabilised by coordinating with four nitrogen atoms to form a Pd–N_4 structure. Anchoring individual Pd atoms minimises pore blockage, preserving high surface area, and facilitating rapid gas diffusion. Although the sensor's response was only around –9.8% at 2 ppm NO_2, the SAC-based sensors exhibited excellent stability and reversibility, maintaining full recovery after 10 cycles.

H_2S sensing

Initially, only a few studies from Mirica's group reported H_2S detection by using Ni-HXTP/Cu-HXTP-based sensors.[120, 121] In 2022, Kim's group developed an ultra-thin Ni-HHTP film sensor via their MiCS method (previously applied to NO_x detection) that achieved an extraordinary response of approximately 2085% to 5 ppm H_2S, sparking significant interest in H_2S sensing.[129]

Among various strategies, the most effective approach involves integrating additional substances into conductive MOFs to form heterostructured chemiresistors.[130-133] In one example, a conductive 2D MOF (Ni-HHTP) was grown as a shell onto a porous 3D MOF core (UiO-66-NH_2) via a seed-mediated reaction, forming a well-integrated core-shell structure (Ni-HHTP@UiO-66-NH_2).[130] This design leveraged the high conductivity and redox activity of Ni-HHTP together with the high porosity and robust structure of UiO-66-NH_2 to create an interface with enhanced gas transport and charge transfer characteristics. When it was applied as a

chemiresistive sensor at room temperature, Ni-HHTP@UiO-66-NH_2 exhibited a 4.7-fold increase in response to H_2S compared to pristine Ni-HHTP, with a response of 337% to 5 ppm H_2S and an ultra-low limit of detection of 1.4 ppb.

In another example, a recent study integrated Zn-MOF-74—a 3D MOF known for its high H_2S uptake—by physically mixing it with Cu-HHTP.[132] This composite, Cu-HHTP@Zn-MOF-74, demonstrated markedly high sensing responses of 2752% to 5 ppm H_2S with an ultra-low LOD of 0.064 ppb. Zn-MOF-74 here acted as a reservoir to capture and release H_2S, facilitating better interaction with the Cu-based 2D c-MOF to enhance the overall sensor performance. The work further demonstrated the feasibility of integrating these materials into a real-time, wireless, portable sensing module, highlighting their potential for practical H_2S detection at room temperature.

The evolution of HXTP-based c-MOFs for chemiresistive gas sensing has progressed remarkably since the initial demonstration of $Cu_3(HITP)_2$ sensors by Dinca et al. in 2015. Early studies by Mirica's group expanded the application scope by developing sensor arrays and employing various deposition techniques to detect gases such as NH_3, H_2S, and NO_x. Building on these foundations, subsequent advances in synthesis methods, device fabrication, and material modifications have dramatically improved sensor performance (summarised in Table 2.1). These innovations have not only broadened the range of detectable gases (NH_3, H_2S, and NO_x) but also enhanced key parameters such as sensitivity, LODs, response time, and reversibility. Collectively, these studies underscore the immense potential of HXTP-based c-MOFs for real-time, portable, and high-performance gas sensing applications in environmental and industrial monitoring.

Table 2.1 Comparison of M-HXTP-based gas sensors: material types, target analytes, sensor responses, exposure times, and LODs.

Year	Materials	Analyte	Response	Time	LOD	Ref
2015	Cu-HITP	NH_3	1.1% (5 ppm)	30 s	0.5 ppm	73
2016	Cu-HHTP	NH_3	0.7% (80 ppm)	5 min	10 ppm	110
		NO	–1.8% (80 ppm)	5 min	40 ppm	
		H_2S	0.5% (80 ppm)	5 min	40 ppm	
	Ni-HHTP	NH_3	/	5 min	/	
		NO	–1.7% (80 ppm)	5 min	40 ppm	
		H_2S	4.2% (80 ppm)	5 min	40 ppm	
2017	Cu-HHTP@graphite	NH_3	4.6% (80 ppm)	5 min	19 ppm	111
		NO	–7.2% (80 ppm)	5 min	17 ppm	
		H_2S	1.5% (80 ppm)	5 min	35 ppm	
	Ni-HHTP@graphite	NH_3	2.8% (80 ppm)	5 min	19 ppm	
		NO	–9.0% (80 ppm)	5 min	17 ppm	
		H_2S	/	5 min	/	
2017	Cu-HHTP nano-thin film	NH_3	33% (5 ppm)	5 min	0.5 ppm	74
2017	Ni-HHTP on textile	NO	–49% (80 ppm)	1 h	1.4 ppm	120
		H_2S	98% (80 ppm)	1 h	230 ppb	
	Ni-HITP on textile	NO	81% (80 ppm)	1 h	160 ppb	
		H_2S	97% (80 ppm)	1 h	520 ppb	
2019	Pd@Cu-HHTP	NO_2	–62.1% (5 ppm)	20 min	/	123
2019	MOF-on-Cu-HHTP film	NH_3	25% (5 ppm)	5 min	/	112
2020	Cu-HHTP-THQ film	NH_3	4% (5 ppm)	5 min	20 ppb	113
2020	Cu-HITP-HHTP film	NH_3	240% (100 ppm)	5 min	/	114
2021	Cu-HHTP 3D-nano-film	NH_3	53% (5 ppm)	5 min	87 ppt	115
2021	Fe_2O_3@Cu-HHTP	NO_2	–89.4% (5 ppm)	30 min	11 ppb	124
2021	Ru@Pt@Cu-HHTP	NO_2	–53% (2 ppm)	1 h	0.2 ppm	125
2021	Pt@Cu-HHTP	NO_2	–53.7 (3 ppm)	20 min	0.1 ppm	126
2022	Cu-HHTP nano-thin film	NH_3	200% (100 ppm)	5 min	/	116
2022	Cu-HHTP on cotton	NO	–87% (80 ppm)	2 h	1 ppm	121
		H_2S	98% (80 ppm)	2 h	1 ppm	
2022	Ni-HITP nano-thin film	H_2S	2085% (5 ppm)	1 h	3 ppb	129
2022	Ni-HHTP@UiO-66-NH_2	H_2S	337% (5 ppm)	1 h	1.4 ppb	130
2023	hollow Zn-HHTP film	NH_3	43.8% (50 ppm)	1 min	39.9 ppb	117
2023	Pd_2@CoHITP	H_2S	880% (100 ppm)	200 s	1.4 ppb	131
2023	rGO@PDDA@Co-HITP	NO_2	9.05% (1 ppm)	40 s	6.8 ppb	127
		NO	11.00% (1 ppm)	40 s	11.2 ppb	
2024	Cu-HHTP@Cu_2O	NH_3	12% (5 ppm)	2 min	10 ppb	117
2024	Cu-HHTP@Zn-MOF-74	H_2S	2752% (5 ppm)	1 h	64 ppt	132

Table 2.1 (Continued)

Year	Materials	Analyte	Response	Time	LOD	Ref
2024	Pd@Cu-HITP	NO_2	–9.8% (2 ppm)	10 min	0.3 ppm	128
2025	Co-Cu-HHTP film	NH_3	9% (5 ppm)	1750 s	290 ppb	119
2025	Cu-HHTP on textile	NO	–400% (80 ppm)	5 min	3.7 ppm	122

2.3.4 Sensing mechanism of HXTP-based c-MOFs

HXTP-based c-MOF sensors function through the chemical or physical interactions between analyte molecules and the active MOF layer. Unlike classical metal-oxide sensors that rely on surface redox reactions at high temperatures, they operate at ambient conditions. Their sensing mechanisms are more complex, often involving a combination of electronic and structural effects.[4]

2.3.4.1 Coordination to metal nodes

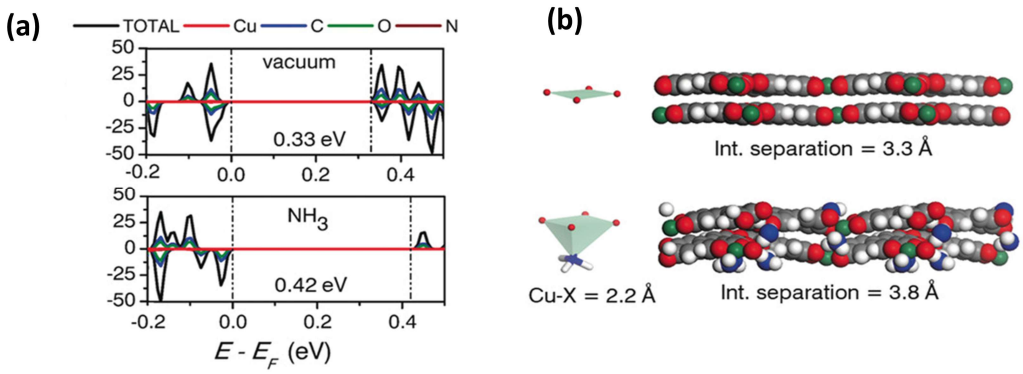

Figure 2.10. (a) Electronic density of states (DOS) of Cu-HHTP in vacuum and in presence of NH_3. (b) Representation of the coordination sphere of Cu^{II} centres (left) and DFT-calculated structure (right) in vacuum (above) and in presence of NH_3 (bottom). Reproduced from reference 135.

HXTP-based c-MOFs feature open metal sites that serve as strong binding sites for gas molecules. For example, unsaturated Cu(II) centres in $Cu_3(HHTP)_2$ can serve as the Lewis-acid to directly coordinate Lewis-basic analytes like NH_3.[134] Rubio-Gimenez et al. confirmed via IR spectroscopy and DFT that NH_3 binds at Cu nodes in this $Cu_3(HHTP)_2$.[135] As shown in Figure 2.10a, the band gap energy calculated from the electronic density of states (DOS) indicates this

binding increases the band gap of $Cu_3(HHTP)_2$ from 0.33 to 0.42 eV, which reduces the overall conductivity of the $Cu_3(HHTP)_2$.

2.3.4.2 Interaction with organic linkers

The π-conjugated linkers with heteroatoms, such as O, N, and S, provide sites for hydrogen bonding with analytes. For instance, Dinca et al. observed that $Cu_3(HITP)_2$ gave opposite resistance responses to primary amine $^nBuNH_2$ vs. tertiary amine Et_3N, which was attributed to hydrogen bonding at the –NH sites of HITP linkers.[79] Such interactions can alter the charge density on the aromatic linkers, thereby affecting conductivity. Even non-coordinating gases can interact via van der Waals or π–π interactions with MOFs, subtly shifting the electronic structure.

2.3.4.3 Framework distortion

Gas adsorption can also induce physical changes in the MOF lattice. Many c-MOFs are held together by π–π stacking, and insertion of guest molecules (especially in interlayer voids) can increase the interlayer spacing or cause lattice strain. Rubio-Giménez et al. showed that adsorption of N_2, H_2O, or NH_3 in $Cu_3(HHTP)_2$ slightly expanded the layer separation.[135] For example, the introduction of NH_3 can expand the interlayer distance of $Cu_3(HHTP)_2$ from 3.3 Å to 3.8 Å, as shown in Figure 2.10b. This small structural distortion can dramatically change out-of-plane charge transport, effectively altering the conductivity of materials.

The overall sensing response of HXTP-based c-MOF sensors is therefore a sum of several contributions, including structural distortion and coordination chemistry at both metal nodes and ligands. This complexity means that precise HXTP-based c-MOF sensing mechanisms remain under active investigation.[4] Nonetheless, it is clear that the chemiresistive response in c-MOFs originates from analyte-induced disruptions in the charge transport pathways within

the material, whether by changing the charge carrier density or by physically modifying the conductive network.

2.4 Percolation in chemiresistive gas sensors

Percolation phenomena play a crucial role in chemiresistive gas sensors that are composed of particulate or composite networks. Percolation theory describes how connectivity in a random network emerges only beyond a critical threshold. In chemiresistive gas sensors, operating near this percolation threshold can dramatically amplify the sensor response.[136] The following sections first discuss the percolation theory in gas sensors and then outline the development and strategies of creating percolation sensors.

2.4.1 Percolation theory in chemiresistive gas sensors

Percolation theory was developed in the mid-20th century to describe the random mechanism in many physical situations where fluid randomly spreads through a porous medium, with the key focus being on the random structure of the medium itself rather than on the random motion of fluid.[137] One example is the case of whether the interior of a porous stone (medium) gets wet when the stone is immersed in water (fluid). Suppose each pore in each stone has an independent probability, p, of transmitting the fluid. If p exceeds a critical threshold p_0, water will percolate through the stone and wet a significant fraction of its interior. Conversely, if the p is lower than p_0, the whole stone will remain dry.

In the context of chemiresistive gas sensors, the active porous materials can be regarded as the medium and electrical current through conductive pathways as the fluid, where the sensor's conductivity exhibits a distinct percolation curve, as shown in Figure 2.11. As the fraction of conductive connections increases, the system undergoes a transition at the percolation threshold where a connected pathway first forms. Below this threshold, there is no continuous pathway

for electrical current (the network behaves as an insulator), whereas above the threshold a connected pathway allows current to flow (the network becomes conductive). Near the threshold, conductivity follows a significant change in the fraction of conducting pathways, indicating that small changes in connectivity yield large changes in conductivity around the threshold. If the sensor is engineered to lie near the percolation threshold, then the addition or removal of even a few conductive pathways–for example, due to gas adsorption/desorption changing the conductivity of certain regions–strongly varies the overall conductance.[138, 139]

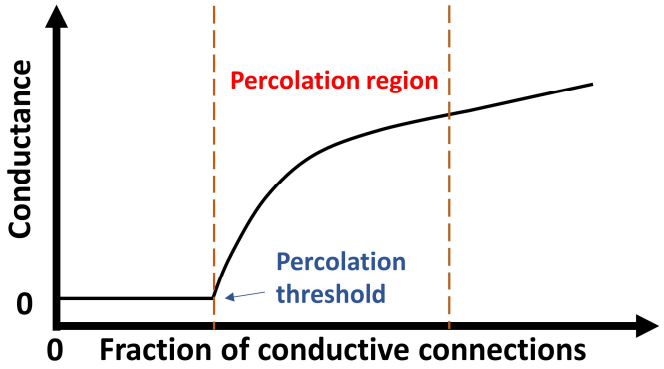

Figure 2.11. Percolation curve of chemiresistive gas sensors.

In short, percolation provides a mechanism to greatly amplify the effect of gas–material interactions on electrical signals in a chemiresistive gas sensor. This is in contrast to a fully conductive film with many redundant pathways, where the gas-induced changes have a smaller relative effect on total conductance. By leveraging percolation, sensor designers can achieve steeper response curves and potentially lower detection limits for target gases.

2.4.2 Development and strategies for creating percolation sensors

Tuning composition and morphology are key to engineering sensors that operate near the percolation threshold. Several strategies have emerged for creating percolation sensors.

2.4.2.1 Grain size control

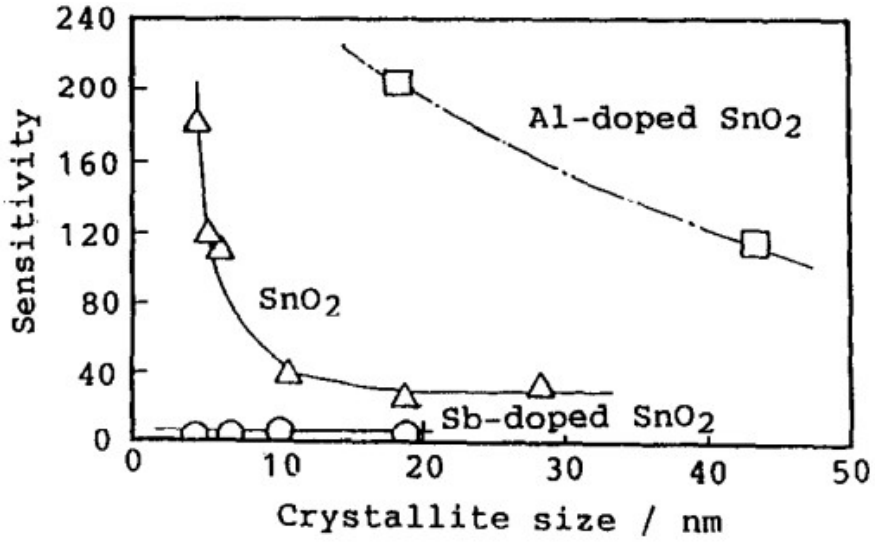

Figure 2.12. Correlation between gas sensitivity at 300°C and SnO_2 crystallite size. The analyte is H_2 fixed at 800 ppm. Reproduced from reference 140.

The influence of the active material's grain size on sensor sensitivity has been noticed and investigated. For example, in 1991, Xu et al. studied the effects of grain size by using porous SnO_2 nanocrystals with grain diameters D between 5 and 32 nm as active material.[140] SnO_2 is an n-type metal-oxide semiconductor with free electrons on its surface. In the presence of ambient oxygen molecules, these molecules adsorb onto the surface of SnO_2, taking the electrons from SnO_2 to form a depletion layer on its surface with a depletion depth L of ~3 nm. When reducing gas is introduced, the analyte reacts with the depletion layer and changes the conductivity. The sensing results shown in Figure 2.12 found that the sensitivity of SnO_2 sensors increased steeply only when D decreased to around $2L$ (6 nm), implying the grain sites greatly influenced the sensor sensitivity.

The phenomenon in the above work was precisely explained by Ulrich et al. through correlating the grain size of SnO_2 with percolation theory.[138, 141] In their theory, when the grain diameter D was comparable to or less than twice the depletion layer depth $2L$, the nanoparticles became fully depleted of free electrons and behaved as an insulator in air, corresponding to the insulating region in percolation theory. As the analyte gas was introduced, it consumed the

depletion layer, making a part of SnO_2 nanoparticles conductive again. When only a fraction of SnO_2 nanoparticles was conductive, no continuous conductive pathway existed across the sensor. After the concentration of analyte gas reached a critical concentration, the conductive pathway across the sensor was established and the conductivity of sensor scales dramatically, corresponding to the behaviour near the percolation threshold in percolation theory. Therefore, the sensitivity of a sensor is much higher when D is close to $2L$.

This strategy highly relies on the unique sensing mechanism of metal-oxide and can hardly be adapted to other systems.

2.4.2.2 Conductive–insulating Composite

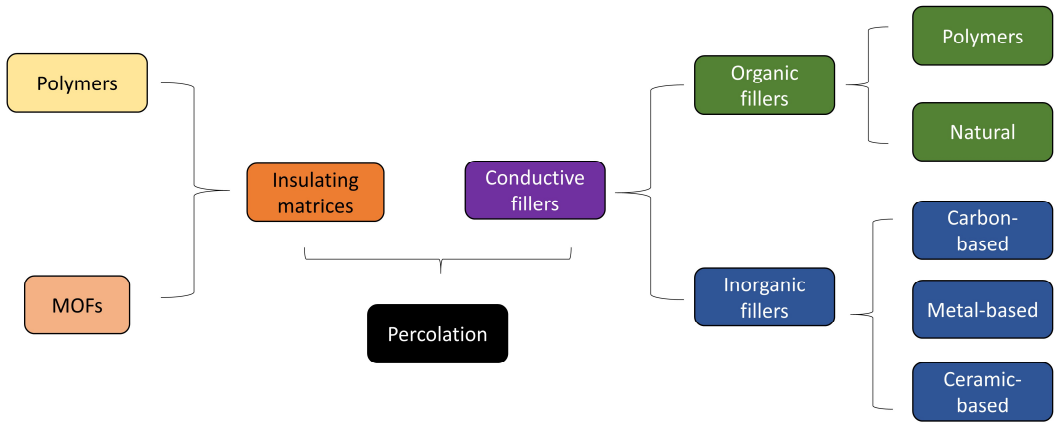

Figure 2.13. Examples of the fillers and matrices in conductive-insulating composite for percolation.

This strategy involves incorporating conductive fillers into an insulating matrix to achieve the percolation networks (see Figure 2.13 for examples of various fillers and matrices). Early attempts to exploit percolation with conductive-insulating composites mainly involved conductive filler–polymer systems. Since pure intrinsically conductive polymers (CPs) often have limited conductivity, controlled doping was essential to bring them into a useful conductive range.[142] Alternatively, conductive fillers (e.g. carbon-based materials,[136, 143] metal nanoparticles,[144, 145] CPs[146, 147]) were introduced into an insulating polymer matrix to achieve satisfactory electrical conductivity.[148] Instead of relying on doping chemistry, these composites

have a physical percolation network of the conductive filler dispersed in a polymer matrix, providing the mixture with excellent electrical conductivity and better mechanical properties.

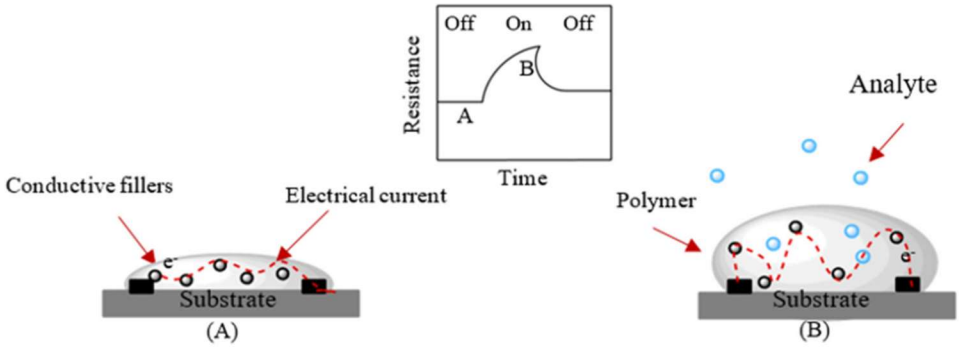

Figure 2.14. Schematic representation of chemiresistor mechanism based on swelling effect. The red dashed line gives the electrical current along the percolation pathway (A) before and (B) after swelling. Reproduced from reference 138.

Pioneering work by Lewis and co-workers demonstrated that carbon black–polymer composite resistors could serve as broad-spectrum vapour sensors.[149] The paper discussed two distinct percolation transition phenomena. The first was the concentration-induced percolation transition. As the carbon black content increased, a continuous conductive network formed within the polymer matrix once a critical concentration was reached, resulting in a sharp transition of conductivity. The second was the swelling-induced percolation transition (Figure 2.14). When the composite was exposed to vapours, the polymer swelled, which increased the volume of polymer and the distance between adjacent conductive nanofillers. This phenomenon disrupted the conductive network formed by the conductive filler. If the swelling was sufficient, the system was forced to cross its percolation threshold, leading to a dramatic change in conductance. This mechanism was the basis for many "electronic nose" sensor arrays in the 1990s, where different polymers (each with carbon black) provided different vapour response patterns.

In the 2000s and 2010s, the rise of nanotechnology impacted polymer composite sensors, since nanofillers like carbon nanotubes (CNTs) and graphene became available and were

incorporated as new conductive components. CNT-polymer composites often reach percolation at much lower filler loadings than carbon black due to the high aspect ratio of nanotubes, which can form networks more efficiently.[150, 151] This means more of the polymer's surface remains available for gas interaction at the threshold, improving sensitivity. For example, Philip et al. developed a wireless gas sensor composed of CNT and PMMA, exhibiting fast response (2-5 s) and a 100-1000 times increase in resistance when exposed to saturated vapours of dichloromethane, chloroform, and acetone.[152] The swelling-induced percolation is also the main mechanism in this work.

This strategy has also been applied to MOFs. In 2017, Freund et al. integrated a few insulating MOFs into conductive carbon nanoparticles to create percolation networks.[153] In a typical example, $[Cu(BF_4)_2(4,4'\text{-bipyridine})_2]$ (ELM-11) was selected as the matrix and carbon black as the conductive filler. They first investigated the percolation threshold concentration of carbon black in the mixture, which was 2.0 wt% by ball mixing. The sensing ability of the composite sensors to *n*-butane was then tested at different partial pressures. It should be noted that ELM-11 is a unique MOF featuring a dynamic "gate-opening" behaviour: when exposed to some gases with a specific threshold pressure, the interlayer distance of ELM-11 expands suddenly. By leveraging this unique property, ELM-11 showed a sudden expansion when the partial pressure of *n*-butane reached 30%. This expansion follows the swelling-induced percolation mechanism and the sensor showed an extremely big response up to 5000%.

Composites made from inorganic fillers embedded in a polymer matrix have been extensively reviewed above in the context of chemiresistive gas sensing. In contrast, organic components, such as CPs, can also serve as fillers.[154, 155] While inorganic filler systems such as carbon black or CNTs rely on a swelling-induced percolation transition to produce resistance changes, CP-based systems derive their sensing capabilities primarily from the inherent charge transport and

molecular interactions of the CPs. In fact, CP-based systems should be specifically designed to minimise swelling effects, which could otherwise impair the performance of the CPs.

The conductive-insulating composites remain a very important strategy to leverage percolation in chemiresistive gas sensors nowadays, as they yield devices with excellent electrical conductivity, robust mechanical properties, and enhanced stability. However, the overall system design is crucial, as different systems can operate via distinct mechanisms. Moreover, even though the application of purely organic or inorganic conductive fillers has been extensive, hybrid materials such as c-MOFs have been underexplored. Incorporating c-MOF fillers within an insulating matrix offers an intriguing approach by combining the advantages of both material classes to potentially enhance sensor performance.

2.4.2.3 Deposition control

The unpredictable formation of percolation networks in randomly dispersed conductive–insulating composite systems remains a significant challenge, making it difficult to control the growth of percolation networks.[156] An alternative approach is the deposition-control strategy, which achieves the percolation transition by directly depositing a conductive material onto sensor electrodes until connectivity is just attained. Techniques such as electrochemistry can be used for this purpose, enabling precise control over the growth of c-MOFs that bridge the electrode gaps.

In 2004, Reemts et al. studied the direct electrochemical deposition of polyaniline (PANI) across an 8 μm insulating gap between gold IDEs.[157] The electrodeposition was carried out by cyclic voltammetry (CV) through sweeping the potential between -0.2 and +0.9 V relative to the silver reference electrode. The IDEs were bridged after the second cycle and both the conductivity and thickness of the PANI film increased with additional cycles. Even though their

work mainly focused on the doped state of devices rather than the percolation behaviour during electrodeposition, it demonstrated a controlled way to form continuous conductive pathways.

Liu et al. conducted the early research focusing on the percolation theory via a deposition-control strategy.[158] In their experiments, PANI was electrochemically deposited on gold IDEs with 100 μm gaps using chronoamperometry (CA), where deposition was regulated by time rather than by cycles. The result showed the device stayed insulating after 900 s, while the resistance decreased significantly after 1800 s. The resistance tended to level off after 3600 s. The obtained PANI devices were tested as chemiresistive gas sensors to 4 ppm ammonia gas. It turns out the sensitivity of sensors increases as the deposition time increases, while it drops significantly after deposition time is over 3600 s. They ascribed the drop in sensitivity to the thickening in film thickness that prevents gas diffusion into the film.

Our research group has made significant contributions to this field. For instance, Murugappan et al. fabricated percolation networks of poly(3,4-ethylenedioxythiophene) (PEDOT) on IDEs with 20-micron gaps via CV cycles.[159] In the paper, an idealised percolation curve was presented in Figure 2.15a to systematically describe the percolation behaviour. Initially, the polymer was exclusively grown on electrodes, leaving the device insulating, corresponding to the behaviour in the insulating region. As the deposition continued, the growth of polymer extended from the electrodes toward the gap. Once the percolation threshold was reached, the gap was bridged, marking the onset of the percolation region where device conductance varies significantly. Finally, when the gap is fully covered, the conductance levels off, indicating the end of the percolation region and the beginning of the thin film region. The successful creation of percolation networks was clearly confirmed by conductance measurements and scanning electron microscopy (SEM) (Figure 2.15b and c, respectively).

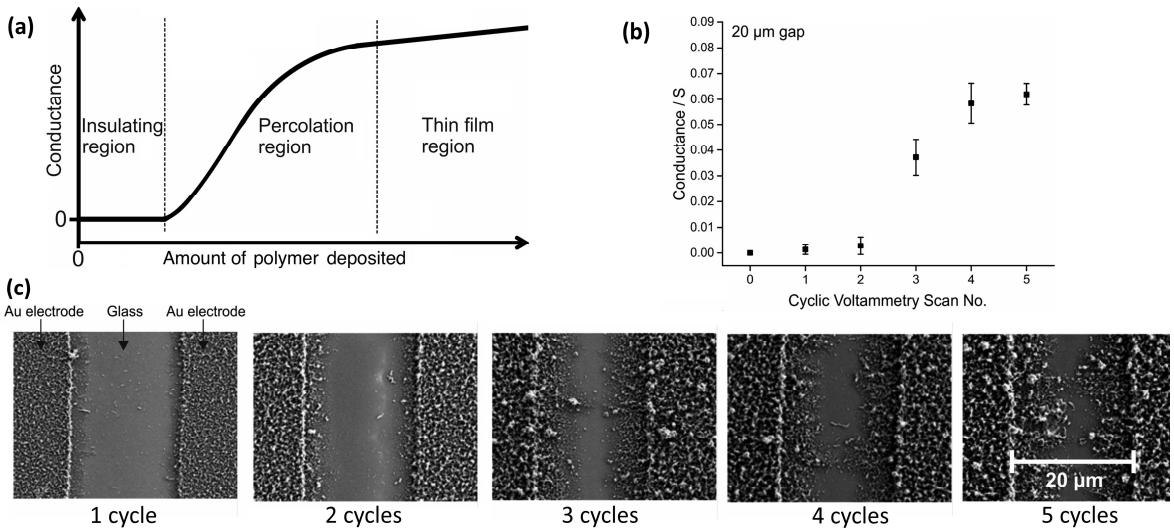

Figure 2.15. (a) Illustration of an idealised percolation curve showing how conductance between electrodes varies with polymer deposition. (b) Plot of conductance vs CV scans for IDEs with 20 µm gaps. (c) SEM images of Au IDEs with 20 µm gaps after 1 to 5 CV scan cycles. Reproduced from reference 155.

Moreover, Armitage et al. employed CA to directly deposit polypyrrole (PPy) on IDEs with 100-micron gaps,[139] forming percolation networks by controlling deposition time that were subsequently evaluated as chemiresistive gas sensors for NH_3. The sensing results indicated the sensors operating in the percolation region exhibit much higher sensitivity than the sensors operating in the thin film region. This heightened sensitivity is attributed to the reduced number of conductive pathways between the electrode fingers in percolation sensors, where even minor interactions can generate substantial responses. However, regarding limits of detection (LODs), as shown in Figure 2.16, some percolation sensors exhibited higher values than thin-film devices. This is likely because sensors operating near the percolation threshold have higher resistance, which in turn leads to increased noise levels. Thus, the interrelationship among percolation theory, deposition-controlled polymerisation on IDEs, and their chemiresistive sensing behaviours is tightly correlated.

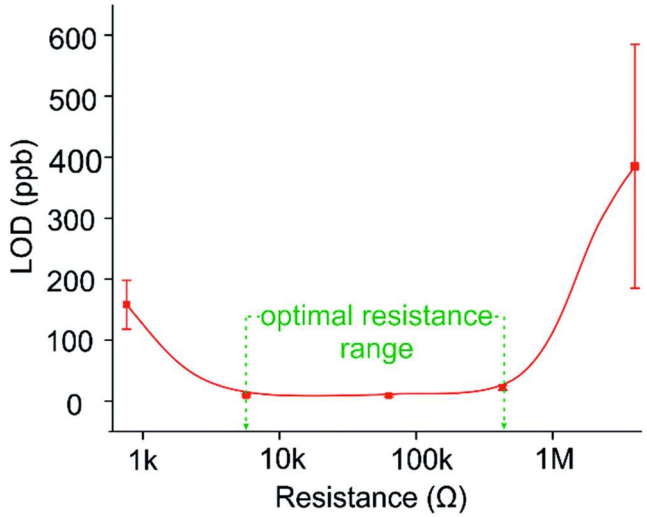

Figure 2.16. LODs for the PPy sensors investigated. The optimal resistance range represents the resistances with the highest sensitivity and lowest LOD, corresponding to the optimum deposition zone of the percolation region.

From the discussion above, percolation networks are generally achieved by controlling deposition times via CA or deposition cycles via CV, approaches that do not allow continuous monitoring of conductance. To overcome this limitation, Li et al. implemented in-situ conductance measurements to monitor real-time data and control electropolymerisation in the percolation region.[160] In the setup, the electrochemical workstation supplies the faradaic current to drive the electrochemical reaction, while a source/measure unit (SMU) applies a small potential (60 mV) across the IDEs and records the drain current (i_d). This arrangement enables the generation of a percolation curve (i_d vs deposition time) that allows for continuous tracking of the deposition process, thereby producing more reproducible sensors. Notably, the sensor behaviour aligns with the theory proposed by Armitage et al., with optimal performance achieved at an operating point between the onset and end of the percolation region.

To further enhance sensor sensitivity, Li et al. introduced a templating strategy for the formation of percolation networks, suggesting the possibility of fabricating nanostructured percolation networks.[161] Rather than directly depositing polymer on IDEs, a monolayer of polystyrene (PS) nanospheres was pre-deposited on IDEs. PPy was then electrochemically deposited onto the PS

on IDEs. Finally, the PS template was removed by solvent, resulting in the templated sensors. By controlling the deposition time, PS-templated PPy percolation sensors were obtained. However, the optimal templated PPy percolation sensor in this experiment showed lower sensitivity compared with conventional PPy percolation sensors. The reduced sensitivity was attributed to the fact that only a monolayer of PS was deposited and the PS on the substrate was completely covered by PPy. Consequently, the PS could not be removed effectively, and an open, porous inverse-opal structure was almost not formed.

In summary, the fundamental aspects of percolation sensors formed via deposition-control strategies have been well elucidated. Recent work in this field has focused on enhancing the reproducibility of these methods and improving sensor sensitivity. Looking ahead, future research should explore the incorporation of alternative active materials including c-MOFs rather than relying on polymers. Additionally, exploring other deposition techniques, such as printing techniques is necessary, which offers promising new strategies for advancing percolation sensor development.

2.5 Electrohydrodynamic (EHD) jet printing for chemiresistive gas sensors

Implementing the percolation concepts in practical sensing devices requires precise patterning and deposition of materials. Electrohydrodynamic (EHD) jet printing has emerged as an advanced fabrication method well-suited for depositing materials with fine control.[162, 163] EHD printing uses electric fields to eject and direct features, allowing the creation of micro-to-nanoscale features on various substrates. This section outlines its operating principles, different categories, and recent applications in gas sensing.

2.5.1 Principles of EHD jet printing

EHD jet printing relies on the fundamental balance of electrostatic force and fluid dynamics. During printing, a conductive ink is fed through a fine nozzle, and a high voltage is applied between the nozzle and the substrate. The electric field induces charges in the ink and pulls the liquid meniscus into a conical shape known as the Taylor cone. When the electrostatic force overcomes the liquid's surface tension, the cone emits a thin jet of ink from its tip. Under stable cone-jet conditions, EHD printing can continuously draw filaments or droplets of ink to write features such as dots, lines, or complex patterns with high resolution. The resulting jet has a diameter determined by the interplay of several parameters:[163]

Applied voltage (V): A higher voltage increases the electric field strength, reducing the jet diameter and yielding finer features. However, an over-high voltage can destabilise the jet and produce satellite droplets.

Stand-off height (d): The nozzle-to-substrate distance affects the electric field distribution. A shorter distance yields a stronger field and finer features, while an excessively low height may lead to ink spreading or splashing.

Nozzle diameter (d_n): Although the jet diameter can be much smaller than the nozzle's physical diameter due to electrostatic stretching, the nozzle's size and wettability still critically influence the initial formation of the Taylor cone. Smaller nozzle sizes and more hydrophilic inner walls tend to confine the ink more effectively, leading to a narrower jet and reduced pattern width.

Ink Surface tension (γ): The ink surface tension γ determines the force holding the ink at the nozzle. A higher γ requires a higher voltage to form a stable Taylor cone.

Ink Viscosity and Conductivity: The viscosity (η) and electrical conductivity (K) of ink are critical. Low-viscosity and highly conductive inks yield a smaller droplet size. Conversely, high viscosity may stabilise the jet but also slow down droplet breakup, leading to broader features.

Flow rate (Q): Flow rate here refers to the speed of ink delivered into the nozzle. A higher flow rate can lead to thicker lines or satellite droplets, while a too-low one may cause discontinuities.

Only when all the parameters are finely tuned can a desired Taylor cone be formed during printing. However, the final resolution of the printed pattern is not only influenced by the jet-generation parameters (including the parameters discussed above) but also by the properties of the surface of substrate:

Substrate Translation Speed: Faster movement limits ink accumulation, reducing the printed line width. Conversely, slower speeds allow more ink to be deposited, broadening the pattern.

Substrate surface energy: Substrates with higher surface energy are more wettable, causing the printed material to spread extensively in order to minimise its potential energy.

2.5.2 Types of EHD jet printing techniques

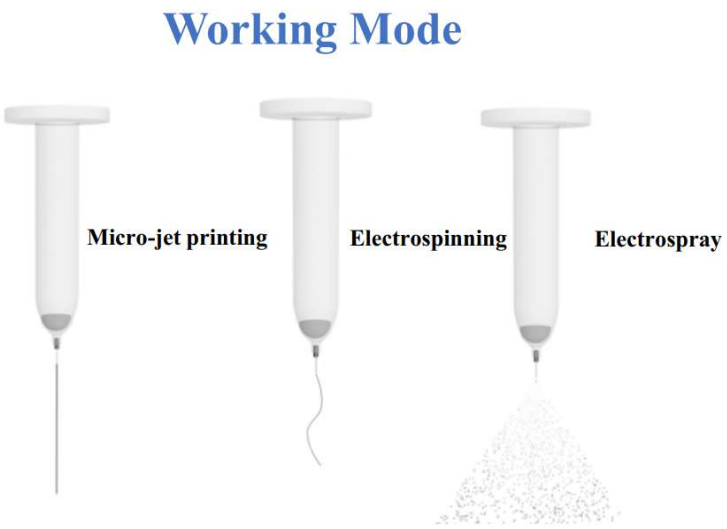

Figure 2.17. Three working modes for EHD printing. Reproduced from reference 158.

Depending on the applied voltage and working distance, EHD printing with a stable Taylor cone can be classified into different modes, including micro-jet mode, electrospinning mode, and electrospray mode (see Figure 2.17), each suitable for particular outcomes.[162]

Micro-jet printing: In micro-jet mode, the process is characterised by a stable Taylor cone-jet formation under near-field conditions. It allows high-resolution features with a few micrometres or even sub-micron in width to be fabricated. Typical operating conditions are a low voltage (~0.5–3 kV) and a short stand-off height (~0.1–1 mm). This is the mode generally referred to as EHD jet printing, used to write conductive tracks, sensor patterns, or precise spots of material.

Electrospinning: When the voltage and stand-off distance are increased (~1–10 kV and ~10–50 mm, respectively), the EHD jet can stretch and solidify into an ultra-thin continuous fibre rather than breaking into droplets. In this mode, the ink is drawn into an elongated, unbroken filament that solidifies as it travels through the air, forming nanofibres upon deposition. The fibre diameter is largely controlled by the ink's viscosity and the balance between the applied electric field and the ink flow rate. Unlike micro-jet mode, where the focus is on forming features with high positional accuracy, electrospinning is typically used to create nonwoven mats or aligned fibrous networks that are valued for their high surface area and porosity. These fibrous structures are particularly useful in applications where a large interfacial area is needed.

Electrospray: At even higher voltages (15–30 kV) and larger stand-off distances (100–250 mm), the jet becomes unstable and disperses into a mist of charged droplets. Rather than depositing continuous lines or fibres, the electrospray produces a uniform, spray-like deposition of microdroplets, resulting in a consistent coating or thin film. This mode is particularly useful when a homogeneous coating is required over a large area, rather than well-defined patterned lines.

While EHD jet printing offers multiple modes, each with its unique advantages, the micro-jet printing mode stands out for its mild operating conditions and its ability to create patterns with

high resolution and high positional accuracy. These features make it particularly suitable for fabricating electronic devices such as gas sensors.

2.5.3 Applications of EHD jet printing in chemiresistive gas sensors

The advantages of EHD jet printing make it useful in additive manufacturing,[164, 165] biological applications,[166, 167] and the development of flexible electronic devices.[168, 169] The aim of this section is to review the application of EHD jet printing focusing on chemiresistive gas sensors. Although its application in chemiresistive gas sensors is still emerging, a range of key materials, including metal oxides, polymers, and c-MOFs, has been explored.

Metal-oxide-based EHD gas sensor

One challenge with printing active materials on substrates is ink formulation, as some active materials like metal oxides are typically insoluble powders with rigid structures, leading to the obstruction of the nozzle easily. Kang et al. developed a new method for fabricating gas sensors by using EHD printing of metal oxide nanofibre fragments.[170] The process started with the synthesis of metal oxide nanofibres, such as SnO_2, WO_3, In_2O_3, and NiO, via electrospinning. To enable precise patterning, the long nanofibres were fragmented into shorter pieces through ultrasonication in ethanol. After drying, these fragments were redispersed in organic solvents again to create a printable ink.

EHD printing was then used to micropattern the nanofibre ink onto sensor substrates. In the printing system, a syringe with a fine nozzle (~90 μm inner diameter) ejected the ink under a controlled voltage of 1.3–1.5 kV and a stand-off height of ~200 μm. The obtained EHD-printed sensors were evaluated by sensing tests to NO_2, H_2S, and CO. The sensors were capable of detecting NO_2 down to 0.1 ppm, H_2S to 1 ppm, and CO to 20 ppm, with response and recovery

times varying by material. For instance, In_2O_3 and NiO typically showed faster dynamics than SnO_2 and WO_3.

In another report, a micro-bilayer sensor fabricated in situ via EHD jet printing was developed.[171] In this process, a nozzle with a 100 μm inner diameter was employed under an applied voltage of 1.1–1.3 kV and a stand-off distance of ~800 μm. The sensor consists of a ZnO/SnO_2/Au (ZSA) sensing layer and a Pt-loaded mesocellular silica foam (Pt-MCF) catalytic filter layer. To prevent nozzle clogging during printing, each ink was formulated as a precursor solution containing corresponding metal salts. The sensing layer was built through multiple printing cycles followed by calcination at approximately 500°C, whereas the catalytic filter layer was printed on top and subsequently calcined at around 300°C.

The calcined ZSA sensing layer exhibited a unique vertically grown nanosheet structure with a width of about 3–5 μm and a thickness of less than 10 nm. The vertical alignment and porous arrangement provide a high specific surface area and efficient gas diffusion. Meanwhile, the Pt-MCF catalytic filter layer enhanced selectivity. For example, when incoming mixtures encountered Pt-MCF layer, interfering gases such as CO were oxidised to CO_2, significantly reducing their influence on H_2. The sensor showed high sensitivity, a low LOD (94 ppb), high selectivity, and quick response (24 s/35 s, 50 ppm).

Polymer-based EHD gas sensor

In 2012, an EHD impulse printing technique was applied to fabricate polymer-based chemiresistive gas sensors.[172] Unlike continuous EHD jet printing, this method employed a high-voltage impulse to generate polyaniline (PANI) droplets doped with camphorsulfonic acid (CSA) using a nozzle of approximately 0.2 mm inner diameter. The research investigated how key parameters—applied voltage, voltage frequency, and duty ratio—influenced the droplet diameter and ejection frequency. Under optimal conditions (2450 V, 70 Hz, 40% duty ratio, 1

mm stand-off height distance, and 100 μL/h flow rate), the study achieved a printed line width of ~92 μm. The fabricated sensor exhibited a rapid response to NH_3, with an LOD of ~300 ppm. While this work established the feasibility of using EHD impulse printing for fabricating PANI-based gas sensors, its sensitivity was relatively limited.

Murugappen et al. further improved the sensitivity of PANI-based gas sensors by employing EHD printing to create discrete patterns on IDEs.[173] Three doping strategies were investigated to convert undoped PANI into its conductive state: HCl-doping, CSA-doping, and a co-doped blend of HCl and CSA. The different PANI blends were first drop-cast on either glass IDEs or flexible IDEs. Even though the sensing test indicated all the drop-cast films exhibited weak and irreversible sensing responses to ammonia, the SEM and XRD revealed that CSA doping produces a more crystalline and finely dispersed polyaniline, while HCl-doped and co-doped polyaniline tend to aggregate into larger particles.

Different inks were then deposited on both glass and flexible IDEs via EHD printing. A gold coated glass nozzle (5–10 μm inner diameter) was used for the EHD printing under a voltage ranging from 2–10 kV and a stand-off height of 50–100 μm. On rigid glass substrates, sensors fabricated with CSA-doped polyaniline achieved a sensitivity of 2.5% per ppm with an LOD of approximately 0.22 ppm. Co-doped sensors exhibited a slightly lower sensitivity (0.5% per ppm) with an LOD of around 0.86 ppm. In contrast, HCl-doped sensors faced printing challenges, such as nozzle clogging, leading to inadequate sensor performance. When printed on flexible substrates, only the HCl-doped polyaniline showed successful deposition. The difference in substrate influenced the film thickness and the sensor's electrical response, with the flexible sensor showing an LOD of 0.74 ppm and an exceptional sensitivity of 6.9% per ppm.

c-MOF-based EHD gas sensor

The application of EHD jet printing to c-MOF materials has recently been achieved.[122] Ahmadipour et al. (2025) developed a nitric oxide (NO) sensor by integrating an ink of $Cu_3(HHTP)_2$ mixed with an ionic liquid (IL) onto electrospun fibrous mats made from polylactic acid (PLA). The integration was carried out by EHD printing with a nozzle of 100 μm, an applied potential of 2.5 kV, and a stand-off height of 2 mm. The use of IL in the ink served multiple purposes, where it improved the ink's printability, enhanced the electrical connectivity between MOF crystals, and provided additional functional groups to interact with the target gas.

The printed $Cu_3(HHTP)_2$ sensors showed not only a 582-fold increase in conductivity compared to $Cu_3(HHTP)_2$ powders but also an enormously enhanced response of ~570% to 100 ppm NO compared to the ~5% response of the drop-cast counterpart. The printed $Cu_3(HHTP)_2$ sensors were capable of detecting NO down to ~3.7 ppm and operated reliably under ambient humidity, illustrating the viability of printed MOFs in real-world conditions.

The applications of EHD jet printing for metal oxide, polymers, and c-MOFs demonstrate its capability to integrate various materials into practical sensor devices. This technique can produce highly responsive sensors by uniting advanced materials with precision printing. As printing technology and ink chemistry continue to improve, a wider adoption of EHD printing to fabricate MOF-based gas sensor networks can be anticipated.

2.6 Summary

C-MOFs uniquely combine the high specific surface area, porosity, and crystallinity of conventional MOFs with exceptional intrinsic electrical conductivity, making them ideal candidates for various applications, including room-temperature gas sensing. Among all categories of c-MOFs, the HXTP-based MOFs stand out because of their efficient charge

transport, abundant active sites, and structural tunability. Their extended π-conjugation and planar geometry facilitate charge delocalisation through both in-plane and out-of-plane pathways, ensuring notable electrical conductivity while retaining high porosity and active sites. These features make HXTP-based MOFs particularly promising for gas sensing.

Chemiresistive gas sensors based on HXTP-based c-MOFs have demonstrated significant progress. In parallel with material design, advances in synthesis and deposition techniques have played a crucial role in enhancing sensor performance regarding responses, LODs, selectivity, and response time. Traditional approaches, such as powder drop-casting, have been complemented by modern methods including layer-by-layer liquid-phase epitaxy, template-induced nanostructuring, and electrochemical deposition. Each of these methods offers varying degrees of control over film thickness, uniformity, and orientation, which are critical for achieving superior sensitivity. Emerging techniques like electrohydrodynamic (EHD) printing also hold promise and deserve further exploration.

Creating percolation networks has proven effective for improving sensor sensitivity in polymer and metal oxide-based chemiresistive gas devices. However, the application of percolation theory to c-MOFs has remained largely unexplored. Developing c-MOF-based percolation networks, through either conductive-insulating composites or precise deposition control, presents a promising approach to further improve sensitivity.

Overall, the integration of advanced HXTP-based c-MOF design, percolation theory, and innovative fabrication strategies is paving the way for highly sensitive, selective, and reproducible gas sensors for real-time environmental and industrial monitoring at room temperature.

Chapter 3

Experimental techniques

The fabrication of a chemiresistive gas sensor involves two critical steps: synthesis of the sensing materials and their deposition onto substrates. This chapter introduces the essential chemicals, substrates, general experimental methods, and characterisation techniques applied in experimental Chapters 4 to 7.

3.1 Chemicals and substrates

Unless otherwise specified, all the chemicals were purchased from Sigma-Aldrich and used as received. Necessary reagents used in this thesis comprised 2,3,6,7,10,11-hexahydroxytriphenylene (H_6HHTP, Tokyo Chemical Industry, 95%), copper nitrate trihydrate ($Cu(NO_3)_2 \cdot 3H_2O$, 98%), copper acetate hydrate ($Cu(CO_2CH_3)_2 \cdot H_2O$, 98%), zinc nitrate hexahydrate ($Zn(NO_3)_2 \cdot 6H_2O$, 98%), and zinc acetate dihydrate ($Zn(CO_2CH_3)_2 \cdot 2H_2O$, 98%). Detailed information on the chemicals is presented in each experimental chapter. Gases including nitrogen (zero grade), oxygen (industrial grade), argon (industrial grade), ammonia (10 ppm, filled with nitrogen), and carbon monoxide (10 ppm, filled with nitrogen) were obtained from BOC Gases.

Indium tin oxide (ITO) glass slide substrates (25 × 25 × 1 mm) were purchased from Sigma-Aldrich. Two types of platinum on glass interdigitated electrodes (Pt IDEs) were employed as substrates. The Pt IDEs with 10 μm gaps (Figure 3.1a) were purchased from Metrohm. Each IDE consists of 125 pairs of 10 μm wide Pt electrode fingers separated by a gap of 10 μm on insulating glass. The platinum IDEs with 5 μm gaps (Figure 3.1b) were obtained from MicruX

Technologies. Each IDE consists of 180 pairs of 5 µm wide Pt electrode fingers separated by a gap of 5 µm on insulating glass. Prior to the experiments, all the substrates were sonicated in acetone and ethanol for 30 s.

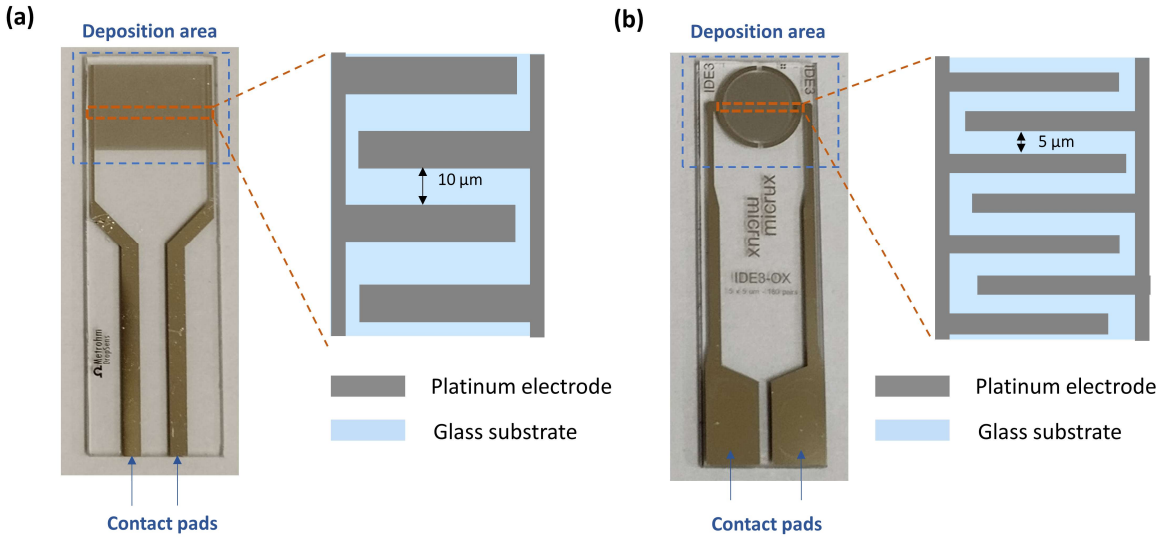

Figure 3.1. Platinum interdigitated electrodes bought from (a) Metrohm and (b) MicruX Technologies were used. The width of the platinum electrode fingers is 10 µm for Metrohm and 5 µm for MicruX Technologies, with corresponding gaps between the electrode fingers being 10 µm for Metrohm and 5 µm for MicruX Technologies.

3.2 Sensor fabrication

This section discusses the fabrication methods used to create the sensors. Two main categories of fabrication are addressed: in-situ and ex-situ methods. In-situ techniques involve fabricating the sensing material directly onto the electrode surface, while ex-situ methods involve synthesising the sensing material separately before depositing it onto the electrode.

3.2.1 In-situ sensor fabrication

In-situ fabrication methods applied in this thesis comprise electrochemical deposition and electrohydrodynamic jet printing techniques. Electrochemical deposition can be further

classified into two types: anodic electrochemical deposition and cathodic electrochemical deposition.

3.2.1.1 Electrochemical deposition

The electrochemical deposition of $Cu_3(HHTP)_2$ was carried out at room temperature using a PGSTAT204 Autolab electrochemical workstation (Eco Chemie) interfaced to a PC with NOVA version 2.1 software. A standard three-electrode system was employed (Figure 3.2), with the IDEs or ITO slides as the working electrode, a Pt coil (BASi) as the counter electrode, and an Ag/AgCl (saturated KCl, CH Instruments) as the reference electrode. An electrochemical cell (100 mL, Alvatek) was used, and the volumes used for the electrochemical reactions are 50 mL. $Cu_3(HHTP)_2$ was deposited on the working electrodes via chronoamperometry at an appropriate potential. This potential is either negative or positive, depending on whether cathodic or anodic electrochemical deposition is being performed. Cathodic electrochemical deposition was applied in Chapter 4, while anodic electrochemical deposition was used in Chapter 5.

Cathodic electrochemical deposition was carried out in a precursor solution of H_6HHTP (0.66 mM), $Cu(NO_3)_2 \cdot 3H_2O$ (1 mM), tetrabutylammonium hexafluorophosphate ($(NBu_4)PF_6$, 1 mM), and dimethylformamide (DMF).[90] The mixed solution was first purged with O_2 for 30 mins, before applying a −0.2 V potential onto the working electrode. O_2 in the solution serves as the probase, whereby the negative potential reduces the O_2 into O_2^-. O_2^- subsequently deprotonates H_6HHTP and promotes the formation of $Cu_3(HHTP)_2$.

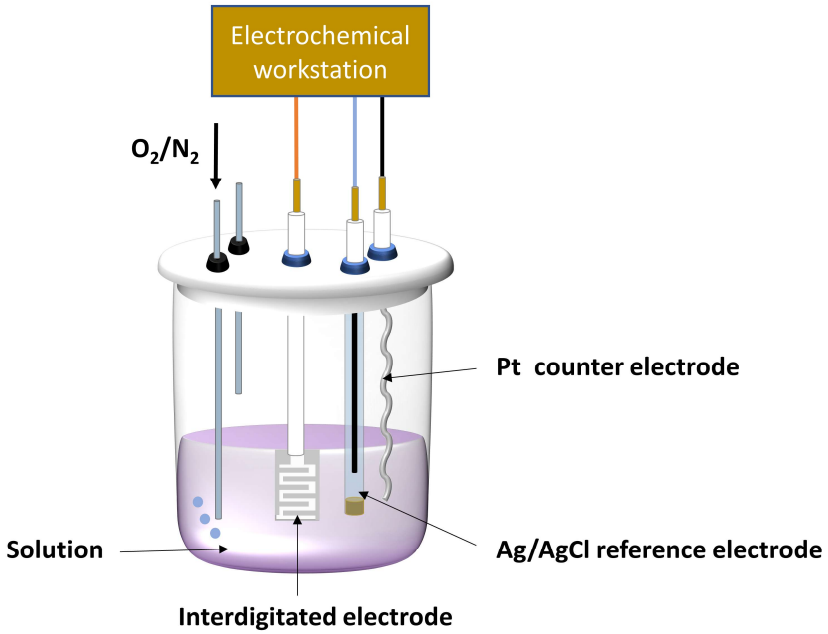

Figure 3.2. Schematic diagram of a three-electrode system employed in this thesis. The interdigitated electrode functions as the working electrode, a platinum coil is used as the counter electrode, and an Ag/AgCl electrode serves as the reference electrode.

Comparatively, anodic electrochemical deposition was performed using a precursor solution containing H_6HHTP (1.125 mM), $Cu(NO_3)_2 \cdot 3H_2O$ (2.25 mM), potassium chloride (KCl, 100 mM), DMF/H_2O (V:V, 1/15), and nitric acid (0.5 mM).[88] After purging the solution with N_2 for 10 minutes, a positive potential of +0.3 V was applied to the working electrode. The anodic or cathodic electrochemical deposition of $Cu_3(HHTP)_2$ on the working electrode was halted at different deposition times. After deposition, the prepared samples were immersed in DMF to remove residues and dried under an ambient environment overnight. Then, the resistance/conductance of each sample was measured using an RS PRO IDM 98IV handheld digital multimeter.

3.2.1.2 Electrohydrodynamic jet printing

Electrohydrodynamic (EHD) jet printing was performed using a home-built EHD jet printer (Figure 3.3), which consists of a PWS4205 DC power supply (Tektronix), a 3590-1320 voltage

amplifier (Applied Kilovolts), a 25 mm motorized translation Z stage (Thorlabs), 551 high-precision linear XY stages (Physik Instrumente), and an AM7915MZTL USB microscope (Dino-Lite). DinoCapture software (Dino-Lite) was used to capture optical images from the microscope and to measure the nozzle-to-substrate distance and strip width. Glass pipettes (World Precision Instruments) with a diameter of 30 μm were selected as the nozzles used for EHD printing. An adhesive layer of 50-70 nm Au was coated onto the nozzle surface by thermal evaporation to make the nozzles electrically conductive.

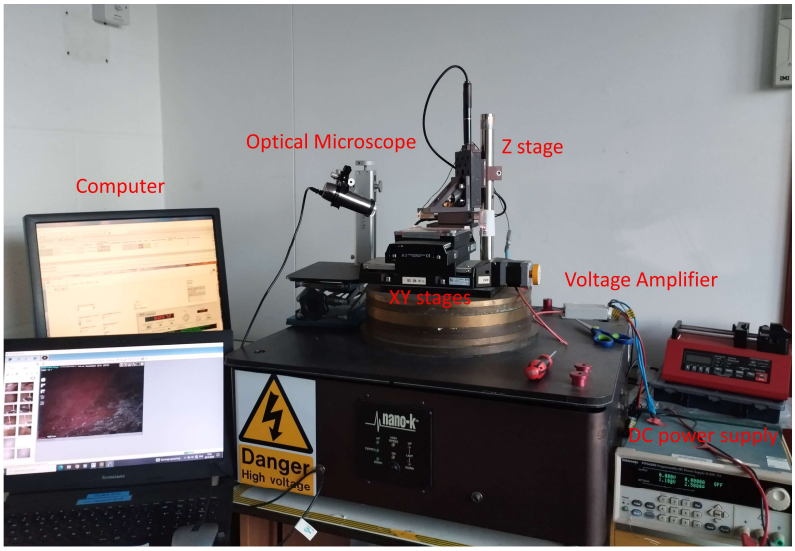

Figure 3.3. Photograph of EHD printer, including computer, optical microscope, XY stages, Z stage, voltage amplifier, and DC power supply.

A typical printing ink was prepared from a precursor solution of either $Cu(NO_3)_2 \cdot 3H_2O$ (5 mM) or $Zn(NO_3)_2 \cdot 6H_2O$ (5 mM) combined with H_6HHTP (3.3 mM) in DMF/ethanol/ethylene glycol solvent mixture (V:V:V, 6:1:10). The concentration of H_6HHTP in the ink can be further diluted as needed. The inks were loaded into the coated nozzles using 20 μL microloader pipette tips. Since the substrate of IDEs is insulating glass, the contact pads of IDEs are connected to the EHD platform using copper tape. During the printing, a voltage bias was applied between the nozzles and IDEs to generate the necessary electrostatic force for printing. The range of applied voltages is between 1.4 kV and 2.4 kV. The height between nozzles and IDEs is between 150

and 300 μm. The precursor strips were first formed on the substrate after the precursor solution was printed. The MOF strips were in situ developed by baking the precursor strips in an oven at 60°C for 4 h. The dried samples were then immersed in DMF for 2 hours to remove any unreacted species.

3.2.2 Ex-situ sensor fabrication

Ex-situ fabrication processes involve separate steps for the preparation and deposition of functional materials onto substrates. The preparation and deposition methods employed in this thesis are the hydrothermal solution synthesis method and the drop-casting deposition method, respectively.

3.2.2.1 Solvothermal solution synthesis

Two types of conductive metal-organic frameworks $Cu_3(HHTP)_2$ and $Zn_3(HHTP)_2$ were prepared via hydrothermal solution synthesis. For $Cu_3(HHTP)_2$, Copper acetate hydrate (60 mg) and H_6HHTP (60 mg) were mixed in a glass vial with 50 mL of methanol as the solvent. The mixture was sonicated for 2 min to enhance the uniformity of the solution. Then, this mixture was maintained at 65°C for 24 h. Black $Cu_3(HHTP)_2$ powder formed at the bottom of the vial and was collected. The powder was washed with methanol three times and dried at 80°C for 4 hours.

3.2.2.2 Drop-casting deposition

2 mg of prepared $Cu_3(HHTP)_2$ or $Zn_3(HHTP)_2$ powders were added into 1 mL of acetone in a glass vial to form a suspension. The suspension was sonicated for 5 min to disperse the powder. 20 μL of suspension was pipetted onto the deposition area of Pt IDEs. Then, IDEs were left in the ambient environment to allow the solvent to evaporate overnight.

3.3 Characterisation techniques

This section introduces several characterisation techniques employed in this thesis to identify the electrochemical, structural, chemical, or gas sensing properties of sensor samples.

3.3.1 Cyclic voltammetry

Cyclic voltammetry (CV) is a widely used electrochemical technique to evaluate the electrochemical properties of redox-active materials by measuring the current response of a system as the applied potential is varied in a cyclic manner. In a typical CV experiment, the potential of the working electrode is swept linearly in one direction and then reversed within the selected potential window. Figure 3.4 shows a characteristic 'duck-shaped' CV curve, featuring anodic and cathodic peaks.[174] The anodic peak arises during the forward potential sweep, indicating oxidation, while the cathodic peak appears in the reverse sweep, corresponding to reduction.

As anodic and cathodic electrochemical deposition methods were used to fabricate $Cu_3(HHTP)_2$ sensors in Chapters 4 and 5, respectively, CV was conducted to understand the electrochemical reactions and mechanisms involved in the sensor fabrication. The CV experiments were carried out in a three-electrode system (described in Section 3.2.1.1) using the Pt IDEs as the working electrode with a scan rate of 100 $mV \cdot s^{-1}$. By analysing the anodic and cathodic peaks in the CV curves, it is possible to track the formation of $Cu_3(HHTP)_2$, assess the efficiency of deposition, and optimise the fabrication conditions.

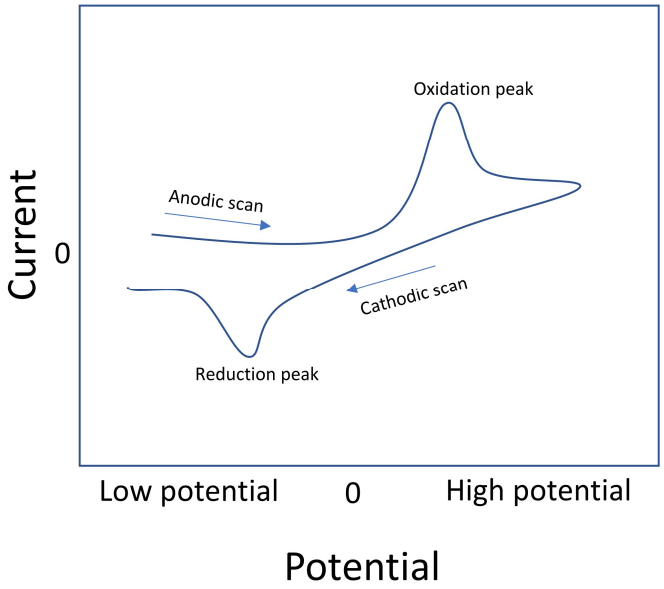

Figure 3.4. Typical 'duck shaped' cyclic voltammetry curve.

3.3.2 Scanning electron microscopy

Scanning electron microscopy (SEM) is a powerful characterisation technique used to examine the surface morphology and topography of materials at high magnification. SEM utilises a focused electron beam to scan the sample's surface, generating high-resolution images by detecting the secondary electrons emitted from it. This technique allows researchers to observe the distribution, size, and shape of particles, providing insights into the materials' properties.

In this thesis, a Zeiss Merlin Analytical SEM instrument with an in-lens detector was employed to image the morphology of the conductive MOF (c-MOF) sensors on Pt IDEs. As the substrate of IDEs is insulating glass, a holder equipped with two metal clips was used to connect the holder and the contact pads of Pt IDEs. The charging effect is detrimental to the image quality due to the insulating behaviour of the glass IDE substrate.[175] Operating voltages from 1 kV to 5 kV and working distances from 1.8 mm to 6.5 mm were selected to mitigate the charging effect. The probe current was 200 pA.

3.3.3 Energy-dispersive X-ray spectroscopy

Energy-dispersive X-ray spectroscopy (EDX) is an analytical technique used in conjunction with SEM to provide elemental composition data of a material. When the sample surface is bombarded with the focused electron beam in SEM, the electrons in the inner shells of an atom are knocked out, which subsequently leads to the emission of characteristic X-rays as outer-shell electrons transition to fill these vacancies. The EDX sensor can detect the characteristic X-rays and analyse their energies to determine the qualitative and quantitative elemental makeup of the sample.

In this thesis, EDX was employed using the same Merlin instrument in SEM to confirm the elemental composition of the conductive $Cu_3(HHTP)_2$ sensors deposited on Pt IDEs. The analysis focused on detecting the presence of copper (Cu) and the organic ligands (elements such as carbon and oxygen from HHTP). EDX mapping was also used to visualise the distribution of copper within the MOF.

3.3.4 X-ray diffraction

X-ray diffraction (XRD) determines the crystal structure, phase identification, and degree of crystallinity of materials including MOFs. In an XRD experiment, a metal target (normally copper) was used to generate X-rays with a characteristic wavelength (commonly Cu Kα radiation, with a wavelength of about 1.54 Å). XRD works by directing generated X-rays onto a sample and measuring the intensity and angles of the diffracted beams. When the X-rays meet the crystal lattice at specific angles, they are scattered by the atoms in a constructive interference pattern. This occurs only when Bragg's law is satisfied:

$$n\lambda = 2d \sin\theta$$

where n is an integer, λ is the X-ray wavelength, d is the distance between the crystal planes, and θ is the diffraction angle. Bragg's Law indicates that the path difference between X-rays scattered from successive crystal planes must be an integer multiple of the X-ray wavelength.

In this thesis, XRD was utilised to identify the characteristic peaks of the c-MOFs. Since the c-MOFs synthesised via the hydrothermal solution method have been extensively reported and characterised in previous studies, the XRD peaks of c-MOFs obtained by this method served as a verification step. The successful synthesis of c-MOFs was confirmed by comparing the XRD peaks of the samples with those in the published literature.[73] The experiment in Chapter 4 was carried out on a Bruker D8 Advance diffractometer with a tube voltage of 40 kV and a current of 40 mA, while that in Chapter 5 was conducted on a Malvern Panalytical Empyrean X-ray Diffractometer with a tube voltage of 40 kV and a current of 40 mA. Those in Chapters 6 and 7 were performed on a Rigaku Miniflex diffractometer with a tube voltage of 40 kV and a current of 10 mA. All instruments are equipped with a 1.54 Å Cu Kα X-ray source. Since the amount of c-MOFs on IDEs is insufficient to produce discernible XRD peaks, c-MOFs were fabricated on an indium tin oxide-coated glass slide square (ITO) to improve the quality of XRD analysis. The synthesis procedure was identical to that used for c-MOF fabrication on the IDEs with the deposition time adjusted as required; only the substrate was changed from IDEs to an ITO-coated glass slide to obtain sufficient material for XRD analysis.

3.3.5 X-ray photoelectron spectroscopy

X-ray Photoelectron Spectroscopy (XPS) analyses the elemental composition and chemical states of materials. In an XPS experiment, X-rays were generated typically from an Al Kα source to bombard the sample, causing the emission of core electrons. The kinetic energy of these emitted electrons is measured, and the binding energy is calculated, providing detailed information about the atomic species and their chemical environments.

In this thesis, XPS was performed on a PHI VersaProbe III photoelectron spectroscope with a monochromatic Al Kα X-ray radiation source (1486.6 eV) to analyse the elemental composition and element valency of c-MOF, focusing on the oxidation states of metal centres and the binding configurations of HHTP. The high-resolution spectra of the Cu 2p, O 1s, and C 1s regions help to confirm the successful formation of $Cu_3(HHTP)_2$ without impurities. This technique also provided insight into the interactions between the metal centres and organic ligands.

3.3.6 Fourier-transform infrared spectroscopy

Fourier-transform infrared spectroscopy (FTIR) is used to identify and study the chemical bonds and functional groups present in materials by measuring their absorption of infrared light. The resulting spectrum provides a fingerprint of molecular vibrations and the bonding environment within the material.

In this work, FTIR spectra were obtained by a Nicolet iS10 FTIR spectrometer equipped with an attenuated total reflectance (ATR) module, which enables the in-situ characterisation of c-MOFs deposited on Pt IDEs. The FTIR spectra of H_6HHTP and c-MOFs synthesised via the hydrothermal solution method serve as the controls. Functional groups like O-H, C=O, C=C, and C-O were tracked to verify the coordination of HHTP ligands with copper ions and the successful synthesis of c-MOFs.

3.3.7 Raman spectroscopy

Raman spectroscopy is another vibrational spectroscopy technique, complementary to FTIR, that provides information about molecular vibrations, phonon modes, and crystal structures. It is based on inelastic scattering of light, known as Raman scattering, which occurs when a

monochromatic light source interacts with the molecular vibrations or other excitations within a sample.

In this thesis, Raman spectroscopy was performed on a RENISHAW Raman spectrometer with a 633 nm laser. Raman spectroscopy has certain strengths that FTIR cannot fully replace. While both techniques allow for in-situ characterisation of c-MOFs on Pt IDEs, the penetration depth of the FTIR with an ATR module we utilised is typically a few micrometres, which means that substrate interference can affect the result. In the IDEs used in this thesis, the Si-O vibration from the glass produces a strong peak at low wavenumbers, potentially overshadowing the Cu-O vibration for the FTIR. In contrast, Raman spectroscopy probes only a shallow depth of the sample, minimising substrate interference. Additionally, Raman spectroscopy can detect some peaks that FTIR might miss. For example, specific in-plane vibrational modes in c-MOFs are visible in Raman as D and G bands, which do not appear in the FTIR.

3.3.8 Atomic force microscopy

Atomic Force Microscopy (AFM) is a high-resolution imaging technique that provides information on surface topology, roughness, and mechanical properties. AFM works by scanning a sharp tip over the sample surface while measuring the forces between the tip and the sample to create a topographical map.

In this thesis, AFM was performed by a scattering-type scanning nearfield optical microscope (Neaspec s-SNOM), with a non-contact mode applied. AFM enables the precise measurement of the morphology of c-MOFs on glass substrates between Pt IDE fingers at the nanoscale. Furthermore, it allows for 3D visualisation of the sample morphology, offering a more precise representation of its spatial structure.

3.3.9 Gas sensing tests

The gas sensing experiments were performed at atmospheric pressure in a custom-made sensing chamber (Figure 3.5). The chamber is made from a stainless-steel cylinder with an internal diameter of 21.05 ± 0.05 cm and an internal depth of 9.25 ± 0.05 cm. Ammonia (NH_3) was selected as the primary analyte in this thesis, which is sourced from an NH_3 cylinder (10 ppm, balanced with nitrogen (N_2)), while another N_2 cylinder (zero grade) was selected as background gas to further dilute the NH_3. The flow rate of background gas and that of analyte gas were controlled by each mass flow controller (Alicat), and the concentration of analyte gas was controlled by changing the relative gas flow via mass flow controllers, with a total flow rate fixed at 500 standard cubic centimetres per minute (sccm). The background and analyte gases were then mixed at a T-junction and passed through the inlet into the chamber.

A Keysight source/measure unit was employed to apply a 1.0 V direct current (DC) potential across the IDEs to monitor the conductance of samples with c-MOFs on IDEs. The current values of samples were recorded by the source/measure unit at a sampling rate of approximately 2.4 Hz (median sampling interval ≈0.42 s), corresponding to the measurement bandwidth in this thesis. Baseline noise was evaluated over a fixed time window prior to gas exposure containing ~50 data points.

Before the test, each sample was placed in the sensing chamber under nitrogen gas flow until its resistance was stable. In each test, the sample was exposed to different concentrations of each analyte gas for several min. The sample was then purged with nitrogen to recover the resistance before the next exposure cycle. The exposure durations were adjusted based on the specific properties of each sample in different chapters, and the detailed procedures are described in Chapters 4-7.

During the sensing measurements, the resistance did not fully stabilise within the selected response–recovery time window. To ensure consistency across devices within the same chapter,

all sensor responses were therefore evaluated at fixed time points following gas exposure and removal. Sensing parameters, including response and sensitivity, were calculated using data collected at these fixed time points. This approach enables direct comparison between devices measured under identical conditions; however, it may underestimate the final steady-state response for sensors with slower response dynamics. Nevertheless, this trade-off was considered acceptable in order to maintain comparability across measurements.

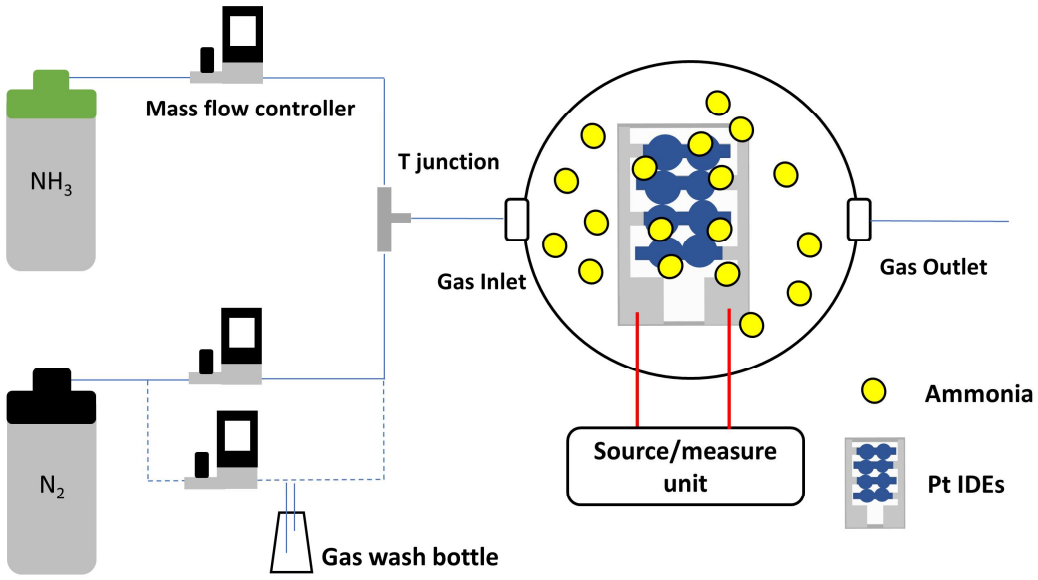

Figure 3.5. Schematic diagram of the home-built set up for gas sensing test. This setup consists of gas sources, mass flow controllers, a gas sensing chamber, and a source/measure unit.

In the selectivity test, water and typical reducing gases including carbon monoxide (CO), acetone, isopropanol, ethanol, and methanol were selected as comparative analytes. The CO was obtained from a CO cylinder (10 ppm), while vapours of water, acetone, isopropanol, ethanol, and methanol were generated by bubbling N_2 through liquid via a gas wash bottle.[176, 177] The concentration of each generated vapour (methanol, ethanol, isopropanol, or acetone) was calculated by $C_{VOC} = P_{VOCs} / P_A$, where P_{VOCs} is the saturated pressure of analytes and P_A is the atmospheric pressure at 25°C. The test procedure is similar to that of ammonia.

Chapter 4

Electrochemically grown $Cu_3(HHTP)_2$ percolation networks for chemiresistive gas sensing

This chapter presents the first demonstration of applying percolation theory in developing c-MOF-based percolation networks for chemiresistive gas sensors with enhanced sensitivity. To achieve this, $Cu_3(HHTP)_2$ was deposited in situ on Pt interdigitated electrodes (IDEs) with 10-micron gaps using a cathodic electrochemical deposition method. Chronoamperometry (CA) was employed to control the deposition time, enabling the identification of the percolation region. The chemical composition of $Cu_3(HHTP)_2$ was confirmed through various characterisation techniques, including XRD, FTIR, XPS, and Raman spectroscopy. Furthermore, the evolution of electrical percolation behaviour during deposition was observed and confirmed through electrical measurements and SEM imaging. The chemiresistive sensing responses to ammonia were evaluated and compared for sensors working in the percolation region and in the dense film region, and for a sensor prepared with powder.

4.1 Introduction

Challenges remain in enhancing the sensitivity of c-MOF-based chemiresistive gas sensors due to limitations in conventional fabrication strategies. Typically, c-MOF powders are obtained through solvothermal synthesis and then deposited onto electrodes through coating methods.[3, 73] However, these ex-situ techniques could lead to not only contact resistance due to poor contact at grain-to-grain and/or grain-to-electrode interfaces but also sample damage during deposition. Recent advances include in-situ deposition techniques such as layer-by-layer liquid-

phase epitaxy (LPE), which have shown improved sensitivity, particularly in ammonia detection.[74] However, it is still necessary to explore straightforward and effective approaches to achieve highly sensitive MOF-based gas sensors.

In chemiresistive gas sensors, percolation theory explains how sensor sensitivity is enhanced by engineering the sensing material near the percolation threshold—where continuous conductive pathways begin to form throughout the material.[139] This has been successfully applied to develop metal-oxide and polymer-based gas sensors with improved sensitivity, offering a promising pathway for c-MOF-based sensors as well.[153, 160, 178-180] The main challenge lies in selecting an appropriate synthesis method to conduct the primary research on c-MOF-based percolation networks. Percolation networks were typically obtained through either conductive-insulating composites or deposition control. The deposition-control strategy is particularly attractive since it leverages electrochemical deposition to achieve in-situ growth of materials.[159]

The electrochemical deposition of c-MOFs can be achieved via anodic or cathodic methods.[181, 182] In typical anodic methods, a pre-deposited metal layer on the working electrode is oxidised to the corresponding metal salts, which complexes with ligands in the solution to form MOFs.[183] However, this process complicates conductance monitoring because the growing MOF layer may detach from the substrate as the metal is continuously released.[184, 185] In contrast, the cathodic method does not require a pre-deposited metal layer. Instead, it is performed in a solution containing metal salts, organic ligands, and pro-bases.[90, 186, 187] A negative potential is applied onto the working electrode to reduce the pro-bases into basic species that deprotonate the ligands and facilitate their complexation with metal ions. This approach offers a more reliable pathway for studying conductive MOF-based percolation networks.

In this chapter, $Cu_3(HHTP)_2$-based chemiresistive percolation sensors were developed using a cathodic electrochemical deposition method. $Cu_3(HHTP)_2$ was selected because it has been reported as one of the most sensitive sensing materials to various analytes, including ammonia.[4, 73, 79] In addition to $Cu_3(HHTP)_2$, preliminary screening experiments were also performed on analogous $Ni_3(HHTP)_2$ and $Co_3(HHTP)_2$ [9] powders under identical sensing conditions. When tested under 5 ppm ammonia, neither $Ni_3(HHTP)_2$ nor $Co_3(HHTP)_2$ based device exhibited a discernible or reproducible resistance change beyond the noise level. As a result, these materials were not pursued further as chemiresistive sensors. Chronoamperometry at –0.2 V was applied for sensor fabrication, yielding devices with resistances ranging from 5.05 MΩ down to 0.88 kΩ. The successful synthesis of materials was confirmed through various analytical techniques, including XRD, XPS, FTIR, and Raman spectroscopy. The electrical percolation behaviour during the MOF growth was observed through electrical measurements. The morphologies of $Cu_3(HHTP)_2$-based percolation networks were investigated via SEM and AFM. With a resistance value of 365.13 kΩ, a chemiresistive percolation sensor prepared at 60 s showed significantly improved sensing performance to ammonia gas compared to its counterparts, exhibiting a reversible response of 17.06% ± 0.45% to 5 ppm ammonia and a theoretical limit of detection of 0.6 ± 0.1 ppb.

4.2 Experimental section

4.2.1 Chemicals and substrates

Common reagents have been described in Section 3.1. Only reagents specific to this chapter are described here. Tetrabutylammonium hexafluorophosphate ($(NBu_4)PF_6$, 99%), and all chemical solvents—including dimethylformamide (anhydrous, 99.8%), acetone (99%), methanol (99.8%), ethanol (99.8%), and isopropanol (99.5%)—were obtained from Sigma-Aldrich. The

Pt interdigitated electrodes (IDEs) featuring 10-micron gaps were provided by Metrohm (Figure 3.1a). A low-concentration ammonia cylinder (NH_3, 450 ppb, filled with N_2) was purchased from BOC.

4.2.2 Cathodic electrochemical deposition

The three-electrode setup used for the electrochemical experiments is detailed in Section 3.2.1.1. ITO slides (Sigma-Aldrich) or IDEs featuring 10-micron gaps (Metrohm) were selected as the working electrodes. The deposition was terminated at deposition times of 5, 15, 30, 60, 90, 120, 150, 180, 240, 300, and 420 s, with each sample designated as T_x, where x corresponds to the deposition time. After deposition, the prepared samples were immersed in DMF for 1 hour and dried under an ambient environment overnight.

Since the IDE devices used in this work are two-terminal structures with only two contact pads, the resistance of each sample was measured via a two-probe measurement using an RS PRO IDM 981V digital multimeter under ambient conditions. A digital multimeter was used as it provides a rapid and reliable way to compare the resistance values and conductivity trends of the samples.

4.2.3 Gas sensing tests

Gas sensing tests were performed as described in Section 3.3.9. In this chapter, each sample was exposed to different concentrations of the analyte gas for 1 min. After each exposure, the sample was purged with nitrogen for 2 min before the next exposure. The exposure at each concentration was repeated for three consecutive cycles.

Since the drying procedure employed does not completely remove all DMF molecules adsorbed within the c-MOF framework. As a result, the first complete sensing sequence over the full concentration range primarily serves as an activation cycle, during which residual DMF is

removed. All sensing data presented in this thesis correspond to subsequent full sensing cycles after this initial activation cycle.

4.2.4 Attribution statement

In this chapter, FTIR and AFM measurements were conducted by Jiahao Ye using the facilities in Jin-Chong Tang's group. XPS measurements were carried out by Axel C. O. Forssberg using the instrumentation located in the Rex Richard building. All other experiments were conducted by the author.

4.3 Results and discussion

4.3.1 Cathodic electrochemical deposition and characterisation

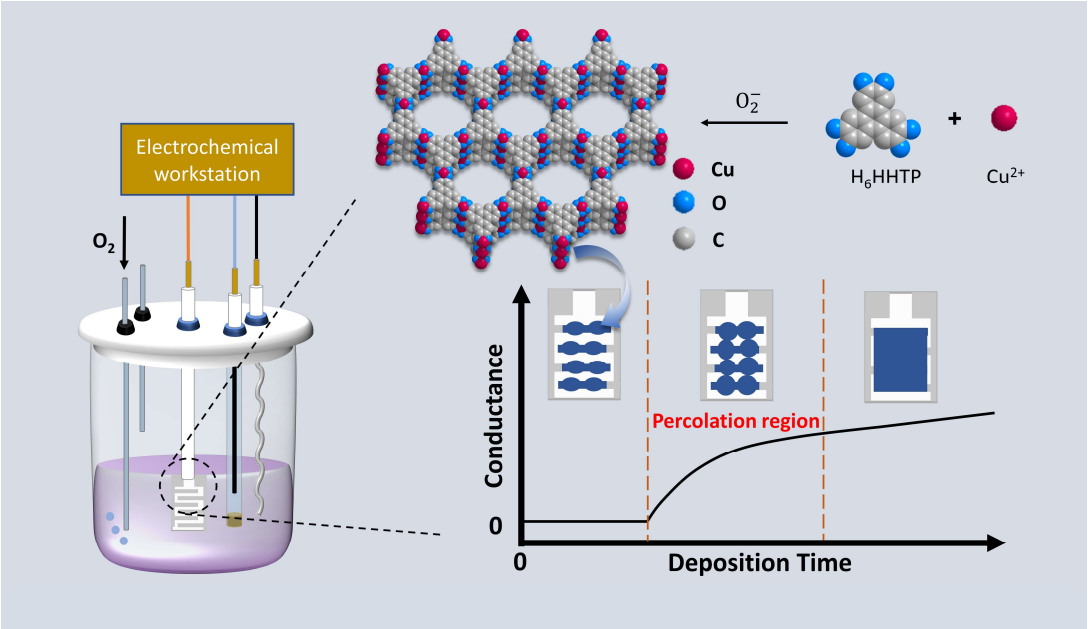

Figure 4.1. Schematic illustration of the strategy for electrochemically developing $Cu_3(HHTP)_2$ percolation network-based chemiresistive gas sensors.

Figure 4.1 shows a schematic diagram of the strategy for developing $Cu_3(HHTP)_2$ percolation network-based chemiresistive gas sensors. The $Cu_3(HHTP)_2$ was electrochemically deposited onto Pt interdigitated electrodes (IDEs) with 10 μm gaps using an oxygen-assisted cathodic

electrochemical synthesis method via chronoamperometry (CA) at −0.2 V from a solution containing $Cu(NO_3)_2$ and H_6HHTP in DMF. By running the electrochemical deposition process for different time periods, samples corresponding to various MOF growth stages and conductance levels were obtained.

To understand the oxygen-assisted cathodic deposition behaviour of $Cu_3(HHTP)_2$ in the environment under this study, cyclic voltammetry (CV) experiments were performed in a 3 mM $Cu(NO_3)_2$ solution in DMF and a precursor solution containing both 3 mM $Cu(NO_3)_2$ and 2 mM H_6HHTP in DMF. The Pt IDEs served as the working electrode and the electrolyte was 1 mM $(NBu_4)PF_6$. Figure 4.2a shows CV curves of $Cu(NO_3)_2$ and precursor (P-$Cu_3(HHTP)_2$) solutions under argon (Ar). For the $Cu(NO_3)_2$ solution, there are two cathodic peaks (I) and (II) corresponding to the reduction processes of Cu^{2+} to Cu^{1+} at −0.36 V and Cu^{2+} to Cu at −0.61 V, respectively. The precursor solution shows similar electrochemical behaviour to that of the $Cu(NO_3)_2$ solution, with two cathodic peaks at −0.47 V and −0.62 V.

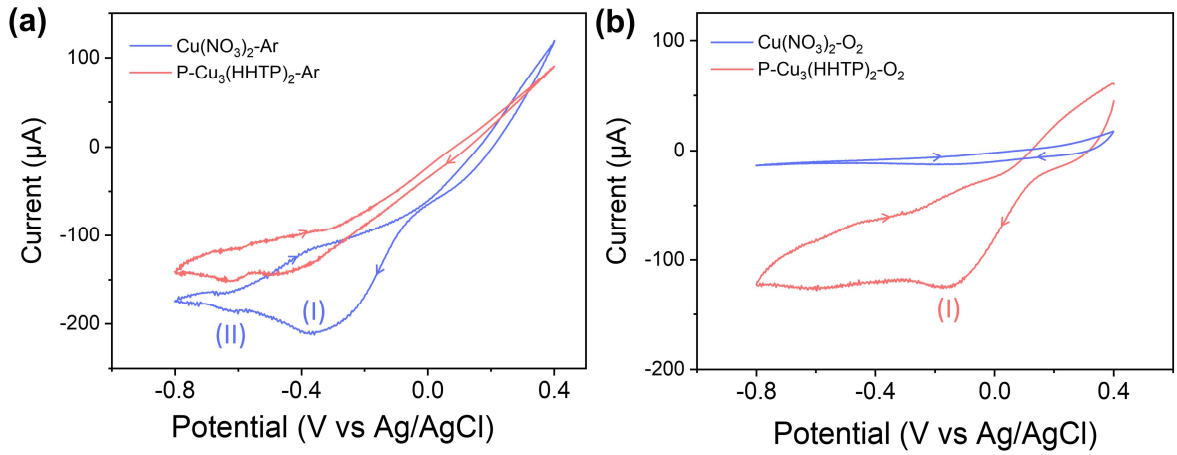

Figure 4.2. CV curves of the $Cu(NO_3)_2$ (3 mM) and the precursor mixture of $Cu(NO_3)_2$ (3 mM) and H_6HHTP (2 mM) in (a) Ar-saturated and (b) O_2-saturated DMF solutions containing 1 mM $(NBu_4)PF_6$. The CV experiments were carried out with a scan rate of 100 $mV \cdot s^{-1}$ using the Pt IDEs as the working electrode. The arrow indicates the direction of CV scans.

Figure 4.2b shows the comparative CV curves in $Cu(NO_3)_2$ and precursor solutions under O_2. Only a broad peak with significantly lower current intensity is observed for the cathodic scan in $Cu(NO_3)_2$ solution compared with its counterpart under argon. This is because the reduction of O_2 to O_2^- occurs during the cathodic scan. Interaction between copper ion and O_2^- gives rise to dicopper–dioxygen species that decompose into insoluble Cu_2O, thereby leading to the passivation on the surface of the working electrode.[188] This also implies that the reduction process of copper ions to copper is greatly inhibited with the help of O_2^-. In the precursor solution, contrarily, two discernible cathodic peaks at −0.16 V and −0.60 V are observed. The H_6HHTP ligands should greatly consume the generated O_2^- during deprotonation. These deprotonated ligands then coordinate with Cu^{2+}, forming conductive $Cu_3(HHTP)_2$. These processes collectively avoid the generation of Cu_2O and its passivation effect. The peak (I) at −0.16 V belongs to the reduction of oxygen on the electrode surface, indicating that the electrochemical deposition of $Cu_3(HHTP)_2$ on IDEs mainly happens around this peak. To mostly electrodeposit MOFs on the electrode surface, a negative potential at −0.2 V was applied in this study.

The electrodeposition of the $Cu_3(HHTP)_2$ was observed by a controlled experiment, where a potential of −0.2 V was applied to only one side of the IDEs for cathodic electrodeposition for 60 s, with no potential on the other side. The SEM image (Figure 4.3a) of the resulting device shows that $Cu_3(HHTP)_2$ mainly grows on the side with the negative potential and almost nothing grows on the other side without applied potential. This was further proved by EDS. Figure 4.3b and Figure 4.3c show the distribution of the Pt element in the Pt electrode and the copper element in $Cu_3(HHTP)_2$, where the majority of the copper element is located on the Pt electrode with the negative potential, indicating the growth of $Cu_3(HHTP)_2$ in the electrochemical deposition is promoted by the negative potentials.

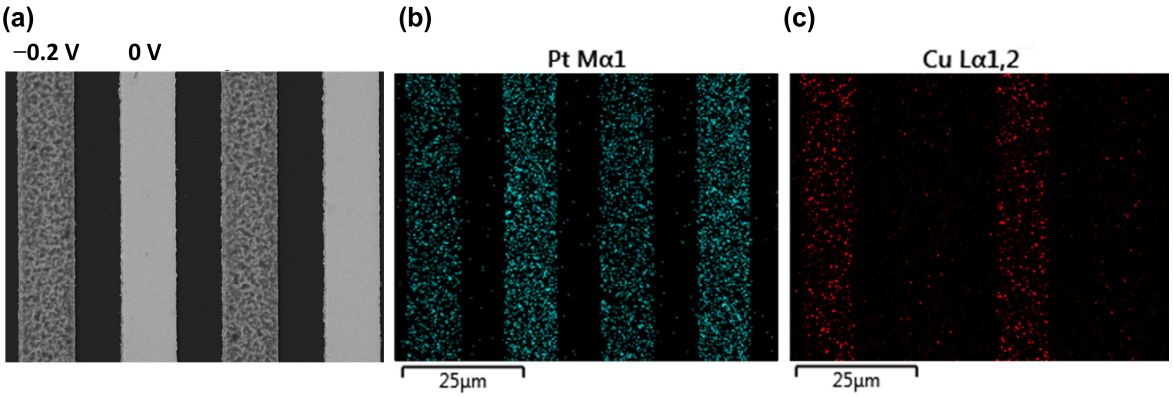

Figure 4.3. SEM image of IDEs with a potential applied on only one side. The corresponding EDS images

For convenience, the prepared samples were designated as T_x, where x represents the respective deposition time in seconds. Figure 4.4 presents the photographs of the samples, including T_5, T_{15}, T_{30}, T_{60}, T_{90}, T_{120}, and T_{300}, synthesised from cathodic electrochemical deposition on Pt IDEs with 10-micron gaps. The dark blue regions represent the growth of $Cu_3(HHTP)_2$. No discernible material was observed on the surface of T_5 or T_{15}, similar to the appearance of control IDEs, due to the short deposition time. As the deposition time increased, a progressively denser and darker blue layer formed, indicating the continued growth of the MOFs.

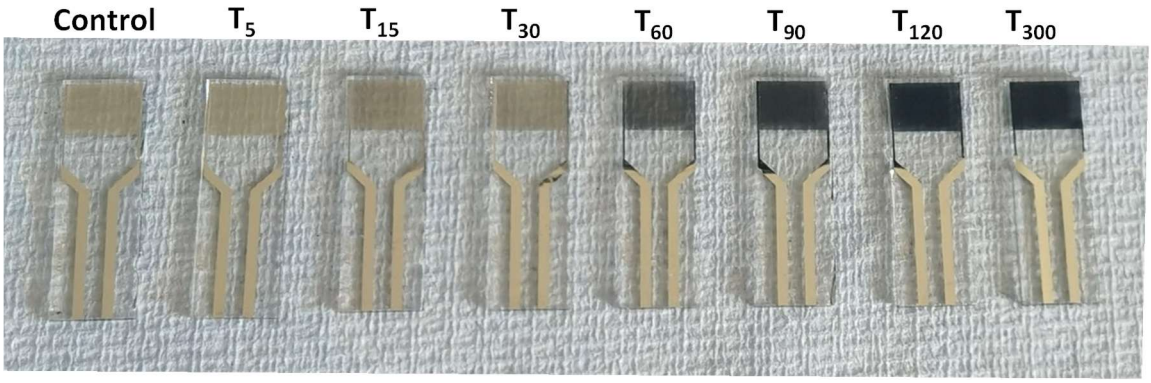

Figure 4.4. Photographs of samples, including T_5, T_{15}, T_{30}, T_{60}, T_{90}, T_{120}, and T_{300}, prepared by cathodic electrochemical deposition.

Figure 4.5 presents the characterisations of the samples. A sample of S-$Cu_3(HHTP)_2$, synthesised via a solvothermal method (detailed in Section 3.2.2), served as the control due to previous widespread reports of its structure.[4] All characterisations of the electrochemically deposited $Cu_3(HHTP)_2$ (E-$Cu_3(HHTP)_2$) were performed on samples synthesised with a

deposition time of 300 s (T_{300}) on IDE substrates. For XRD analysis, the amount of MOF on IDEs was insufficient to produce discernible XRD peaks. $Cu_3(HHTP)_2$ was therefore deposited on an ITO-coated glass slide square under the identical procedure for 2 h to improve the quality of XRD analysis. The extended deposition time enabled both reliable structural identification and verification that no crystalline metallic copper was formed during the electrochemical deposition process.

Figure 4.5a shows the representative top-view SEM images of E-$Cu_3(HHTP)_2$ on IDEs. The images indicate the morphology of the product is near-spherical. SEM analysis was performed on multiple samples prepared using the same deposition parameters, and no significant morphological variation was observed. An SEM imaging (Figure 4.5b) was conducted for E-$Cu_3(HHTP)_2$ on ITO substrates using the same deposition time (300 s) as that employed for device fabrication on IDEs. The SEM image indicate that E-$Cu_3(HHTP)_2$ deposited on ITO and IDE substrates exhibits similar near-spherical morphology under identical deposition conditions.

The XRD patterns (Figure 4.5b) show E-$Cu_3(HHTP)_2$ on ITO exhibits characteristic peaks at ~4.9°, ~9.7°, ~12.8°, and ~27.9°, matched well with that of S-$Cu_3(HHTP)_2$. The four peaks correspond to the (100), (200), (210), and (001) crystal plane reflections of $Cu_3(HHTP)_2$, respectively. Therefore, it is fair to believe the $Cu_3(HHTP)_2$ on IDEs have the the same XRD results with that on ITO. In addition, compared with the simulated peaks of CuO and Cu, no discernible peaks of them are observed for E-$Cu_3(HHTP)_2$, indicating almost no Cu or CuO was produced during the electrochemical deposition.

As shown in Figure 4.5c, the E-$Cu_3(HHTP)_2$ shows a similar FTIR spectrum to S-$Cu_3(HHTP)_2$, with identical C=C stretching peaks at 1440 cm^{-1} and C-O stretching peaks at 1210 cm^{-1}. H_6HHTP exhibits two broad peaks at 3405 and 3264 cm^{-1} which are characteristic phenolic O-

H stretching vibration bands.[189] Adsorption peaks at ~1620 cm^{-1} were assigned to the bending vibration bands of O-H.[116, 190, 191] Compared with H_6HHTP, the disappearance of the stretching and bending vibration bands of O-H for E-$Cu_3(HHTP)_2$ or S-$Cu_3(HHTP)_2$ indicates the coordination between Cu centre and H_6HHTP ligand.

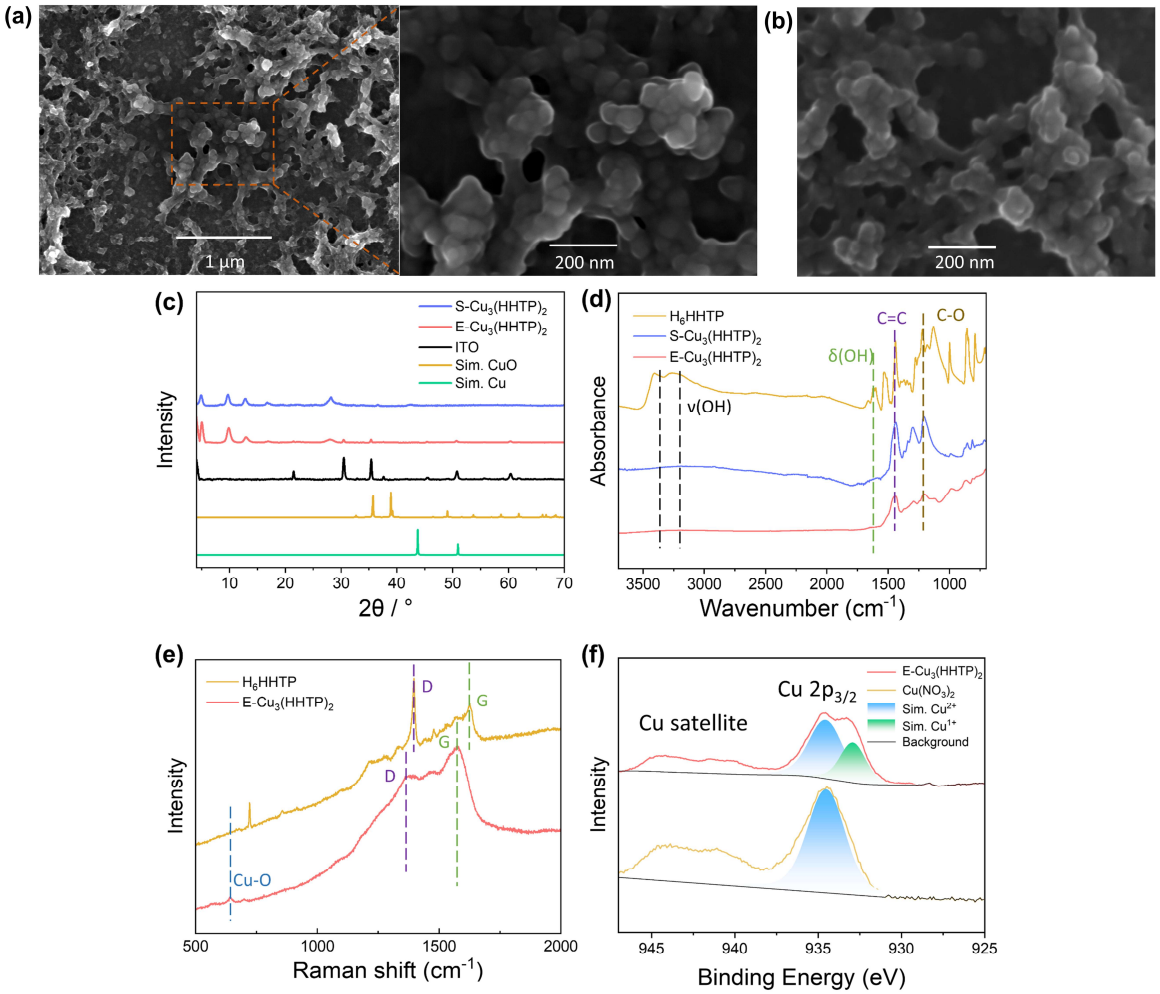

Figure 4.5. (a) SEM images of E-$Cu_3(HHTP)_2$ on IDEs. (b) SEM image of E-$Cu_3(HHTP)_2$ on ITO. (c) XRD patterns of S-$Cu_3(HHTP)_2$ (blue line), E-$Cu_3(HHTP)_2$ (red line) on the indium tin oxide (ITO), ITO (black line), simulated CuO (yellow line), and simulated Cu (green line). (d) FTIR spectra of H_6HHTP (yellow line), S-$Cu_3(HHTP)_2$ (blue line), and E-$Cu_3(HHTP)_2$ on IDEs (red line). (e) Raman spectra of H_6HHTP (yellow line) and E-$Cu_3(HHTP)_2$ on IDEs (red line). (f) XPS results of E-$Cu_3(HHTP)_2$ on IDEs (red line) and $Cu(NO_3)_2$ powder (yellow line). All E-$Cu_3(HHTP)_2$ samples on IDE substrates using a deposition time of 300 s. The SEM image on ITO (b) corresponds to a 300 s deposition, whereas the XRD sample on ITO (c) was prepared using an extended deposition time of 2 h to obtain sufficient material for structural analysis.

The Raman spectrum of E-$Cu_3(HHTP)_2$ (Figure 4.5d) shows a characteristic Cu-O adsorption peak at 642 cm^{-1},[83, 191] further proving the coordination between H_6HHTP and Cu centre. The peaks at ~1380 and ~1570 cm^{-1} of E-$Cu_3(HHTP)_2$ were reported to be the D and G bands.[191-193] Generally, the G and D bands exhibit the characteristics of materials composed of sp_2 hybridised carbon ring like graphene, where the G band represents the in-plane stretching vibration of carbon in sp_2 hybridised carbon ring, while D band represents the breathing mode of carbon in sp_2 hybridised carbon ring adjacent to the edge or defect. Compared with the free ligand H_6HHTP, the G and D bands in E-$Cu_3(HHTP)_2$ exhibit a slight red shift in the Raman spectra. This shift arises because the coordination of the ligand to the metal centres enables electron withdrawal from the ligand's aromatic system. The resulting decrease in electron density weakens the C=C bonds, thereby reducing the vibrational force constant and leading to a lower vibrational frequency (red shift) of these Raman-active modes. Meanwhile, the increased ratio of G peak to D peak of E-$Cu_3(HHTP)_2$ indicates the increment of ordered sp_2 hybridised carbon ring in E-$Cu_3(HHTP)_2$ crystal lattice, in agreement with the formation of MOF from ligand molecules. High-resolution XPS Cu $2p_{3/2}$ spectra of E-$Cu_3(HHTP)_2$ and $Cu(NO_3)_2$ (Figure 4.5e) show the Cu element in E-$Cu_3(HHTP)_2$ has a mixed valency of +2 (934.6 eV) and +1 (933.0 eV), suggesting the redox reaction occurs during the coordination between Cu centre and H_6HHTP. Since Cu^{2+} has a higher positive charge and fewer electrons than Cu^+, Cu^{2+} acts as a stronger Lewis acid. Over time, exposure to oxygen can increase the Cu^{2+}/Cu^+ ratio, which may enhance the interaction between Cu sites and reducing gases such as ammonia, potentially leading to increased sensor responses. The above results indicate the successful electrochemical deposition of $Cu_3(HHTP)_2$.

It should be noted that the cathodic electrochemical synthesis employed in this chapter was adapted from a previous report,[90] in which the E-$Cu_3(HHTP)_2$ was deposited on ITO substrates and the resulting morphology was confirmed to be near-spherical with a −0.2V potential.

Furthermore, the previous report also demonstrated that E-$Cu_3(HHTP)_2$ on ITO exhibits identical material properties, including FTIR, XRD and XPS, to those of conventionally synthesised $Cu_3(HHTP)_2$ powder. In the present work, the chracterisation results similarly confirm that E-$Cu_3(HHTP)_2$ on IDEs exhibits the same near-spherical morphology as that deposited on ITO substrates, as well as consistent XPS and FTIR with conventional $Cu_3(HHTP)_2$ powder. On this basis, it is reasonable to conclude the use of an alternative substrate does not affect the interpretation of the material properties or the overall conclusions of this work.

4.3.2 Electrical percolation

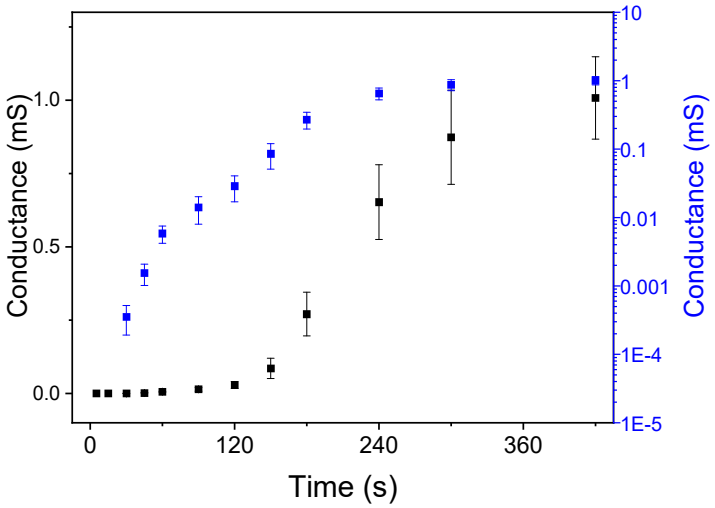

Figure 4.6. The plot of conductance across IDEs vs deposition time (in black) and its semilogarithmic plot (in blue). The error bars are the standard deviation of the conductance values of four separate samples.

The growth of E-$Cu_3(HHTP)_2$ on IDE substrates was investigated through the trend of conductance within the deposition times ranging from 5 to 420 s (Figure 4.6). The semi-logarithmic plot in Figure 4.6 is shown to determine the percolation region. Initially, since the MOFs exclusively grow on the IDE electrode fingers, no conductance of each sample can be detected until 30 s. The measurable conductance indicates that MOFs expand from the IDE

fingers and then bridge the insulating gaps at 30 s. The conductance of samples shows a significant increment from 30 to 300 s, reflecting the electrical percolation behaviour of E-$Cu_3(HHTP)_2$ on IDE substrates. Finally, the increase in conductance levels off after 300 s as dense MOF-based films form, marking the end of the percolation region. The details of the data were shown in Table 4.1.

Table 4.1 The conductance data (unit: mS) of the devices. The conductance of each device was evaluated from four independently fabricated samples, with each data point corresponding to a separate device. The data were calculated by converting each resistance value to conductance (G = 1/R). Only samples with measurable conductance are presented.

Device	Data 1	Data 2	Data 3	Data 4	Average	Standard Deviation
T_{30}	4.7×10^{-4}	5.1×10^{-4}	2.5×10^{-4}	1.8×10^{-4}	3.5×10^{-4}	1.6×10^{-4}
T_{45}	7.8×10^{-4}	1.9×10^{-3}	1.3×10^{-3}	1.1×10^{-3}	1.3×10^{-3}	4.6×10^{-4}
T_{60}	7.0×10^{-3}	7.4×10^{-3}	4.0×10^{-3}	4.9×10^{-3}	5.8×10^{-3}	1.6×10^{-3}
T_{90}	2.3×10^{-2}	8.4×10^{-3}	1.3×10^{-2}	1.2×10^{-2}	1.4×10^{-2}	6.1×10^{-2}
T_{120}	3.3×10^{-2}	4.4×10^{-2}	1.8×10^{-2}	2.1×10^{-2}	2.9×10^{-2}	1.2×10^{-2}
T_{150}	9.2×10^{-2}	4.3×10^{-2}	8.0×10^{-2}	1.2×10^{-1}	8.6×10^{-2}	3.5×10^{-2}
T_{180}	2.5×10^{-1}	3.1×10^{-1}	3.5×10^{-1}	1.8×10^{-1}	2.7×10^{-1}	7.4×10^{-2}
T_{240}	4.9×10^{-1}	8.0×10^{-1}	6.8×10^{-1}	6.3×10^{-1}	6.5×10^{-1}	1.3×10^{-1}
T_{300}	7.8×10^{-1}	1.1×10^{0}	7.7×10^{-1}	8.3×10^{-1}	8.7×10^{-1}	1.6×10^{-1}
T_{420}	1.3×10^{0}	8.9×10^{-1}	9.2×10^{-1}	1.0×10^{0}	1.0×10^{0}	1.4×10^{-1}

The growth of E-$Cu_3(HHTP)_2$ was also investigated via the SEM and AFM. SEM images in Figure 4.7a-f present the morphologies of the E-$Cu_3(HHTP)_2$ in T_5, T_{15}, T_{30}, T_{45}, T_{60}, and T_{300}, respectively. The black regions represent the insulating glass gaps while the grey regions represent the Pt electrode fingers. Additionally, the bright spots and networks observed on the gaps or the electrode fingers are the grown $Cu_3(HHTP)_2$. Initially, a slight amount of $Cu_3(HHTP)_2$ is observed on the electrode fingers of T_5 (Figure 4.7a), and more MOFs accumulate on the electrode fingers as time proceeds to 15 s (Figure 4.7b). Then, MOFs grow from the electrode fingers to the insulating gap and a discernible electrical bridge between the

fingers was formed at 60 s (Figure 4.7c-e). Eventually, the surface of the sample was fully covered by MOFs at 300 s (Figure 4.7f).

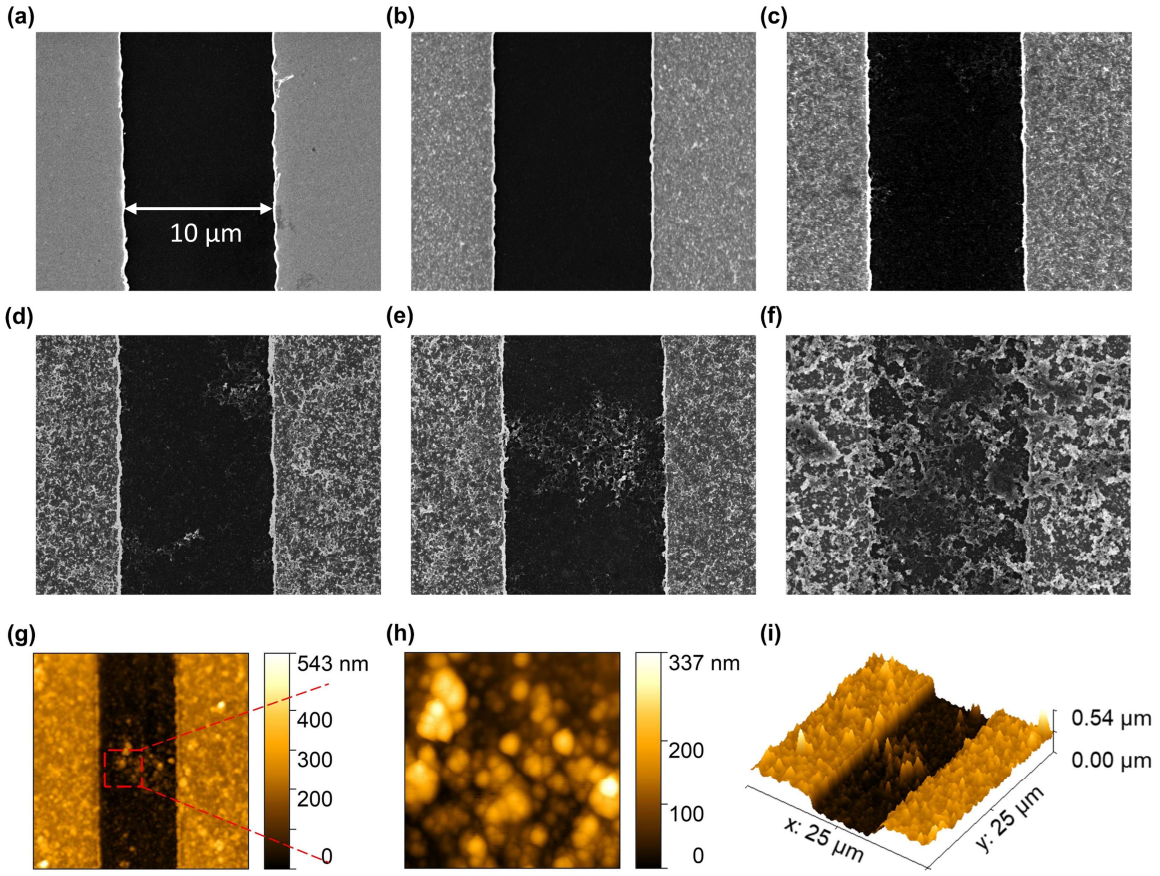

Figure 4.7. Characteristic SEM images of E-$Cu_3(HHTP)_2$ prepared at –0.2 V for (a) 5, (b) 15, (c) 30, (d) 45, (e) 60, and (f) 300 s. The gap of electrode was 10 µm. (g) Characteristic AFM image of T_{60} and (h) a high-resolution AFM image on the gap. (i) The 3d-AFM image of T_{60}.

The electrical bridge of T_{60} was further investigated by AFM. Figure 4.7g shows a characteristic AFM image of T_{60} electrical bridge. A high-resolution AFM image of the gap (Figure 4.7h) was obtained to reveal the morphology of the electrical bridge. The morphology of the deposited $Cu_3(HHTP)_2$ is near-spherical, consistent with the aforementioned high-resolution SEM image. A 3D AFM image of T_{60} was also presented to allow readers to observe the electrical bridge in three dimensions, providing a more accurate representation of its spatial structure.

4.3.3 Gas sensing tests

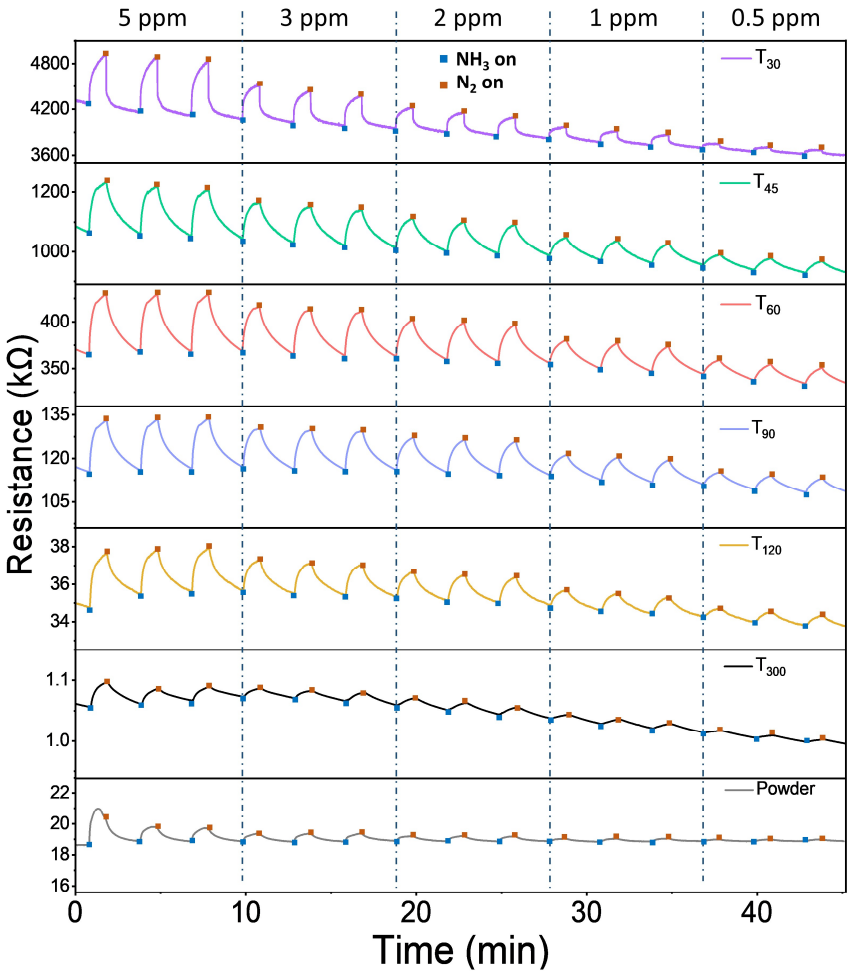

Figure 4.8. Sensing response-recovery curves of $Cu_3(HHTP)_2$-based chemiresistive gas sensors of T_{30} (purple), T_{45} (green), T_{60} (red), T_{90} (blue), T_{120} (yellow), T_{300} (black), and powder (gray) to ammonia diluted in N_2 at various concentrations (5 to 0.5 ppm). Data shown were obtained after the initial activation full cycle.

Ammonia is a toxic, corrosive, and environmentally hazardous gas that poses a potential threat to human health and the environment.[194, 195] Additionally, as a by-product of amino acid metabolism during protein breakdown, the concentration of ammonia in human exhaled breath (reported ranging from 50 ppb to 5 ppm) helps clinicians assess diseases and overall health.[196-198] These reasons make ammonia the primary analyte for evaluating the sensing performance of sensors based on $Cu_3(HHTP)_2$ which are capable of detecting ammonia at ppb-level concentration at room temperature.[74] To investigate the sensing responses to ammonia of

prepared samples, sensing experiments were conducted for samples obtained in the percolation region, including T_{30}, T_{45}, T_{60}, T_{90}, and T_{120}. For further comparison, a sample obtained in the dense film region (T_{300}) and a drop-cast powder sample were studied during the sensing tests. Each sample was placed in a home-built chamber under nitrogen flow before the test and then was exposed to 5-0.5 ppm ammonia gas for 1 min, followed by 2-min nitrogen flow to recover the resistance. The process was repeated three consecutive times for each concentration. The response in the test was calculated by the variation of resistance over the original resistance before exposure to ammonia (ΔR / R_0).

Figure 4.8 shows the response-recovery curve of each chemiresistive sensor to ammonia at different concentrations, where small blue and red squares were used to denote the point of diluted NH_3 introduction and pure N_2 introduction, respectively. All the samples show reversible increments of resistance after exposure to ammonia since ammonia donates electrons to reduce the hole charge carriers of $Cu_3(HHTP)_2$, a reported p-type semiconductor.[4, 74, 191] When the concentrations of ammonia decrease, all the sensing responses decrease accordingly.

In several cases, the resistance did not fully stabilise within the selected response–recovery time window. To ensure comparability across devices, each sensor's response and sensitivity was calculated using the data collected under an identical response-recovery time window. This approach enables direct comparison between devices measured under the same protocol. Nevertheless, differences in response and recovery speeds between devices were also observed. For example, T_{30} shows a faster response, attributed to its lower MOF deposition amount and consequently fewer active sites. As a result, the use of a fixed response–recovery time window may underestimate the final steady-state response and sensitivity for sensors with slower response dynamics. However, this approach was considered acceptable in order to maintain comparability across measurements and is also a commonly adopted method for the initial

assessment of sensor performance.[4, 74, 115,139] Similar behaviour is observed in the sensing results presented in the subsequent chapters.

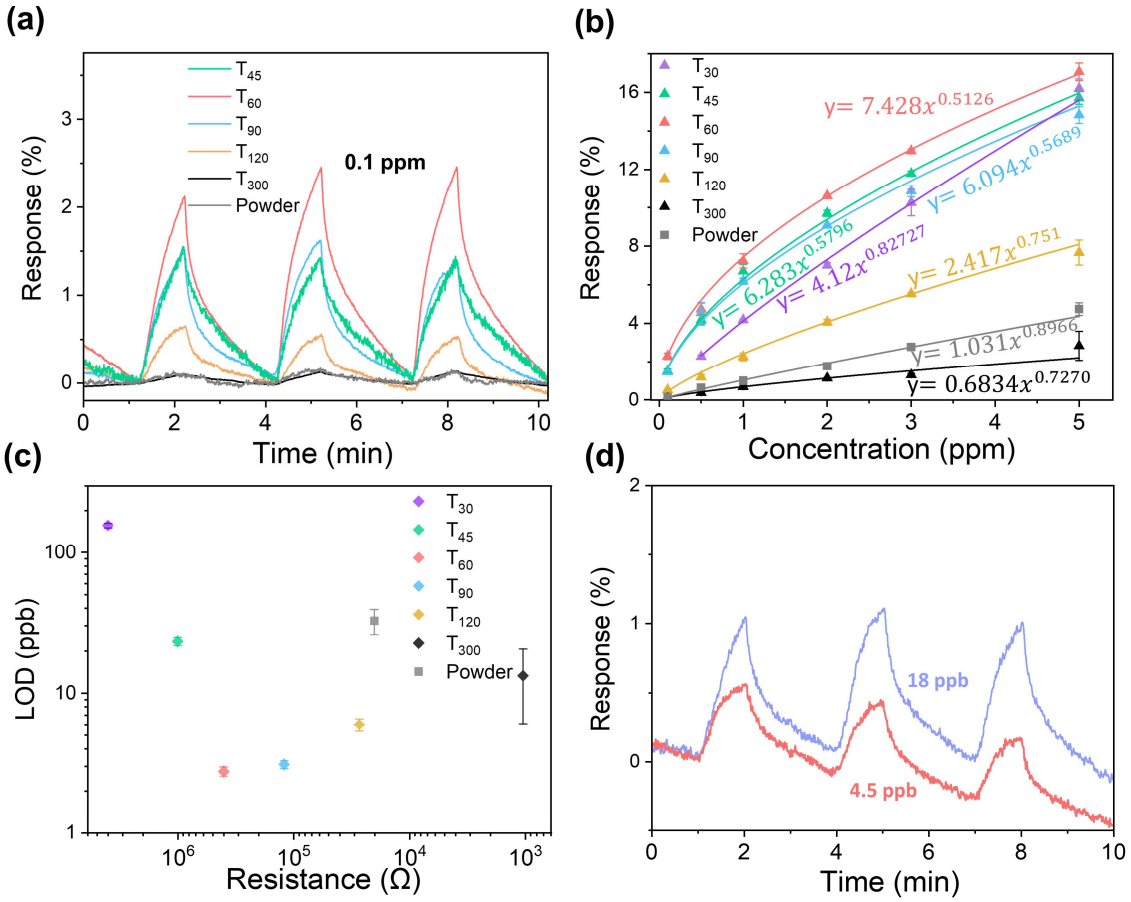

Figure 4.9. (a) Sensing response-recovery curves of $Cu_3(HHTP)_2$ sensors to 100 ppb ammonia. (b) Sensing response ($(R_t - R_0) / R_0$) of each sensor at different concentrations of ammonia. (c) Limits of detection of samples, calculated using the sensitivity obtained at the lowest detected concentration (500 ppb for T_{30} and 100 ppb for others). (d) Responses of T_{60} to 18-ppb and 4.5-ppb ammonia.

Since the ability to detect ammonia at ppb-level concentrations is beneficial for improving current medical testing methods,[196] responses to 100-ppb ammonia of the sensors were investigated (Figure 4.9a). T_{30} is not included due to its high noise level covering all signals. Among all the sensors in this work, T_{60} shows the highest response to 100-ppb ammonia of 2.29% ± 0.17%. Compared with percolation sensors, the thin film sensor T_{300} shows a much lower response of 0.12% ± 0.02%, similar to the powder device exhibiting 0.14% ± 0.01%.

Figure 4.9b shows the plots of the response vs ammonia concentration. Compared to other samples, T_{60} demonstrates the highest responses across all ammonia concentrations. Specifically, it demonstrates a response of 17.06% ± 0.45% to 5 ppm ammonia, which is more than six times that of T_{300} of 2.83% ± 0.75% and over four times that of the powder device of 4.23% ± 0.33%. As previously discussed, the response of T_{60} to 100-ppb ammonia is over 15 times greater than that of either T_{300} or the powder device. Similar to previous studies on metal oxide,[199-202] polymers,[155, 203] and MOFs,[74, 113, 115, 118, 204-206] the fitting curves in Figure 4.9b indicate that the sensing behaviour of each sample aligns with the conductance model limited by the electron transport across the intergranular potential/Schottky barrier (Equation 4.1):

$$\Delta R / R_0 = A_g p_g^{\beta} \quad (4.1)$$

where p_g is the partial pressure, A_g is a prefactor, and β is the exponent factor.

To further evaluate the performance of the sensors, the theoretical limits of detection (LODs) of samples were calculated. Typically, the LODs were calculated by using the following equation (Equation 4.2):

$$LOD = \left(\frac{3\sigma}{S}\right) \quad (4.2)$$

where σ is the standard deviation of baseline noise, and S is the sensitivity of the devices. Sensitivity is defined as the slope of the calibration curve. However, since the sensing behaviour of the devices is not strictly linear, the slope is not constant. Moreover, as the data points approach the origin, the slope tends toward infinity, which makes it tricky to assess the LODs reasonably.

To address this, a locally linear sub-range below the lowest detected concentration (500 ppb for T_{30} and 100 ppb for others) was defined as the reference for LOD calculation. Within this sub-range, a finite and constant S is obtained to yield a more meaningful sensitivity estimation. As

shown in Figure 4.9c, among all the sensors, T_{60} and T_{90} exhibit the lowest LODs of 2.7 ± 0.2 ppb and 3.1 ± 0.2 ppb, respectively, demonstrating their superior sensitivity to ammonia.

To sum up, all the samples obtained in the percolation region exhibit significantly improved sensing responses compared to their counterpart obtained in the dense film region. This enhancement is attributed to the fact that significantly fewer conductive pathways are built up in the percolation network by controlling the deposition times. Compared with an almost infinite number of conductive connections in the dense-film sample, E-$Cu_3(HHTP)_2$ based percolation networks are more sensitive to the interaction with ammonia molecules. As T_{30} should have the fewest percolation networks among all the samples, ideally, it might be the optimal sensor in this study. However, T_{60} exhibits the highest responses across all ammonia concentrations and the lowest LOD. This is attributed to the fact that the sensing performance also depends on many other factors, such as the background noise during sensing tests and the crystallinity of prepared materials. Generally, such factors may result in the finding that the optimal deposition time for preparing the sensor normally lies at some point later than the onset of the percolation region. For instance, our previous studies have shown that fewer percolation networks may accompany higher noise levels. The competitive effects between percolation and noise would lead to higher LODs.[139, 160, 161]

The low-concentration sensing ability of the optimal sensor T_{60} was further evaluated using a 450-ppb ammonia cylinder to generate 18-ppb and 4.5-ppb ammonia, with 4.5 ppb being the lowest experimentally accessible concentration. As shown in Figure 4.9d, T_{60} exhibits responses of 1.05% ± 0.04% at 18 ppb and 0.48% ± 0.08% at 4.5 ppb, demonstrating effective sensing capability at low concentrations. By using Equation 4.2 and the sensitivity determined at 100 ppb, the limit of detection (LOD) was initially estimated as 2.7 ± 0.2 ppb. The measurable

response at 4.5 ppb supports the validity of this procedure. Re-evaluating with the local sensitivity around 4.5 ppb updates the LOD to 0.6 ± 0.1 ppb.

LOD_{SE} (defined in Section 2.3.2.4) was also evaluated to reflect the theoretical improvement in detection limit that is achievable through temporal averaging and the associated reduction in effective measurement bandwidth. Using the sentivity determined from data acquired at an ammonia concentration of 4.5 ppb, the LOD_{SE} of T_{60} was therefore confirmed to be 0.09 ± 0.01 ppb.

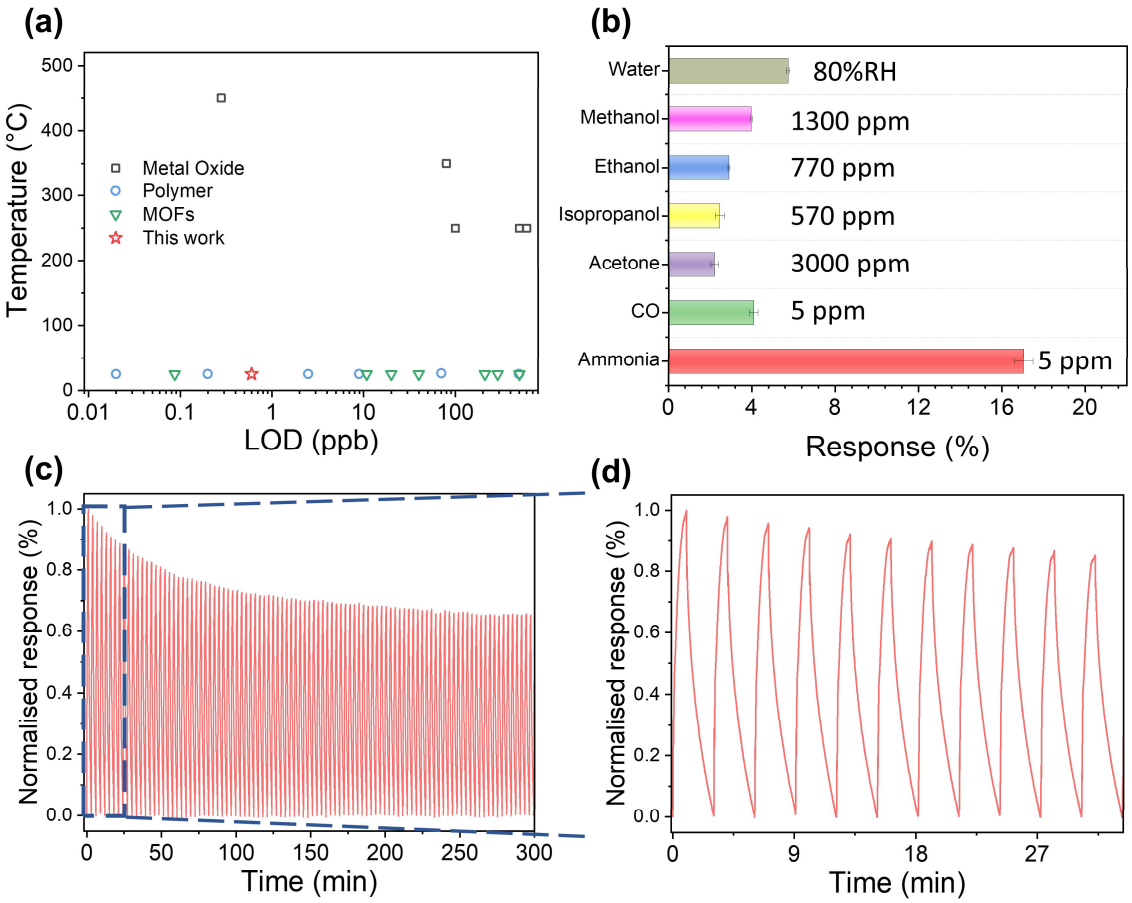

Figure 4.10. (a) The plot of temperature vs LOD of sensors including metal oxide, polymer, and MOFs. (b) Comparison among responses to different reducing gases of T_{60}. The concentration of each gas is labelled. The relative humidity in the test toward reducing gases was lower than 3%RH. (c) Repeatability test of T_{60} under 100 cycles (5-ppm ammonia). (d) Enlarged figure of data in (c) for just the initial 11 cycles.

Comparing the performance of different gas sensors under the same conditions is challenging due to the realistic differences in substrates, exposure times, and setups between each reported work. Furthermore, the sensitivity to a specific analyte, defined as the slope of the calibration curve of a sensor, is generally a significant parameter for performance comparison. However, specifying a sensitivity value for a sensor exhibiting a nonlinear sensing behaviour would be tricky due to its non-constant slope. Although challenges mentioned above persist, attempts (Figure 4.10a) have been made to compare our optimal sensor (T_{60}) with other reported sensors in terms of other critical parameters including their LODs and operating temperatures. To evaluate our work at a broad scope, chemiresistive sensors based on metal oxide,[207-211] polymer,[139, 161, 212-215] or MOFs[74, 113, 115, 118, 204, 205, 216] have been carefully selected. These sensors show the lowest reported LODs in their respective categories within the past 10 years. As the major sensing components of these counterparts are nanofilms, the significantly reduced number of conductive pathways in the $Cu_3(HHTP)_2$ percolation network allows a significantly low LOD of T_{60} at room temperature, indicating its highly sensitive performance and broad applicability. At an ammonia concentration of 5 ppm, the response of the T_{60} device is comparable to or exceeds that of several previously reported chemiresistive sensors operating at room temperature. The details of these sensors are shown in Table 4.2.

Table 4.2 Comparison of chemiresistive gas sensors based on metal oxide, polymers, and c-MOFs for NH_3 detection. The sensing response was evaluated at an ammonia concentration of 5 ppm and the slash symbol indicates that the sensor was not measured at 5 ppm NH_3.

Materials	Operating Temperature	Response	Exposure Time	LOD (ppb)	Ref
$Cu_3(HHTP)_2$ percolation network	RT	~17%	1 min	0.6	This work
V_2O_5 film	150°C	/	10 min	80	207
α-MoO_3 nanoribbons	450°C	~225	10 min	50	208
SnO_2 flakes	260°C	/	5 min	600	209
WO_3 nanorods	250°C	~464%	1 min	100	210

Table 4.2 (Continued)

Materials	Operating Temperature	Response	Exposure Time	LOD (ppb)	Ref
In_2O_3/Co_3O_4 nanocomposite	250°C	/	2 min	500	211
PPy percolation network	RT	~197%	1 min	9	139
Discrete PANI patterns	RT	~28%	1 h	220	173
PPy nanocrystal	RT	/	1 h	0.05	212
PANI hexagonal mesh	RT	~5%	2 min	2.5	213
PANI film	RT	~100%	5 min	100	214
Templated PPy percolation network	RT	~13%	6 min	71	215
$Cu_3(HHTP)_2$ nanofilm	RT	~33%	5 min	500	74
$Cu_3(HHTP)(THQ)$	RT	~4%	5 min	20	113
TiO_2-templated $Cu_3(HHTP)_2$ nanofilm	RT	~53%	5 min	0.087	115
Zn-HHTP hollow film	RT	/	1 min	39.9	119
Cu-BHT	RT	~4%	10 min	230	204
Cu-TBTT	RT	~9%	5 min	10.8	205
Co/Cu-MOF	RT	~13%	30 min	29	216

More experiments were conducted to further understand the sensing performance of the optimal sensor T_{60} in this study. The selectivity of T_{60} was first investigated (Figure 4.10b), where the selectivity was calculated as the ratio of the NH_3 response (5 ppm) to that of an interfering gas, including CO and vapours of water, methanol, ethanol, isopropanol, and acetone, at a certain concentration. The sensing test follows a similar protocol to the test for ammonia, with three consecutive periods of exposure to certain concentrations. The selectivity of NH_3 to the vapour of water (80%RH) was first tested and determined to be 3.0, implying its response to ammonia can be recognised when the relative humidity is lower or equal to 80%RH. The selectivity of NH_3 to VOC vapours, including methanol (1300 ppm), ethanol (770 ppm), isopropanol (570 ppm), and acetone (3000 ppm), are 4.3, 5.9, 6.9, and 7.7, respectively. CO is a typical reducing gas and the selectivity of ammonia to CO (5 ppm) is 4.2. These results demonstrate that T_{60}

exhibits high selectivity to ammonia against reducing gases including VOCs (methanol, ethanol, isopropanol, and acetone) and CO. These reducing analytes are reported to be detected in human exhaled breath. The ultra-low LOD and high selectivity to these reducing gases demonstrate the potential of T_{60} in detecting ammonia in human exhaled breath.

Its repeatability was further assessed by subjecting it to 100 cycles of 5-ppm ammonia sensing tests. Figure 4.10c displays the plot of its normalised response over time, where its response gradually decreases and stabilises at ~70% of the initial value. The enlarged view (Figure 4.10d) shows that T_{60} maintained stable and reversible responses at ~90% of the initial value after 11 cycles, indicating their good repeatability to sustain a consistent and reliable sensing performance over extended use.

4.4 Conclusion and outlook

$Cu_3(HHTP)_2$-based percolation networks have been successfully developed by running the electrochemical reaction for different periods between 30 and 300 s. The percolation region was confirmed by analysing the trend of conductance after deposition. The formation of percolation networks was further observed in the SEM and AFM images. Then, the samples obtained in both the percolation (T_{30}, T_{45}, T_{60}, T_{90}, and T_{120}) and the dense film (T_{300}) regions, as well as a powder-drop-casting sample, were compared in the gas sensing experiments. The sensing performance of each device to ammonia gas was systematically studied. Among all the samples, T_{60} exhibits the highest responses across all the ammonia concentrations from 100 ppb to 5 ppm within 1-min exposure, with responses of 17.06% ± 0.45% to 5 ppm ammonia and 2.29% ± 0.17% to 100 ppb ammonia. Additionally, T_{60} also shows the lowest theoretical limit of detection at 0.6 ± 0.1 ppb, which is one of the lowest among recently reported outstanding chemiresistive sensors. T_{60}'s excellent selectivity, low LOD, and good repeatability

demonstrate its potential for real-world applications. The exceptional performance of T_{60} underscores its remarkable sensing performance and efficacy as a promising chemiresistive gas sensor for detecting ammonia. The successful transfer of percolation network knowledge to c-MOFs provides a straightforward and insightful approach to significantly enhancing the sensing performance of chemiresistive sensors.

Chapter 5

Nanostructured $Cu_3(HHTP)_2$ percolation networks via polystyrene templates for chemiresistive gas sensing

In Chapter 4, percolation theory has been successfully introduced to improve the sensitivity of c-MOF-based sensors. Building on this, this chapter presents an integrated approach that combines bottom-up electrochemical deposition with a top-down templating approach to fabricate nanostructured $Cu_3(HHTP)_2$ percolation networks. Polystyrene (PS) latex was first deposited onto interdigitated electrode (IDE) substrates as a template layer. Percolation networks were developed by running the electrochemical deposition for different time periods, while subsequent removal of PS yielded a porous and hollow nanostructure. The electrical percolation behaviour of the sensors was investigated through electrical measurements and SEM. The sensing performance for ammonia was evaluated by comparing sensors operating in the percolation region and the dense film region.

5.1 Introduction

The practical deployment of c-MOFs in chemiresistive sensors is often constrained by relatively low sensitivity, particularly when deployed as thick films.[4] Even though a few c-MOF nano-thin films have been introduced to improve the sensitivity, the restricted surface area and inefficient gas diffusion pathways led to only limited improvement.[74] To address these challenges, attention has been directed toward designing sensor architectures that facilitate efficient analyte diffusion, maximise surface exposure, and enhance sensitivity.[115, 161]

In chemiresistive gas sensors, percolation theory explains how sensor sensitivity is enhanced by tuning the sensing material to operate near the percolation threshold. In Chapter 4, this principle was effectively applied to c-MOF systems, where percolation networks with improved sensing performance were achieved by controlling the MOF growth through tailored electrochemical deposition intervals.

In parallel, template-assisted synthesis offers precise control over morphology, particle size, and internal architecture of materials during synthesis.[217-219] By employing rigid solids as sacrificial templates—such as polystyrene (PS) nanospheres—well-defined hollow or porous structures can be fabricated, which significantly enhances gas diffusion and increases specific surface area. The process typically involves depositing the target material onto the template, which is subsequently removed to develop nanostructures that closely replicate the size and shape of the original scaffold. This strategy has been successfully employed in the fabrication of highly sensitive nanostructured sensors, including those constructed from polymers and MOFs.[161, 220]

This chapter introduces a hybrid strategy that combines bottom-up electrochemical deposition with a top-down PS-templating approach to fabricate nanostructured $Cu_3(HHTP)_2$ percolation networks. In this method, PS latex spheres serve as sacrificial templates, chosen due to their ease of processability and compatibility with aqueous systems. PS particles were first deposited onto interdigitated electrodes (IDEs) substrates to form closely packed layers. Electrochemical growth was then employed to grow $Cu_3(HHTP)_2$ on the IDEs, allowing the MOF to coat the PS templates. Samples with tailored deposition durations were treated with solvent to remove the PS nanoparticles, resulting in nanostructured and interconnected MOF percolation networks featuring a porous architecture and limited connecting electrical bridges. The successful deposition of $Cu_3(HHTP)_2$ was proved by XRD, FTIR, Raman, and XPS spectroscopy, while

SEM and AFM verified its rod-like morphology and porous structures. The electrical behaviour was investigated by electrical measurements and SEM imaging. Among all the tested sensors, a percolation sensor TT_{120} demonstrates exceptional ammonia detection, with responses of 68.15% ± 4.58% at 5 ppm and 11.39% ± 0.30% at 0.5 ppm ammonia, as well as a sub-ppb-level limit of detection (LOD) calculated to be 0.52 ± 0.03 ppb.

5.2 Experimental section

5.2.1 Chemicals and substrates

Potassium chloride (KCl, 98%), nitric acid (69%), 10 wt% aqueous suspension of polystyrene latex (PS, ~300 nm diameter) were obtained from Sigma-Aldrich. The Pt interdigitated electrodes (IDEs) with 5-micron gaps were obtained from MicruX Technologies (Figure 3.1b). A low-concentration ammonia (NH_3, 450 ppb, diluted with N_2) was purchased from BOC.

5.2.2 PS template deposition

Prior to deposition, the surfaces of the Pt interdigitated electrodes (IDEs) were cleaned using Piranha solution (a 3:1 v/v mixture of sulfuric acid and hydrogen peroxide). The Piranha solution was prepared in a glass container (e.g., a 25 mL beaker), and the IDEs were vertically suspended using a clamp. The immersion depth was carefully controlled such that only the deposition area of the IDEs was submerged in the solution, while the contact pads remained above the liquid level.

Subsequently, a 10 μL volume of a 0.4 wt% suspension of polystyrene (PS) in a mixture of water and ethanol (17:3 volume ratio) was drop-cast onto the Pt IDEs. The addition of ethanol effectively reduces the surface tension of the suspension and controls the evaporation rate,[221] thereby improving the deposition quality. During the deposition process, a Petri dish was placed

over the IDEs to promote uniform solvent evaporation, which was carried out at a controlled temperature of 37°C.

5.2.3 Anodic electrochemical deposition

The three-electrode setup used for the electrochemical experiments is detailed in Section 3.2.1.1. ITO slides or IDEs with 5-micron gaps were selected as the working electrodes. The deposition was run for time periods of 5, 15, 30, 60, 90, 120, 180, 240, 300, and 600 s, with each sample designated as TT_x, where x corresponds to the deposition time. After deposition, the prepared samples were immersed in DMF overnight to completely remove the PS template. The samples were then dried in an ambient environment overnight. Then, the resistance/conductance of each sample was measured using an RS PRO IDM 98IV handheld digital multimeter.

5.2.4 Gas sensing tests

Gas sensing tests were performed as described in Section 3.3.9 and Section 4.2.3. During the test, each sensor was exposed to diluted NH_3 gas for 1 min, which was then purged with nitrogen for 15 min before the next exposure. The exposure at each concentration was repeated for three consecutive cycles. Since the drying procedure are not able to remove all the DMF adsorbed in the c-MOFs.

Since that the drying procedure employed does not completely remove all DMF molecules adsorbed within the c-MOF framework. As a result, the first complete sensing sequence over the full concentration range primarily serves as an activation cycle, during which residual DMF is removed. All sensing data presented in this thesis correspond to subsequent full sensing cycles after this initial activation cycle.

5.2.5 Attribution statement

In this chapter, FTIR, nano-FTIR, and AFM measurements were conducted by Jiahao Ye using the facilities in Jin-Chong Tang's group. XPS measurements was conducted by Axel C. O. Forssberg using the instrumentation in the Rex Richard building. All other experiments were conducted by the author.

5.3 Results and discussion

Figure 5.1 illustrates the fabrication procedure of a polystyrene (PS)-templated $Cu_3(HHTP)_2$ percolation network on Pt IDEs (5 μm gaps). PS nanoparticles (~300 nm in diameter) were first deposited onto the Pt IDEs, followed by anodic electrochemical deposition of $Cu_3(HHTP)_2$ onto PS templates. By running electrochemical deposition for different time periods, sensors at various MOF growth stages were fabricated, each exhibiting distinct electrical resistances. Subsequent removal of PS templates yielded hollow, porous structures.

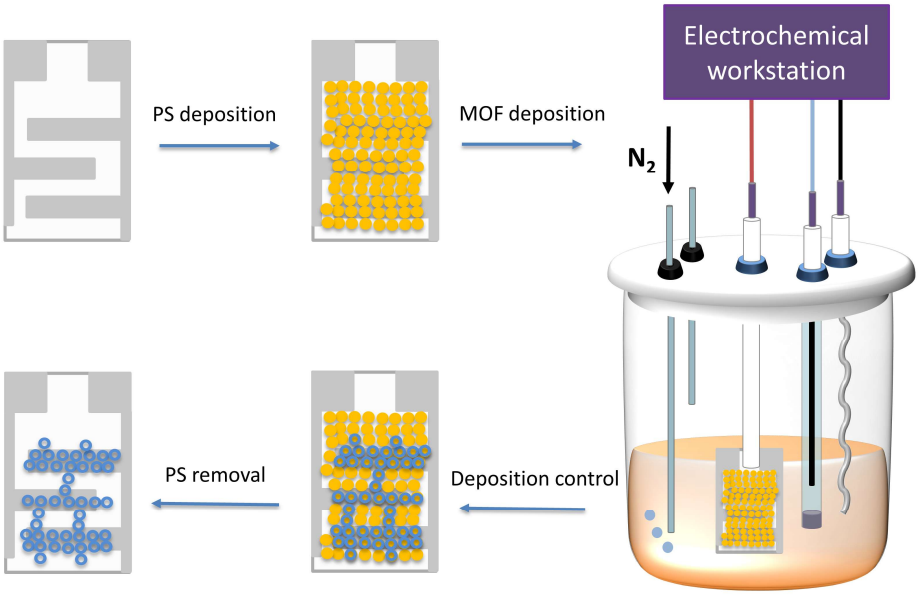

Figure 5.1. Schematic diagram of the preparation of a templated $Cu_3(HHTP)_2$ percolation network on Pt IDEs.

5.3.1 Preparation of templated MOF and characterisation

To investigate the appropriate potential for anodic electrochemical deposition using Pt IDEs as the working electrode under this study, cyclic voltammetry (CV) experiments were conducted in two types of solutions: one containing 2.25 mM $Cu(NO_3)_2$, and another precursor solution (P-$Cu_3(HHTP)_2$) containing 2.25 mM $Cu(NO_3)_2$ and 1.125 mM H_6HHTP. Both solutions also contained 100 mM KCl and 0.5 mM nitric acid in a water/DMF mixture at a 15:1 volume ratio. The reference electrode employed is Ag/AgCl (saturated). Prior to each experiment, the solutions were purged with nitrogen for 30 min.

Given that water is the predominant component of the solvent, the applied potential window was carefully selected to avoid the onset of the oxygen evolution reaction (OER), which could otherwise interfere with the electrochemical measurements. It is known that the theoretical onset potential for OER is 1.229 V versus the normal hydrogen electrode (NHE) in a strongly acidic aqueous environment.[222] The conversion between the potentials of Ag/AgCl (saturated) and NHE is described by Equation (5.1):

$$E(Ag/AgCl) = E(NHE) - 0.197V \quad (5.1)$$

Furthermore, the dependence of the OER potential on pH can be calculated by the Nernst equation (Equation 5.2):

$$E(O_2/H_2O) = E^o(O_2/H_2O) - 0.059 \times pH \quad (5.2)$$

With the pH calculated to be ~3.3 in this study, the theoretical onset of the oxygen evolution reaction (OER) is determined to be approximately 0.837 V versus Ag/AgCl (saturated) under these conditions. In practice, the actual OER onset occurs at a much higher potential due to the large kinetic overpotential (typically higher than 0.5 V) associated with Pt electrodes.[223] However, the Pt electrode is reported to undergo oxidation to surface oxides (e.g. PtO, PtO_2) at potentials between the theoretical and actual OER onsets, which negatively influences the

electrode activity.[224] Therefore, it is advisable to select a potential window below 0.8 V to ensure the avoidance of the oxidation of Pt and OER, thereby minimising their interference with the CV investigation of MOF deposition.

The experiments of CV for the solvent with different potential windows were first conducted to verify the above assumption. As shown in Figure 5.2a, when the selected window is below 0.8 V, no discernible reduction or oxidation peaks are observed, indicating electrochemical stability within this range. However, when the window extends to 1.0 V, the current intensity increases from 22.3 μA at 0.8 V to 47.5 μA at 1.0 V. Additionally, a discernible reduction peak (I) was observed at ~0.35 V, which is probably attributed to the reduction of Pt oxides, implying the oxidation of Pt electrode begins to occur between 0.8 and 1.0 V. As potential is further increased to 1.2 V, a pronounced surge of current intensity is observed, suggesting the significant Pt oxidation activity. The intensified oxidation is also accompanied by a more prominent reduction peak (II) during the reverse scan at a more negative potential, indicating more complex Pt oxides were formed at higher potential.

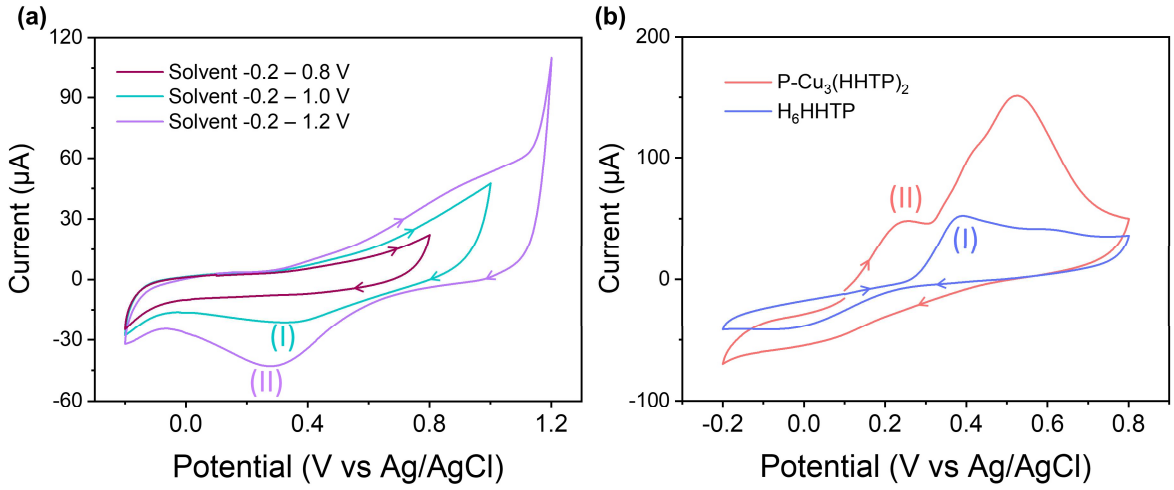

Figure 5.2. (a) CV curves of the solvent under different potential windows. (b) $Cu(NO_3)_2$ (2.25 mM) and the precursor containing $Cu(NO_3)_2$ (2.25 mM) and H_6HHTP (1.125 mM). The electrolyte is 100 mM KCl and the solvent is water/DMF mixture at a 15:1 volume ratio. The arrow indicates the initial direction of CV scans.

In this system, the acidic and nitrogen-enriched environment significantly limits the deprotonation of H_6HHTP, making the applied potential the critical factor for deprotonation. Figure 5.2b presents the CV curves for both P-$Cu_3(HHTP)_2$ and H_6HHTP. In the H_6HHTP solution, a distinct peak (I) appears at 0.38 V, indicating the onset of deprotonation. In the presence of the metal salt, this peak (II) shifts to a more negative potential (~0.25 V), as the metal salt consumes the deprotonated ligand and promotes the reaction. A potential of 0.3 V was selected to achieve controlled electrochemical deposition of $Cu_3(HHTP)_2$ on Pt IDEs at a moderate growth rate.

Figure 5.3 shows the results for characterising the templated electrochemically deposited $Cu_3(HHTP)_2$ (T-E-$Cu_3(HHTP)_2$). A sample synthesised via solvothermal solution synthesis (S-$Cu_3(HHTP)_2$) was introduced as a control, as this method is widely reported in the literature.[4] Except for XRD analysis, where samples were deposited on indium tin oxide (ITO) substrates under identical procedure with an extended deposition time of 2 h, all other electrochemically synthesised samples were deposited on Pt IDE glass substrates and grown for 120 s. Figure 5.3a presents XRD patterns of $Cu_3(HHTP)_2$ samples. The S-$Cu_3(HHTP)_2$ exhibits characteristic peaks at ~5°, ~10°, ~13°, and ~28°, corresponding to the (100), (200), (210), and (001) crystal planes of $Cu_3(HHTP)_2$, respectively. The electrochemically deposited sample without templating (E-$Cu_3(HHTP)_2$) on ITO substrates only displays a pronounced and sharp XRD peak at ~28°, corresponding to the (001) reflection and indicative of well-aligned crystalline structures.[89] In comparison, the sample synthesised with PS nanosphere templating (T-E-$Cu_3(HHTP)_2$) on ITO shows additional small peaks near 5° and 10°, implying a slightly less favourable c-axis alignment to the substrate compared to the E-$Cu_3(HHTP)_2$.

Figure 5.3b and c show representative SEM images of the T-E-$Cu_3(HHTP)_2$ surface, confirming the presence of porous nanostructures. Prior to templating, the dominance of the (001) reflection

indicates that these MOFs grow face-on to the substrate. However, after templating, the presence of PS particles slightly alters the MOF growth orientation due to their spherical structures. This explains the emergence of new XRD peaks.

FTIR spectroscopy results are presented in Figure 5.3d. The spectrum of T-E-$Cu_3(HHTP)_2$ closely resembles that of S-$Cu_3(HHTP)_2$. The free ligand, H_6HHTP, exhibits two O–H stretching peaks (3410 and 3252 cm^{-1}), O-H bending (~1615 cm^{-1}), two C=C stretching peaks (1533 and 1439 cm^{-1}), and a C–O stretching peak (1221 cm^{-1}). In contrast to H_6HHTP, the O–H stretching and bending bands are all absent in T-E-$Cu_3(HHTP)_2$, indicating successful coordination between the ligand and the metal centres. Both H_6HHTP and T-E-$Cu_3(HHTP)_2$ display a C=C peak at 1439 cm^{-1}. The C=C peak at 1533 cm^{-1} in H_6HHTP exhibits a slight red shift and merges with the 1439 cm^{-1} peak after coordination, resulting in a broadened band at around 1440 cm^{-1} in T-E-$Cu_3(HHTP)_2$. The triphenylene structure comprises four benzene rings: one central (core) ring and three fused rings. The 1533 cm^{-1} peak is likely attributed to the C=C vibration in the fused benzene rings. Coordination with the metal centre withdraws electrons from the fused rings, weakening the C=C bond and causing a red shift. In contrast, this effect is less pronounced in the core benzene ring, so the 1439 cm^{-1} peak is assigned to the C=C vibration of the core ring. The C-O peak at 1221 cm^{-1} in H_6HHTP also shows a slight red shift to 1209 cm^{-1} in T-E-$Cu_3(HHTP)_2$.

As shown in Figure 5.3e, Raman spectroscopy indicates the Cu-O vibration at 640 cm^{-1},[83] further proving the coordination between ligand and metal centre. Additionally, the D and G bands appear at 1363 cm^{-1} and 1541 cm^{-1} in T-E-$Cu_3(HHTP)_2$, respectively, red-shifted from 1396 cm^{-1} and 1626 cm^{-1} in the free H_6HHTP ligand. This red shift aligns with the FTIR results, suggesting electron withdrawal from the aromatic rings upon coordination with Cu^{2+} ions. Moreover, an increased G/D intensity ratio in T-E-$Cu_3(HHTP)_2$ relative to the ligand indicates

the formation of extended MOF layer structures. As shown in Figure 5.3f, the high-resolution XPS Cu $2p_{3/2}$ spectrum of T-E-$Cu_3(HHTP)_2$ reveals two peaks at 934.4 eV and 932.8 eV, corresponding to Cu^{2+} and Cu^{+} oxidation states, respectively. The above results are consistent with previous literature and collectively prove the successful synthesis of $Cu_3(HHTP)_2$.

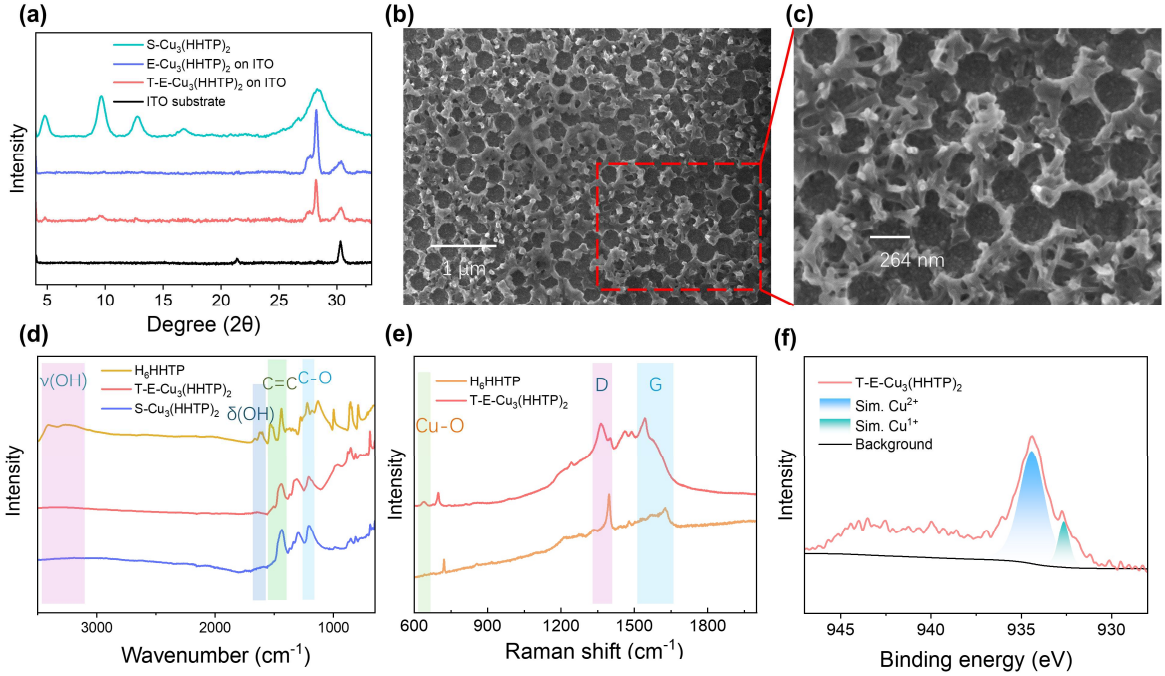

Figure 5.3. (a) XRD scans of S-$Cu_3(HHTP)_2$ (green line), E-$Cu_3(HHTP)_2$ (blue line) on ITO, T-E-$Cu_3(HHTP)_2$ on ITO (red line), ITO (black line). (b) and (c) SEM images of the top view of T-E-$Cu_3(HHTP)_2$ at two magnifications. (d) FTIR spectra of T-E-$Cu_3(HHTP)_2$ (red line), S-$Cu_3(HHTP)_2$ (blue line), and H_6HHTP (yellow line). (e) Raman spectra of H_6HHTP (yellow line) and T-E-$Cu_3(HHTP)_2$ (red line). (f) XPS spectrum of T-E-$Cu_3(HHTP)_2$ (red line). Expect for XRD, all the samples were deposited by 120 s on IDE substrates.

AFM was performed on a T-E-$Cu_3(HHTP)_2$ sample grown on a Pt IDE glass substrate for 120 s to further characterise its surface morphology. Figure 5.4a shows a 10 × 10 μm² AFM image of a region, where the dark area corresponds to the gap between electrode fingers, and the bright white and yellow regions denote the MOF growth on the electrodes. Three representative line scans were extracted from this image, with their corresponding height profiles displayed in Figure 5.4b. All three profiles exhibit a clearly defined step feature with a flat base and elevated

platforms, corresponding to the gap and the electrodes, respectively. A gap width just under 4 μm is observed—smaller than the original 5 μm—indicating that the MOF has grown from the electrode edges into the gap. The height difference between the Pt electrode fingers and the gap is designed to be ~0.15 μm. On the electrode surfaces, minor height fluctuations of up to ~0.4 μm are observed. Given that the diameter of the PS nanospheres is approximately 300 nm, this highet variation corresponds well to the presence of one or two layers of the PS-modified structures.

To reveal the porous architecture, AFM was performed at a higher magnification. Figure 5.4c presents a $5 \times 5\ \mu m^2$ AFM image of the sample, where regular porous structures are clearly apparent. A selected region, indicated by a white square, was subsequently imaged at $1.5 \times 1.5\ \mu m^2$ resolution (see Figure 5.4d), revealing the fine pore structures in greater detail. Three selected regions marked by black squares in Figure 5.4c were chosen for nano-FTIR spectroscopy, a technique that enables in-situ FTIR analysis at the nanoscale. The nano-FTIR measurements were facilitated by AFM integrated with scattering-type scanning near-field optical microscopy (s-SNOM).[225] Although the FTIR spectroscopy with the ATR module has already enabled the in-situ characterisation of the sample, it requires the sample to be firmly pressed against the window using a screw-down cover—an action that risks damaging the porous architecture.

Figure 5.4e presents nano-FTIR spectra of T-E-$Cu_3(HHTP)_2$ and S-$Cu_3(HHTP)_2$, each obtained by averaging three measurements acquired from distinct regions. The characteristic C=C (~1470 cm^{-1}) and C-O (~1220 cm^{-1}) stretching vibration bands of $Cu_3(HHTP)_2$ were recognised in both forms. Notably, nearly all peaks in T-E-$Cu_3(HHTP)_2$ exhibit slight red shifts compared to those in S-$Cu_3(HHTP)_2$. In contrast to the bulk-like morphology of S-$Cu_3(HHTP)_2$ (Figure 5.4f and g), the T-E-$Cu_3(HHTP)_2$ displays highly porous architectures. It has been reported that

morphological factors such as porosity can markedly influence the dielectric function which governs the optical response of materials.[226, 227] Therefore, the red shift is probably attributed to the PS-templated porous structures and higher surface area of the T-E-$Cu_3(HHTP)_2$, which alters the local electromagnetic field distribution and the effective dielectric environment, leading to subtle but measurable shifts in vibrational frequencies.

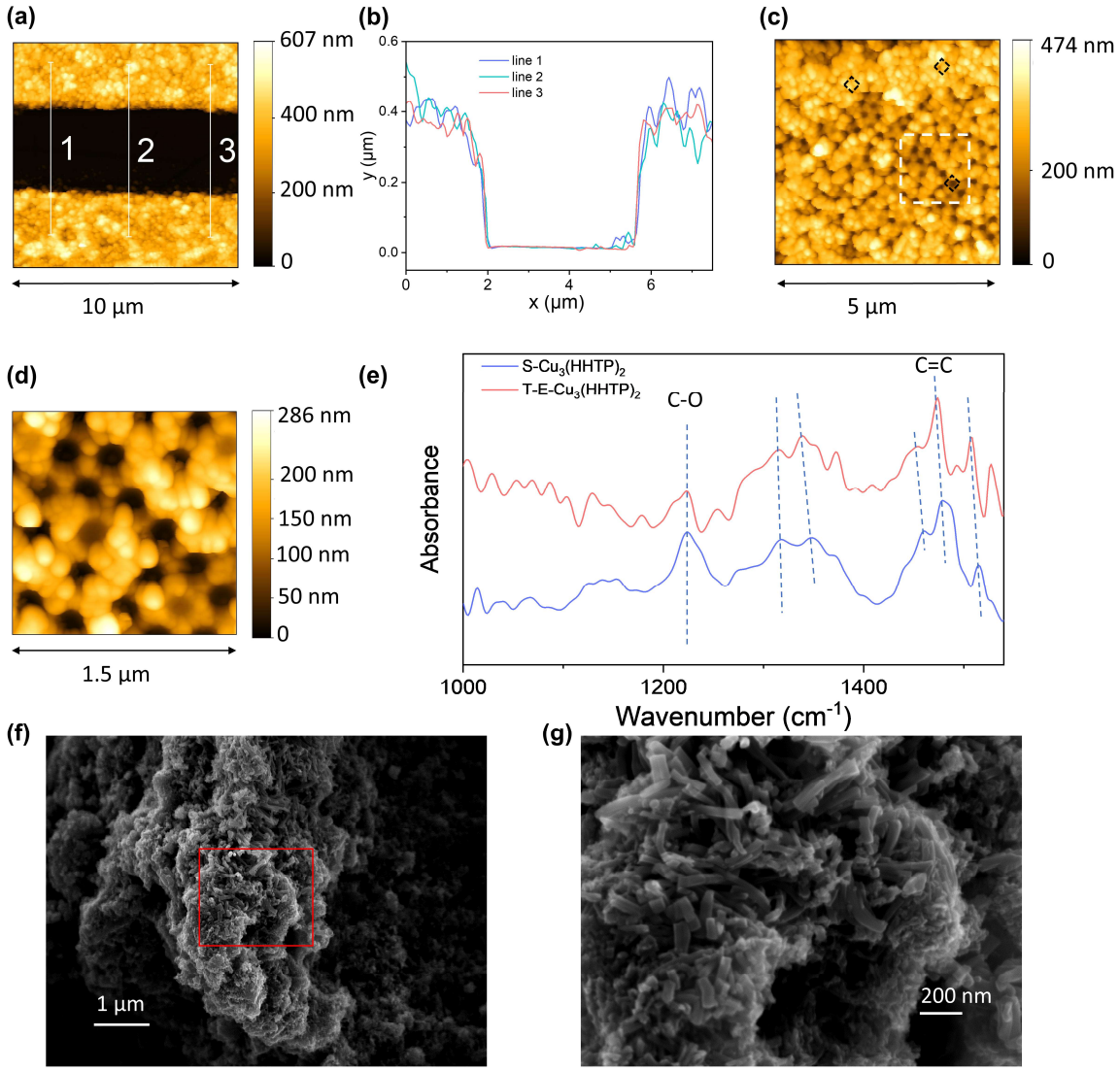

Figure 5.4. (a) A 10 × 10 µm^2 AFM image of T-E-$Cu_3(HHTP)_2$ and (b) corresponding height line profiles. (c) and (d) AFM images of T-E-$Cu_3(HHTP)_2$ at 5 × 5 µm^2 and 1.5 × 1.5 µm^2 image sizes, respectively. The white and black sqaures in (c) denote the region corresponding to (d) and the regions used for nano-FTIR measurements, respectively. (e) Nano-FTIR spectra of samples. (f) A representative SEM image of S-$Cu_3(HHTP)_2$ and (g) the enlarged view of the region highlighted in red in (f).

5.3.2 Electrical percolation

Samples were prepared via amperometric deposition at 0.3 V for varying durations of 5, 15, 30, 60, 90, 120, 180, 240, 300, and 600 s. For clarity, each sample is designated as TT_x, where x denotes the deposition time in seconds. The recorded conductance of the samples as a function of deposition time is shown in Figure 5.5, alongside its corresponding semi-logarithmic plot, which highlights the percolation region.

No measurable conductance is observed in samples TT_5, TT_{15}, and TT_{30}, indicating that the MOFs have not yet formed continuous pathways bridging the IDE fingers within 30 s. The first measurable conductance appears at TT_{60}, marking the onset of the percolation region. As more conductive pathways form between IDE fingers, the conductance increases sharply until 300 s, beyond which the curve plateaus, signifying the end of the percolation region. The conductance data of the devices are shown in Table 5.1.

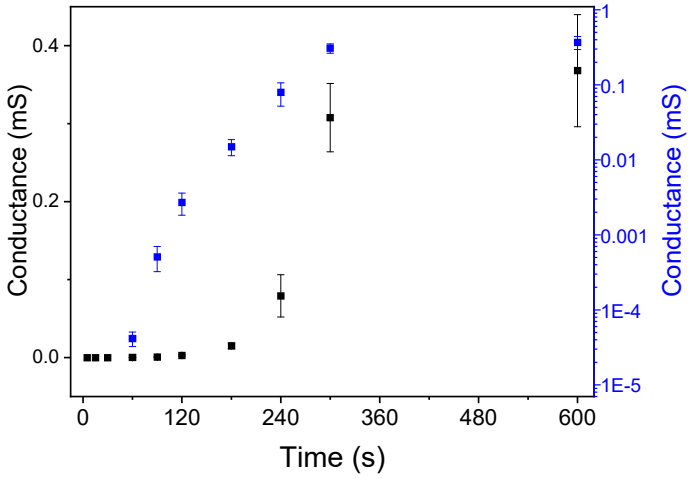

Figure 5.5. Conductance across Pt IDEs as a function of deposition time (in black), along with its semilogarithmic plot (in blue). Error bars represent the standard deviation from five independently prepared samples.

Compared with the conductance trend shown in Figure 4.6, even though both percolation curves have the same endpoint at 300 s, the plateau conductance obatined here is almost half (from 8.7×10^{-1} mS to 3.7×10^{-1} mS). This difference can be attributed to the presence of PS

nanospheres during the electrochemical synthesis. The retained PS occupies a significant fraction of the inter-electrode space, thereby reducing the number of available conductive pathways and leading to a lower overall conductance at the percolation plateau. This behaviour is consistent with observations reported in our previous studies.[160, 161]

Table 5.1 The conductance data (unit: mS) of the devices. The conductance of each device was evaluated from five independently fabricated samples, with each data point corresponding to a separate device. The data were calculated by converting each resistance value to conductance (G = 1/R). Only samples with measurable conductance are presented.

Device	Data 1	Data 2	Data 3	Data 4	Data 5	Ave.	SD
TT_{60}	5.4×10^{-5}	3.5×10^{-5}	4.8×10^{-5}	3.3×10^{-5}	3.8×10^{-5}	4.2×10^{-5}	9.1×10^{-6}
TT_{90}	2.9×10^{-4}	4.0×10^{-4}	5.6×10^{-4}	7.9×10^{-4}	5.3×10^{-4}	5.1×10^{-4}	1.9×10^{-4}
TT_{120}	1.4×10^{-3}	2.4×10^{-3}	3.2×10^{-3}	3.8×10^{-3}	2.9×10^{-3}	2.7×10^{-3}	8.9×10^{-4}
TT_{180}	1.1×10^{-2}	1.5×10^{-2}	1.3×10^{-2}	1.5×10^{-2}	2.1×10^{-2}	1.5×10^{-2}	3.6×10^{-3}
TT_{240}	5.3×10^{-2}	5.2×10^{-2}	1.0×10^{-1}	7.8×10^{-2}	1.1×10^{-1}	7.9×10^{-2}	2.7×10^{-2}
TT_{300}	2.5×10^{-1}	2.7×10^{-1}	3.4×10^{-1}	3.5×10^{-1}	3.3×10^{-1}	3.1×10^{-1}	4.4×10^{-2}
TT_{600}	3.2×10^{-1}	3.5×10^{-1}	3.0×10^{-1}	3.9×10^{-1}	4.8×10^{-1}	3.7×10^{-1}	7.2×10^{-2}

SEM imaging was performed to visualise the evolution of morphology corresponding to the electrical behaviour of $Cu_3(HHTP)_2$ on the IDEs after the removal of the PS nanospheres. Figure 5.6 presents SEM images of representative regions from selected samples: TT_5, TT_{15}, TT_{30}, TT_{60}, TT_{90}, and TT_{300}. In each image, the black region in the centre corresponds to the insulating glass substrate, while the grey areas on either side represent the electrode fingers. The black spots or grey circular features observed on the electrodes indicate the presence of the grown MOF material.

In TT_5 (Figure 5.6a), scattered black spots appear on the electrodes, indicating the initial nucleation of $Cu_3(HHTP)_2$. In TT_{15} (Figure 5.6b), well-defined circular features are observed on the electrode surfaces, attributed to PS-assisted nanostructuring. By 30 s (Figure 5.6c), the MOFs with circular morphology cover the entire electrode areas, and a small amount of material is observed extending toward the inter-electrode gap. At 60 s (Figure 5.6d), a substantial amount of MOF growth extends from electrodes to the gap. This becomes more pronounced in TT_{90} (Figure 5.6e), where a well-developed porous percolation network between the electrodes is clearly visible. Finally, in TT_{300} (Figure 5.6f), the MOF grows as a dense film with extensive overgrowth, covering nearly the entire electrode surface and bridging the inter-electrode gap completely.

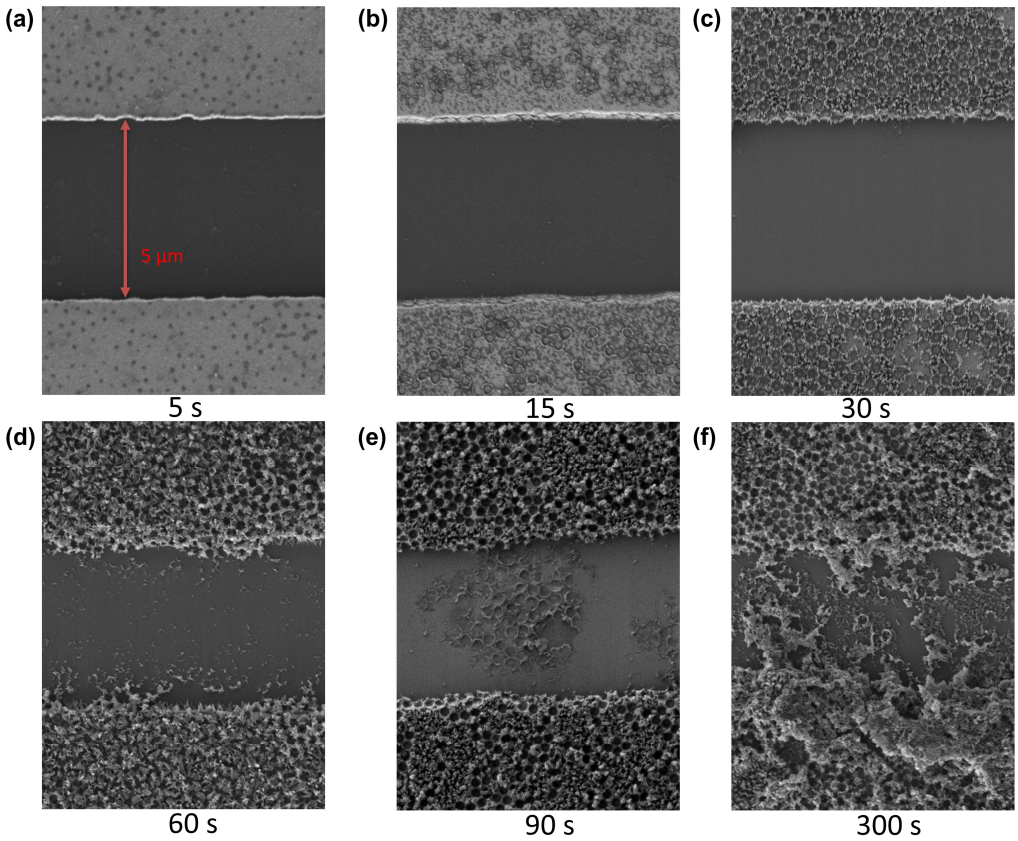

Figure 5.6. Representative SEM images of $Cu_3(HHTP)_2$ prepared via amperometric deposition by 5 s (a), 15 s (b), 30 s (c), 60 s (d), 90 s (e), and 300 s (f).

5.3.3 Gas sensing tests

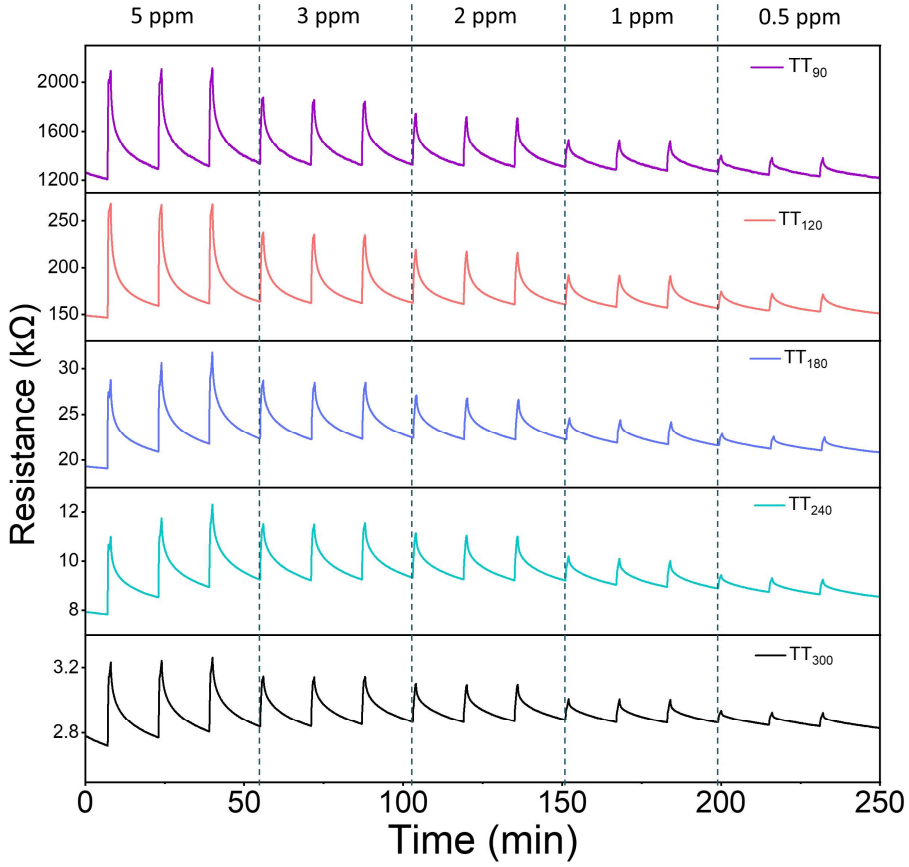

Figure 5.7. Response-recovery plots of samples to different concentrations of ammonia, including TT_{90}, TT_{120}, TT_{180}, TT_{240}, and TT_{300}. Data shown were obtained after the initial conditioning full cycle.

In Chapter 4, ammonia was chosen as the target analyte to assess the sensing capabilities of the chemiresistive gas sensors based on percolation networks. To evaluate the sensing performance of templated percolation sensors and verify the percolation theory in this study, ammonia sensing tests were conducted on sensors operating in the percolation region, including TT_{90}, TT_{120}, TT_{180}, and TT_{240}, as well as on TT_{300}, a sensor operating in the dense film region. All sensors were exposed to ammonia for 1 minute at sequential concentrations of 5 ppm, 3 ppm, 2 ppm, 1 ppm, and 0.5 ppm, with each exposure followed by a 15-minute recovery in nitrogen. Each concentration was tested in triplicate. Figure 5.7 shows the response–recovery curves for the selected sensors. All devices exhibit reversible responses to ammonia, with a marked increase in resistance upon exposure—consistent with the p-type

semiconducting behaviour of $Cu_3(HHTP)_2$. For each sensor, the response magnitude decreases with decreasing ammonia concentration, confirming a concentration-dependent sensing behaviour.

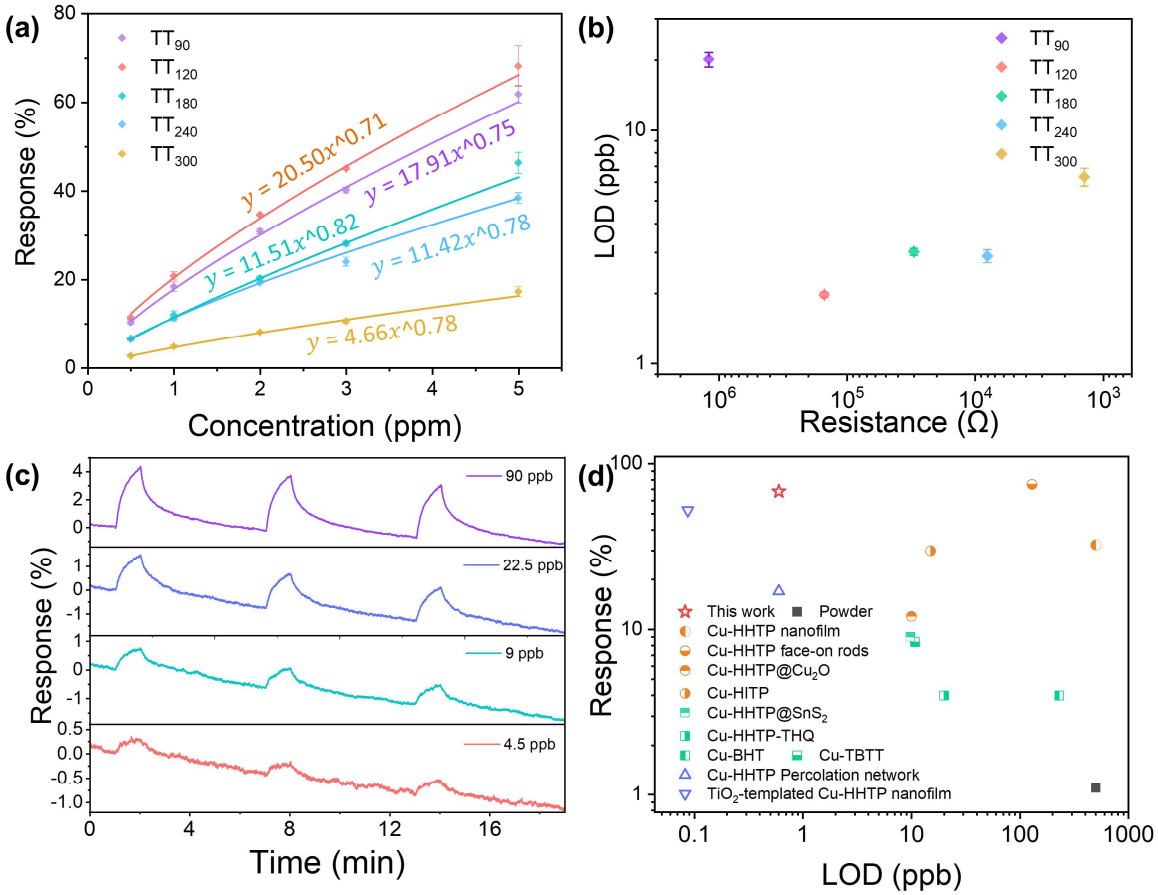

Figure 5.8. (a) Response-concentration curves of sensors. (b) LODs of samples, calculated by using the sensitivity obtained at 500 ppb. (c) Response-recovery curves of TT_{120} to low-concentration ammonia. (d) The plot of response vs LOD of c-MOF-based chemiresistive gas sensors.

The sensor responses were calculated and plotted as a function of ammonia concentration. The response was defined as the relative change in resistance upon ammonia exposure, expressed as $\Delta R / R_0$, where ΔR is the change in resistance and R_0 is the baseline resistance before exposure. As shown in Figure 5.8a, consistent with the sensing behaviour discussed in Chapter 4, the fitting curves of all sensors in this chapter follow the conductance model limited by electron transport across intergranular potential or Schottky barriers, as described by Equation 5.1:

$$\Delta R / R_0 = A_g p_g^{\beta} \quad (5.1)$$

where p_g is the partial pressure, A_g is a prefactor, and β is the exponent factor.

Among all the tested sensors, TT_{120} demonstrates the highest responses across all NH_3 concentrations, with exceptional responses of 68.15% ± 4.58% at 5 ppm and 11.39% ± 0.30% at 0.5 ppm ammonia. TT_{90} also exhibits excellent performance, with responses of 61.80% ± 1.98% at 5 ppm and of 10.32% ± 0.52% at 0.5 ppm. In contrast, TT_{180} and TT_{240}, which are engineered further from the percolation threshold, show weaker sensing responses. TT_{300}, the only sensor operating in the dense film region in the test, has the lowest sensing performance, with responses of 17.25% ± 1.16% at 5 ppm and 2.62% ± 0.22% at 0.5 ppm.

The theoretical LOD of each sensor was determined to further evaluate its sensing capability, which was calculated using the sensitivity determined by the lowest detected concentration (500 ppb). Figure 5.8b presents the LODs of samples. TT_{90} has the highest LOD of 20.14 ± 1.01 ppb among all the tested sensors. In contrast, TT_{120} demonstrates a LOD of 1.97 ± 0.05 ppb, the lowest among all the tested sensors. After TT_{120}, the LODs of sensors engineered further percolation threshold gradually increase to 6.32 ± 0.55 ppb for TT_{300}.

To sum up, sensors engineered near the percolation threshold exhibit significantly higher responses. As deposition time increases, the sensors move further beyond the percolation threshold, resulting in a gradual decrease in response. The sensor operating in the dense film region displays the lowest response among all, due to the presence of numerous redundant electrical pathways between the electrode fingers. In this case, individual connections contribute minimally to the overall resistance change and are less sensitive to the analyte. In contrast, sensors near the percolation threshold rely on a limited number of critical conduction pathways, making each connection highly responsive to analyte exposure. Although both TT_{90}

and TT_{120} exhibit excellent sensing responses, the LOD of TT_{120} is one order of magnitude lower. This observation is consistent with the findings in Chapter 4: samples with higher resistance were shown to produce higher noise when measured by a potentiostat, making the optimal sensor performance achieved slightly beyond the percolation threshold.

In conclusion, percolation theory has been effectively applied to develop a series of sensors operating in the percolation region, demonstrating significantly enhanced sensing performance compared to the sensor in the dense film region. Among them, TT_{120} exhibits the highest responses and the lowest LOD, making it the optimal sensor in this study.

To further evaluate the sensing performance of the optimal TT_{120} sensor at low concentrations, we conducted ammonia detection tests using a 450 ppb stock cylinder to generate target concentrations of 90, 22.5, 9, and 4.5 ppb—with 4.5 ppb being the lowest reliably accessible concentration in our lab. As shown in Figure 5.8c, TT_{120} shows responses of $4.01 \pm 0.23\%$, $1.48 \pm 0.25\%$, $0.71 \pm 0.04\%$, and $0.39 \pm 0.02\%$ at 90, 22.5, 9, and 4.5 ppb, respectively, demonstrating excellent sensitivity even at sub-10 ppb levels. The LOD was then revised to 0.52 ± 0.03 ppb using the sensitivity calculated at 4.5 ppb. In addition, the LOD_{SE} of TT_{120} was also confirmed to be 0.074 ± 0.004 ppb.

Systematic comparison of different samples is challenging due to differences in exposure times, substrates, and experimental setups. Nevertheless, we made efforts to benchmark TT_{120} against published c-MOF-based chemiresistive gas sensors. In Figure 5.8d, each sensor's response to 5 ppm ammonia as a function of its LOD (all measured at room temperature) was plotted. TT_{120} is among the top performers, exhibiting one of the highest responses and the lowest LODs reported for chemiresistive c-MOF sensors. The details of sensors are shown in Table 5.2.

These exceptional results for TT_{120} arise from its dual fabrication strategy: the top-down templating method introduces porous architectures to enhance gas diffusion and increase

specific surface area, while the bottom-up electrochemical deposition establishes percolation networks that effectively reduce redundant electrical pathways. Compared with most sensors that rely on thin-film structure alone, the integration of both top-down and bottom-up techniques enables TT_{120} to exhibit high responses and sub-ppb-level LOD, indicating its outstanding sensing capability and broad sensing applicability.

Table 5.2 Comparison of chemiresistive gas sensors based on c-MOFs. All sensors were operated at room temperature, and the responses were measured against 5 ppm ammonia.

Materials	Response	Exposure Time	LOD (ppb)	Ref
Templated $Cu_3(HHTP)_2$ percolation network	~68%	1 min	0.52	This work
$Cu_3(HHTP)_2$ percolation network	~17%	1 min	0.6	Chapter 4
EHD-printed percolation network	~17%	1 min	23.1	Chapter 6 (See below)
MOF-PS composite percolation network	~9%	1 min	6.3	Chapter 7 (See below)
$Cu_3(HHTP)_2$ nanofilm	~33%	5 min	500	74
TiO_2-templated $Cu_3(HHTP)_2$ nanofilm	~53%	5 min	0.087	115
Cu-HHTP face-on rods	~75%	5 min	129	228
Cu-HHTP@Cu_2O	~12%	2 min	10	117
Cu-HHTP@SnS_2	~9%	10 min	9.84	229
Cu-HITP	~30%	40 s	15	230
Cu-HHTP-THQ	~4%	5 min	20	113
Cu-BHT	~4%	10 min	230	204
Cu-TBTT	~9%	5 min	10.8	205
Cu-HHTP powder	~1%	30 s	500	73

5.4 Conclusion and outlook

In this chapter, a series of templated $Cu_3(HHTP)_2$ percolation networks have been established by integrating a top-down PS-assisted nanostructuring technique with a bottom-up electrochemical deposition control strategy. The top-down PS-assisted method enables the formation of a porous architecture, which effectively improves the gas diffusion and increases the specific surface area. Furthermore, by running the deposition for specific periods, templated samples with different resistance values and growth stages were developed. The electrical percolation behaviour of the obtained templated sensors was investigated through electrical conductance measurements and SEM imaging. The gas sensing performance of templated percolation networks (TT_{90}, TT_{120}, TT_{180}, and TT_{240}) was evaluated by using ammonia as the analyte and compared with that of TT_{300}, a sensor operating in the dense film regime. Among these, TT_{120} emerged as the optimal sensor, exhibiting one of the highest responses of 68.15% ± 4.58% to 5 ppm ammonia and the lowest theoretical LOD of 0.52 ± 0.03 ppb among the reported chemiresistive gas sensors based on c-MOFs.

Chapters 4 and 5 presented a systematic investigation of constructing c-MOF percolation networks via electrochemical synthesis, confirming that the application of percolation theory significantly enhances sensor sensitivity in c-MOF-based chemiresistive gas sensors. However, the current strategies for forming c-MOF percolation networks are dependent on electrochemical deposition. Future research should explore and develop alternative deposition methods to broaden the applicability and scalability of this strategy.

Chapter 6

Electrohydrodynamic jet-printed c-MOFs for chemiresistive gas sensing

The previous chapters have examined the development of c-MOF-based percolation networks via electrochemical synthesis. This chapter explores another alternative fabrication technique, electrohydrodynamic (EHD) jet-printing, to achieve the percolation behaviour through controlled material deposition. By optimising the precursor solution formulation as printable inks, c-MOF strips were successfully patterned onto substrates. Tuning the concentration of the ligand H_6HHTP in the ink enabled the formation of strips with varying c-MOF deposition levels. The successful synthesis of c-MOF strips was confirmed through XRD and FTIR. Percolation behaviour was further confirmed by electrical measurements and SEM imaging. Finally, the chemiresistive gas sensing responses to ammonia were evaluated and compared across samples.

6.1 Introduction

Percolation theory, implemented through deposition-control strategies, has proven effective in enhancing the sensitivity of chemiresistive gas sensors based on polymers and c-MOFs. This approach involves fine-tuning the deposition of sensing materials to achieve the percolation threshold, thereby minimising the conductive bridges and amplifying the influence of gas analytes on active materials. However, the strategy relies heavily on electrochemical synthesis methods, which can present limitations such as scalability and compatibility with various substrates.

To overcome these challenges, applying alternative synthesis approaches to achieve percolation networks is necessary. Existing deposition approaches for c-MOFs include drop-casting, film transfer obtained via gas-liquid/liquid-liquid interfacial synthesis, vapour-assisted conversion, and a layer-by-layer liquid-phase epitaxial method.[74, 85, 86] These techniques typically generate films with excessive electrical connections and do not facilitate the deposition of discrete patterns onto substrates.

Electrohydrodynamic (EHD) printing is an emerging additive manufacturing technique that utilises high electric fields to deposit micro- and nanoscale patterns with exceptional precision, which is particularly promising for fabricating high-performance electronic devices.[163] While EHD printing has been extensively explored for depositing materials like conductive polymers, metal oxides, and nanocomposites (detailed in Section 2.5.3),[164, 170, 171, 173] comprehensive investigations into its application for depositing c-MOFs remain limited. The technique's high resolution and material versatility suggest potential for patterning c-MOFs, which could be advantageous for developing c-MOF percolation sensors with high sensitivity.

In this study, EHD jet printing was employed to fabricate discrete $Cu_3(HHTP)_2/Zn_3(HHTP)_2$ percolation patterns on Pt interdigitated electrode substrates. By tuning the composition of the precursor solution used as ink, $Cu_3(HHTP)_2/Zn_3(HHTP)_2$ patterns with feature sizes between 250 and 350 μm were prepared. The percolation networks of $Cu_3(HHTP)_2$ patterns were further developed by adjusting the ligand (H_6HHTP) concentration in the ink, with lower concentrations leading to less electrical connections within the printed patterns. The percolation behaviour was confirmed through electrical conductance measurements and SEM imaging. Subsequently, the sensing performance to ammonia of EHD-printed $Cu_3(HHTP)_2$ percolation networks with different growth stages and resistances was evaluated. The P_{80} sensor, fabricated using an ink with a 2.6 mM concentration of ligand, shows a resistance of ~7.2 kΩ,

demonstrating the optimal sensing performance in this study, with an excellent response of 12.18 ± 1.51% to 5 ppm ammonia and the lowest limit of detection (LOD) of 23.1 ± 0.7 ppb.

6.2 Experimental section

6.2.1 Chemicals and substrates

2,3,6,7,10,11-hexahydroxytriphenylene (H_6HHTP, 95%) was purchased from Tokyo Chemical Industry. Copper nitrate trihydrate ($Cu(NO_3)_2 \cdot 3H_2O$, 98%), zinc nitrate hexahydrate ($Zn(NO_3)_2 \cdot 6H_2O$, 98%), dimethylformamide (DMF, 99.8%), ethylene glycol (EG), and ethanol were obtained from Sigma-Aldrich. The 5-micron Pt interdigitated electrodes (IDEs) from MicruX Technologies and indium tin oxide (ITO) glass were employed as substrates. Gas cylinders of nitrogen (N_2, zero grade), ammonia (NH_3, 10 ppm, filled with N_2) were purchased from BOC.

6.2.2 Ink preparation

An optimised printing ink was prepared from a precursor solution containing either $Cu(NO_3)_2 \cdot 3H_2O$ (5 mM) or $Zn(NO_3)_2 \cdot 6H_2O$ (5 mM) combined with H_6HHTP (3.3 mM) in a DMF/ethanol/ethylene glycol (EG) solvent mixture (volume ratio 1:6:8). The ink formulation was optimised through a series of preliminary trials in which the DMF/EG solvent ratio were systematically varied (6:1, 3:4, and 1:6) to achieve stable EHD patterns. The concentrations of metal salt and EG were fixed to ensure the conductivity and viscosity of the ink, respectively. While the concentration of the metal salt was fixed to ensure adequate ink conductivity for EHD printing, the concentration of H_6HHTP could be further diluted as required. All inks used were freshly prepared before the printing and used within 4 h. No visible signs of MOF formation was observed in the ink within this time window.

6.2.3 Electrohydrodynamic jet printing

The electrohydrodynamic (EHD) jet printing procedure has been presented in Section 3.2.1.2. Gold-coated glass pipettes with a diameter of 30 μm were used as nozzles for printing. The inks were loaded into the coated nozzles using 20 μL microloader pipette tips. The applied voltage ranged from 1.4 to 2.4 kV, while the working distance between the nozzle and substrate was between 150 and 300 μm. The inks were printed onto the substrate to form precursor strips/patterns, which were subsequently dried in an oven at 60 °C for 4 h. The dried samples were then immersed in DMF for 2 h to remove any unreacted species. This process yielded the final $Cu_3(HHTP)_2$ strips/patterns.

6.2.4 Gas sensing tests

In each test, the exposure time to NH_3 was 1 min, and exposure to nitrogen was 15 min for recovery before the next exposure. The exposure at each concentration was repeated for three consecutive cycles.

Since that the drying procedure employed does not completely remove all DMF molecules adsorbed within the c-MOF framework. As a result, the first complete sensing sequence over the full concentration range primarily serves as an activation cycle, during which residual DMF is removed. All sensing data presented in this thesis correspond to subsequent full sensing cycles after this initial activation cycle.

6.2.5 Attribution statement

In this chapter, FTIR measurements were conducted by Jiahao Ye using the facilities in Jin-Chong Tang's group. Printing experiments were conducted by Yu Shu and the author using the printer in Harish Bhaskaran's research group. The author developed the inks formulations with different compositions, and Yu Shu conducted the initial printing experiments to determine the

optimal formulation. All subsequent printing related to the percolation investigation was conducted by the author. All other experiments were performed by the author.

6.3 Results and discussion

Figure 6.1 illustrates the schematic diagram of fabricating MOF percolation networks via the electrohydrodynamic (EHD) jet printing technique. In this process, MOF precursor solutions were patterned onto Pt IDEs with a 5-μm gap by using a gold-coated glass nozzle. The EHD-MOF strips were developed in situ on the substrates through a baking step. By adjusting the ligand concentration in the ink formulation, sensors with varying growth of MOFs were achieved, enabling control over the formation of conductive pathways within the printed MOF structures.

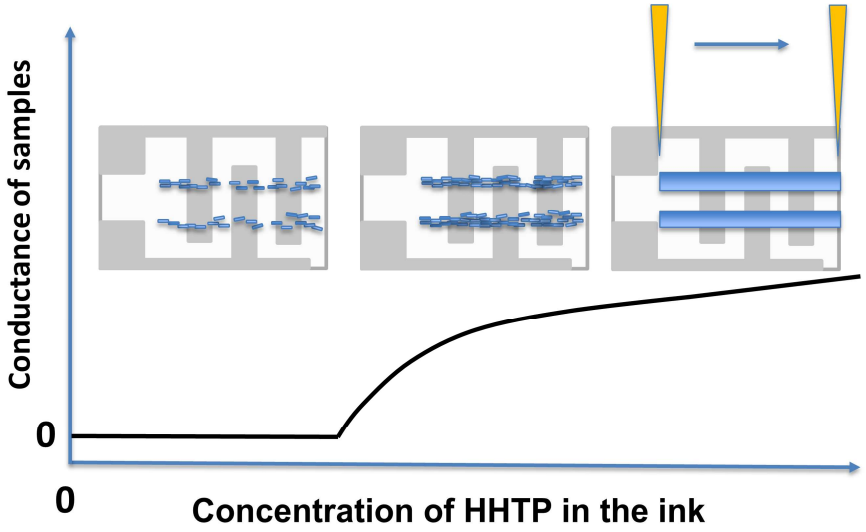

Figure 6.1. Schematic diagram of the preparation for EHD-$Cu_3(HHTP)_2$ percolation network on Pt IDEs.

6.3.1 Ink optimisation

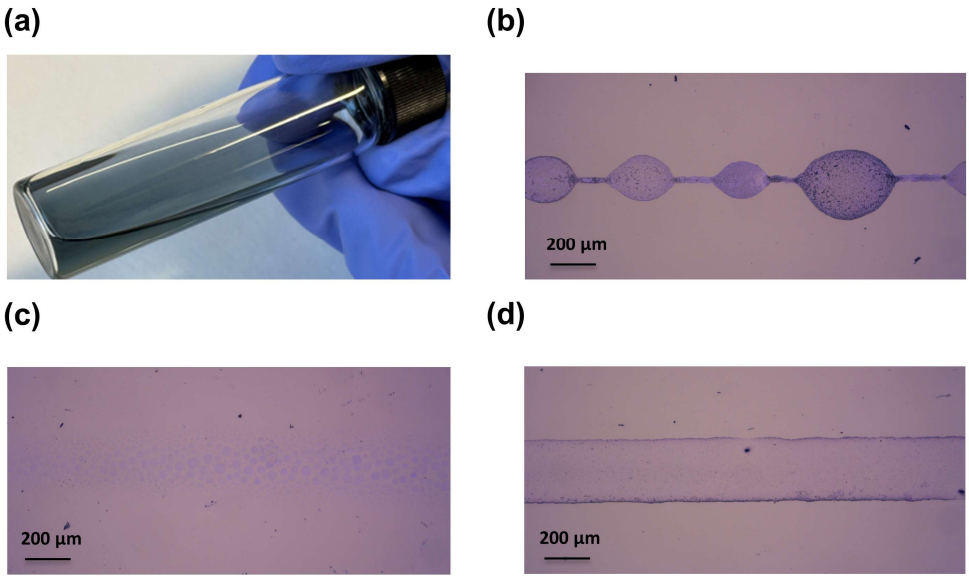

Figure 6.2. (a) A photograph of the precursor solution of $Cu_3(HHTP)_2$. $Cu_3(HHTP)_2$ strips obtained after baking the precursor strips formed by printing inks with different DMF and ethanol ratios: 6:1 (b), 3:4 (c), and 1:6 (d).

Figure 6.2a displays a photograph of a typical $Cu_3(HHTP)_2$ ink, comprising $Cu(NO_3)_2 \cdot 3H_2O$ (5 mM) and H_6HHTP (3.3 mM) dissolved in a solvent mixture of DMF, ethanol, and EG in a volume ratio of 1:6:8. The formulation was carefully optimised to balance key factors—conductivity, viscosity, and surface tension—essential for stable printing. The concentrations of metal salt and EG were fixed to ensure the conductivity and viscosity of the ink, respectively. DMF effectively dissolves both the metal salt and the ligand, ensuring a homogeneous solution. Ethanol was introduced to reduce the surface tension of the ink. The impact of solvent composition was assessed by EHD jet printing performed on ITO glass substrates. Figure 6.2 b-c show results of $Cu_3(HHTP)_2$ strips obtained by baking the precursor strips printed from inks with different DMF and ethanol ratios. As shown in Figure 6.2b, when the DMF-to-ethanol ratio is 6:1, the high surface tension leads to uneven strip formation, as droplets accumulate at the nozzle until gravity causes them to fall onto the substrate. Increasing the ethanol content reduces the surface tension, resulting in more uniform strip formation (Figure 6.2c). At a DMF-to-ethanol ratio of 1:6, as depicted in Figure 6.2d, the ink produces even and neat strips,

demonstrating the critical role of solvent composition in achieving optimal printing performance.

Figure 6.3 shows a representative photograph of a printed $Zn_3(HHTP)_2$ strip onto ITO, prepared using the same ink formulation as for $Cu_3(HHTP)_2$, with the Cu salt replaced by $Zn(NO_3)_2 \cdot 6H_2O$. In contrast to $Cu_3(HHTP)_2$, the resuting $Zn_3(HHTP)_2$ strip exhibits visible voids, which are indicative of weaker adhesion between $Zn_3(HHTP)_2$ and the substrate.

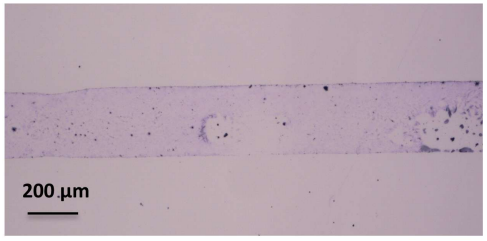

Figure 6.3. A photograph of a strip of $Zn_3(HHTP)_2$ after baking.

6.3.2 EHD jet-printed MOF patterns and characterisation

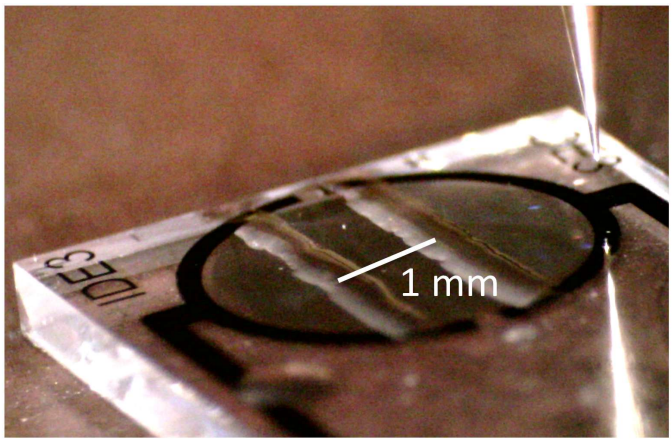

Figure 6.4. A representative photograph of precursor strips printed on a Pt IDE substrate.

Figure 6.4 shows a representative photograph of printed $Cu_3(HHTP)_2$ precursor solution patterns on a Pt IDE substrate, with the distance between the centres of the two strips separated by 1 mm via the XY linear stages (Physik Instrumente Ltd, resolution: 0.2 µm). The resolution of the printed precursor strips was determined to be between 250 and 350 µm. Strip widths were

measured from optical images using DinoCapture software (Dino-Lite). This resolution range was obtained by measuring two strips from each of three independently printed samples.

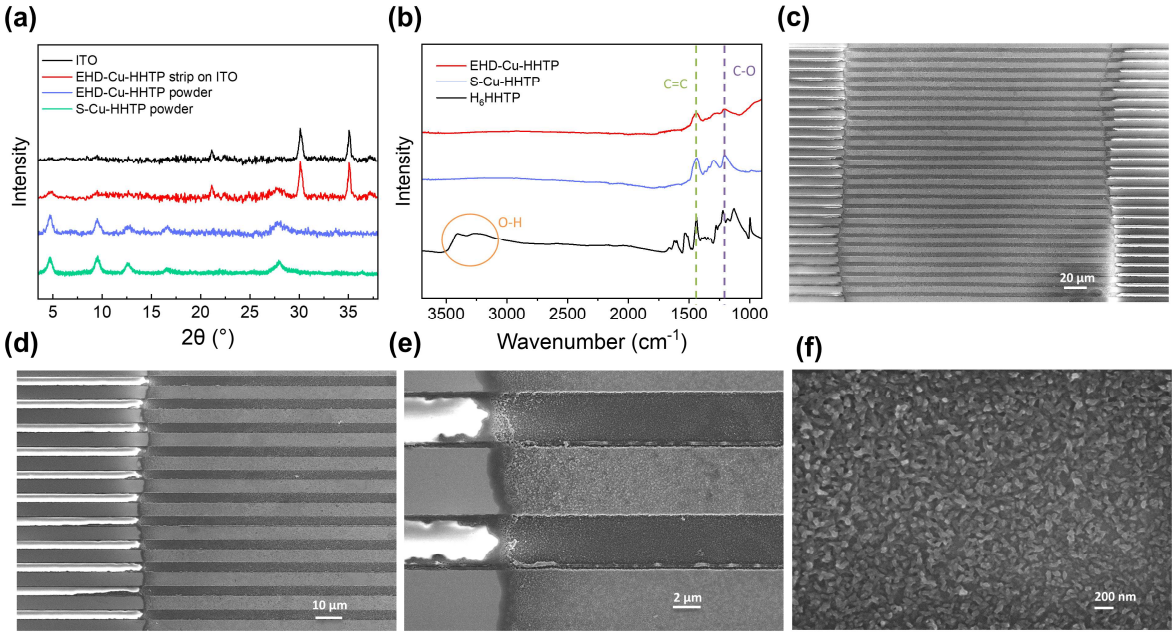

Figure 6.5. (a) XRD scans of ITO (black line), EHD-$Cu_3(HHTP)_2$ on ITO (red line), powder scraped from EHD printed regions (blue line), and powder prepared from solvothermal solution synthesis (green line). (b) FTIR spectra of EHD-Cu-HHTP pattern (red line), powder from solvothermal synthesis (blue line), and ligand (black line). (c-f) SEM images of a Cu-HHTP EHD pattern at different magnifications.

Figure 6.5a presents the XRD patterns of $Cu_3(HHTP)_2$ deposited on an ITO glass substrate. The EHD-printed $Cu_3(HHTP)_2$ strip displays discernible diffraction peaks at ~4.8° and ~27.8°, indicating the presence of a crystalline structure. To enable more detailed analysis, EHD-printed $Cu_3(HHTP)_2$ was gently scraped into a powder form on the ITO substrate, revealing additional peaks at ~9.5° and ~12.8°. These peaks are consistent with those observed in powder-form $Cu_3(HHTP)_2$ (S-Cu-HHTP) synthesised via solvothermal methods, as widely reported in previous studies.[73] An FTIR spectrum of the EHD-printed $Cu_3(HHTP)_2$ pattern on IDEs was obtained in situ (Figure 6.5b), which closely resembles that of S-$Cu_3(HHTP)_2$. Both spectra exhibit characteristic C=C stretching vibrations at 1435 cm^{-1} and C–O stretching vibrations at

1205 cm^{-1}. In contrast, the FTIR spectrum of the free ligand H_6HHTP displays two prominent hydroxyl (O–H) stretching bands at ~3407 cm^{-1} and ~3265 cm^{-1}. The disappearance of the O–H stretching bands suggest successful deprotonation of the hydroxyl groups and subsequent coordination of the phenolic oxygen atoms to the copper centres.

Figure 6.5c shows a SEM image of a representative EHD-Cu-HHTP strip on Pt IDEs. The boundary of the strip is distinguishable by the presence of uncovered gaps, which appear bright due to charging effects from the underlying glass substrate. At higher magnification (Figure 6.5d), the boundary becomes more clearly defined. Upon further magnification (Figure 6.5e), $Cu_3(HHTP)_2$ crystals are observed uniformly covering the gaps. As shown in Figure 6.5f, the $Cu_3(HHTP)_2$ consists of small crystals with a length of around 100 nm.

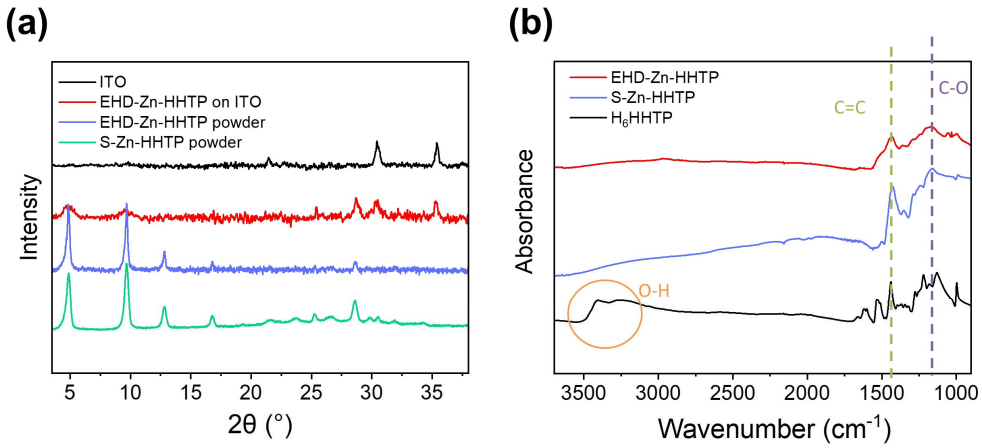

Figure 6.6. (a) XRD scans of ITO (black line), EHD-$Zn_3(HHTP)_2$ pattern (red line), powder scraped from EHD patterns (blue line), and powder prepared from solvothermal solution synthesis (green line). (b) FTIR spectra of EHD-$Zn_3(HHTP)_2$ pattern (red line), powder from solvothermal synthesis (blue line), and ligand (black line).

Figure 6.6 presents the XRD patterns and FTIR spectra of $Zn_3(HHTP)_2$-based samples, showing strong similarity to those of $Cu_3(HHTP)_2$-based counterparts. The XRD data shows EHD-$Zn_3(HHTP)_2$ pattern exhibits peaks at approximately 4.8°, 9.7°, 12.8°, and 28.7°, consistent with the crystalline structure of EHD-$Cu_3(HHTP)_2$ or S-$Zn_3(HHTP)_2$. The FTIR spectrum of

EHD-$Zn_3(HHTP)_2$ shows characteristic C=C and C–O stretching vibrations at 1435 cm^{-1} and 1160 cm^{-1}, respectively, mirroring those observed in EHD-$Cu_3(HHTP)_2$ or S-$Zn_3(HHTP)_2$. These spectroscopic similarities confirm the successful synthesis of EHD-$Zn_3(HHTP)_2$ with chemical features analogous to its copper-based analogue.

6.3.3 Electrical percolation

Due to the weak adhesion between EHD-$Zn_3(HHTP)_2$ and the substrate, the MOF layers were easily removed during solvent-based cleaning processes for residue removal. This instability led to significant variability in the conductance measurements, with values differing by up to four orders of magnitude when using the same ink formulation. Consequently, the electrical percolation behaviour of EHD-$Zn_3(HHTP)_2$ was not investigated.

The electrical percolation behaviour of EHD-$Cu_3(HHTP)_2$ on IDEs was controlled by diluting the concentration of H_6HHTP in the original ink formulation. For convenience, the resulting samples were labelled as P_x, where X represents the ligand concentration as a percentage of the original value, 3.3 mM. For example, an ink containing 0.33 mM of ligand is labelled as P_{10}. Figure 6.7 presents a plot of sample conductance versus the relative ligand percentage in an ink, along with a semi-logarithmic plot (in blue) to highlight the percolation threshold.

At low ligand concentrations, only a limited amount of $Cu_3(HHTP)_2$ formed on the IDEs, resulting in insulating behaviour. The conductance of P_{10} becomes measurable, indicating the onset of the percolation region. As the ligand concentration increases, the conductance rises sharply. A plateau in conductance is not observed, as the metal ion concentration was fixed at 5 mM, and the maximum ligand concentration was limited to 3.3 mM, maintaining the stoichiometric metal-to-ligand ratio of 3:2. Notably, P_{100} exhibits a high conductance of 1.07 ± 0.13 S. SEM imaging above also confirms that the gaps between IDEs were fully bridged at

this point, suggesting that this composition is near the upper limit of the percolation region. The conductance data of the devices are shown in Table 6.1.

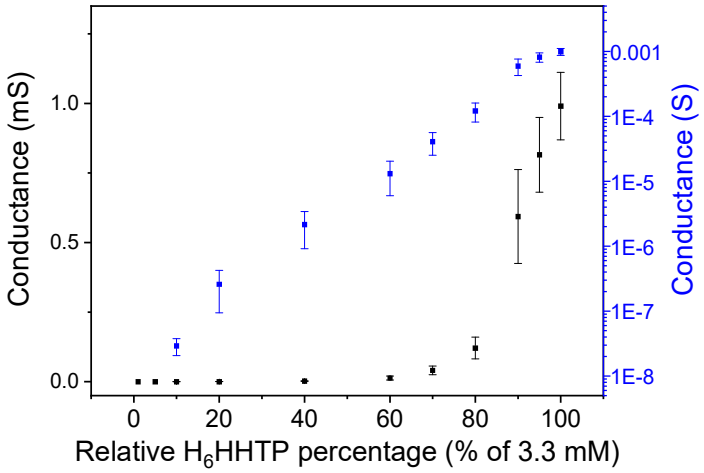

Figure 6.7. The plot of conductance across $Cu_3(HHTP)_2$ IDE samples vs relative HHTP percentage (in black) and its semilogarithmic plot (in blue). The relative percentage refers to the ligand concentration expressed as a percentage of 3.3 mM. The error bars are the standard deviation of the conductance values of three independent samples.

Table 6.1 The conductance data (unit: mS) of the devices. The conductance of each device was evaluated from three independently fabricated samples, with each data point corresponding to a separate device. The data were calculated by converting each resistance value to conductance (G = 1/R). Only samples with measurable conductance are presented.

Device	Data 1	Data 2	Data 3	Average	Standard Deviation
R_{10}	3.9×10^{-5}	2.3×10^{-5}	2.6×10^{-5}	2.9×10^{-5}	8.5×10^{-6}
R_{20}	1.7×10^{-4}	4.4×10^{-4}	2.2×10^{-4}	2.6×10^{-4}	1.6×10^{-4}
R_{40}	1.3×10^{-3}	3.6×10^{-3}	1.5×10^{-3}	2.2×10^{-3}	1.3×10^{-3}
R_{60}	2.1×10^{-2}	6.9×10^{-3}	1.2×10^{-2}	1.3×10^{-2}	7.2×10^{-3}
R_{70}	2.3×10^{-2}	4.6×10^{-2}	5.3×10^{-2}	4.1×10^{-2}	1.6×10^{-2}
R_{80}	1.6×10^{-1}	1.2×10^{-1}	8.1×10^{-2}	1.2×10^{-1}	4.0×10^{-2}
R_{90}	4.6×10^{-1}	7.8×10^{-1}	5.3×10^{-1}	5.9×10^{-1}	1.7×10^{-1}
R_{95}	8.0×10^{-1}	9.6×10^{-1}	6.9×10^{-1}	8.2×10^{-1}	1.3×10^{-1}
R_{100}	1.0×10^{-0}	8.7×10^{-1}	1.1×10^{-0}	9.9×10^{-1}	1.2×10^{-1}

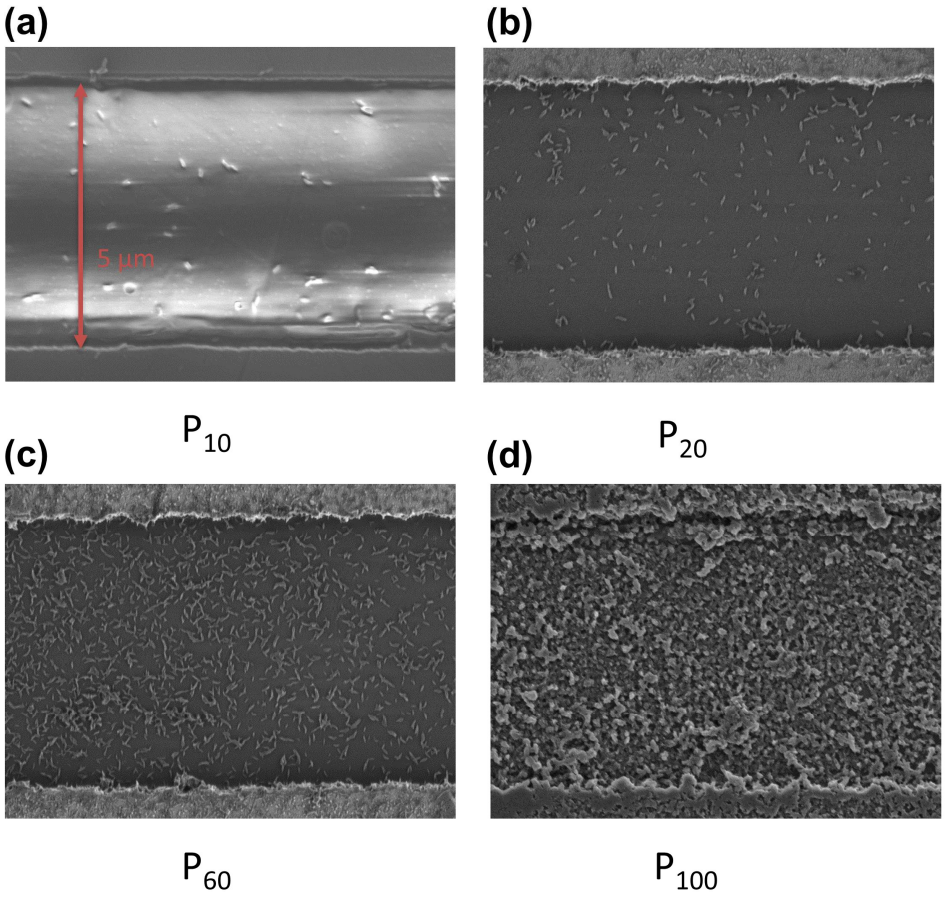

Figure 6.8. Typical SEM images of P_{10} (a), P_{20} (b), P_{60} (c), and P_{100} (d).

The different growth of $Cu_3(HHTP)_2$ on IDEs was further observed by SEM imaging. Figure 6.8 shows representative SEM images of the in-situ grown MOF crystals on a 5-µm glass substrate situated between two platinum electrode fingers, whereby the observed small particles correspond to the $Cu_3(HHTP)_2$ crystals. In Figure 6.8a, corresponding to the P_{10} sample with a low ligand concentration, only a sparse distribution of crystals is evident, indicating limited crystal growth. Significant contrast variations are observed due to charging effects associated with the insulating nature of the glass substrate. As the ligand concentration increases, as seen in the P_{20} sample (Figure 6.8b), a denser coverage of $Cu_3(HHTP)_2$ crystals was developed on the gap between electrodes. This increased coverage enhances electron pathways, thereby mitigating charging effects during SEM imaging. Further increases in ligand concentration result in near-complete (P_{60}) and complete (P_{100}) coverage of the electrode gaps (see Figure

6.8c and 6.8d, respectively), demonstrating a progressive enhancement in MOF film formation with higher ligand concentrations. SEM images and conductance measurements collectively confirm that percolation networks were successfully developed by controlling the ligand concentration of inks.

6.3.4 Gas sensing tests

The sensing performance of sensors based on EHD-percolation networks was evaluated among samples of P_{20}, P_{40}, P_{60}, P_{80}, and P_{100} with ammonia as a primary analyte. For further comparison, an additional sensor was fabricated via drop-casting onto IDE substrates using the P_{100} ink formulation. Each sample was placed in a home-built chamber under nitrogen flow for at least 45 min to ensure a stable baseline resistance. Subsequently, the sensors were exposed to NH_3 gas for 1 min, followed by a recovery period under N_2 flow for 15 min. Due to the suboptimal performance of the drop-cast sensor, its recovery period was limited to 2 min. The sensors were tested across a range of NH_3 concentrations, from 5 ppm down to 0.2 ppm. Each concentration level was tested in triplicate. The sensor response was calculated as $(R_t - R_0) / R_0$, where R_t represents the sample resistance after 1 min of exposure to ammonia, and R_0 denotes the initial resistance prior to exposure.

6.3.4.1 Drop-cast sensors

The sensing performance of the drop-cast sensor was initially evaluated as a control to benchmark against EHD printed sensors. SEM images (Figure 6.9a and 6.9b) reveal that the IDE gaps are fully covered by the drop-cast film, indicating continuous material deposition across the electrode fingers. Figure 6.9c presents the response-recovery behaviour of the drop-cast sensor upon exposure to ammonia. The sensor exhibits a low baseline resistance of approximately 68.7 Ω and shows reversible responses to ammonia exposure. However, despite the low resistance, noticeable baseline noise is present, and the sensor's response becomes

indistinct at ammonia concentrations as low as 0.2 ppm. These observations suggest that the drop-cast sensor has poor sensitivity and a high LOD.

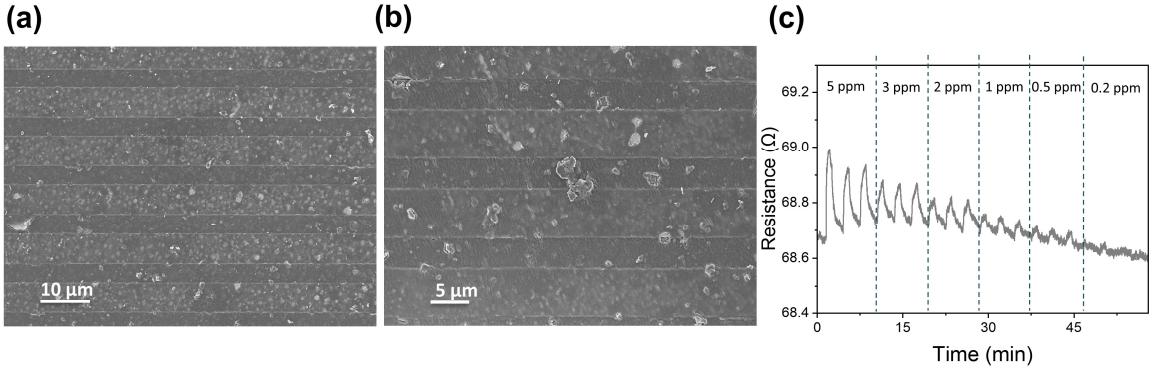

Figure 6.9. (a) and (b) SEM images of the drop-cast sensor on an IDE at different magnifications. (c) Response-recovery curve of the drop-cast sensor. Data shown were obtained after the initial activation full cycle.

6.3.4.2 EHD printed sensors

The sensing performance of each EHD printed sensor was then tested. Figure 6.10a shows the response-recovery plots of P_{20}, P_{40}, P_{60}, P_{80}, and P_{100}. All the sensors show reversible responses to ammonia across the tested concentrations, with responses decreasing accordingly as the ammonia concentration declines. P_{20} displays the highest resistance and also the most pronounced baseline noise.

Figure 6.10b presents the sensor responses plotted against analyte concentrations. The drop-cast film shows the lowest responses across all ammonia concentrations, with a weak response of 0.38% ± 0.06% to 5 ppm ammonia. In contrast, all EHD-printed sensors exhibit significantly stronger responses. P_{100} achieves a response of 2.11% ± 0.11% to 5 ppm ammonia, over five times greater than that of the drop-cast film. Notably, P_{80} yields an even higher response of 12.17 ± 1.5% under the same conditions. The responses were further improved when sensors were printed with inks of lower ligand concentration, with P_{20} displaying the highest sensitivity

among all samples, achieving responses of 17.16% ± 2.14% and 3.42% ± 0.50% at 5 ppm and 0.2 ppm ammonia, respectively.

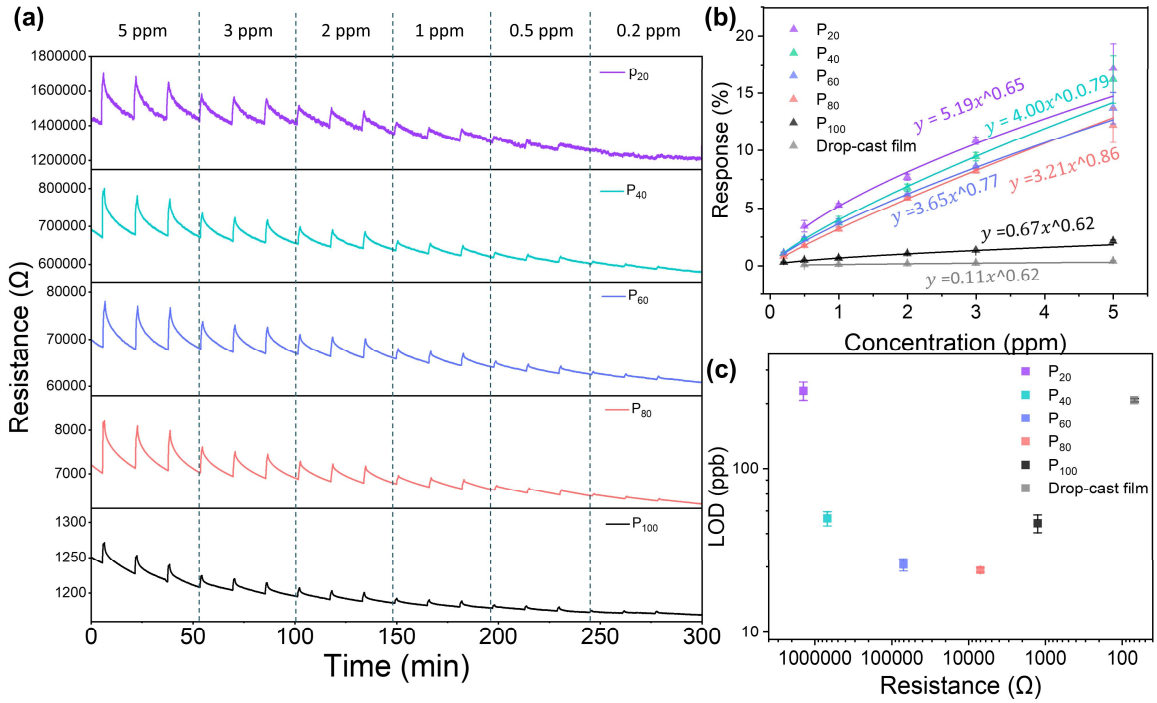

Figure 6.10. (a) Response-recovery plots of EHD printed sensors, including P_{20}, P_{40}, P_{60}, P_{80}, and P_{100}. (b) Plots of sensing responses ($(R_t - R_0) / R_0$) of each sensor versus different concentrations of ammonia. (c) Limits of detection of samples. Data shown were obtained after the initial activation full cycle.

Consistent with previous chapters, the fitting curves indicate that the sensing behaviour of all EHD-printed sensors aligns with the conductance model limited by the electron transport across the intergranular potential/Schottky barrier (Equation 6.1):

$$\Delta R / R_0 = A_g p_g^{\beta} \tag{6.1}$$

where p_g is the partial pressure, A_g is a prefactor, and β is the exponent factor. LODs of samples were then determined, calculated as three times the standard deviation of the baseline noise divided by the sensitivity evaluated at the lowest detected concentration. As shown in Figure 6.10c, P_{20} shows the highest LOD of 298.8 ± 38.1 ppb among all sensors, despite its highest

responses across all analyte concentrations. Such a high LOD is attributed to its higher baseline noise, which arises from its high resistance. In contrast, other EHD-printed sensors achieve significantly lower LODs compared to the drop-cast sensor (262.2 ± 6.4 ppb) or P_{20}, with P_{80} demonstrating the lowest LOD of 23.1 ± 0.7 ppb. The LOD_{SE} of P_{80} was evaluated to be 3.3 ± 0.1 ppb.

In summary, a comparison between P_{100} and the drop-cast sensor—two devices fabricated using identical ink formulation but different deposition techniques—demonstrates that the discrete patterns employed in P_{100} significantly enhance both sensitivity and LOD. This improvement, relative to the continuous film covering the whole substrate formed in the drop-cast sensor, is primarily attributed to the increased externally accessible surface area provided by the discrete patterning.

Furthermore, percolation theory has been effectively applied to further optimise the sensing performance of EHD-printed sensors. By reducing the ligand concentration in the ink, the electrical connectivity across electrode gaps diminishes, thereby amplifying the effect of the analyte on the circuit. This results in a substantial enhancement in sensor sensitivity. However, sensors engineered close to the percolation threshold, while exhibiting the highest sensitivity, also show elevated LODs due to increased baseline noise arising from higher resistance. As a result, the optimal sensing performance is achieved at a point beyond the threshold, identified as P_{80} in this project.

6.4 Conclusion and outlook

Discrete $Zn_3(HHTP)_2$ and $Cu_3(HHTP)_2$ patterns were successfully fabricated through the EHD jet printing technique. Percolation networks of EHD-printed $Cu_3(HHTP)_2$ were developed by controlling the ligand concentration in the ink. The resulting percolation behaviour was investigated through electrical conductance measurements and SEM imaging. The gas sensing

performance of the obtained EHD-printed percolation networks, including P_{20}, P_{40}, P_{60}, P_{80}, and P_{100}, was evaluated by the sensing tests to ammonia. A film sensor prepared by drop-casting was also included as a reference for comparison. All the EHD-printed sensors exhibit significantly higher sensitivity than the drop-cast sensor. Among these, P_{20}—fabricated near the percolation threshold—demonstrates the highest response. However, its elevated resistance resulted in increased baseline noise and the highest LOD among the samples. The optimal performance was observed in the P_{80} sensor, which achieved the lowest LOD of 23.1 ± 0.7 ppb and an excellent response of $12.18 \pm 1.51\%$ to 5 ppm ammonia.

This study explores and highlights the potential of EHD jet printing for fabricating c-MOF patterns and expands the methodology for constructing percolation-based sensor architectures. While EHD jet printing has been employed to generate percolation networks, several limitations call for critical consideration. Notably, although the percolation curve was derived from electrical conductance measurements, the variability in conductance among samples prepared under identical conditions is significantly greater than that observed with electrochemical synthesis. This discrepancy arises from fluctuations in printing parameters, including applied voltage and nozzle-to-substrate distance, which can vary a lot between different IDEs due to minor fabrication inconsistencies.

Furthermore, as precursor solutions are utilised to produce printable inks, the MOF is formed in situ during the printing process. While this approach effectively minimises contact resistance, it also introduces uncontrollable effects such as the coffee-ring phenomenon, which can negatively impact sensor performance. Additionally, ink formulation imposes strict constraints on conductivity, viscosity, and surface tension. In particular, the concentration of copper salt must be fixed to maintain optimal printability, thereby limiting the maximum achievable ligand

concentration and resulting in an incomplete percolation curve. These limitations currently hinder the applicability of EHD jet printing for real-world manufacturing.

Chapter 7

Percolation networks created by $Cu_3(HHTP)_2$/polystyrene composites for chemiresistive gas sensing

In previous chapters, the formation of percolation networks via deposition control strategies has been extensively explored. In this chapter, a different approach—based on a conductive–insulating composite strategy—is employed to achieve percolation networks. To achieve this, polystyrene (PS) nanoparticles were selected as the insulating matrix, and a solution-processable $Cu_3(HHTP)_2$-PVP was used as the conductive matrix. The chemical composition of $Cu_3(HHTP)_2$-PVP was confirmed through XRD and FTIR. By varying the composition of PS and MOF, samples with different resistance values and growth stages were obtained. The electrical percolation behaviour was confirmed through electrical conductance measurements. Finally, the sensing behaviours of obtained sensors were evaluated by ammonia sensing tests.

7.1 Introduction

Percolation networks can be achieved mainly through two approaches: deposition control and conductive-insulating composite strategies. The deposition control strategy, explored in previous chapters, has successfully introduced percolation theory into chemiresistive gas sensors based on c-MOFs, leading to significantly improved sensitivity. However, this approach is heavily dependent on electrochemical synthesis, which poses challenges in real-life manufacturing, such as complex experimental setups, limited scalability, and poor compatibility with a wide range of substrates. Although Chapter 6 introduced an alternative electrohydrodynamic (EHD) jet printing technique, this method also suffers from several

drawbacks. For example, the ink requirements constrain the concentration of copper salt, which in turn limits the upper bound of ligand concentration, resulting in incomplete percolation curves.

In comparison, the conductive–insulating composite strategy offers a more straightforward and mature approach. This method involves incorporating conductive fillers into an insulating matrix to formulate composite dispersions. By drop-casting these dispersions onto substrates with varying filler-to-matrix ratios, a series of sensors with different resistance values and growth stages can be produced. This enables the identification of the percolation threshold through systematic electrical characterisation.

Although this strategy has been extensively explored in the context of conductive polymers,[147, 154, 155] its application to c-MOFs remains largely unexplored. One key limitation lies in the intrinsic nature of c-MOFs. These materials are typically synthesised using ligands bearing multiple functional groups, such as –OH or $–NH_2$, which promote strong intermolecular interactions and lead to severe aggregation when dispersed in solvents.[231] As a result, it is often difficult to obtain a true solution or even a stable suspension. This aggregation results in a wide particle size distribution upon drop-casting, which introduces high contact resistance, reduced specific surface area, and substantial variability in electrical measurements among samples prepared under identical conditions.

To address this issue, polyvinylpyrrolidone (PVP) was introduced to synthesise solution-processable $Cu_3(HHTP)_2$ ($Cu_3(HHTP)_2$-PVP) via a surfactant-assisted solvothermal method. In contrast to $Cu_3(HHTP)_2$ synthesised through the conventional solvothermal method, the resulting material exhibited significantly reduced aggregation when dispersed in solvents and was uniformly dispersed to form a homogeneous dispersion. The successful preparation of $Cu_3(HHTP)_2$-PVP was confirmed through a series of characterisation techniques, including

XRD and FTIR. To establish a complete percolation curve, a $Cu_3(HHTP)_2$-PVP dispersion of varying concentrations were first drop-cast onto Pt IDE substrates. A clear percolation region with well-defined onset and endpoint concentrations was observed, with the endpoint confirmed at 1.0 mg/mL. Subsequently, polystyrene (PS) particles were employed as the insulating matrix to dilute the 1.0 mg/mL $Cu_3(HHTP)_2$-PVP dispersion. Since this concentration corresponds to the endpoint of the percolation region, increasing the PS content reduces the number of conductive pathways, enabling the formation of percolation networks via the composite approach. Finally, the sensing performance of the sensors fabricated from both pure $Cu_3(HHTP)_2$–PVP dispersions and PS-diluted composites was systematically evaluated through ammonia sensing tests.

7.2 Experimental section

7.2.1 Chemicals and substrates

Polyvinylpyrrolidone (PVP, Mw ≈ 40,000), 10 wt% aqueous suspension of polystyrene latex (PS, ~300 nm diameter), were obtained from Sigma-Aldrich. The 5-micron Pt interdigitated electrodes (IDEs) from MicruX Technologies and indium tin oxide (ITO) glass slide were employed as substrates.

7.2.2 Solution-processable $Cu_3(HHTP)_2$ synthesis

A solid mixture of HHTP (32.4 mg, 0.10 mmol) and PVP (200.0 mg) was dispersed in 10 mL DMF and 15 mL EtOH in a 75 mL round-bottom pressure vessel fitted with a PTFE bushing (Synthware). A solution of $Cu(NO_3)_2 \cdot 3H_2O$ (36.2 mg, 0.15 mmol) in 5 mL DI H_2O was added dropwise to the mixture in the pressure vessel at a rate of 4 μL s^{-1} controlled by a syringe pump (Ossila), under continuous stirring at 500 rpm. The resulting solutions in the capped pressure vessel were then heated at 85 °C under stirring at 500 rpm for 18 h, after which they were

centrifuged at 6000 rpm for 30 min using a centrifuge from Thermo Electron Corporation. The precipitate was washed twice through the ultrasonic re-dispersion in MeOH for 10 min, followed by centrifugation at 6000 rpm for 30 min. The process was repeated three times. Subsequently, the washed precipitates were dried under vacuum at room temperature in a Heraeus vacutherm oven overnight.

7.2.3 Sensor fabrication

The sensors were fabricated using a simple drop-casting method. The solution-processable $Cu_3(HHTP)_2$ was dispersed in a 1:1 (v/v) solvent mixture of deionised water and ethanol to prepare dispersions at various concentrations: 0.0005 mg/mL, 0.001 mg/mL, 0.005 mg/mL, 0.01 mg/mL, 0.05 mg/mL, 0.1 mg/mL, 0.5 mg/mL, 1 mg/mL, and 2 mg/mL. Due to the resolution limit of balance, all the suspensions were prepared by diluting a stock dispersion with a concentration of 2 mg/mL. Therefore, above concentrations were chosen as convenient sub-multiples of the stock concentration, allowing accurate dilution using simple integer volume ratios and minimising weighing and pipetting errors. For each concentration, a total volume of 100 µL was prepared. Prior to use, each dispersion was sonicated for 10 min to ensure homogeneity. Subsequently, a volume of 10 µL from each solution was drop-cast onto the substrates to produce the corresponding samples.

Subsequently, a 10 wt% aqueous suspension of PS was diluted to 1 mg/mL using the same 1:1 (v/v) mixture of deionised water and ethanol. Composite inks were then prepared by mixing the 1 mg/mL PS dispersion with the 1 mg/mL MOF dispersion in varying volumetric ratios: 99:1, 19:1, 9:1, 1:1, and 1:9. These ratios were chosen to preserve the same effective concentration of $Cu_3(HHTP)_2$ used for the pure MOF dispersions, enabling direct comparison between the composite and pure MOF samples. For each composite dispersion, a total volume of 100 µL

was prepared. A volume of 10 μL from each ink was drop-cast onto the substrates to produce the corresponding samples.

7.2.4 Gas sensing tests

In each test, the exposure time to NH_3 was 2 min, and exposure to nitrogen was 5 min for recovery before the next exposure. The sensors were exposed to a range of NH_3 concentrations, including 5, 3, 2, 1, 0.5, and 0.2 ppm, as a full sensing cycle. Each full sensing cycle was performed in triplicate.

7.2.5 Attribution statement

In this chapter, FTIR measurements were conducted by Jiahao Ye. All other experiments were carried out by the author.

7.3 Results and discussion

7.3.1 Materials characterisation

Polyvinylpyrrolidone (PVP) was introduced to synthesise solution-processable $Cu_3(HHTP)_2$ via a surfactant-assisted hydrothermal method, and the obtained sample was designated as $Cu_3(HHTP)_2$-PVP. The crystalline structure of the as-prepared powder was first characterised by powder XRD. For comparison, a control sample synthesised via a conventional hydrothermal method—widely reported in the literature—was also analysed.[4] As shown in Figure 7.1, $Cu_3(HHTP)_2$-PVP exhibits characteristic diffraction peaks at 4.7°, 9.5°, 12.5°, and 27.8°, corresponding to the (100), (200), (210), and (001) crystal planes, respectively. These peaks are consistent with those observed in the control $Cu_3(HHTP)_2$ sample. Notably, the (001) peak at 27.8° is significantly sharper in the $Cu_3(HHTP)_2$-PVP sample, suggesting a more well-ordered crystalline structure. Both $Cu_3(HHTP)_2$-PVP and control $Cu_3(HHTP)_2$ show small

peaks (marked as black squares) around the (001) peaks, indicating different c-axis stacking of Cu-HHTP exists in each sample.

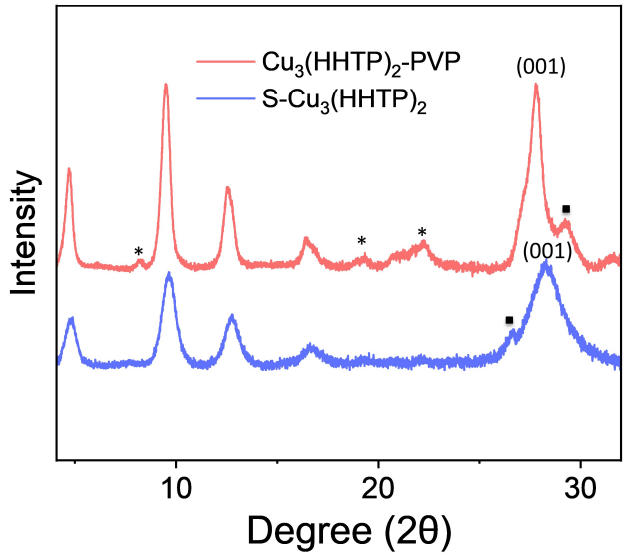

Figure 7.1. XRD patterns of $Cu_3(HHTP)_2$-PVP (in red) and $Cu_3(HHTP)_2$ (in blue). Several minor peaks (marked with *) were also observed. These peaks could not be unambiguously assigned and are therefore denoted as unidentified reflections. The peaks marked with black squares are attributed to different stacking modes along the c-axis of $Cu_3(HHTP)_2$.

$Cu_3(HHTP)_2$-PVP powder was further characterised by FTIR and compared with spectra of the ligand H_6HHTP, $Cu_3(HHTP)_2$ control, and pure PVP (see Figure 7.2). $Cu_3(HHTP)_2$-PVP exhibits characteristic C=C and C-O stretching vibrations at ~1429 and ~1197 cm^{-1}, respectively, aligning with the peaks observed in both ligand and $Cu_3(HHTP)_2$ control. The disappearance of the O-H vibration at 3367 and 3266 cm^{-1} further confirms the coordination between ligands and Cu centre. Compared to $Cu_3(HHTP)_2$, an additional weak peak at 1661 cm^{-1} was observed in the $Cu_3(HHTP)_2$-PVP spectrum, which likely originates from the C=O stretching vibration of a small amount of residual PVP remaining on the external surface of the MOF frameworks.[212, 213]

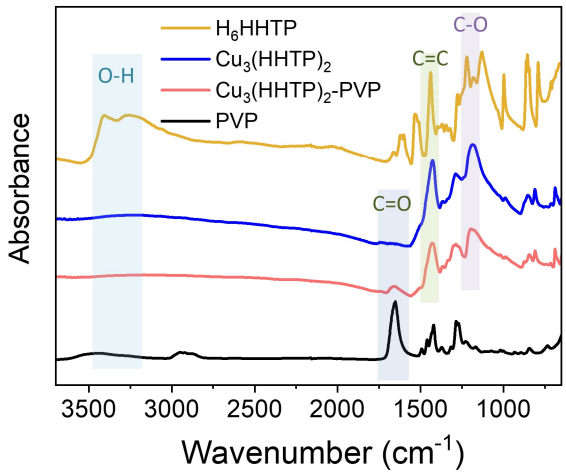

Figure 7.2. FTIR spectra of H_6HHTP (in yellow), $Cu_3(HHTP)_2$ (in blue), $Cu_3(HHTP)_2$-PVP (in red), and PVP (in black).

The $Cu_3(HHTP)_2$-PVP powder was subsequently dispersed in deionised water in a vial to evaluate its aqueous dispersibility. Figure 7.3 presents a photograph of the resulting 1 mg/mL dispersion of $Cu_3(HHTP)_2$-PVP. For comparison, an additional dispersion containing 1 mg/mL of $Cu_3(HHTP)_2$ with varying amounts of PVP, designated as $Cu_3(HHTP)_2$@5%PVP, $Cu_3(HHTP)_2$@10%PVP, and $Cu_3(HHTP)_2$@50%PVP, were also prepared. In this notation, $Cu_3(HHTP)_2$@x%PVP refers to the dispersion containing 1 mg/mL of $Cu_3(HHTP)_2$ and x% by mass of PVP relative to the MOF content. For example, $Cu_3(HHTP)_2$@10%PVP corresponds to a dispersion with 1 mg/mL $Cu_3(HHTP)_2$ and 0.1 mg/mL PVP. All the dispersions were obtained by sonification for 30 min.

$Cu_3(HHTP)_2$-PVP and $Cu_3(HHTP)_2$@x%PVP systems were prepared using fundamentally different approaches. In the $Cu_3(HHTP)_2$-PVP system, $Cu_3(HHTP)_2$ was synthesised in situ in the presence of PVP under prolonged heating (85 °C for 18 h) and stirring, which promotes more intimate contact and stronger interactions between PVP and the $Cu_3(HHTP)_2$ particles. In contrast, the $Cu_3(HHTP)_2$@x%PVP samples were prepared by post-synthetic mixing, involving simple stirring and sonication for 30 min. Under these milder conditions, the interaction between PVP and the MOF is expected to be weaker. The comparison presented here therefore

focuses on the dispersion behaviour of $Cu_3(HHTP)_2$ assisted by PVP under these two distinct preparation conditions.

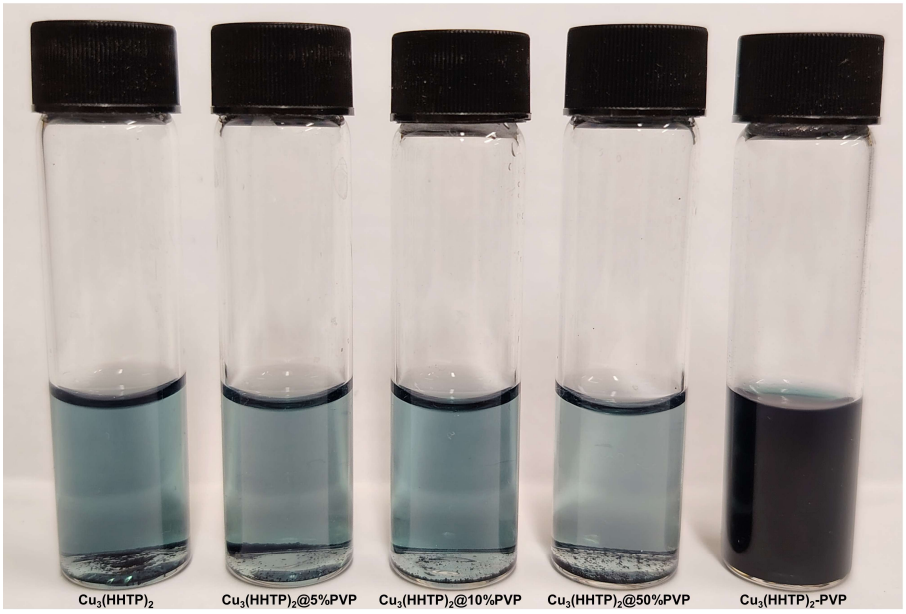

Figure 7.3. Photographs of $Cu_3(HHTP)_2$, $Cu_3(HHTP)_2$@5%PVP, $Cu_3(HHTP)_2$@10%PVP, $Cu_3(HHTP)_2$@50%PVP, and $Cu_3(HHTP)_2$-PVP aqueous dispersion.

$Cu_3(HHTP)_2$ dispersion shows a light blue colour, with a substantial amount of black powder visibly settled at the bottom of the vial. Notably, the $Cu_3(HHTP)_2$-PVP sample demonstrates significantly enhanced solubility, forming a homogeneous dark blue dispersion. For $Cu_3(HHTP)_2$@5%PVP, $Cu_3(HHTP)_2$@10%PVP, and $Cu_3(HHTP)_2$@50%PVP samples, the addition of varying amounts of PVP does not improve the solubility of $Cu_3(HHTP)_2$, whereby the black powder remains clearly observed at the bottom of the vials. This experiment extracts the role of PVP and demonstrates that simple physical mixing of $Cu_3(HHTP)_2$ with PVP, within the investigated concentration range, does not enhance its solubility. Therefore, it can be concluded that $Cu_3(HHTP)_2$-PVP has much greater solubility compared with $Cu_3(HHTP)_2$@x%PVP. Additionally, the markedly improved solubility of $Cu_3(HHTP)_2$-PVP arises from the stronger interaction between $Cu_3(HHTP)_2$ and PVP. The $Cu_3(HHTP)_2$-PVP

dispersion was subsequently stored at ambient conditions for one month, during which it remains stable and homogenous.

The $Cu_3(HHTP)_2$-PVP dispersion was drop-casted onto ITO glass substrate to visualise its crystal structures under SEM imaging. Figure 7.4a shows the rod-like morphology of $Cu_3(HHTP)_2$-PVP crystals, with a length ranging from ~100 to ~300 nm. Compared with conventional bulk $Cu_3(HHTP)_2$ prepared by the solvothermal synthesis (Figure 7.4b), the $Cu_3(HHTP)_2$-PVP system exhibits a more dispersed morphology, with reduced aggregation and suppressed bulk-like particle formation.

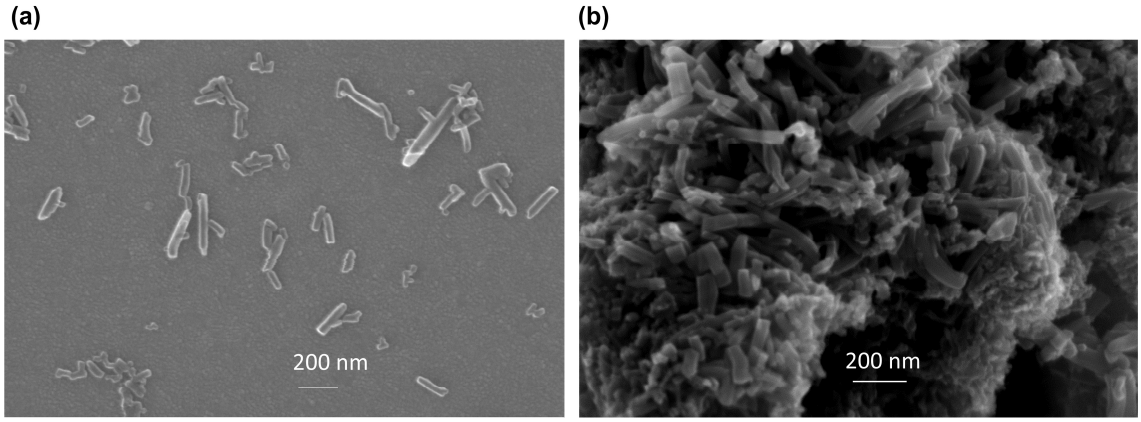

Figure 7.4. Characteristic SEM images of $Cu_3(HHTP)_2$-PVP crystals (a) and conventional bulk $Cu_3(HHTP)_2$ powder (b).

7.3.2 Electrical percolation of pure $Cu_3(HHTP)_2$-PVP devices

To study the electrical percolation behaviour of $Cu_3(HHTP)_2$-PVP, varying concentrations (0.0005, 0.001, 0.005, 0.01, 0.05, 0.1, 0.5, 1, and 2 mg/mL) of $Cu_3(HHTP)_2$-PVP suspension were obtained using a deionised-water/ethanol mixture (V:V = 1:1). Due to the resolution limit of balance, all the suspension was prepared by diluting a stock suspension with a concentration of 2 mg/mL. For convenience, the samples were designated as C_x, where x refers to their concentration. A volume of 10 μL from each suspension was pipetted and drop-cast onto the IDEs.

The electrical conductance of each sample was measured and is presented in Figure 7.5. A logarithmic scale was also used to more clearly illustrate the percolation region. At low concentrations, no measurable conductance is observed, indicating that the IDEs remained insulating up to 0.005 mg/mL. As the concentration increases, conductance of samples rises sharply. Beyond 1 mg/mL, the rate of increase in conductance begins to plateau. These results confirm that the percolation region lies between 0.005 mg/mL and 1 mg/mL. The conductance data of devices are shown in Table 7.1.

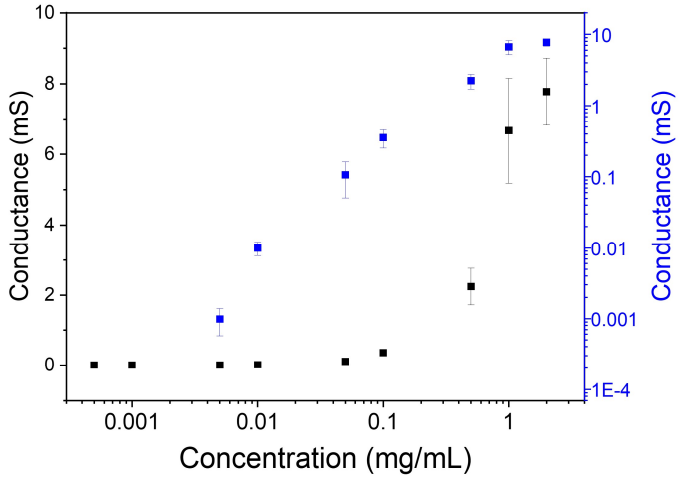

Figure 7.5. Plots of concentration on the x-axis (logarithmic scale) versus conductance of samples on the y-axis, shown on a linear scale in black and a logarithmic scale in blue.

Table 7.1 The conductance data (unit: mS) of the devices. The conductance of each device was evaluated from four independently fabricated samples, with each data point corresponding to a separate device. The data were calculated by converting each resistance value to conductance (G = 1/R). Only samples with measurable conductance are presented.

Device	Data 1	Data 2	Data 3	Data 4	Average	Standard Deviation
$C_{0.005}$	1.4×10^{-3}	9.4×10^{-4}	1.1×10^{-3}	4.4×10^{-4}	9.8×10^{-4}	4.1×10^{-4}
$C_{0.01}$	7.5×10^{-3}	1.0×10^{-2}	1.3×10^{-2}	9.7×10^{-3}	1.0×10^{-2}	2.1×10^{-3}
$C_{0.05}$	4.9×10^{-2}	7.8×10^{-2}	1.8×10^{-1}	1.2×10^{-1}	1.1×10^{-1}	5.6×10^{-2}
$C_{0.1}$	3.8×10^{-1}	3.9×10^{-1}	2.1×10^{-1}	4.4×10^{-1}	3.5×10^{-1}	1.0×10^{-2}
$C_{0.5}$	2.9×10^{0}	2.4×10^{0}	1.7×10^{0}	2.0×10^{0}	2.2×10^{0}	5.2×10^{-1}

Table 7.1 (Continued)

Device	Data 1	Data 2	Data 3	Data 4	Average	Standard Deviation
C_1	6.1×10^0	5.7×10^0	8.9×10^0	5.9×10^0	6.7×10^0	1.5×10^0
C_2	6.4×10^0	8.4×10^0	8.3×10^0	8.0×10^0	7.7×10^0	9.5×10^{-1}

7.3.3 Gas sensing tests for pure $Cu_3(HHTP)_2$-PVP devices

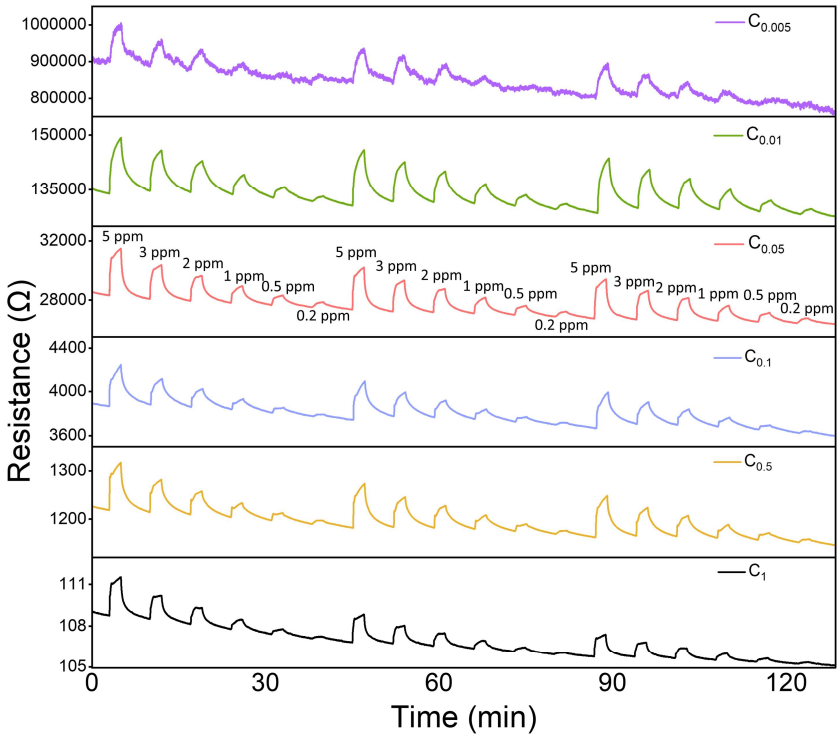

Figure 7.6. Response-recovery curves of sensors based on pure MOF. In each test cycle, the sensor was sequentially exposed to ammonia of 5, 3, 2 ,1 ,0.5, and 0.2 ppm.

The gas sensing performance of sensors operating in the percolation region ($C_{0.005}$, $C_{0.01}$, $C_{0.05}$, $C_{0.1}$, and $C_{0.5}$) and a sensor operating in the dense film region (C_1) was evaluated by ammonia sensing tests. In each sensing test, the sensors were exposed to NH_3 gas for 2 min, followed by a recovery period under N_2 flow for 5 min. The sensors were tested across a range of NH_3 concentrations, including 5, 3, 2, 1, 0.5, and 0.2 ppm, as a full sensing cycle. Each full sensing cycle was performed in triplicate to ensure reproducibility. The sensor response was defined as

($R_t - R_0$) / R_0, where R_t represents the sample resistance after 2 min of exposure to ammonia, and R_0 denotes the baseline resistance prior to exposure.

Figure 7.6 presents the sensing responses of sensors prepared from pure $Cu_3(HHTP)_2$-PVP. All the sensors exhibit an increase in resistance after exposure to ammonia, consistent with the p-type semiconducting nature of $Cu_3(HHTP)_2$. The response decreases with decreasing ammonia concentration, indicating a clear concentration-dependent behaviour. The $C_{0.005}$ sample shows a more pronounced noise level compared to the other sensors.

Figure 7.7a displays the response-concentration curve for each sensor. $C_{0.005}$ shows a response of 11.73% ± 0.48% to 5 ppm ammonia, comparable to that of $C_{0.01}$ (11.68% ± 0.11%). As the suspension concentration increases, the response to 5 ppm ammonia decreases accordingly, with 10.37% ± 0.32% for $C_{0.05}$, 8.64% ± 0.37% for $C_{0.1}$, 7.75% ± 0.27% for $C_{0.5}$, and 1.86% ± 0.32% for C_1. Similar trends were also observed for the responses under other concentrations. For example, the response to 0.2 ppm ammonia is 1.11% ± 0.06% for $C_{0.01,}$ while it drops significantly to 0.18% ± 0.05% for C_1.

Consistent with previous chapters, the sensing behaviour of each sensor aligns with the conductance model limited by the electron transport across the intergranular potential/Schottky barrier (Equation 7.1):

$$\Delta R / R_0 = A_g p_g^{\beta} \tag{7.1}$$

where p_g is the partial pressure, A_g is a prefactor, and β is the exponent factor. The calibration curves clearly reflect the decreasing trend as the $Cu_3(HHTP)_2$-PVP suspension concentration increases.

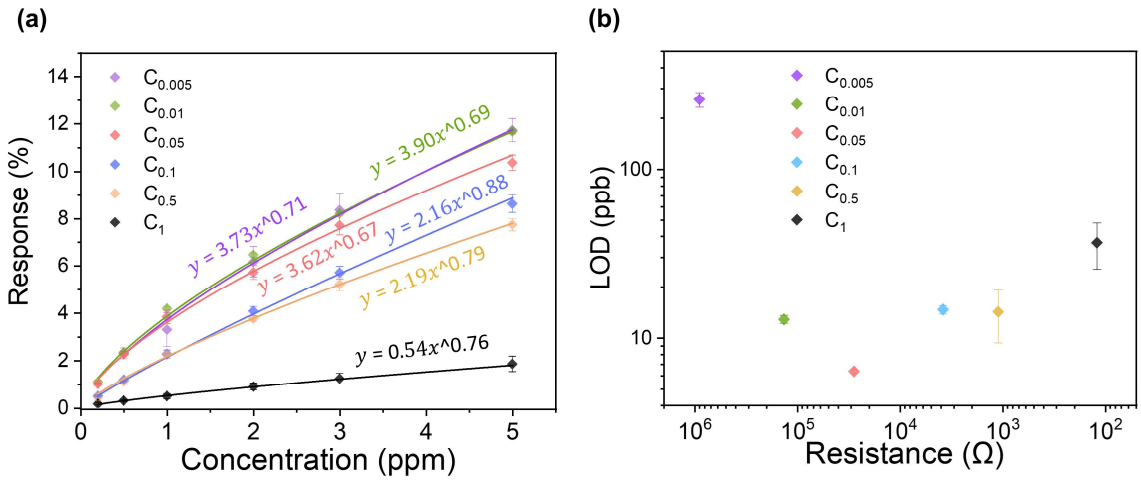

Figure 7.7. (a) Sensing response of each sensor as a function of ammonia concentration. (b) Limits of detection of samples.

The sensing performance of each sample was further investigated through the limits of detection (LODs), calculated as three times the standard deviation of the baseline noise divided by the sensitivity evaluated at the lowest detected concentration (200 ppb in this study). As shown in Figure 7.7b, the LOD shows a downward trend followed by an upward trend, with the lowest LOD observed for $C_{0.05}$ at 6.3 ± 0.1 ppb. The LOD_{SE} of $C_{0.05}$ was confirmed to be 0.70 ± 0.01 ppb.

In summary, the above results are consistent with percolation theory, where sensors engineered near the percolation threshold demonstrate enhanced responses. As the suspension concentration increases, additional redundant electrical pathways are formed, leading to a gradual decrease in sensor response. However, sensors operating near the percolation threshold also possess higher resistance, which is associated with increased noise levels. Consequently, these sensors with high responses also tend to exhibit higher noise. Among all samples, $C_{0.05}$ demonstrates the lowest LOD of 6.3 ± 0.1 ppb.

7.3.4 Gas sensing tests for PS-MOF composite devices

Achieving percolation networks using conductive-insulating composites has been explored in conductive polymers, whereby the introduction of the insulating matrix greatly improves their sensing performance. However, the application of this strategy to c-MOFs remains underexplored. Following our investigation of the electrical behaviour of pure $Cu_3(HHTP)_2$-PVP and the identification of 1 mg/mL as the end point of the percolation region, a 1 mg/mL suspension of polystyrene (PS) nanoparticles (~300 nm in diameter) was introduced into 1 mg/mL MOF suspension to prepare PS@$Cu_3(HHTP)_2$-PVP composite suspension. This suspension was formulated with varying PS:MOF volume ratios of 99:1, 19:1, 9:1, 1:1, and 1:9, where the PS:MOF ratios refer to the relative volumes of the two dispersions mixed. Each suspension was then drop-cast onto IDE substrates to fabricate sensors, which were designated as R_x, where x refers to the volume ratio of PS to MOF.

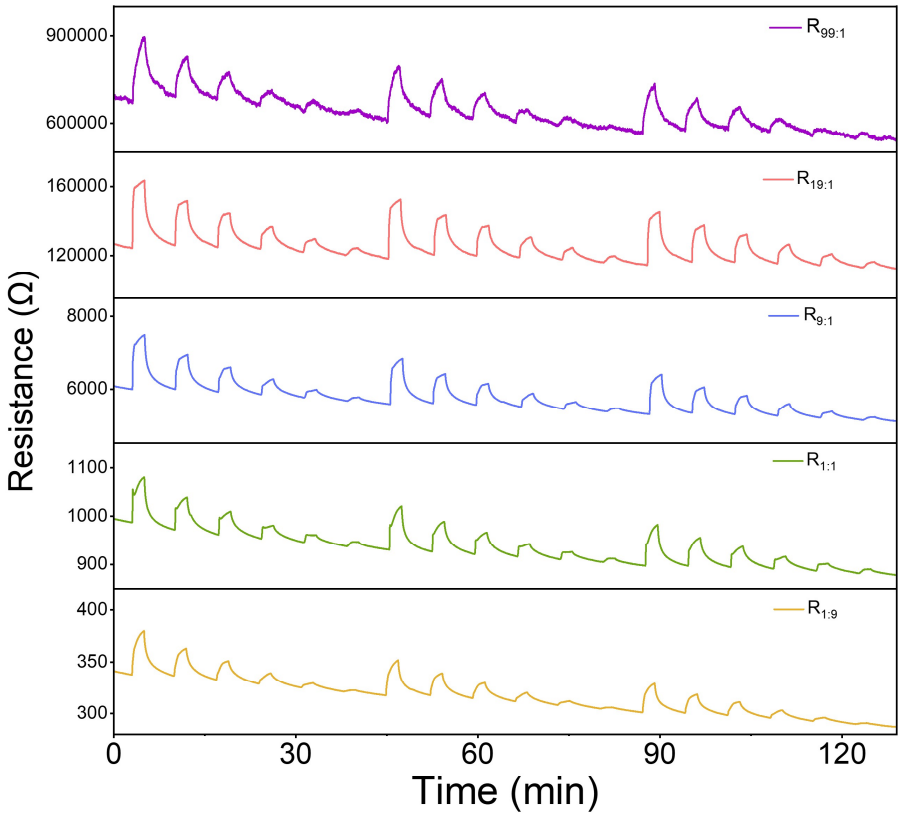

Figure 7.8. Response-recovery curves of sensors based on PS-MOF composites. In each test cycle, the sensor was sequentially exposed to ammonia of 5, 3, 2 ,1 ,0.5, and 0.2 ppm.

The obtained sensors were then subjected to ammonia sensing tests. Figure 7.8 presents the response-recovery curves of the sensors, including $R_{99:1}$, $R_{19:1}$, $R_{9:1}$, $R_{1:1}$, and $R_{1:9}$. As the content of MOF increases, the baseline resistance decreases, indicating the formation of additional electrical pathways. Consistent with the results observed for the C_x series, the resistance of each sample based on PS-MOF composites increases upon exposure to ammonia, and the response exhibits a concentration-dependent behaviour. Among all the samples, $R_{99:1}$ shows the highest resistance, accompanied by the most discernible noise level.

The responses of each sensor at different ammonia concentrations were calculated and displayed in Figure 7.9a. For comparison, the sensor $R_{0:1}$ (also referred to as sensor C_1), which operates in the dense film region, was also included. Consistent with C_x samples, the composite-based sensors exhibit a consistent trend, where increasing MOF content leads to reduced sensing responses. However, the responses of composite-based percolation networks are much higher, with the highest response of 31.36% ± 0.65% at 5 ppm ammonia for $R_{99:1}$. This value is nearly three times as high as the highest response observed in the pure MOF-based series, which is 11.73% ± 0.48% for $C_{0.005}$. $R_{19:1}$ and $R_{9:1}$ sensors also demonstrate excellent responses to 5 ppm ammonia of 29.11% ± 1.73% and 22.50% ± 1.52%, respectively. All the behaviour of sensors also satisfies the conductance model limited by the electron transport across the intergranular potential/Schottky barrier (Equation 7.1).

LODs of the sensors were calculated and are shown in Figure 7.9b. Even though $R_{99:1}$ exhibits the highest response among all tested sensors, it also shows the highest LOD at 69.8 ± 12.7 ppb, due to its pronounced noise level. $R_{19:1}$ demonstrates the lowest LOD of 4.4 ± 0.3 ppb, along with an excellent response comparable to that of $R_{99:1}$, which is the optimal sensor among the R_x series. The LOD_{SE} of $R_{19:1}$ was confirmed to be 0.63 ± 0.04 ppb.

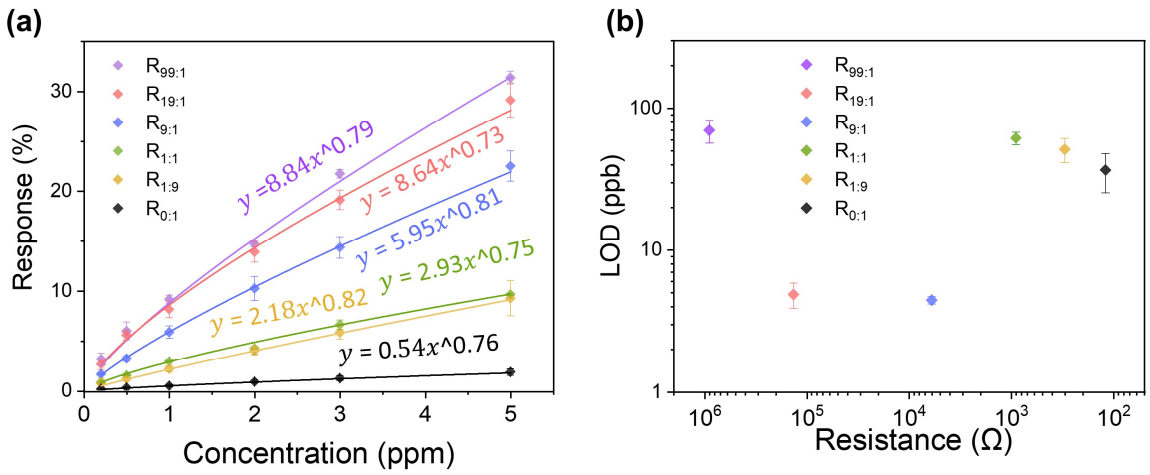

Figure 7.9. (a) Sensing response of each sensor as a function of ammonia concentration. (b) Limits of detection of samples.

A comparison was made between $R_{19:1}$ and $C_{0.05}$, the optimal sensors from the R_x and C_x series, respectively. It should be noted, since $R_{19:1}$ was obtained by diluting a 1 mg/mL suspension of $Cu_3(HHTP)_2$–PVP, both sensors were fabricated using the same MOF deposition concentration of 0.05 mg/mL. The key difference lies in the incorporation of PS particles in $R_{19:1}$, which leads to a significant enhancement in response—from 10.37% ± 0.32% for $C_{0.05}$ to 29.11% ± 1.73% for $R_{19:1}$.

To investigate the contribution of PS particles, SEM imaging was conducted to visualise the deposition of PS@$Cu_3(HHTP)_2$–PVP composite on IDE electrodes with 5 μm gaps. Figure 7.10 presents the typical SEM images of composite sensors with varying PS:MOF volume ratios. The central region corresponds to the 5 μm gap between electrodes, while the areas on either side represent the electrodes themselves. The rod-like structures are attributed to the MOF, and the spherical features are PS particles.

At a PS:MOF ratio of 0:1 (Figure 7.10a), a dense and relatively smooth film is observed, consistent with the expectation that sensors fabricated using 1 mg/mL suspension are engineered at the end point of the percolation region. As the PS content increases to 1:9 and 1:1

(Figure 7.10b and c), the film morphology becomes progressively rougher, with noticeable increases in surface porosity and heterogeneity. In the higher PS content samples (Figure 7.10d and e), including ratios of 9:1 and 19:1, distinct PS spheres are clearly visible, forming highly porous structures with larger voids. MOF begins to form a loose network surrounding PS clusters, and the overall morphology becomes significantly rougher. In Figure 7.10f, due to the very low MOF content at a PS:MOF ratio of 99:1, image quality is affected by charging effects, and only densely packed PS particles are visible within the electrode gap.

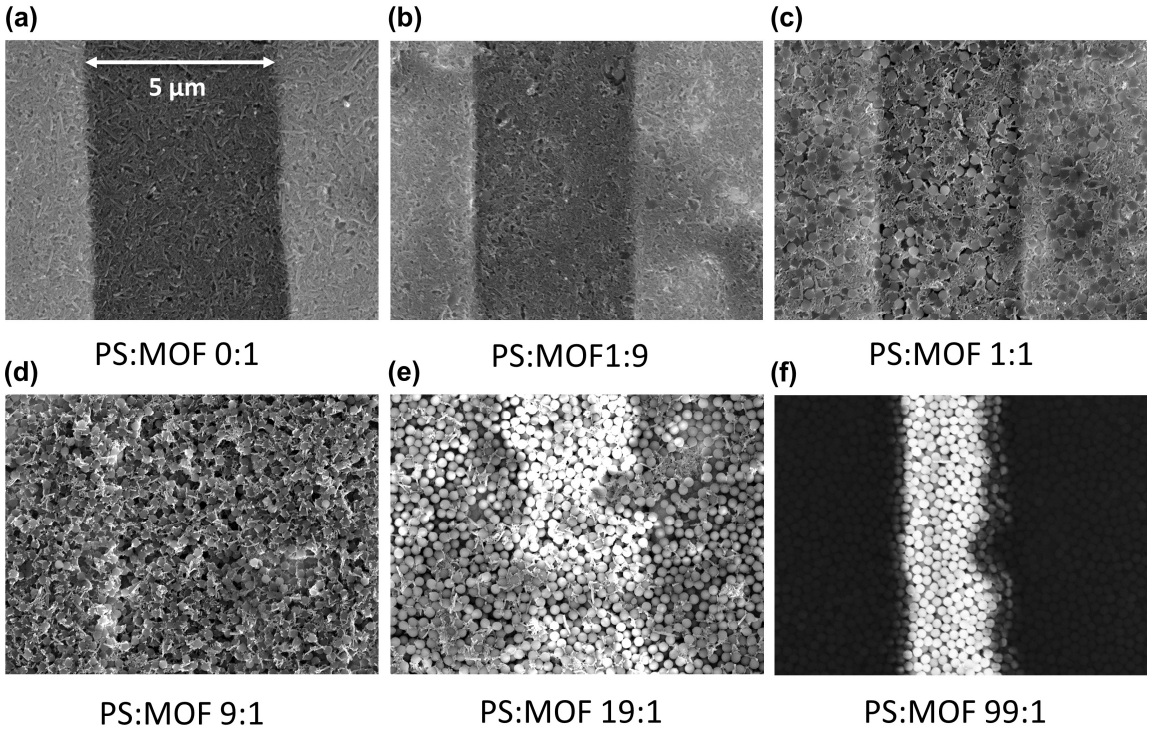

Figure 7.10. SEM images of samples based on PS@$Cu_3(HHTP)_2$–PVP composite, with different PS MOF volume ratio.

In conclusion, the introduction of PS particles significantly enhances the sensors' sensitivity by increasing the surface roughness and porosity of the morphologies of composites, which facilitates greater gas diffusion and interaction with the active MOF sites. As PS content increases, the formation of a more open and heterogeneous network allows for more accessible

pathways and higher surface area for gas molecules to adsorb and react, thereby amplifying the sensing response.

7.4 Conclusion and outlook

The strategy of achieving percolation networks through a conductive–insulating matrix has been successfully applied to c-MOFs. In this study, a solution-processable MOF, $Cu_3(HHTP)_2$–PVP, was prepared, and its successful synthesis has been proved by XRD and FTIR analysis. Its solubility was evaluated by dissolving it in water. The electrical percolation of sensors prepared by pure $Cu_3(HHTP)_2$–PVP was investigated via electrical conductance measurements, with 1 mg/mL identified to be the end point of the percolation region. The sensing performance of pure MOF-based sensors was evaluated by ammonia sensing tests. The sensors engineered near the percolation threshold demonstrate better sensitivity. $C_{0.05}$ was identified as the optimal sensor among pure MOF-based sensors with a good response to 5 ppm ammonia of 10.37% ± 0.32% and the lowest LOD of 6.3 ± 0.1 ppb.

Based on the above findings, 1 mg/mL of $Cu_3(HHTP)_2$–PVP suspension was subsequently used to achieve composite suspension with varying PS:MOF volume ratios. The sensing performance of resulting composite-based sensors was also evaluated. $R_{19:1}$ demonstrates a significantly improved response to 5 ppm ammonia of 29.11% ± 1.73%, while maintaining the lowest LOD of 4.4 ± 0.3 ppb among composite-based sensors. SEM imaging was conducted to investigate the contribution of PS. It is confirmed that the introduction of PS leads to a more porous and rougher surface morphology, accounting for the enhanced sensitivity. The introduction of PS and formation of percolation networks collectively render $R_{19:1}$ the optimal sensor among all tested devices in this study.

In this study, achieving percolation networks through a combination of spherical PS particles and rod-like c-MOF has been systematically investigated. Looking ahead, more investigation

on the different matrices or shapes of MOFs should be included. For example, the combination of spherical or plate-like c-MOF with rod-like insulating matrix is intriguing.

Chapter 8

Summary and outlook

8.1 Summary

This thesis demonstrates the application of percolation theory in highly sensitive, room-temperature chemiresistive gas sensors based on c-MOFs, through diverse fabrication strategies, including electrochemical deposition, electrohydrodynamic (EHD) jet printing, and conductive–insulating composites.

Chapter 4 introduces the development of $Cu_3(HHTP)_2$ percolation sensors fabricated by cathodic electrochemical deposition. The formation of $Cu_3(HHTP)_2$ was proved by SEM, XRD, XPS, FTIR, and Raman. Systematic control of growth time revealed a percolation region, identified by electrical measurements and SEM. The sensors working within this region exhibit markedly improved performance than a thin-film device and a powder drop-cast control. The optimal sensor T_{60} delivers a response of 17.06% ± 0.45% at 5 ppm NH_3 and a theoretical LOD of 0.6 ± 0.1 ppb, with good repeatability and selectivity.

Building on these findings, Chapter 5 combines PS-templating with anodic electrochemical deposition to create porous and hollow percolation architectures that significantly boost gas diffusion and specific surface area of sensors. Running deposition at different durations enables the identification of the percolation region, as confirmed by electrical measurements and SEM. The $Cu_3(HHTP)_2$ porous structures, achieved by the removal of the PS template, were characterised through XRD, FTIR, Raman, XPS, SEM, and AFM. In addition, an advanced technique nano-FTIR was employed to compare porous and non-porous $Cu_3(HHTP)_2$. The templated percolation sensors outperform a templated thin-film device, the non-templated

percolation devices from Chapter 4, and the powder drop-cast control. The optimal sensor TT_{120} demonstrates an exceptional response of 68.15% ± 4.58% at 5 ppm NH_3 and a theoretical LOD of 0.52 ± 0.03 ppb among the lowest reported for c-MOF chemiresistors.

Chapter 6 explores EHD jet printing as an alternative approach to developing percolation networks. By tailoring the ethanol/DMF/EG composition of the ink, discrete $Cu_3(HHTP)_2$/$Zn_3(HHTP)_2$ patterns were fabricated and verified by XRD and FTIR. $Cu_3(HHTP)_2$ percolation networks were developed by lowering ligand concentration in the ink, as identified by electrical measurements and SEM. The optimal sensor P_{80} shows a response of 12.18% ± 1.51% at 5 ppm NH_3 with a theoretical LOD of 23.1 ± 0.7 ppb.

Chapter 7 investigates a conductive-insulating composite strategy to achieve percolation networks, with a solution-processable $Cu_3(HHTP)_2$-PVP as the conductive filler and PS nanoparticles as the insulating matrix. The composition and solubility of $Cu_3(HHTP)_2$-PVP were investigated by XRD, FTIR, and solubility tests. The percolation behaviour of pure MOF was first investigated, with the optimal sensor $C_{0.05}$ showing a response of 10.37% ± 0.32% at 5 ppm ammonia and a theoretical LOD of 6.3 ± 0.1 ppb. MOF-PS composite percolation sensors were then developed. The optimal composite percolation sensor $R_{19:1}$ delivers much improved performance with a response of 29.11% ± 1.73% at 5 ppm with a theoretical LOD of 4.4 ± 0.3 ppb, compared to $C_{0.05}$. SEM images reveal rougher, more porous composite morphologies after PS is introduced, which explains the improved sensing performance.

Overall, this thesis demonstrates that electrical percolation can be deliberately engineered in c-MOFs and used as a practical design rule for c-MOF chemiresistive gas sensors. Devices operated in the percolation region exhibit significantly improved ammonia detection—large responses and low LODs—relative to dense film and powder drop-cast controls. Particularly, TT_{120}, the optimal sensor developed in Chapter 5, achieves a response of 68.15% ± 4.58% at 5

ppm NH_3 and a theoretical LOD of 0.52 ± 0.03 ppb, among the best reported for c-MOF chemiresistors. In short, translating percolation-network concepts to c-MOFs broadens the methodological toolbox for c-MOF sensor development and provides a simple, effective strategy to substantially amplify chemiresistive transduction.

8.2 Future outlook

Looking ahead, several priorities emerge.

8.2.1 Methodologies and fabrication control

$Cu_3(HHTP)_2$ percolation networks have been systematically developed by electrochemical deposition under mild conditions, providing a reliable strategy to obtain c-MOF percolation sensors. However, electrochemical growth can restrict the accessible MOF chemistries because different metal–ligand systems demand distinct redox windows, electrolytes, and complexation conditions.

EHD jet printing has also been demonstrated, but the largest challenge is the wide device-to-device resistance spread, arising from the printing parameter drift due to small substrate-to-substrate fabrication differences. The conductive–insulating composite strategy is straightforward and effective, yet the random microstructure makes it difficult to track morphology–performance changes and implement targeted modifications.

To broaden the toolbox and improve reproducibility, additional scalable methods—e.g., vapor-induced conversion, MOF-CVD/interfacial growth, and advanced printing (e.g., spray, inkjet, and slot-die) with environmental/process control—should be introduced.

8.2.2 From labs to real-world applications

To translate these findings into deployable sensors, the following directions are proposed.

8.2.2.1 Application fit and integration

C-MOF percolation sensors can deliver large responses and sub-ppb-level LODs far below typical occupational NH_3 thresholds (NIOSH Recommended Exposure Limit: 25 ppm). This points to low-level monitoring applications such as healthcare/breath analysis, where exhaled ammonia in healthy subjects often lies in the sub-ppm range and can be used as a marker for disease. To enable such use cases, sensors can be integrated onto flexible substrates (e.g., textiles), and low-power readout electronics can be co-designed for wearable deployments.

8.2.2.2 Comprehensive performance assessment and stability

This thesis investigates an initial step toward applying c-MOF percolation sensors in chemiresistive sensing, where evaluation has primarily focused on key figures of merit such as responses and LODs. Going forward, a systematic assessment of selectivity, reproducibility, repeatability, long-term stability, response time, and recovery time is needed. Stability under moisture/thermal/chemical conditions should also be evaluated.

8.2.2.3 Data and artificial intelligence

It would be interesting and promising to introduce machine-learning analysis to distinguish analytes from subtle differences in response amplitude/kinetics/frequency-domain features, and to perform drift and environmental compensation. Multi-sensor arrays can be deployed to provide richer fingerprints for robust classification and quantitation.

Bringing these strands together, this thesis has shown how marrying percolation theory with c-MOFs can translate materials' promise into device performance. By combining systematic control of $Cu_3(HHTP)_2$ growth on interdigitated electrodes with microstructural and interfacial

engineering, percolation sensors that deliver strong responses with low LODs were fabricated. Conceptually, the work clarifies how proximity to the percolation threshold contributes to transduction in c-MOF networks; practically, it provides processing guidelines for building less-connected MOF layers on devices. I therefore anticipate that these findings will contribute to the rational design and eventual deployment of c-MOF-based percolation gas sensors—first as lab-scale prototypes and ultimately as manufacturable, real-world products.

References

1. O. M. Yaghi, M. O'Keeffe, N. W. Ockwig, et al., Reticular synthesis and the design of new materials. *Nature* **2003,** *423*, 705.
2. M. Ko, L. Mendecki, K. A. Mirica, Conductive two-dimensional metal-organic frameworks as multifunctional materials. *Chemical Communications* **2018,** *54*, 7873.
3. J. Liu, G. Xing, L. Chen, 2D conjugated metal–organic frameworks: Defined synthesis and tailor-made functions. *Accounts of Chemical Research* **2024,** *57*, 1032.
4. C. Park, J. W. Baek, E. Shin, et al., Two-dimensional electrically conductive metal–organic frameworks as chemiresistive sensors. *ACS Nanoscience Au* **2023,** *3*, 353.
5. C. Wu, P. Geng, G. Zhang, et al., Synthesis of conductive MOFs and their electrochemical application. *Small* **2024,** *20*, e2308264.
6. S. Takaishi, M. Hosoda, T. Kajiwara, et al., Electroconductive porous coordination polymer $Cu[Cu(pdt)_2]$ composed of donor and acceptor building units. *Inorganic chemistry* **2009,** *48*, 9048.
7. L. S. Xie, G. Skorupskii, M. Dinca, Electrically conductive metal–organic frameworks. *Chemical Reviews* **2020,** *120*, 8536.
8. R. Saha, K. Gupta, C. J. Gómez García, Strategies to improve electrical conductivity in metal–organic frameworks: A comparative study. *Crystal Growth & Design* **2024,** *24*, 2235.
9. M. Hmadeh, Z. Lu, Z. Liu, et al., New porous crystals of extended metal-catecholates. *Chemistry of Materials* **2012,** *24*, 3511.
10. Z. Jin, J. Yan, X. Huang, et al., Solution-processed transparent coordination polymer electrode for photovoltaic solar cells. *Nano Energy* **2017,** *40*, 376.
11. X. Huang, S. Zhang, L. Liu, et al., Superconductivity in a copper(ii)-based coordination polymer with perfect kagome structure. *Angewandte Chemie International Edition* **2018,** *57*, 146.
12. T. Kambe, R. Sakamoto, K. Hoshiko, et al., Pi-conjugated nickel bis(dithiolene) complex nanosheet. *Journal of the American Chemical Society* **2013,** *135*, 2462.
13. T. Kambe, R. Sakamoto, T. Kusamoto, et al., Redox control and high conductivity of nickel bis(dithiolene) complex pi-nanosheet: a potential organic two-dimensional topological insulator. *Journal of the American Chemical Society* **2014,** *136*, 14357.
14. J. H. Dou, L. Sun, Y. Ge, et al., Signature of metallic behavior in the metal-organic frameworks M_3(hexaiminobenzene)$_2$ (M = Ni, Cu). *Journal of the American Chemical Society* **2017,** *139*, 13608.
15. J. Park, A. C. Hinckley, Z. Huang, et al., Synthetic routes for a 2D semiconductive copper hexahydroxybenzene metal–organic framework. *Journal of the American Chemical Society* **2018,** *140*, 14533.
16. H. Nagatomi, N. Yanai, T. Yamada, et al., Synthesis and electric properties of a two-dimensional metal-organic framework based on phthalocyanine. *Chemistry–A European Journal* **2018,** *24*, 1806.
17. Z. Meng, A. Aykanat, K. A. Mirica, Welding metallophthalocyanines into bimetallic molecular meshes for ultrasensitive, low-power chemiresistive detection of gases. *Journal of the American Chemical Society* **2019,** *141*, 2046.
18. H. Jia, Y. Yao, J. Zhao, et al., A novel two-dimensional nickel phthalocyanine-based metal–organic framework for highly efficient water oxidation catalysis. *Journal of Materials Chemistry A* **2018,** *6*, 1188.

19. M. Wang, H. Shi, P. Zhang, et al., Phthalocyanine-based 2D conjugated metal-organic framework nanosheets for high-performance micro-supercapacitors. *Advanced Functional Materials* **2020,** *30*, 2002664.
20. R. Dong, Z. Zhang, D. C. Tranca, et al., A coronene-based semiconducting two-dimensional metal-organic framework with ferromagnetic behavior. *Nature Communications* **2018,** *9*, 2637.
21. M. Jeon, M. Kim, J.-S. Lee, et al., Computational prediction of stacking mode in conductive two-dimensional metal–organic frameworks: An exploration of chemical and electrical property changes. *ACS Sensors* **2023,** *8*, 3068.
22. Y. Liu, S. Li, L. Dai, et al., The synthesis of hexaazatrinaphthylene-based 2D conjugated copper metal-organic framework for highly selective and stable electroreduction of CO_2 to methane. *Angewandte Chemie International Edition* **2021,** *133*, 16545.
23. M. Yang, Y. Zhang, R. Zhu, et al., Two-dimensional conjugated metal–organic frameworks with a ring-in-ring topology and high electrical conductance. *Angewandte Chemie International Edition* **2024,** *63*, e202405333.
24. Y.-Y. Liu, H.-L. Zhu, Z.-H. Zhao, et al., Insight into the effect of the d-orbital energy of copper ions in metal–organic frameworks on the selectivity of electroreduction of CO_2 to CH_4. *Acs Catalysis* **2022,** *12*, 2749.
25. N. L. Rosi, J. Kim, M. Eddaoudi, et al., Rod packings and metal−organic frameworks constructed from rod-shaped secondary building units. *Journal of the American Chemical Society* **2005,** *127*, 1504.
26. L. Sun, C. H. Hendon, S. S. Park, et al., Is iron unique in promoting electrical conductivity in MOFs? *Chemical Science* **2017,** *8*, 4450.
27. L. Sun, C. H. Hendon, M. A. Minier, et al., Million-Fold Electrical Conductivity Enhancement in Fe_2(DEBDC) versus Mn_2(DEBDC) (E = S, O). *Journal of the American Chemical Society* **2015,** *137*, 6164.
28. F. Gándara, F. J. Uribe-Romo, D. K. Britt, et al., Porous, conductive metal-triazolates and their structural elucidation by the charge-flipping method. *Chemistry–A European Journal* **2012,** *18*, 10595.
29. J. G. Park, M. L. Aubrey, J. Oktawiec, et al., Charge delocalization and bulk electronic conductivity in the mixed-valence metal-organic framework Fe(1,2,3-triazolate)$_2$(BF_4)$_x$. *Journal of the American Chemical Society* **2018,** *140*, 8526.
30. P. Li, B. Wang, Recent development and application of conductive MOFs. *Israel Journal of Chemistry* **2018,** *58*, 1010.
31. F. Wudl, G. Smith, E. Hufnagel, Bis-1, 3-dithiolium chloride: an unusually stable organic radical cation. *Journal of the Chemical Society D: Chemical Communications* **1970**, 1453.
32. S. S. Park, E. R. Hontz, L. Sun, et al., Cation-dependent intrinsic electrical conductivity in isostructural tetrathiafulvalene-based microporous metal–organic frameworks. *Journal of the American Chemical Society* **2015,** *137*, 1774.
33. J. Castells-Gil, S. Mañas-Valero, I. J. Vitórica-Yrezábal, et al., Electronic, structural and functional versatility in tetrathiafulvalene-lanthanide metal–organic frameworks. *Chemistry–A European Journal* **2019,** *25*, 12636.
34. D. Chen, H. Xing, Z. Su, et al., Electrical conductivity and electroluminescence of a new anthracene-based metal-organic framework with pi-conjugated zigzag chains. *Chemical Communications* **2016,** *52*, 2019.
35. G. Haider, M. Usman, T. P. Chen, et al., Electrically driven white light emission from intrinsic metal-organic framework. *ACS Nano* **2016,** *10*, 8366.
36. L. Qu, H. Iguchi, S. Takaishi, et al., Porous molecular conductor: Electrochemical fabrication of through-space conduction pathways among linear coordination polymers. *Journal of the American Chemical Society* **2019,** *141*, 6802.

37. M. Patra, S. K. Dubey, B. Mondal, et al., Design of π-conjugated flexible semiconductive 2D MOF and MOF derived CuO nano-spheres for solvent free C-X (S, O) hetero-coupling catalysis with enhanced conductivity. *Nano-Structures & Nano-Objects* **2021,** *26*, 100756.
38. S. Lin, P. M. Usov, A. J. Morris, The role of redox hopping in metal–organic framework electrocatalysis. *Chemical Communications* **2018,** *54*, 6965.
39. F. Afshariazar, A. Morsali, Mixed-valence metal–organic frameworks: concepts, opportunities, and prospects. *Chemical Society Reviews* **2025,** *54*, 1318.
40. L. S. Xie, L. Sun, R. Wan, et al., Tunable mixed-valence doping toward record electrical conductivity in a three-dimensional metal–organic framework. *Journal of the American Chemical Society* **2018,** *140*, 7411.
41. J. A. DeGayner, I.-R. Jeon, L. Sun, et al., 2D conductive iron-quinoid magnets ordering up to T_c= 105 K via heterogenous redox chemistry. *Journal of the American Chemical Society* **2017,** *139*, 4175.
42. Y. Wang, X. Liu, X. Li, et al., Direct radiation detection by a semiconductive metal–organic framework. *Journal of the American Chemical Society* **2019,** *141*, 8030.
43. L. E. Darago, M. L. Aubrey, C. J. Yu, et al., Electronic conductivity, ferrimagnetic ordering, and reductive insertion mediated by organic mixed-valence in a ferric semiquinoid metal–organic framework. *Journal of the American Chemical Society* **2015,** *137*, 15703.
44. A. A. Talin, A. Centrone, A. C. Ford, et al., Tunable electrical conductivity in metal-organic framework thin-film devices. *Science* **2014,** *343*, 66.
45. M. N. Gueye, A. Carella, J. Faure-Vincent, et al., Progress in understanding structure and transport properties of PEDOT-based materials: A critical review. *Progress in Materials Science* **2020,** *108*, 100616.
46. B. Wessling, Dispersion as the link between basic research and commercial applications of conductive polymers (polyaniline). *Synthetic Metals* **1998,** *93*, 143.
47. S. Raman, A. Ravi Sankar, Intrinsically conducting polymers in flexible and stretchable resistive strain sensors: a review. *Journal of Materials Science* **2022,** *57*, 13152.
48. B. Le Ouay, M. Boudot, T. Kitao, et al., Nanostructuration of PEDOT in porous coordination polymers for tunable porosity and conductivity. *Journal of the American Chemical Society* **2016,** *138*, 10088.
49. J. Liu, X. Song, T. Zhang, et al., 2D conductive metal–organic frameworks: an emerging platform for electrochemical energy storage. *Angewandte Chemie International Edition* **2021,** *133*, 5672.
50. T. A. Le, N. D. Hai, T. T. N. Tran, et al., Electrically conductive metal–organic framework-based electrocatalysts: from synthesis strategies to catalytic applications. *Chemical Communications* **2025,** *61*, 13543.
51. D. Sheberla, J. C. Bachman, J. S. Elias, et al., Conductive MOF electrodes for stable supercapacitors with high areal capacitance. *Nature Materials* **2017,** *16*, 220.
52. D. Feng, T. Lei, M. R. Lukatskaya, et al., Robust and conductive two-dimensional metal−organic frameworks with exceptionally high volumetric and areal capacitance. *Nature Energy* **2018,** *3*, 30.
53. Y.-F. Wang, S.-Y. Yang, Y. Yue, et al., Conductive copper-based metal-organic framework nanowire arrays grown on graphene fibers for flexible all-solid-state supercapacitors. *Journal of Alloys and Compounds* **2020,** *835*, 155238.
54. S. Zhou, X. Kong, B. Zheng, et al., Cellulose nanofiber@ conductive metal–organic frameworks for high-performance flexible supercapacitors. *ACS Nano* **2019,** *13*, 9578.
55. R. Hou, M. Miao, Q. Wang, et al., Integrated conductive hybrid architecture of metal–organic framework nanowire array on polypyrrole membrane for all-solid-state flexible supercapacitors. *Advanced Energy Materials* **2020,** *10*, 1901892.

56. L. Shao, Q. Wang, Z. Ma, et al., A high-capacitance flexible solid-state supercapacitor based on polyaniline and metal-organic framework (UiO-66) composites. *Journal of Power Sources* **2018,** *379*, 350.
57. K. Wada, K. Sakaushi, S. Sasaki, et al., Multielectron-transfer-based rechargeable energy storage of two-dimensional coordination frameworks with non-innocent ligands. *Angewandte Chemie International Edition* **2018,** *57*, 8886.
58. L. Guo, J. Sun, W. Zhang, et al., Bottom-up fabrication of 1D Cu-based conductive metal–organic framework nanowires as a high-rate anode towards efficient lithium storage. *ChemSusChem* **2019,** *12*, 5051.
59. J. Yan, Y. Cui, M. Xie, et al., Immobilizing redox-active tricycloquinazoline into a 2D conductive metal–organic framework for lithium storage. *Angewandte Chemie International Edition* **2021,** *60*, 24467.
60. M. E. Ziebel, C. A. Gaggioli, A. B. Turkiewicz, et al., Effects of covalency on anionic redox chemistry in semiquinoid-based metal–organic frameworks. *Journal of the American Chemical Society* **2020,** *142*, 2653.
61. R. Dong, M. Pfeffermann, H. Liang, et al., Large-area, free-standing, two-dimensional supramolecular polymer single-layer sheets for highly efficient electrocatalytic hydrogen evolution. *Angewandte Chemie International Edition* **2015,** *54*, 12058.
62. A. J. Clough, J. W. Yoo, M. H. Mecklenburg, et al., Two-dimensional metal–organic surfaces for efficient hydrogen evolution from water. *Journal of the American Chemical Society* **2015,** *137*, 118.
63. X. Huang, H. Yao, Y. Cui, et al., Conductive copper benzenehexathiol coordination polymer as a hydrogen evolution catalyst. *ACS Applied Materials & Interfaces* **2017,** *9*, 40752.
64. C. A. Downes, A. J. Clough, K. Chen, et al., Evaluation of the H_2 evolving activity of benzenehexathiolate coordination frameworks and the effect of film thickness on H_2 production. *ACS Applied Materials & Interfaces* **2018,** *10*, 1719.
65. J. Duan, S. Chen, C. Zhao, Ultrathin metal-organic framework array for efficient electrocatalytic water splitting. *Nature Communications* **2017,** *8*, 15341.
66. E. M. Miner, T. Fukushima, D. Sheberla, et al., Electrochemical oxygen reduction catalysed by Ni3 (hexaiminotriphenylene) 2. *Nature Communications* **2016,** *7*, 10942.
67. H. Yoon, S. Lee, S. Oh, et al., Synthesis of bimetallic conductive 2D metal–organic framework (CoxNiy-CAT) and its mass production: enhanced electrochemical oxygen reduction activity. *Small* **2019,** *15*, 1805232.
68. J. D. Yi, D. H. Si, R. Xie, et al., Conductive two-dimensional phthalocyanine-based metal–organic framework nanosheets for efficient electroreduction of CO_2. *Angewandte Chemie International Edition* **2021,** *133*, 17245.
69. Z. Meng, J. Luo, W. Li, et al., Hierarchical tuning of the performance of electrochemical carbon dioxide reduction using conductive two-dimensional metallophthalocyanine based metal–organic frameworks. *Journal of the American Chemical Society* **2020,** *142*, 21656.
70. H. Zhong, M. Ghorbani-Asl, K. H. Ly, et al., Synergistic electroreduction of carbon dioxide to carbon monoxide on bimetallic layered conjugated metal-organic frameworks. *Nature Communications* **2020,** *11*, 1409.
71. J. Yang, J. Zhou, Z. Lv, et al., A real-time monitoring system of industry carbon monoxide based on wireless sensor networks. *Sensors* **2015,** *15*, 29535.
72. X. Peng, X. Wu, M. Zhang, et al., Metal–organic framework coated devices for gas sensing. *ACS Sensors* **2023,** *8*, 2471.
73. M. G. Campbell, D. Sheberla, S. F. Liu, et al., Cu_3(hexaiminotriphenylene)$_2$: an electrically conductive 2D metal–organic framework for chemiresistive sensing. *Angewandte Chemie International Edition* **2015,** *54*, 4349.

74. M. S. Yao, X. J. Lv, Z. H. Fu, et al., Layer-by-layer assembled conductive metal–organic framework nanofilms for room-temperature chemiresistive sensing. *Angewandte Chemie International Edition* **2017,** *56*, 16510.
75. G. Wu, J. Huang, Y. Zang, et al., Porous field-effect transistors based on a semiconductive metal–organic framework. *Journal of the American Chemical Society* **2017,** *139*, 1360.
76. N. Ingle, P. Sayyad, G. Bodkhe, et al., ChemFET sensor: Nanorods of nickel-substituted metal–organic framework for detection of SO_2. *Applied Physics A* **2020,** *126*, 723.
77. N. Contreras-Pereda, S. Pané, J. Puigmartí-Luis, et al., Conductive properties of triphenylene MOFs and COFs. *Coordination Chemistry Reviews* **2022,** *460*, 214459.
78. B. Hoppe, K. D. J. Hindricks, D. P. Warwas, et al., Graphene-like metal–organic frameworks: morphology control, optimization of thin film electrical conductivity and fast sensing applications. *CrystEngComm* **2018,** *20*, 6458.
79. M. G. Campbell, S. F. Liu, T. M. Swager, et al., Chemiresistive sensor arrays from conductive 2D metal–organic frameworks. *Journal of the American Chemical Society* **2015,** *137*, 13780.
80. T. Chen, J.-H. Dou, L. Yang, et al., Continuous electrical conductivity variation in M_3 (hexaiminotriphenylene)$_2$ (M= Co, Ni, Cu) MOF alloys. *Journal of the American Chemical Society* **2020,** *142*, 12367.
81. A. C. Hinckley, J. Park, J. Gomes, et al., Air-stability and carrier type in conductive M_3 (hexaaminobenzene)$_2$,(M= Co, Ni, Cu). *Journal of the American Chemical Society* **2020,** *142*, 11123.
82. R. W. Day, D. K. Bediako, M. Rezaee, et al., Single crystals of electrically conductive two-dimensional metal–organic frameworks: Structural and electrical transport properties. *ACS Central Science* **2019,** *5*, 1959.
83. Z.-Z. Ma, Q.-H. Li, Z. Wang, et al., Electrically regulating nonlinear optical limiting of metal-organic framework film. *Nature Communications* **2022,** *13*, 6347.
84. J. W. Gittins, C. J. Balhatchet, S. M. Fairclough, et al., Enhancing the energy storage performances of metal-organic frameworks by controlling microstructure. *Chemical Science* **2022,** *13*, 9210.
85. T. Ohata, A. Nomoto, T. Watanabe, et al., Air/liquid interfacial formation process of conductive metal–organic framework nanosheets. *Journal of Colloid and Interface Science* **2023,** *651*, 769.
86. K. Yuan, T. Song, X. Zhu, et al., Construction of large-area ultrathin conductive metal–organic framework films through vapor-induced conversion. *Small* **2019,** *15*, 1804845.
87. V. Rubio-Giménez, M. Galbiati, J. Castells-Gil, et al., Bottom-up fabrication of semiconductive metal–organic framework ultrathin films. *Advanced Materials* **2018,** *30*, 1704291.
88. Y. Liu, Y. Wei, M. Liu, et al., Electrochemical synthesis of large area two-dimensional metal–organic framework films on copper anodes. *Angewandte Chemie International Edition* **2021,** *60*, 2887.
89. M. Song, J. Jia, P. Li, et al., Ligand-oxidation-based anodic synthesis of oriented films of conductive m-catecholate metal–organic frameworks with controllable thickness. *Journal of the American Chemical Society* **2023,** *145*, 25570.
90. P. Li, X. Shi, Y. Wu, et al., Cathodic synthesis of a Cu-catecholate metal–organic framework. *CrystEngComm* **2021,** *23*, 1828.
91. M. A. Franco, P. P. Conti, R. S. Andre, et al., A review on chemiresistive ZnO gas sensors. *Sensors and Actuators Reports* **2022,** *4*, 100100.
92. S. M. Kanan, O. M. El-Kadri, I. A. Abu-Yousef, et al., Semiconducting metal oxide based sensors for selective gas pollutant detection. *Sensors* **2009,** *9*, 8158.

93. H.-J. Kim, J.-H. Lee, Highly sensitive and selective gas sensors using p-type oxide semiconductors: Overview. *Sensors and Actuators B: Chemical* **2014,** *192*, 607.
94. Q. Li, W. Zeng, Y. Li, Metal oxide gas sensors for detecting NO_2 in industrial exhaust gas: Recent developments. *Sensors and Actuators B: Chemical* **2022,** *359*, 131579.
95. Y. C. Wong, B. C. Ang, A. Haseeb, et al., Conducting polymers as chemiresistive gas sensing materials: A review. *Journal of the Electrochemical Society* **2020,** *167*, 037503.
96. P. Recum, T. Hirsch, Graphene-based chemiresistive gas sensors. *Nanoscale Advances* **2024,** *6*, 11.
97. R. Tang, Y. Shi, Z. Hou, et al., Carbon nanotube-based chemiresistive sensors. *Sensors* **2017,** *17*, 882.
98. N. Joshi, T. Hayasaka, Y. Liu, et al., A review on chemiresistive room temperature gas sensors based on metal oxide nanostructures, graphene and 2D transition metal dichalcogenides. *Microchimica Acta* **2018,** *185*, 1.
99. M. Ko, L. Mendecki, K. A. Mirica, Conductive two-dimensional metal–organic frameworks as multifunctional materials. *Chemical Communications* **2018,** *54*, 7873.
100. E.-X. Chen, H. Yang, J. Zhang, Zeolitic imidazolate framework as formaldehyde gas sensor. *Inorganic chemistry* **2014,** *53*, 5411.
101. H. Wei, H. Zhang, B. Song, et al., Metal–organic framework (MOF) derivatives as promising chemiresistive gas sensing materials: A Review. *International Journal of Environmental Research and Public Health* **2023,** *20*, 4388.
102. M. S. Yao, W. X. Tang, G. E. Wang, et al., MOF thin film-coated metal oxide nanowire array: significantly improved chemiresistor sensor performance. *Advanced Materials* **2016,** *28*, 5229.
103. W.-T. Koo, S. Qiao, A. F. Ogata, et al., Accelerating palladium nanowire H_2 sensors using engineered nanofiltration. *ACS Nano* **2017,** *11*, 9276.
104. G. Benedetto, K. A. Mirica, Conductive framework materials for chemiresistive detection and differentiation of toxic gases. *Accounts of Chemical Research* **2024,** *57*, 2775.
105. N. Goel, K. Kunal, A. Kushwaha, et al., Metal oxide semiconductors for gas sensing. *Engineering Reports* **2023,** *5*, e12604.
106. T. Soga, Chapter 1 - Fundamentals of solar cell. In nanostructured materials for solar energy conversion, Soga, T., Ed. Elsevier: Amsterdam, **2006**; pp 3.
107. A. G. González, M. Á. Herrador, A practical guide to analytical method validation, including measurement uncertainty and accuracy profiles. *TrAC Trends in Analytical Chemistry* **2007,** *26*, 227.
108. L. A. Currie, Nomenclature in evaluation of analytical methods including detection and quantification capabilities (IUPAC Recommendations 1995). *Pure and Applied Chemistry* **1995,** *67*, 1699.
109. G. L. Long, J. D. Winefordner, Limit of detection. A closer look at the IUPAC definition. *Analytical Chemistry* **1983,** *55*, 712A.
110. M. K. Smith, K. E. Jensen, P. A. Pivak, et al., Direct self-assembly of conductive nanorods of metal–organic frameworks into chemiresistive devices on shrinkable polymer films. *Chemistry of Materials* **2016,** *28*, 5264.
111. M. Ko, A. Aykanat, M. K. Smith, et al., Drawing sensors with ball-milled blends of metal-organic frameworks and graphite. *Sensors* **2017,** *17*, 2192.
112. M. S. Yao, J. W. Xiu, Q. Q. Huang, et al., Van der waals heterostructured MOF-on-MOF thin films: Cascading functionality to realize advanced chemiresistive sensing. *Angewandte Chemie* **2019,** *131*, 15057.
113. M. S. Yao, J. J. Zheng, A. Q. Wu, et al., A dual-ligand porous coordination polymer chemiresistor with modulated conductivity and porosity. *Angewandte Chemie International Edition* **2020,** *59*, 172.

114. A.-Q. Wu, W.-Q. Wang, H.-B. Zhan, et al., Layer-by-layer assembled dual-ligand conductive MOF nano-films with modulated chemiresistive sensitivity and selectivity. *Nano Research* **2021,** *14*, 438.
115. Y. Lin, W. H. Li, Y. Wen, et al., Layer-by-layer growth of preferred-oriented MOF thin film on nanowire array for high-performance chemiresistive sensing. *Angewandte Chemie International Edition* **2021,** *60*, 25758.
116. R. Zheng, Z. H. Fu, W. H. Deng, et al., The growth mechanism of a conductive MOF thin film in spray-based layer-by-layer liquid phase epitaxy. *Angewandte Chemie International Edition* **2022,** *61*, e202212797.
117. H. Zhang, Z. Yan, Y. Ying, et al., In situ generation of cuprous oxide in metal-organic framework for significantly enhanced room-temperature ammonia sensing: Synergy enabling excellent sensitivity and selectivity. *Journal of Environmental Chemical Engineering* **2024,** *12*, 114391.
118. C. Huang, X. Shang, X. Zhou, et al., Hierarchical conductive metal-organic framework films enabling efficient interfacial mass transfer. *Nature Communications* **2023,** *14*, 3850.
119. Y. Jiang, X. Hou, Y. Zhou, et al., Mapping the nexus of electrical conductivity and gas sensing for tailored design of transition metal (Cu, Co, Ni)-based bimetallic 2D conjugated MOF. *ACS Materials Letters* **2025,** *7*, 76.
120. M. K. Smith, K. A. Mirica, Self-organized frameworks on textiles (SOFT): conductive fabrics for simultaneous sensing, capture, and filtration of gases. *Journal of the American Chemical Society* **2017,** *139*, 16759.
121. A. M. Eagleton, M. Ko, R. M. Stolz, et al., Fabrication of multifunctional electronic textiles using oxidative restructuring of copper into a Cu-based metal–organic framework. *Journal of the American Chemical Society* **2022,** *144*, 23297.
122. M. Ahmadipour, P. Damacet, C. Xiang, et al., Smart textile: Electrohydrodynamic jet printing of ionic liquid-functionalized $Cu_3(HHTP)_2$ metal–organic frameworks for gas-sensing applications. *ACS Applied Materials & Interfaces* **2025,** *17*, 12425−12439.
123. W. T. Koo, S. J. Kim, J. S. Jang, et al., Catalytic metal nanoparticles embedded in conductive metal–organic frameworks for chemiresistors: highly active and conductive porous materials. *Advanced Science* **2019,** *6*, 1900250.
124. Y.-M. Jo, K. Lim, J. W. Yoon, et al., Visible-light-activated type II heterojunction in Cu_3 (hexahydroxytriphenylene)$_2$/Fe_2O_3 hybrids for reversible NO_2 sensing: critical role of π–π* transition. *ACS Central Science* **2021,** *7*, 1176.
125. C. Park, W. T. Koo, S. Chong, et al., Confinement of ultrasmall bimetallic nanoparticles in conductive metal–organic frameworks via site-specific nucleation. *Advanced Materials* **2021,** *33*, 2101216.
126. J.-O. Kim, W.-T. Koo, H. Kim, et al., Large-area synthesis of nanoscopic catalyst-decorated conductive MOF film using microfluidic-based solution shearing. *Nature Communications* **2021,** *12*, 4294.
127. S. Xu, X. Liu, J. Wu, et al., NO_x sensor constructed from conductive metal–organic framework and graphene for airway inflammation screening. *ACS Sensors* **2023,** *8*, 2348.
128. C. Park, H. Shin, M. Jeon, et al., Single-atom catalysts in conductive metal–organic frameworks: Enabling reversible gas sensing at room temperature. *ACS Nano* **2024,** *18*, 26066.
129. T. Lee, J. O. Kim, C. Park, et al., Large-area synthesis of ultrathin, flexible, and transparent conductive metal–organic framework thin films via a microfluidic-based solution shearing process. *Advanced Materials* **2022,** *34*, 2107696.
130. S. Cho, C. Park, M. Jeon, et al., Interface-sensitized chemiresistor: Integrated conductive and porous metal-organic frameworks. *Chemical Engineering Journal* **2022,** *449*, 137780.

131. Y. Sun, B. Wang, Y. Hou, et al., Noble metal nanoparticles functionalized conductive Co_3(hexaiminotriphenylene)$_2$ chemiresistor for hydrogen sulfide detection at Room-Temperature. *Chemical Engineering Journal* **2023,** *465*, 142818.
132. M. Jeon, J.-S. Lee, M. Kim, et al., Triphenylene-based 2D cMOFs: Unraveling the H_2S sensing mechanism and applications for a real-time wireless chemiresistive sensor. *ACS Applied Materials & Interfaces* **2024,** *16*, 62382.
133. C. Huang, W. Sun, Y. Jin, et al., A general synthesis of nanostructured conductive metal–organic frameworks from insulating MOF precursors for supercapacitors and chemiresistive sensors. *Angewandte Chemie International Edition* **2024,** *63*, e202313591.
134. R. M. Stolz, A. Mahdavi-Shakib, B. G. Frederick, et al., Host–guest interactions and redox activity in layered conductive metal–organic frameworks. *Chemistry of Materials* **2020,** *32*, 7639.
135. V. Rubio-Giménez, N. Almora-Barrios, G. Escorcia-Ariza, et al., Origin of the chemiresistive response of ultrathin films of conductive metal–organic frameworks. *Angewandte Chemie* **2018,** *130*, 15306.
136. W. Bauhofer, J. Z. Kovacs, A review and analysis of electrical percolation in carbon nanotube polymer composites. *Composites Science and Technology* **2009,** *69*, 1486.
137. H. Frisch, J. Hammersley, Percolation processes and related topics. *Journal of the Society for Industrial and Applied Mathematics* **1963,** *11*, 894.
138. M. Ulrich, A. Bunde, C.-D. Kohl, Percolation and gas sensitivity in nanocrystalline metal oxide films. *Applied Physics Letters* **2004,** *85*, 242.
139. B. I. Armitage, K. Murugappan, M. J. Lefferts, et al., Conducting polymer percolation gas sensor on a flexible substrate. *Journal of Materials Chemistry C* **2020,** *8*, 12669.
140. C. Xu, J. Tamaki, N. Miura, et al., Grain size effects on gas sensitivity of porous SnO_2-based elements. *Sensors and Actuators B: Chemical* **1991,** *3*, 147.
141. M. Ulrich, C.-D. Kohl, A. Bunde, Percolation model of a nanocrystalline gas sensitive layer. *Thin Solid Films* **2001,** *391*, 299.
142. M. Ehsani, P. Rahimi, Y. Joseph, Structure–function relationships of nanocarbon/polymer composites for chemiresistive sensing: A review. *Sensors* **2021,** *21*, 3291.
143. Z.-Y. Xiong, B.-Y. Zhang, L. Wang, et al., Modeling the electrical percolation of mixed carbon fillers in polymer blends. *Carbon* **2014,** *70*, 233.
144. V. Roldughin, V. Vysotskii, Percolation properties of metal-filled polymer films, structure and mechanisms of conductivity. *Progress in Organic Coatings* **2000,** *39*, 81.
145. M. Panda, V. Srinivas, A. Thakur, Percolation behavior of polymer/metal composites on modification of filler. *Modern Physics Letters B* **2014,** *28*, 1450055.
146. H. L. Wang, L. Toppare, J. E. Fernandez, Conducting polymer blends: polythiophene and polypyrrole blends with polystyrene and poly (bisphenol A carbonate). *Macromolecules* **1990,** *23*, 1053.
147. Y. Cao, P. Smith, A. J. Heeger, Counter-ion induced processibility of conducting polyaniline and of conducting polyblends of polyaniline in bulk polymers. *Synthetic Metals* **1992,** *48*, 91.
148. B. Lundberg, B. Sundqvist, Resistivity of a composite conducting polymer as a function of temperature, pressure, and environment: applications as a pressure and gas concentration transducer. *Journal of Applied Physics* **1986,** *60*, 1074.
149. M. C. Lonergan, E. J. Severin, B. J. Doleman, et al., Array-based vapor sensing using chemically sensitive, carbon black− polymer resistors. *Chemistry of Materials* **1996,** *8*, 2298.
150. J. Sandler, J. Kirk, I. Kinloch, et al., Ultra-low electrical percolation threshold in carbon-nanotube-epoxy composites. *Polymer* **2003,** *44*, 5893.

151. R. Rahman, P. Servati, Efficient analytical model of conductivity of CNT/polymer composites for wireless gas sensors. *IEEE Transactions on Nanotechnology* **2014,** *14*, 118.
152. B. Philip, J. K. Abraham, A. Chandrasekhar, et al., Carbon nanotube/PMMA composite thin films for gas-sensing applications. *Smart Materials and Structures* **2003,** *12*, 935.
153. P. Freund, I. Senkovska, S. Kaskel, Switchable conductive MOF–nanocarbon composite coatings as threshold sensing architectures. *ACS Applied Materials & Interfaces* **2017,** *9*, 43782.
154. S. Watcharaphalakorn, L. Ruangchuay, D. Chotpattananont, et al., Polyaniline/polyimide blends as gas sensors and electrical conductivity response to CO–N_2 mixtures. *Polymer International* **2005,** *54*, 1126.
155. J. Wojkiewicz, V. Bliznyuk, S. Carquigny, et al., Nanostructured polyaniline-based composites for ppb range ammonia sensing. *Sensors and Actuators B: Chemical* **2011,** *160*, 1394.
156. C. Wei, L. Dai, A. Roy, et al., Multifunctional chemical vapor sensors of aligned carbon nanotube and polymer composites. *Journal of the American Chemical Society* **2006,** *128*, 1412.
157. J. Reemts, J. Parisi, D. Schlettwein, Electrochemical growth of gas-sensitive polyaniline thin films across an insulating gap. *Thin Solid Films* **2004,** *466*, 320.
158. C. Liu, K. Hayashi, K. Toko, Electrochemical deposition of nanostructured polyaniline on an insulating substrate. *Electrochemistry Communications* **2010,** *12*, 36.
159. K. Murugappan, M. R. Castell, Bridging electrode gaps with conducting polymers around the electrical percolation threshold. *Electrochemistry Communications* **2018,** *87*, 40.
160. W. Li, M. J. Lefferts, B. I. Armitage, et al., Polypyrrole percolation network gas sensors: Improved reproducibility through conductance monitoring during polymer growth. *ACS Applied Polymer Materials* **2022,** *4*, 2536.
161. W. Li, M. J. Lefferts, Y. Wang, et al., Chemiresistive polymer percolation network gas sensor created with a nanosphere template. *Advanced Materials Interfaces* **2023,** *10*, 2202042.
162. C. Cong, X. Li, W. Xiao, et al., Electrohydrodynamic printing for demanding devices: A review of processing and applications. *Nanotechnology Reviews* **2022,** *11*, 3305.
163. N. Mkhize, H. Bhaskaran, Electrohydrodynamic jet printing: Introductory concepts and considerations. *Small Science* **2022,** *2*, 2100073.
164. Y. Han, J. Dong, Electrohydrodynamic printing for advanced micro/nanomanufacturing: Current progresses, opportunities, and challenges. *Journal of Micro and Nano-Manufacturing* **2018,** *6*, 040802.
165. L. Hirt, A. Reiser, R. Spolenak, et al., Additive manufacturing of metal structures at the micrometer scale. *Advanced Materials* **2017,** *29*, 1604211.
166. J. He, B. Zhang, Z. Li, et al., High-resolution electrohydrodynamic bioprinting: a new biofabrication strategy for biomimetic micro/nanoscale architectures and living tissue constructs. *Biofabrication* **2020,** *12*, 042002.
167. Y. Wu, Y. Han, Y. S. Wong, et al., Fibre-based scaffolding techniques for tendon tissue engineering. *Journal of Tissue Engineering and Regenerative Medicine* **2018,** *12*, 1798.
168. H. Abdolmaleki, P. Kidmose, S. Agarwala, Droplet-based techniques for printing of functional inks for flexible physical sensors. *Advanced Materials* **2021,** *33*, 2006792.
169. P. Zhang, Z. Wang, J. Li, et al., From materials to devices using fused deposition modeling: A state-of-art review. *Nanotechnology Reviews* **2020,** *9*, 1594.
170. K. Kang, D. Yang, J. Park, et al., Micropatterning of metal oxide nanofibers by electrohydrodynamic (EHD) printing towards highly integrated and multiplexed gas sensor applications. *Sensors and Actuators B: Chemical* **2017,** *250*, 574.
171. J. Li, S. Li, S. Lu, et al., Selective detection of H2 by Pt-MCF/ZSA bilayer sensor prepared in situ via EHD jet printing. *Sensors and Actuators B: Chemical* **2024,** *418*, 136324.

172. Z. Zhan, G. Zheng, W. Tao, et al., Electrohydrodynamic impulse printing PANI sensor for NH3 gas. *Proceedings of the Institution of Mechanical Engineers, Part N: Journal of Nanoengineering and Nanosystems* **2012,** *226*, 9.
173. N. Mkhize, K. Murugappan, M. R. Castell, et al., Electrohydrodynamic jet printed conducting polymer for enhanced chemiresistive gas sensors. *Journal of Materials Chemistry C* **2021,** *9*, 4591.
174. N. Elgrishi, K. J. Rountree, B. D. McCarthy, et al., A practical beginner's guide to cyclic voltammetry. *Journal of Chemical Education* **2018,** *95*, 197.
175. T. Shaffner, R. Van Veld, 'Charging'effects in the scanning electron microscope. *Journal of Physics E: Scientific Instruments* **1971,** *4*, 633.
176. P. Qin, B. A. Day, S. Okur, et al., VOC mixture sensing with a MOF film sensor array: detection and discrimination of xylene isomers and their ternary blends. *ACS sensors* **2022,** *7*, 1666.
177. C. Li, Z. Zhang, L. Heinke, Mass transfer of toluene in a series of metal–organic frameworks: molecular clusters inside the nanopores cause slow and step-like release. *Physical Chemistry Chemical Physics* **2022,** *24*, 3994.
178. T. Sauerwald, S. Russ, Percolation effects in metal oxide gas sensors and related systems. *Gas Sensing Fundamentals* Springer: **2013**; pp 247.
179. F. Wang, H. Gu, T. M. Swager, Carbon nanotube/polythiophene chemiresistive sensors for chemical warfare agents. *Journal of the American Chemical Society* **2008,** *130*, 5392.
180. H.-J. Choi, M. S. Kim, D. Ahn, et al., Electrical percolation threshold of carbon black in a polymer matrix and its application to antistatic fibre. *Scientific Reports* **2019,** *9*, 6338.
181. H. Ren, T. Wei, Electrochemical synthesis methods of metal-organic frameworks and their environmental analysis applications: a review. *ChemElectroChem* **2022,** *9*, e202200196.
182. X. Wang, P. She, Q. Zhang, Recent advances on electrochemical methods in fabricating two-dimensional organic-ligand-containing frameworks. *SmartMat* **2021,** *2*, 299.
183. U. Müller, M. Schubert, F. Teich, et al., Metal–organic frameworks—prospective industrial applications. *Journal of Materials Chemistry* **2006,** *16*, 626.
184. N. Campagnol, T. R. Van Assche, M. Li, et al., On the electrochemical deposition of metal–organic frameworks. *Journal of Materials Chemistry A* **2016,** *4*, 3914.
185. X. Zhang, K. Wan, P. Subramanian, et al., Electrochemical deposition of metal–organic framework films and their applications. *Journal of Materials Chemistry A* **2020,** *8*, 7569.
186. S. Xie, W. Monnens, K. Wan, et al., Cathodic electrodeposition of MOF films using hydrogen peroxide. *Angewandte Chemie International Edition* **2021,** *60*, 24950.
187. Y. Xiao, Z. Wu, Q. Zhang, et al., Oxygen-assisted cathodic deposition of copper-carboxylate metal–organic framework films. *Crystal Growth & Design* **2020,** *20*, 3997.
188. G. Riveros, A. Garmendia, D. Ramirez, et al., Study of the electrodeposition of Cu_2O thin films from DMSO solution. *Journal of the Electrochemical Society* **2012,** *160*, D28.
189. L. Kafi-Ahmadi, B. Javanpour, Synthesis and characterization of new binuclear Co (II) and Ni (II) complexes derived from N, N′-bis (4-dimethyl-aminobenzylidene)-benzene-1, 3-diamine as active catalysts for hydroxylation of phenol and their antibacterial properties. *Reaction Kinetics, Mechanisms and Catalysis* **2020,** *130*, 935.
190. W. Zhao, F. Liu, X. Feng, et al., Fourier transform infrared spectroscopy study of acid birnessites before and after Pb^{2+} adsorption. *Clay Minerals* **2012,** *47*, 191.
191. S. Gao, Y. Huang, J. Tan, et al., Self-powered infrared photodetectors with ultra-high speed and detectivity based on amorphous Cu-based MOF films. *ACS Applied Materials & Interfaces* **2023,** *15*, 32637.
192. R. Li, S. Li, Q. Zhang, et al., Layer-by-layer assembled triphenylene-based MOFs films for electrochromic electrode. *Inorganic Chemistry Communications* **2021,** *123*, 108354.

193. A. C. Ferrari, J. Robertson, Interpretation of Raman spectra of disordered and amorphous carbon. *Physical Review B* **2000,** *61*, 14095.
194. D. Kwak, Y. Lei, R. Maric, Ammonia gas sensors: A comprehensive review. *Talanta* **2019,** *204*, 713.
195. P. Saxena, P. Shukla, A review on recent developments and advances in environmental gas sensors to monitor toxic gas pollutants. *Environmental Progress & Sustainable Energy* **2023,** *42*, e14126.
196. C. Wang, S. Lei, X. Li, et al., A reduced GO-graphene hybrid gas sensor for ultra-low concentration ammonia detection. *Sensors* **2018,** *18*, 3147.
197. A. D. Aguilar, E. S. Forzani, L. A. Nagahara, et al., A breath ammonia sensor based on conducting polymer nanojunctions. *IEEE Sensors Journal* **2008,** *8*, 269.
198. B. Kanjilal, A. Masoumi, N. Sharifi, et al., Ammonia harms and diseases: ammonia corrosion hazards on human body systems (liver, muscles, kidney, brain). Progresses in ammonia: science, technology and membranes, Elsevier: **2024**; pp 307.
199. P. Clifford, D. Tuma, Characteristics of semiconductor gas sensors II. Transient response to temperature change. *Sensors and Actuators* **1982,** *3*, 255.
200. R. W. Scott, S. Yang, G. Chabanis, et al., Tin dioxide opals and inverted opals: Near-ideal microstructures for gas sensors. *Advanced Materials* **2001,** *13*, 1468.
201. C. O. Park, S. Akbar, Ceramics for chemical sensing. *Journal of Materials Science* **2003,** *38*, 4611.
202. M. D'Arienzo, L. Armelao, A. Cacciamani, et al., One-step preparation of SnO_2 and Pt-doped SnO_2 as inverse opal thin films for gas sensing. *Chemistry of Materials* **2010,** *22*, 4083.
203. D. Zhang, Z. Wu, X. Zong, et al., Fabrication of polypyrrole/Zn_2SnO_4 nanofilm for ultra-highly sensitive ammonia sensing application. *Sensors and Actuators B: Chemical* **2018,** *274*, 575.
204. X. Chen, Y. Lu, J. Dong, et al., Ultrafast in situ synthesis of large-area conductive metal–organic frameworks on substrates for flexible chemiresistive sensing. *ACS Applied Materials & Interfaces* **2020,** *12*, 57235.
205. Z. Shan, J. Z. Xiao, M. Wu, et al., Topologically tunable conjugated metal–organic frameworks for modulating conductivity and chemiresistive properties for NH_3 sensing. *Angewandte Chemie International Edition* **2024,** *63*, e202401679.
206. M. Song, Y. Wu, J. Jia, et al., Catalysis-assisted synthesis of two-dimensional conductive metal–organic framework films with controllable orientation. *Journal of the American Chemical Society* **2025,** *147*, 17058.
207. J. Huotari, R. Bjorklund, J. Lappalainen, et al., Pulsed laser deposited nanostructured vanadium oxide thin films characterized as ammonia sensors. *Sensors and Actuators B: Chemical* **2015,** *217*, 22.
208. D. Kwak, M. Wang, K. J. Koski, et al., Molybdenum trioxide (α-MoO_3) nanoribbons for ultrasensitive ammonia (NH_3) gas detection: Integrated experimental and density functional theory simulation studies. *ACS Applied Materials & Interfaces* **2019,** *11*, 10697.
209. R. Abdelghani, H. S. Hassan, I. Morsi, et al., Nano-architecture of highly sensitive SnO2–based gas sensors for acetone and ammonia using molecular imprinting technique. *Sensors and Actuators B: Chemical* **2019,** *297*, 126668.
210. D. Punetha, S. K. Pandey In Optimization in NH 3 gas response of WO_3 nanorods based sensor array, 2019 IEEE SENSORS, IEEE: 2019; pp 1.
211. A. N. Begi, S. Hussain, M. J. Liaqat, et al., Unlocking low-concentration NH_3 gas sensing: An innovative MOF-derived In_2O_3/Co_3O_4 nanocomposite approach. *Materials Science in Semiconductor Processing* **2024,** *181*, 108641.
212. M. Xue, F. Li, D. Chen, et al., High-oriented polypyrrole nanotubes for next-generation gas sensor. *Advanced Materials* **2016,** *28*, 8265.

213. J. Cai, C. Zhang, A. Khan, et al., Highly transparent and flexible polyaniline mesh sensor for chemiresistive sensing of ammonia gas. *RSC Advances* **2018,** *8*, 5312.
214. C. Zhu, Y. Xu, T. Zhou, et al., Self-assembly polyaniline films for the high-performance ammonia gas sensor. *Sensors and Actuators B: Chemical* **2022,** *365*, 131928.
215. N. Mkhize, K. Murugappan, M. R. Castell, et al., Conducting polymer percolation gas sensor on a flexible substrate. *Journal of Materials Chemistry C* **2021,** *9*, 4591.
216. Y. Jiang, X. Hou, Y. Zhou, et al., Mapping the nexus of electrical conductivity and gas sensing for tailored design of transition metal (Cu, Co, Ni)-based bimetallic 2D conjugated MOF. *ACS Materials Letters* **2024,** *7*, 76.
217. X. Wang, Z. Mu, P. Shao, et al., Hierarchically porous covalent organic frameworks: synthesis methods and applications. *Chemistry–A European Journal* **2024,** *30*, e202303601.
218. M. Pérez-Page, E. Yu, J. Li, et al., Template-based syntheses for shape controlled nanostructures. *Advances in Colloid and Interface Science* **2016,** *234*, 51.
219. S. Xu, Y. Lei, Template-assisted fabrication of nanostructured arrays for sensing applications. *ChemPlusChem* **2018,** *83*, 741.
220. W.-T. Koo, S.-J. Choi, J.-S. Jang, et al., Metal-organic framework templated synthesis of ultrasmall catalyst loaded $ZnO/ZnCo_2O_4$ hollow spheres for enhanced gas sensing properties. *Scientific Reports* **2017,** *7*, 45074.
221. P. K. Pandey, A. Chandra, Evaporation of Ethanol from Liquid Ethanol and Water–Ethanol Mixtures: Mechanism, Kinetics, and Free Energy Changes for Different Compositions of the Mixtures. *The Journal of Physical Chemistry B* **2025,** *129*, 9737.
222. A. Minguzzi, F.-R. F. Fan, A. Vertova, et al., Dynamic potential–pH diagrams application to electrocatalysts for water oxidation. *Chemical Science* **2012,** *3*, 217.
223. T. Reier, M. Oezaslan, P. Strasser, Electrocatalytic oxygen evolution reaction (OER) on Ru, Ir, and Pt catalysts: a comparative study of nanoparticles and bulk materials. *ACS Catalysis* **2012,** *2*, 1765.
224. C. C. Yang, M. H. Tsai, Z. R. Yang, et al., Revealing the Surface Species Evolution on Low-loading Platinum in an Electrochemical Redox Reaction by Operando Ambient-Pressure X-ray Photoelectron Spectroscopy. *ChemCatChem* **2023,** *15*, e202300359.
225. S. Mollick, Y. Zhang, W. Kamal, et al., Resilient photoswitchable metal–organic frameworks for sunlight-induced on-demand photochromism in the solid state. *Chemical Engineering Journal* **2023,** *476*, 146727.
226. L. Ciambriello, E. Cavaliere, L. Gavioli, Influence of roughness, porosity and grain morphology on the optical properties of ultrathin Ag films. *Applied Surface Science* **2022,** *576*, 151885.
227. L. Mester, A. Govyadinov, S. Chen, et al., Subsurface chemical nanoidentification by nano-FTIR spectroscopy. *Nature Communications* **2020,** *11*, 3359.
228. M. Song, Y. Wu, J. Jia, et al., Catalysis-assisted synthesis of two-dimensional conductive metal–organic framework films with controllable orientation. *Journal of the American Chemical Society* **2025,** *147*, 17058.
229. Y. Huang, X. Zhang, S. Liu, et al., Wireless food-freshness monitoring and storage-time prediction based on ammonia-sensitive MOF@ SnS_2 PN heterostructure and machine learning. *Chemical Engineering Journal* **2023,** *458*, 141364.
230. S. Cai, X. Huang, M. Luo, et al., High-performance ammonia sensor at room temperature based on 2D conductive MOF $Cu_3(HITP)_2$. *Talanta* **2025,** *285*, 127226.
231. X. Wu, M. Niu, X. Tian, et al., Solution-processable $Ni_3(HITP)_2$/MXene heterostructures for ppb-level gas detection. *Journal of Materials Chemistry A* **2024,** *12*, 17382.
232. R. Rajamany, S. Prakash, Y. A. Ismail, Polyvinylpyrrolidone (PVP) assisted synthesis of Ni MOF: Enhanced supercapacitive performance through morphology control. *Next Materials* **2025**, *7*, 100459.

233. M. JIang, X. Cao, P. Lie, et al., ZIF-8@polyvinylpyrrolidone nanocomposites based n-doped porous carbon for highly efficient oxygen reduction reaction in alkaline solution. *Journal of The Electrochemical Society* **2016**, *6*, 163.